SEARCH FOR SUPERSYMMETRY USING DIPHOTON EVENTS IN PROTON-ANTIPROTON COLLISIONS AT A CENTER OF MASS ENERGY OF 1.96 TEV

A Dissertation

by

EUN SIN LEE

Submitted to the Office of Graduate Studies of
Texas A&M University
in partial fulfillment of the requirements for the degree of

DOCTOR OF PHILOSOPHY

May 2010

Major Subject: Physics

SEARCH FOR SUPERSYMMETRY USING DIPHOTON EVENTS IN PROTON-ANTIPROTON COLLISIONS AT A CENTER OF MASS ENERGY OF 1.96 TEV

A Dissertation

by

EUN SIN LEE

Submitted to the Office of Graduate Studies of
Texas A&M University
in partial fulfillment of the requirements for the degree of

DOCTOR OF PHILOSOPHY

Approved by:

Chair of Committee,	David Toback
Committee Members,	Teruki Kamon
	Bhaskar Dutta
	Sherry Yennello
Head of Department,	Edward Fry

May 2010

Major Subject: Physics

ABSTRACT

Search for Supersymmetry Using Diphoton Events
in Proton-Antiproton Collisions
at a Center of Mass Energy of 1.96 TeV. (May 2010)
Eun Sin Lee, B.S., Korea University, Seoul; M.S., Texas A&M University
Chair of Advisory Committee: Dr. David Toback

This dissertation presents the results of a search for supersymmetry in proton-antiproton collisions with a center of mass energy of 1.96 TeV studied with the Collider Detector at Fermilab. Our strategy is to select collisions with two photons in the final state that have the properties of being the decays of very massive supersymmetric particles. This includes looking for large total energy from the decayed particles as well as for the presence of particles that leave the detector without interacting. We find no events using 2.6 fb^{-1} of data collected during the 2004-2008 collider run of the Fermilab Tevatron which is consistent with the background estimate of 1.4±0.4 events. Since there is no evidence of new particles we set cross section limits in a gauge-mediated supersymmetry model with $\widetilde{\chi}_1^0 \rightarrow \gamma\widetilde{G}$, where the $\widetilde{\chi}_1^0$ and $\widetilde{G}$ are the lightest neutralino and the gravitino (the lightest supersymmetric particle), respectively. We set limits on models as a function of the $\widetilde{\chi}_1^0$ mass and lifetime, producing the world's most sensitive search for $\widetilde{\chi}_1^0$ by excluding masses up to 149 GeV/c^2 for $\widetilde{\chi}_1^0$ lifetimes much less than 1 ns.

"The roots of education are bitter,

but the fruit is sweet"

- Aristotle (384 BC-322 BC)

ACKNOWLEDGMENTS

No work in experimental high energy physics can be accomplished without the support of many other people. Their endless effort in building, running, and maintaining the CDF detector at Fermilab Tevatron is greatly appreciated. Since it is impossible to mention all the people and their contributions to my work in a few dissertation pages, I would like to just thank a few people who directly supported me and with whom I worked.

First and foremost I would like to thank my advisor and mentor, Professor Dave Toback. It is his courage, intuition, vast knowledge, and leadership that brought this work to completion. Without him this dissertation would never exist. He is the role model that I aspire to be as a senior scientist, as well as a supervisor. He always had enormous patience to listen to any types of abysmal questions from physics to minute everyday life. It is rare to find a person who believes in me so continuously and keeps me working as much as possible. His exceptional organizational skills enabled me to work on many things so effectively as a senior graduate student. Due to his tough correction style I learned how to professionally write journal papers and present beautiful talks at conferences successfully. Oh, thank God that I could work for such a first-rate person. I hope he is proud of having me as a student and one day I hope to do a hundredth of what he does.

I am also grateful to Teruki Kamon as my graduate academic advisor. He always had an open ear to whatever I had on my mind. Since the beginning of my studies at Texas A&M University he was with me and gave valuable advice when I was in trouble. I would like to thank my preliminary and defense exam committee members, Sherry Yennello and Bhaskar Dutta (who also gave me a nice lecture on Supersymmetry) for

the time they spent and for the interest they showed in my research work.

Many thanks to the excellent faculty members at Texas A&M University for giving me beautiful and valuable lectures that were indispensable to my research. A big thanks to Chris Pope, my former advisor, for his elegant lectures on General Relativity, Differential Geometry and Group Theory. I am especially grateful to Dick Arnowitt for making my eyes re-open to Quantum Mechanics. Thanks to Glenn Agnolet for unbelievably crystal-clear lectures on Statistical Mechanics. Special thanks to Ergin Sezgin for sharing his vast knowledge on Quantum Field Theory. Besides the teaching faculty, however, I am most grateful to Sandi Smith who was certainly the best person in the physics department for her endless effort of helping me and other students on many administrative issues.

I would also like to thank some physicists among the CDF collaboration at Fermilab. Ray Culbertson was certainly the best researcher to ask any technical questions that have to do with anything about photons at CDF, Stntuple software, and all other software tools. Many special thanks to Sasha Pronko who developed the METMODEL technique, one of the most important tools on my analysis. He always had enormous patience to explain this sophisticated tool in a easy way and tried to help me understand every single detail about it. Thanks to Monica D'onofrio, Tom Wright, and Ben Brau as exotic conveners for their valuable advice and help to get this analysis out the door. Special thanks also go to the Godparents and reviewers for my paper, Daniela Bortoletto, Andrey Loginov, and Sunil Somalwar who helped the analysis paper get through the collaboration so quickly.

Personally, I am indebted to Yeon-Sei Chung and his family, and other Korean friends for their hospitality during the last two years in Chicago. Special thanks to Dong-Hoon Kang and his family for their hospitality and support during my visit to Texas for my dissertation defense. Many thanks go to Han-gil Lee and Kyungwan

Kim, my fellow TAMU physics Korean graduate students for their help, encouragement, time and friendship for my first five years which were spent in College Station, TX. I am especially grateful to Matt Cervantes, Lucas Naveira, Dave Maffei and Mandy Woodward, who spent the better part of the first two years in the trenches with me. I will never forget playing racquetball, softball, soccer and even pictionary late night with them.

Finally, I would like to thank my parents, Jiha and Gyewon Jung, as well as my only brother, Euntaek and his family for their prayers and dedication; they have always given me great support in whatever I did. I am also grateful to my parents-in-law, Yongsin Kim and Gyungsun Jung, and brothers-in-law, Yooyoen and Daechang for their endless support. Special thanks to Pastor Hyunjun Park, who has been another father to me, for his agape love and financial support. And last, but absolutely not least, to Grace, who makes my life complete with her endless love and sacrifice. I could never survive and even exist in this world without her. May God bless my two precious sons, Benjamin and Joel for coming into my life!

TABLE OF CONTENTS

CHAPTER Page

CHAPTER Page

LIST OF FIGURES

FIGURE Page

FIGURE Page

FIGURE Page

FIGURE Page

FIGURE Page

FIGURE Page

FIGURE Page

FIGURE Page

FIGURE Page

LIST OF TABLES

TABLE Page

TABLE Page

TABLE Page

TABLE Page

TABLE Page

CHAPTER I

INTRODUCTION

A. Introduction

A 'Standard Model' is a theoretical framework built from observations that predict and describe old data and make quantitative predictions about outcomes of new experiments. For example, Mendeleev's table of the elements was an early example of this type of structure; from the periodic table one could predict the properties of many hitherto unstudied or undiscovered elements and/or compounds. Nonrelativistic quantum theory is another Standard Model that has made predictions that are confirmed by countless experiments. Like its precursors in other fields, the Standard Model of particle physics [1], hereafter denoted the SM, has been enormously successful in predicting a wide range of phenomena and in correlating vast amounts of data.

However, a major aspect of the SM is as yet untested, namely the origin of electroweak symmetry breaking [1]. The electroweak interaction is the unified description of two of the four fundamental interactions of nature: electromagnetism and the weak interactions. Although these two forces appear very different at everyday low energies, the theory models them as two different aspects of the same force. Above the unification energy, on the order of 100 GeV, they merge into a single electroweak force. The corresponding force carriers, the gauge bosons, are the photon of electromagnetism and the W and Z bosons of the weak force. In the SM, the weak gauge

---

This dissertation follows the style of Physical Review D.

bosons get their mass from the spontaneous symmetry breaking of the electroweak symmetry, caused by the Higgs mechanism [2].

The Higgs mechanism is just the simple ansatz that a gauge invariant theory undergoes spontaneous symmetry breaking as its potential develops a non-trivial value (non-zero vacuum expectation value) for the Higgs scalar field at its minimum. Unfortunately, the introduction of this Higgs scalar field has problems. The most famous is the infamous "hierarchy problem" [3], which describes the calculation of the Higgs mass which must take into account large quantum corrections from SM particles that can diverge. However, because the Higgs self-interaction terms are proportional to $G_F m_H^2$, where $G_F^{-1/2} \approx 300$ GeV is the Fermi constant and the m_H is the Higgs boson mass, it has frequently been remarked that a large Higgs boson mass implies a strong interaction among Higgs bosons. It has been emphasized that the Fermi constant is a natural mass scale of nature and that, if the Higgs self-coupling is strong, the effective ultraviolet cutoff would be at this energy [4]. It has also been shown that for Higgs boson masses exceeding approximately this energy the perturbation expansion of weak interactions may well break down [5]. These and other theoretical reasons [6, 7] suggest that the Higgs boson mass is most likely bounded by [8]:

$$m_H \leq \left(\frac{8\pi\sqrt{2}}{3G_F} \right)^{1/2} \simeq 1 \text{ TeV}/c^2. \tag{1.1}$$

It is not clear how large quantum corrections to the Higgs mass can exist and leave a Higgs mass below a TeV. Moreover, a strongly interacting scalar field theory is not self-consistent as a fundamental theory: the coupling constant grows with energy and therefore any finite coupling at high energy implies a weakly coupled theory at low energy. There is, therefore, compelling reason to believe that the SM Higgs mechanism is incorrect or incomplete, and that electroweak symmetry breaking must

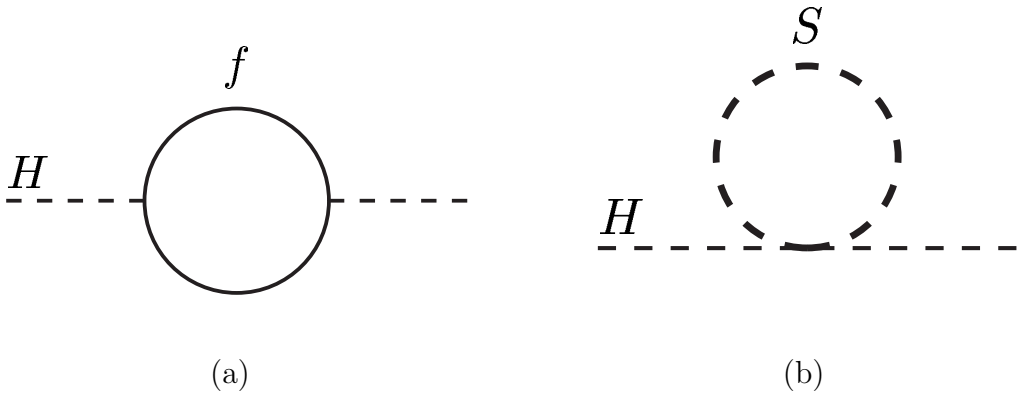

FIG. 1: The one-loop quantum corrections to the Higgs squared mass parameter m_H^2, due to (a) a Dirac fermion f, and (b) a scalar S. In supersymmetric extensions of the SM the contributions to the mass corrections produce a near cancellation of the Higgs boson quadratic mass correction due to the equal number of fermion (a) and scalar (b) loop Feynman diagrams for each particle type.

be associated with fundamentally "new" physics beyond the SM.

A remarkably elegant solution for the problem of the huge quantum corrections to the Higgs mass from SM particles can be overcome by extending the symmetry of the theory to one that relates gauge particles (bosons) to matter particles (fermions), known as supersymmetry (SUSY) [9]. In other words, the number of particles that can exist in nature is doubled; for every boson that currently exists in nature there is a fermionic "version". Similarly, for every fermion in nature there is a bosonic "version". Since quantum corrections from fermions and bosons have opposite signs in the loop corrections to the Higgs mass, as shown in Figure 1, many of them cancel in a supersymmetric theory; exactly if the masses are equal, and approximately if the partners are less than the TeV scale.

The most striking implication of the SUSY hypothesis is that each of the known particles, each of the quarks, leptons and gauge bosons, must have an associated partner, a "superpartner", that in principle should be observable. However, despite

multiple searches for these particles [10], none of the superpartners have been directly observed. These searches constrain the masses of most of them to be above the 100 GeV range or to have very weak couplings to the SM particles. On the other hand, for the Higgs mass corrections to be small (as would be expected), the sparticles are likely to have a mass scale less than the TeV range which should make them observables in high energy collision at current collider experiments.

On the other side of the size scale spectrum, experimental observations of the size scales of cosmology also give reason to believe that a revision of the SM is necessary. On cosmological scales, the structure of the cosmic microwave background suggests that 22% of mass of the universe is missing, called "dark matter", and favors the existence of a non-baryonic particle as a dark matter candidate [11]. While such a particle is not predicted by the SM, SUSY models provide excellent candidates.

To understand more how some of the problems at the biggest scales can be impacted by physics at the smallest scales requires an understanding of the ways that SM particles are likely to interact with SUSY particles. One of the primary features of many supersymmetric theories is that the existence of all these new particles could allow for the SM decay of the proton via SUSY loops. Since this has not yet been observed in nature, it has been postulated (and typically assumed) that there is a conservation law, typically known as "$R-$parity", which states that the number of SUSY particles in an interaction is conserved. This protects the proton lifetime and predicts that the lightest SUSY particle is stable [9]. The lightest SUSY particle, if neutral, would be copiously produced in the high energy collisions of the early Universe or as part of the decays of the other, heavier, SUSY particles. It would be around today because it is stable. Thus, SUSY could both provide a dark matter candidate and help solve the Higgs problems.

The SUSY hypothesis can be tested in particle collider experiments which at-

tempt to directly produce and observe sparticles in collisions. If the lightest SUSY particles are the dark matter, then they are likely to be weakly interacting and neutral and if produced in a collision they are likely to leave the detector without interacting. These particles can be identified by looking for a momentum imbalance in the set of measured final state particles that result from a collision, which is often referred to "missing energy ($\not\!\!E_T$)" [12] (described in detail in Chapter IV). This technique has been used for many years to infer the presence of other neutral weakly interacting particles such as the SM neutrinos. Since these particles are so weakly interacting it is unlikely they would be produced directly. However, SUSY models predict a large number of other heavy exotic, yet unobserved, particles that could be more readily produced (and always in pairs) and then detected by their decays into both visible and non-interacting particles. The essence of SUSY searches at colliders is to look for evidence of the production of SUSY particles which decayed into multiple, high energy particles, two of which left the detector without interacting, thus producing $\not\!\!E_T$. An observation of events with large amounts of $\not\!\!E_T$ and other high energy SM particles would be a golden signature.

In late 1990s an unusual collision ("event") was observed and extensively studied [13] during the Run I of the Fermilab Tevatron, a proton-antiproton ($p\bar{p}$) collider, with a center-of-mass energy ($\sqrt{s}$) of 1.8 TeV. This event produced two electron candidates, two photon candidates and missing energy ('$ee\gamma\gamma\not\!\!E_T$'). It was calculated to have a very tiny probability to come from SM processes. An attempt to understand the event in terms of known SM particles led to the speculation that the electrons and $\not\!\!E_T$ came from $WW \rightarrow e\nu e\nu$ production. Thus, the event would be $WW\gamma\gamma \rightarrow ee\gamma\gamma\not\!\!E_T$, either as a rare fluctuation from SM predictions or some anomalous production. While SM $WW\gamma\gamma$ production should produce roughly 10^{-6} such events in the data, the anomalous $WW\gamma\gamma$ production hypothesis was tested

quantitatively [13]. The anomalous $WW\gamma\gamma$ production would produce many more $WW\gamma\gamma \to q\bar{q}q\bar{q}\gamma\gamma$ events where the quarks are identified as "jets" produced by their hadronization of the quarks since the branching fraction of $WW \to$jets is much larger than $WW \to e\nu e\nu$. Since no anomalous production of these events was observed, it was concluded that the $\not\!\!E_T$ was unlikely to be from a SM neutrino from $W \to e\nu$. The $\not\!\!E_T$ could thus be from some new particle other than the left-handed neutrino. The lightest supersymmetric particle, if neutral, is a natural candidate.

To provide a SUSY explanation for this potential experimental hint we note that a special version of SUSY, known as Gauge Mediated SUSY Breaking or GMSB for short, predicts photons in the final states along with a neutral dark matter candidate that could account for the energy imbalance [14, 15]. These models will be described in the next section. A major feature of this model is that it predicts the production and decay of heavy, supersymmetric electrons. Each supersymmetric electron would then decay to an electron and a "neutralino ($\widetilde{\chi}_1^0$)", which is described more in Section I.B.2, but can be thought of as a supersymmetric photon for now. The $\widetilde{\chi}_1^0$ then decays into a photon and a "gravitino ($\widetilde{G}$)" which is the supersymmetric partner of the as-yet-unobserved graviton. The gravitino is the dark matter candidate as the lightest SUSY particle and is weakly interacting, neutral and stable. As such, it leaves the detector and causes $\not\!\!E_T$. In this case the $ee\gamma\gamma\not\!\!E_T$ event could be the production and decay of a pair of supersymmetric electrons, $\widetilde{e}$, which both decay via $\widetilde{e} \to e + \widetilde{\chi}_1^0 \to e + \gamma\widetilde{G}$.

As described so far theoretical motivations, dark matter observations and the observation of the '$ee\gamma\gamma\not\!\!E_T$' candidate event provide compelling rationale to search for the production and decay of new heavy, neutral SUSY particles that produce events with final state photons with $\not\!\!E_T$ in collider experiments. There are a number of other SUSY theories that have these properties [16], but we focus on GMSB since it is currently the most compelling. In addition it provides a natural framework for

more model-independent search strategies. Within this model, there are a number of free parameters in the theory, including the lifetime of the lightest neutralinos. Each scenario produces a number of different phenomenological features that can produce distinct final states that need to be searched for in an experiment [15, 17]. Thus, a number of searches for both high lifetime ($\tau_{\widetilde{\chi}_1^0} \gtrapprox 5$ ns) [18, 19] and low lifetime [13, 18, 20, 21] neutralinos have already been done. Since at the time of this analysis the Tevatron was the highest energy collider we have taken the opportunity to search for the production of a pair of supersymmetric particles.

This dissertation presents the world's most sensitive search for low-lifetime $\widetilde{\chi}_1^0$ GMSB models by looking at Tevatron collisions for the pair production of SUSY particles, each of which decays into SM particles as well as a neutralino which decays, in turn, to a photon and a gravitino. We search directly for evidence of anomalous production of events with two photons and missing energy in association with a large amount of energy from other SM particles. In this search we focus on the case where the lifetime of the $\widetilde{\chi}_1^0$ is small, less than 2 ns. In doing so we are the first to directly take into account the possibility of the $\widetilde{\chi}_1^0$ having a non-zero lifetime, but still showing up with the two photon final state. This analysis significantly extends the search sensitivity to these models, compared to other previous Tevatron and LEP searches [18–21], and sets the world's best limits. We begin with a more complete description of the theoretical underpinnings of this search.

B. Theory

This section provides a more detailed description of supersymmetry to help motivate our search. We begin with a description of the concepts and main features of the minimal supersymmetric standard model (MSSM) [9], and in the next sections we

outline the phenomenology of the particular version considered, Gauge Mediated Supersymmetry Breaking. Finally, we use the results of previous searches and other constraints to help point to the most favored search region at the Tevatron. These include constraints from cosmology for GMSB [15], astronomical observations of the dark matter [11] and non-observations from previous collider experiments [10].

1. Supersymmetry

Supersymmetry is the idea that at the fundamental level the basic laws of nature are invariant if fermions and bosons are interchanged in the theory (i.e. in the Lagrangian). In the SM quarks and leptons (both fermions) are the matter particles. The particles that mediate the forces are the 'gauge bosons', γ, W, Z, g. Another particle, the Higgs boson, is responsible for giving both fermions and bosons their masses [2]. Within the SM fermions and bosons are treated very differently and a SUSY transformation turns a bosonic state into a fermionic state, and vice versa. The operator Q that generates such transformations must be an anticommuting spinor such that

$$Q|\text{Boson}\rangle = |\text{Fermion}\rangle, \quad \text{Q}|\text{Fermion}\rangle = |\text{Boson}\rangle. \tag{1.2}$$

The single-particle states of a supersymmetric theory fall into irreducible representations of the SUSY algebra, called supermultiplets. Each supermultiplet contains both fermion and boson states, which are commonly known as superpartners of each other. While a combination of a two-component Weyl fermion (left-handed and right-handed) and its own complex scalar partner is called a chiral or matter multiplet, the other combination of spin-1 vector gauge bosons and their fermionic partners are called gauge or vector supermultiplets. The minimal, phenomenologically viable type of supersymmetric model is sometimes called $N = 1$ SUSY, MSSM [9], where N refers

to the number of supersymmetries.

The common names for the spin-0 partners of the quarks and leptons are labeled by prepending an "s", for scalar, and generically are called "squarks" and "sleptons", or sometimes "sfermions". Similarly the fermionic partners to the SM gauge bosons get an "ino" suffix, and are called "gauginos". The symbols for the sfermions and gauginos are the same as for the corresponding fermion and gauge boson, but with a tilde ($\widetilde{}$) used to denote the superpartner of a SM particle. These chiral and gauge supermultiplets make up the particle content of the MSSM. In addition to the known particles of the SM, in the MSSM, there are two complex Higgs doublets $H_u = (H_u^+, H_u^0)$ and $H_d = (H_d^0, H_d^-)$, where the subscript u denotes for coupling to charge $+2/3$ up-type quarks (up, charm, top) and d to charge $-1/3$ down-type quarks (down, strange, bottom) and to the charged leptons, rather than just one in the ordinary SM. There is also the gravitino which is postulated to be the SUSY partner of the as yet undiscovered graviton which, from astronomy observations and General Relativity, is believed to be spin 2 [22]. The particle contents of the MSSM are shown in Table I.

In the chiral supermultiplets of the MSSM the spin-0 fields are complex scalars, and the spin-1/2 fields are left-handed two-component Weyl fermions. The gauge supermultiplets have the W^0, B^0 gauge eigenstates mix to give mass eigenstates Z^0 and γ and the corresponding mixtures of the $\widetilde{W}^0$ and $\widetilde{B}^0$ are called the zino ($\widetilde{Z}^0$) and photino ($\widetilde{\gamma}$), respectively. The higgsinos and electroweak gauginos mix with each other because of the effects of electroweak symmetry breaking. The neutral higgsinos ($\widetilde{H}_u^0$, $\widetilde{H}_d^0$) and the neutral gauginos ($\widetilde{B}$, $\widetilde{W}^0$) combine to form four mass eigenstates called "neutralinos". The charged higgsinos ($\widetilde{H}_u^+$, $\widetilde{H}_d^-$) and winos ($\widetilde{W}^+$, $\widetilde{W}^-$) mix to form two mass eigenstates with charge ± 1 called "charginos". These are denoted as the neutralino and chargino mass eigenstates by $\widetilde{\chi}_i^0$ $(i = 1, 2, 3, 4)$

and $\widetilde{\chi}_i^{\pm}$ $(i = 1, 2)$. By convention, these are labeled in ascending mass order, so that $m_{\widetilde{\chi}_1^0} < m_{\widetilde{\chi}_2^0} < m_{\widetilde{\chi}_3^0} < m_{\widetilde{\chi}_4^0}$ and $m_{\widetilde{\chi}_1^{\pm}} < m_{\widetilde{\chi}_2^{\pm}}$. In the MSSM there are 32 distinct masses corresponding to undiscovered particles, not including the gravitino, which are summarized in Table II, along with their gauge eigenstate particles.

The general superpotential of the MSSM contains terms where the baryon and the lepton numbers are violated. Since both baryon and lepton number conservation have been tested to a high degree of precision [10], in order to forbid this, each particle is assigned a quantum number, $R-$parity [23], which is defined as

$$R = (-1)^{3(B-L)+2s} \tag{1.3}$$

where B (L) is its baryon (lepton) number and s is the spin of the particle. This quantity is constructed so that $R = +1$ for the particles of the SM (including the Higgs bosons) and $R = -1$ for their SUSY partners. The R acts differently on particles of different spin in the same supermultiplet, so $R-$parity is a discrete symmetry. If $R-$parity is conserved, then there can be no mixing between the SM particles and the sparticles. The $R-$parity conservation has extremely important phenomenological consequences [23]. They include:

- The lightest supersymmetric particle, LSP, must be absolutely stable by conservation of energy and $R-$parity. If the LSP is electrically neutral, it interacts only weakly with ordinary matter, and so can make an attractive dark matter candidate for the observed missing mass of the universe [11].

- Each sparticle other than the LSP must eventually decay into a state that contains an odd number of LSPs (usually just one) unless there are other symmetries in nature.

- In collider experiments between SM particles, sparticles can only be produced

TABLE I: The particles of the MSSM. In chiral supermultiplets the spin-0 fields are complex scalars, and the spin-1/2 fields are left-handed two-component Weyl fermions. In the gauge supermultiplets the W^0, B^0 gauge eigenstates mix to give the mass eigenstates Z^0 and γ and the corresponding mixtures of $\widetilde{W}^0$ and $\widetilde{B}^0$ are called zino ($\widetilde{Z}^0$) and photino ($\widetilde{\gamma}$).

Chiral supermultiplets		
Names	spin 0	spin 1/2
squarks, quarks	$(\widetilde{u}_L\ \widetilde{d}_L)$	$(u_L\ d_L)$
($\times$3 families)	$\widetilde{u}^*_R$	$u^\dagger_R$
	$\widetilde{d}^*_R$	$d^\dagger_R$
sleptons, leptons	$(\widetilde{\nu}\ \widetilde{e}_L)$	$(\nu\ e_L)$
($\times$3 families)	$\widetilde{e}^*_R$	$e^\dagger_R$
Higgs, higgsinos	$(H^+_u\ H^0_u)$	$(\widetilde{H}^+_u\ \widetilde{H}^0_u)$
	$(H^0_d\ H^-_d)$	$(\widetilde{H}^0_d\ \widetilde{H}^-_d)$
Gauge supermultiplets		
Names	spin 1/2	spin 1
gluino, gluon	$\widetilde{g}$	g
winos, W bosons	$\widetilde{W}^\pm\ \widetilde{W}^0$	$W^\pm\ W^0$
bino, B boson	$\widetilde{B}^0$	B^0
Other MSSM particles		
Names	spin 1/2 (3/2)	spin 2
goldstino (gravitino), graviton	$\widetilde{G}$	G

TABLE II: The gauge and mass eigenstate particles in the MSSM (with sfermion mixing for the first two families assumed to be negligible). Note that the spin 1/2 goldstino becomes the longitudinal components of the spin 3/2 gravitino, superpartner of the spin 2 graviton. Couplings of the spin 1/2 goldstino components are only directly relevant to collider phenomenology for a gravitino which is much lighter than the energy scale of a collider experiment. In addition, the spin 3/2 components only couple with gravitational strength and are not relevant to the collider phenomenology [24].

Names	Spin	Gauge Eigenstates	Mass Eigenstates
squarks	0	$\widetilde{u}_L\ \widetilde{u}_R\ \widetilde{d}_L\ \widetilde{d}_R$	(same)
		$\widetilde{s}_L\ \widetilde{s}_R\ c_L\ \widetilde{c}_R$	(same)
		$t_L\ \widetilde{t}_R\ \widetilde{b}_L\ \widetilde{b}_R$	$\widetilde{t}_1\ \widetilde{t}_2\ \widetilde{b}_1\ \widetilde{b}_2$
sleptons	0	$\widetilde{e}_L\ \widetilde{e}_R\ \widetilde{\nu}_e$	(same)
		$\widetilde{\mu}_L\ \widetilde{\mu}_R\ \widetilde{\nu}_\mu$	(same)
		$\widetilde{\tau}_L\ \widetilde{\tau}_R\ \widetilde{\nu}_\tau$	$\widetilde{\tau}_1\ \widetilde{\tau}_2\ \widetilde{\nu}_\tau$
neutralinos	1/2	$\widetilde{B}^0\ \widetilde{W}^0\ \widetilde{H}_u^0\ \widetilde{H}_d^0$	$\widetilde{\chi}_1^0\ \widetilde{\chi}_2^0\ \widetilde{\chi}_3^0\ \widetilde{\chi}_4^0$
charginos	1/2	$\widetilde{W}^\pm\ \widetilde{H}_u^+\ \widetilde{H}_d^-$	$\widetilde{\chi}_1^\pm\ \widetilde{\chi}_2^\pm$
gluino	1/2	$\widetilde{g}$	(same)
goldstino (gravitino)	1/2 (3/2)	$\widetilde{G}$	(same)

in pairs, which will always decay into a pair of LSP's plus other SM particles that can be identified.

As previously noted, none of the superpartners have been discovered as of this writing. If SUSY were a perfect symmetry then the SUSY particles would have masses that are exactly equal to the corresponding SM particles (like particles and anti-particles) and these particles would have been easily detected long ago. Clearly, therefore, SUSY is a broken symmetry in the vacuum state chosen by Nature [9].

The mechanism of SUSY breaking is not yet understood. From the example of spontaneous symmetry breaking in the SM, it is reasonable to expect that in the MSSM there is a field whose vacuum expectation value leads to the SUSY breaking. However, in practice, this has not worked for theoretical reasons [9]. A solution to this difficulty is to construct models of spontaneously broken SUSY using a different strategy from the one that we use for electroweak symmetry breaking in the SM. A popular and well motivated choice is to break SUSY by introducing a new "hidden sector", which is a collection of yet-unobserved quantum fields and corresponding hypothetical particles at a much higher mass scale that do not directly interact with the leptons, quarks, or gauge bosons. In this way SUSY breaking relies on a weak coupling of the hidden sector to the observable MSSM particles (in the "visible" sector) to share some interactions that are responsible for mediating the SUSY breaking terms. What is particularly appealing about this solution is that if SUSY is spontaneously broken in this hidden sector, which has no direct coupling to quarks, leptons, and SM gauge bosons, it avoids quadratic divergences of the SUSY breaking terms. This is called a "soft" SUSY breaking interaction. We next turn to the mechanism of SUSY breaking as it has a direct impact on the observables in collider experiments.

2. Gauge Mediated Supersymmetry Breaking

There have been two main competing proposals for what the mediating interactions might be. The first (and historically the more popular) is that they are gravitational in nature, often called gravity-mediated supersymmetry breaking or "Supergravity" [25]. A second possibility is that the interactions for SUSY breaking are gauge-mediated using the ordinary SM gauge interactions. This is known as Gauge Mediated Supersymmetry Breaking or GMSB [14]. While there have been many searches [10] for both types of models, and others, all searches have yielded null results. The bulk of direct searches for SUSY in collider experiments have focused on the Supergravity type models since they provide a heavy (cold) dark matter candidate [26].

Theories with Gauge Mediated SUSY breaking [9, 14, 15] provide an important alternative to the supergravity scenario. These models have the significant advantage that they allow for a natural suppression of flavor violations in the SUSY sector and have very distinctive phenomenological features as they produce photons from decay of $\widetilde{\chi}_1^0 \rightarrow \gamma \widetilde{G}$, for the reasons described below.

a. Theory and Phenomenology

In general, GMSB arises if the breaking mechanism originates in a hidden sector and is then "mediated" to the visible MSSM sector by some massive fields that also transform under the SM gauge groups (see Figure 2). These heavy fields are referred to as messengers, with the messenger masses determining the messenger scale M_m. The breaking mechanism causes fields that couple to the messenger fields to acquire a SUSY breaking vacuum expectation value, $\langle F \rangle$. The messenger fields thus become massive and give masses to the MSSM fields dynamically via loop corrections. If the mass scale of the hidden sector is given by Λ, then the visible MSSM sector

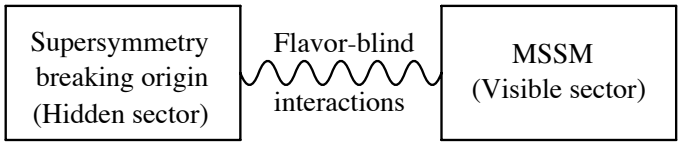

FIG. 2: A schematic of the structure for (flavor-blind) gauge mediated supersymmetry breaking.

superpartner masses are of the order of

$$m \sim \frac{\langle F \rangle}{M_m} \sim \frac{\Lambda^2}{M_m} \tag{1.4}$$

where $\sqrt{F}$ is the fundamental ("intrinsic") SUSY breaking scale. In principle the messenger scale can be anywhere between just above the electroweak scale up to the Plank scale [14]. In GMSB models a messenger scale that is significantly below the Plank scale is generally preferred to be less than 10^{16} GeV/c^2 to realize SUSY breaking at low energy. On the other side, the messenger scale is also required to be greater than $\sqrt{F}$ to avoid flavor breaking [14]. Thus, if M_m and $\sqrt{F}$ are roughly comparable then the scale of SUSY breaking can be as low as about $\sqrt{F} \sim$10 TeV/c^2, while the messenger mass scale is $M_m \sim$100 TeV/c^2 [27]. In this case the gravitino mass is well below the MSSM superpartner masses and electroweak symmetry breaking results in the rest of the sparticles of the MSSM having TeV scale masses given by

$$m_{\tilde{\chi}_1^0} = \frac{F}{\sqrt{3}M_P} \simeq 2.4 \left(\frac{\sqrt{F}}{100 \text{ TeV}} \right)^2 \text{ eV} \tag{1.5}$$

where $M_P = 2.4 \times 10^{18}$ GeV is the Plank mass. This would keep the Higgs mass, due to the loop corrections described previously, both finite and at electroweak masses (below a TeV). Since all the sparticles masses would be below a TeV this has the advantage to experimentalists that they are detectable at the Tevatron.

There are both fundamental and phenomenological differences between Super-

gravity and GMSB. Many are related to the problem of how they solve the problem of lepton flavor or quark flavor violating processes such as $\mu \rightarrow e\gamma$ decay, $K \leftrightarrow \bar{K}$ oscillations, or $b \rightarrow s\gamma$ decay [24]. Most of the new parameters in the soft SUSY breaking terms comply with the observations of these flavor mixing processes that are severely restricted by experimental data. Supergravity models have trouble keeping these processes at low levels [25]. Perhaps the most appealing theoretical feature of GMSB, therefore, is the natural lack of SUSY contributions to flavor violation. This arises because the leading contributions to visible sector soft SUSY breaking involving the squark and slepton superpartners depends only on gauge couplings, which do not distinguish between the three generations of leptons and quarks. All soft SUSY breaking parameters are then automatically flavor independent or aligned with the quark or lepton Yukawa couplings, which are the only relevant sources of flavor violation, as in the SM. This is generally possible if the messenger scale, M_m, is well below the flavor violating scale, which is otherwise expected to be as large as the Plank scale. But with high-scale SUSY breaking arising from Plank scale operators, as in supergravity models, no separation of the messenger and flavor scales is possible and it is difficult to enforce a symmetry in the high energy theory that can prevent flavor violation in the visible sector soft SUSY breaking parameters [14]. Even with GMSB, however, if the messenger scale is not too far below the flavor scale, this presents the possibility of observing small lepton flavor violation with NLSP sleptons [28]. The bottom line is that while there are many advantages and disadvantages of GMSB it provides a compelling theory to search for in data in addition to the fact that it provides a possible explanation for a number of experimental observations which may or may not be artifacts. We next move on to phenomenological studies of GMSB at the Fermilab Tevatron.

b. The Phenomenological Model Line

As there are many different versions of GMSB models we consider a minimal GMSB model in this analysis. While the minimal models are described by only a few parameters, it is useful to reduce the number of parameters even further by making well motivated assumptions about relationships between them. In particular, if we can find relationships that keep the phenomenology to be similar over large portions of the parameter space this is very convenient from an experimental stand point and ideally the model can be parameterized linearly with one or two parameters which are well correlated with observables. A particular combination of parameters that produces a single linear parameterization is known as a "model line". In order to understand our discovery sensitivity and to simplify the search process for a collider experiment it is useful to introduce this notion of a "model line" and to have one of our parameters be the mass of the lightest neutralino, $m_{\tilde{\chi}_1^0}$. We will allow a second parameter to vary to retain more inclusiveness, the lifetime of the lightest neutralino, $\tau_{\tilde{\chi}_1^0}$.

The minimal GMSB model is useful for phenomenological studies since the model is well specified in terms of six free parameters, which can be related using a model line for the masses. Their meaning and importance can be summarized as follows [14]:

- Λ: This parameter describes the mass scale of the visible sector SUSY breaking. As such it sets the overall mass scale for all the MSSM superpartners (see Eq. 1.4). For superpartners with masses at the electroweak mass scale we find this parameter is $\Lambda \sim \mathcal{O}(100 \text{ TeV})/\sqrt{N_m}$, where N_m is the number of messenger generations. To first approximation, all of the MSSM superpartner masses scale linearly with Λ.

- N_m: This is the number of messenger generations. The gaugino masses scale

like the number of messenger generations, N_m, while the squark and slepton masses scale like $\sqrt{N_m}$. Phenomenologically, for low values of N_m, a neutralino, $\widetilde{\chi}_1^0$, is the next-to-lightest SUSY particle (NLSP), while for larger values a right-handed slepton, $\widetilde{l}_R$, is the NLSP.

- M_m: The messenger scale that specifies the mass scale at which the MSSM sparticles obtain their masses radiatively from gauge interaction with the massive messenger fields. The electroweak scale and all of the sparticle masses are a function of M_m, but depend only on its logarithm. We only consider models with $M_m > \Lambda$ since only these models avoid flavor breaking in the messenger sector, which is one of the advantages of GMSB. A second constraint we impose is that $M_m \lesssim 10^{16}$ GeV so SUSY is broken at low energy and helps solve the hierarchy problem.

- $\tan\beta$: The ratio of MSSM Higgs vacuum expectation values. For our purposes we only consider values in a range $1.5 \lesssim \tan\beta \lesssim 60$. The lower limit is from limits on light CP-even Higgs scalars, which are excluded by the LEP experiments [29]. Large value of $\tan\beta$ yield a $\widetilde{\tau}$ slepton which is significantly lighter than the other sleptons [14] and can be the NLSP which would remove the $\widetilde{\chi}_1^0 \to \gamma\widetilde{G}$ final state so we ignore it here.

- sgn(μ): The sign of Higgs and Higgsino supersymmetric mass parameter μ which appears in the chargino and neutralino mass matrices. This is correlated with the sign of the MSSM correction to the anomalous magnetic moment of the muon, $g-2$, which is favored to be positive at the 3σ level [30].

- $C_{\widetilde{G}}$: The ratio of the messenger sector SUSY breaking order parameter (F_s) to the intrinsic SUSY breaking order parameter (F). This controls both the $\widetilde{G}$

mass and the NLSP lifetimes since the NLSP lifetime scales like $C_{\widetilde{G}}^2$.

In this analysis we consider a minimal GMSB model and choose to look at versions with an $\widetilde{\chi}_1^0$ NLSP that decays via $\widetilde{\chi}_1^0 \to \gamma\widetilde{G}$ with a branching ratio of $\sim$100% to maximize the search sensitivity. As there are many GMSB parameter combinations that match this phenomenology, representative model lines have been identified that cover specific characteristics of SUSY model (e.g., GMSB models with an $\widetilde{\chi}_1^0$ NLSP) with only one free parameter that sets the sparticle masses and one parameter that sets the NLSP lifetime. We choose this analysis to follow the Snowmass Points and Slopes (SPS) model line 8 [31], which is:

$$\begin{aligned} M_m &= 2\Lambda \\ \tan\beta &= 15 \\ \mathrm{sgn}(\mu) &= 1 \\ N_m &= 1 \end{aligned}$$

where Λ determines the gaugino and sfermion masses and $C_{\widetilde{G}}$ controls the $\widetilde{G}$ mass and $\widetilde{\chi}_1^0$ lifetime; both are allowed to vary independently. This parametrization has been used in multiple searches at the Tevatron and at LEP.

For this model line the $\widetilde{\chi}_1^0$ is the NLSP and the gravitino is the LSP. Taking these model parameters is the equivalent of taking the $m_{\tilde{\chi}_1^0}$ and $\tau_{\tilde{\chi}_1^0}$, as free parameters, which we do for clarity of presentation and for use for future model builders. As calculated in [15] the $\widetilde{\chi}_1^0$ lifetime, $\tau_{\tilde{\chi}_1^0}$, is given by

$$\tau_{\tilde{\chi}_1^0} = C \cdot \left(\frac{100\ \mathrm{GeV}}{m_{\tilde{\chi}_1^0}}\right)^5 \cdot \left(\frac{m_{\widetilde{G}}}{1\ \mathrm{keV}}\right)^2 \mathrm{ns} \tag{1.6}$$

where $C = 69.33$, with $m_{\widetilde{G}}$ in keV and $m_{\tilde{\chi}_1^0}$ in GeV.

In the next sections we consider further constraints to help us focus our search.

In particular, we consider constraints from collider experiments, astronomy and cosmology, especially using the assumption that the gravitino is the dark matter. Finally, we discuss the phenomenology we would expect to observe from proton-antiproton collisions with $\sqrt{s} = 1.96$ TeV at the Fermilab Tevatron.

c. Cosmological Constraints on GMSB

As described earlier, if R-parity is conserved then the lightest supersymmetric particle (LSP) will be absolutely stable. This conclusion has an important implication for the relation of SUSY to cosmology [27] and observed astronomical observations [11]. Many astronomical observations of dark matter over the last 40 years can be explained by the presence of enormous amounts of invisible, weakly interacting particles. In the past few years, measurements of the cosmic microwave background have given a new source of measurement of the dark matter density in the Universe which has been interpreted multiple ways [11]. Since this data comes from an era in the early universe, before the formation of any structure, it argues strongly that the invisible matter is not made of rocks or brown dwarfs but is actually a new, very weakly interacting form of matter. These measurements also determine quite accurately the overall amount of ordinary matter ($4.6 \pm 0.1\%$) and dark matter ($23.3 \pm 1.3\%$) in the universe (the rest of the universe ($72.1 \pm 1.5\%$) is believed to be dark energy). Evidence from experimental cosmology has now solidified to the point that, with some plausible assumptions, the dark matter density, $\Omega_{\rm DM}$, is measured to be

$$\Omega_{\rm DM} h^2 = 0.110 \pm 0.006 \tag{1.7}$$

where h is the Hubble constant in units of 100 km sec^{-1} Mpc^{-1} and $\Omega_{\rm DM}$ is the average energy density in non-baryonic dark matter divided by the total critical density that would lead to a spatially flat and homogenous universe.

In GMSB models where R-parity is conserved the $\widetilde{G}$ is stable and important upper and lower bounds come from its contribution to the energy density [14]. If gravitinos are in thermal equilibrium in the early universe and freeze out at the temperature T_f, their contribution to the present energy density, $\Omega_{\widetilde{G}}$, is given by [32]

$$\Omega_{\widetilde{G}} h^2 = \frac{m_{\widetilde{G}}}{\text{keV}} \left[\frac{100}{g^*(T_f)} \right] \tag{1.8}$$

where $m_{\widetilde{G}}$ is in keV and $g^*(T_f)$ is the effective number of degrees of freedom at T_f, which is typically between 100 and 200 in a supersymmetric model [33]. This produces an upper bound on the gravitino mass as only $m_{\widetilde{G}} <$ keV would not lead to overclosure of the Universe (causing it to collapse after a short time) [34]. In this case there is no need for a mechanism of late entropy production required to dilute the gravitino abundance which would otherwise cause an overly large and unobserved relic density [35]. On the other side, if the $\widetilde{G}$'s are too light then despite their small interaction strengths there would be so many of them that they could destroy the nuclei produced during the Big Bang Nucleosynthesis and can lead to a cosmic microwave background that is inconsistent with observations [36]. Taking all these things together, gravitinos could be the dark matter and give the dominant contribution to the present energy density from Eq. 1.7 if $m_{\widetilde{G}}$ is about a keV. Thus, gravitinos would behave as "warm" dark matter since they are usually produced as relativistic final states in the decay of heavy particles and may never reach thermal equilibrium, keeping most of their initial energy[1] [35].

For the purpose of this analysis we consider the $\widetilde{G}$ mass range, $0.5 \leq m_{\widetilde{G}} \leq 1.5$ keV/c^2, to be the cosmology favored region. Following Eq. 1.6 we have a relation between the neutralino mass and lifetime as shown in Figure 3. This shows the region

[1]Cold dark matter candidates are usually produced by scattering in the thermal bath, then reach equilibrium and finally decouple after they become non-relativistic.

of $\widetilde{\chi}_1^0$ mass and lifetime that are consistent with these constraints and the model line used in this search.

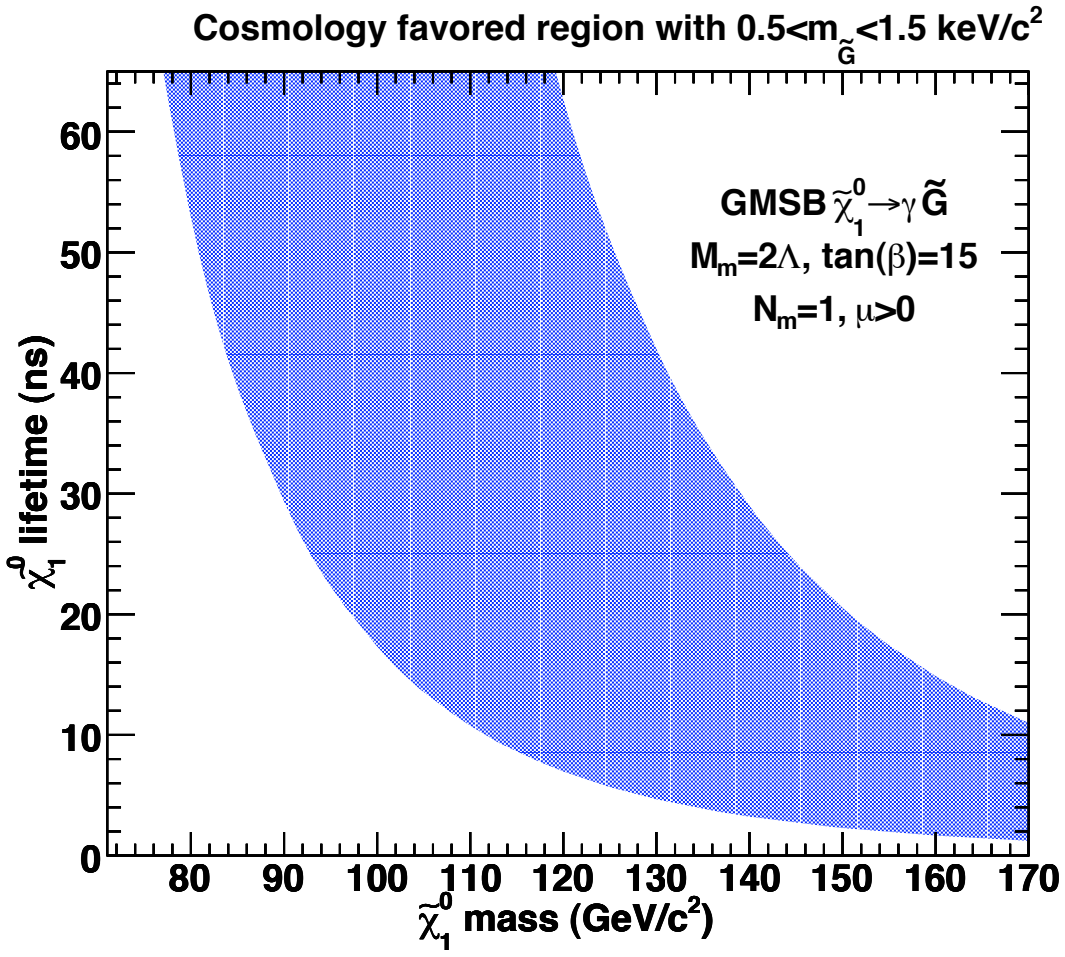

FIG. 3: The cosmology favored region, where the $\widetilde{G}$ could be a warm dark matter candidate, in the $\widetilde{\chi}_1^0$ mass and lifetime region for the model line used in this search. The $\widetilde{G}$ mass range, $\sim$0.5 (lower bound) - 1.5 (upper bound) keV/c^2, is considered.

d. Collider Phenomenology

Non-observation of neutralinos from collider experiments have produced limits on GMSB models, and indicate a heavy $\widetilde{\chi}_1^0$, with a mass greater than 100 GeV [18, 19, 21]. This, according to Figure 3 and for our model line, favors a lifetime on the order of a few tens of nanoseconds or less. Similarly, the lightest $\widetilde{\chi}_1^0$ should always decay to $\gamma\widetilde{G}$ [31]. These limits and mass relations restrict the masses of the squarks and gluinos to be so large ($\sim 600 - 800$ GeV/c^2) that they are too heavy to be produced in $p\bar{p}$ collisions at the Tevatron. Thus, gaugino pair-production channels dominate for much of the available parameter space [37] that is typified by our model line.

The major production and decay diagrams for this mass regime are shown in Figure 4. More quantitatively, $\widetilde{\chi}_1^{\pm}\widetilde{\chi}_2^0$ and $\widetilde{\chi}_1^{+}\widetilde{\chi}_1^{-}$ productions are produced ∼45% and ∼25%, respectively, of all channels. Table III summarizes the GMSB model parameters, the resulting $\widetilde{\chi}_1^0$ mass and lifetime, and the next-to-leading-order (NLO) production cross sections for example points on the SPS 8 model line [31]. The chargino mass is typically the same mass as the $\widetilde{\chi}_2^0$ and is 1.9 times the mass of the $\widetilde{\chi}_1^0$. The differential and total production cross sections are calculated to leading-order (LO) using the PYTHIA Monte Carlo program [38]. The NLO cross sections are calculated in Ref. [39] and we take and use the ratio of the NLO to LO cross sections, defined as k-factors, for our analysis. These are shown in Figure 5 as a function of $\widetilde{\chi}_1^0$ masses for $\widetilde{\chi}_1^{\pm}$ pair and $\widetilde{\chi}_1^{\pm}\widetilde{\chi}_2^0$ production. The values range between 1.1-1.3 for the mass range considered. The production cross section is independent of the $\widetilde{\chi}_1^0$ lifetime, as this only scales with the $\widetilde{G}$ mass for a fixed $\widetilde{\chi}_1^0$ mass [14]. Throughout this search we consider all production, the total production cross section, and use it to estimate the sensitivity as it produces the best search sensitivity [40].

In all cases the heavy sparticles decay promptly to $\widetilde{\chi}_1^0$ plus other high energy SM

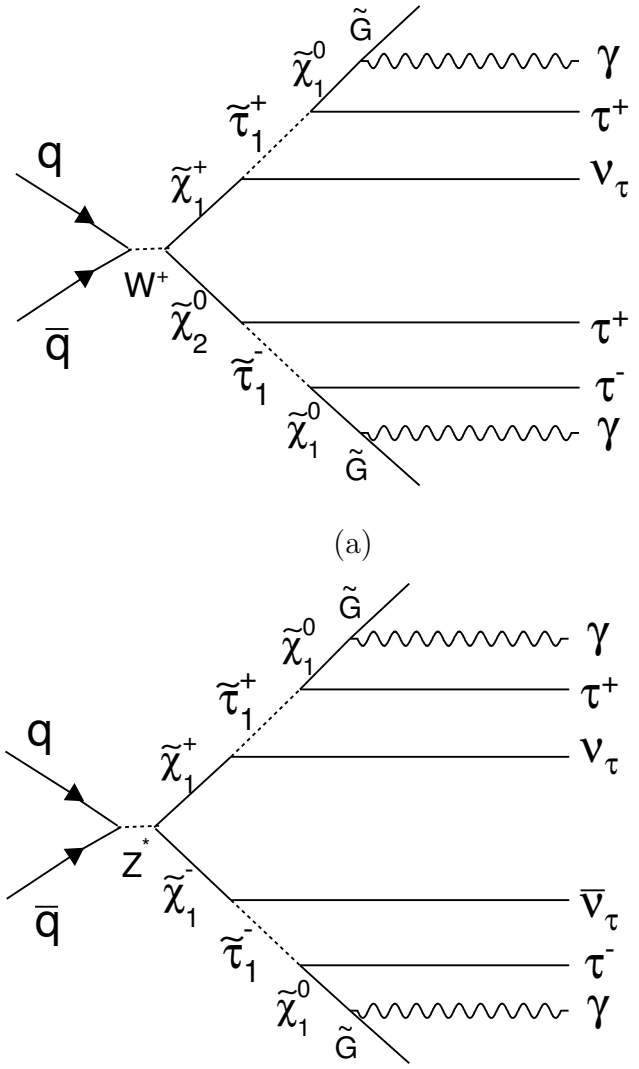

FIG. 4: Feynman diagrams of the dominant production processes at the Tevatron for the GMSB model line considered: $\widetilde{\chi}_1^{\pm}\widetilde{\chi}_2^0$ (45%) (a) and $\widetilde{\chi}_1^+\widetilde{\chi}_1^-$ pair production (25%) (b). Since our model line has a large value of $\tan\beta = 15$, the decay products are dominated by $\widetilde{\tau}$ which in turn decay to τ's. The τ's can be identified as a deposit of energy in the detector which we refer to as a jet (although that term is typically used to describe the hadronization of a light energy quark or gluon). Note that only one choice for the charge is shown. The remaining processes are slepton (τ_1, e_R, μ_R) pair-production, as shown in Figure 5.

particle(s) because of the $\sim$100 GeV/c^2 mass difference between the $\widetilde{\chi}_2^0/\widetilde{\chi}_1^\pm$ and the $\widetilde{\chi}_1^0$. For much of the parameter space in this model the $\widetilde{\chi}_1^0$ can, from Eq. 1.6, have a decay time on the order of nanoseconds which corresponds to decay lengths of meters from the collision if it is relativistic [15, 17]. The $\widetilde{\chi}_1^0$ can decay to a photon and a gravitino inside a detector at collider experiments or, in a fraction of cases, leave the detector volume before it decays. This separates the $\widetilde{\chi}_1^0$ $\widetilde{\chi}_1^0$ decay into the following event signatures: $\gamma\gamma$+$\not\!\!E_T$, γ+$\not\!\!E_T$ or $\not\!\!E_T$, each in association with hadrons and jets from the τ's in the cascade decays. In this analysis we will focus on the $\gamma\gamma$+$\not\!\!E_T$ case as it is more sensitive to lifetimes on the order of nanoseconds (<2 ns), which is favored for $m_{\widetilde{\chi}_1^0} \gtrsim 100$ GeV for regions consistent with the cosmology favored region [17]. While we will take advantage of the other high energy final state particles produced from the decays, we retain a model independent type analysis by not explicitly requiring the identification of taus.

TABLE III: Examples of $\widetilde{\chi}_1^0$ masses and lifetimes relevant for this analysis and their translation to the SUSY parameters in accordance with the GMSB SPS model line 8 [31]. To get different $\widetilde{\chi}_1^0$ masses we vary the SUSY breaking scale, Λ, and the messenger mass scale, M_m, but fix the ratio, $M_m/\Lambda = 2$. Also given are the NLO production cross sections. Note that the production cross section is independent of the $\widetilde{\chi}_1^0$ lifetime. Also note that since we are not yet sensitive to the cosmology favored region, $m_{\widetilde{G}} \approx 1$ keV, we are focusing on $\tau_{\widetilde{\chi}_1^0} \ll 1$ ns cases. Note that $m_{\widetilde{\chi}_1^\pm} \simeq m_{\widetilde{\chi}_2^0} \simeq 1.9 m_{\widetilde{\chi}_1^0}$.

$m_{\widetilde{\chi}_1^0}$ (GeV/c^2)	$\tau_{\widetilde{\chi}_1^0}$ (ns)	$m_{\widetilde{G}}$ (eV/c^2)	Λ (TeV)	k-factor	NLO $\sigma_{\rm prod}$ (fb)
70	$\ll 1$	1.38	53.5	1.23	999.9
90	$\ll 1$	2.18	67.2	1.20	286.8
100	$\ll 1$	2.63	74.0	1.19	169.0
130	$\ll 1$	4.34	95.0	1.16	36.23
130	2	317	95.0	1.16	36.23
140	$\ll 1$	4.99	101.8	1.15	22.97
150	$\ll 1$	5.7	108.8	1.14	14.54

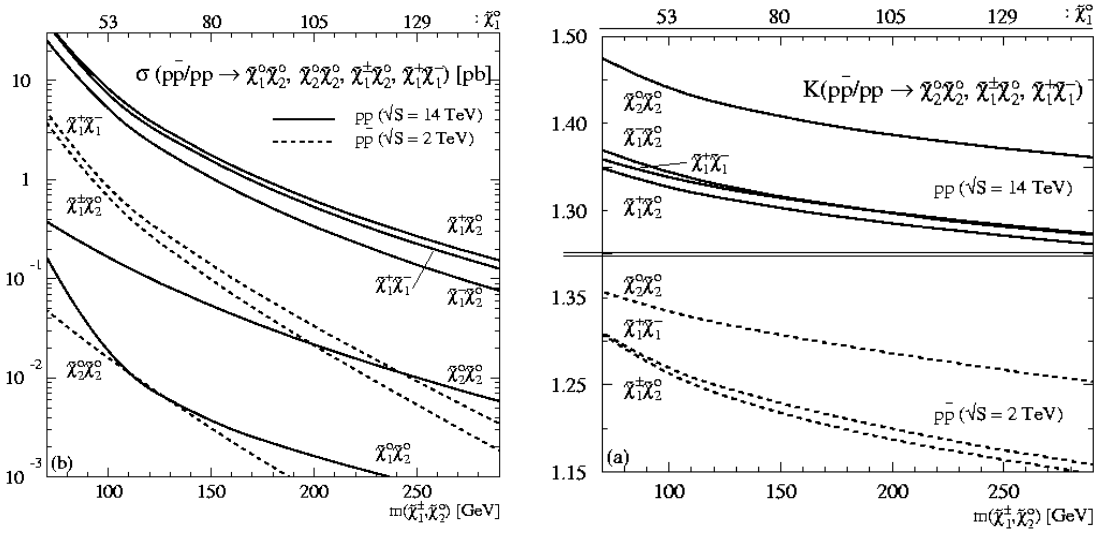

(a) (b)

FIG. 5: In (a) the NLO $\sigma_{\rm prod}$ of $\widetilde{\chi}_1^+\widetilde{\chi}_1^-$ pair and $\widetilde{\chi}_1^\pm\widetilde{\chi}_1^0$ production at the Tevatron and the LHC, and in (b) the ratio of NLO to LO cross section ("k-factor"), both as a function of the average $\widetilde{\chi}_1^\pm$, $\widetilde{\chi}_2^0$ mass. The k-factors are used in calculating the NLO $\sigma_{\rm prod}$ from the LO cross sections, provided by the PYTHIA event generator. The $\widetilde{\chi}_1^\pm$ and $\widetilde{\chi}_2^0$ masses are almost identical in the scenario chosen in Ref. [31]. These figures are taken from Ref. [39].

C. Previous Searches

As previously mentioned, there have been many previous searches for GMSB SUSY production both in general and in anomalous $\gamma\gamma+\not\!\!E_T$ production in collider experiments. In particular, these include Tevatron Run I searches from the Collier Detector at Fermilab experiment (CDF) [13] and the DØ experiment [41] at Fermilab as well as multiple searches from the Large Electron-Positron collider experiment (LEP II) [18] at the European Organization for Nuclear Research (CERN). LEP II collides electrons and positions with a center of mass energy of 209 GeV. Figure 6 shows the limits from the most sensitive search for GMSB from LEP II using the same SPS model line we use and considers a large variety of mass and lifetime combinations. These results, from the Apparatus for LEP PHysics (ALEPH) detector at LEP, are from direct searches for the $\widetilde{\chi}_1^0$ and indirect searches for sleptons and charginos. In indirect searches for high-lifetime ($\tau_{\widetilde{\chi}_1^0} \gg 10$ ns) neutralinos where the neutralinos are expected to leave the detector they used $e^+e^- \rightarrow \widetilde{l}\widetilde{l} \rightarrow l\widetilde{\chi}_1^0 l\widetilde{\chi}_1^0 \rightarrow ll + \not\!\!E_T$ and $e^+e^- \rightarrow \widetilde{\chi}_1^+\widetilde{\chi}_1^- \rightarrow W^{*-}\widetilde{\chi}_1^0 W^{*+}\widetilde{\chi}_1^0 \rightarrow jjjj + \not\!\!E_T$ or $l + jj + \not\!\!E_T$ decay channels that yield a lifetime dependent limit on the $\widetilde{\chi}_1^0$ mass of 60-98 GeV/c^2 [18]. In direct searches for low-lifetime neutralinos they used $e^+e^- \rightarrow \widetilde{\chi}_1^0\widetilde{\chi}_1^0 \rightarrow \gamma\widetilde{G}\gamma\widetilde{G} \rightarrow \gamma\gamma + \not\!\!E_T$ ($\tau_{\widetilde{\chi}_1^0} < 1$ ns) or $\gamma + \not\!\!E_T$ ($1 < \tau_{\widetilde{\chi}_1^0} < 10$ ns), where one of the neutralinos escapes the detector before decaying, decay channels using a photon "pointing" method [18], which measures the photon direction and extrapolates it towards the center of the detector. Separately shown is the impact from Higgs searches in $e^+e^- \rightarrow hZ$ and $e^+e^- \rightarrow hA$ on the $\widetilde{\chi}_1^0$ in this model with an indirect, lifetime independent limit on the $m_{\widetilde{\chi}_1^0}$ at around 90 GeV/c^2 [18]. However, these results are unpublished as of this writing and unlikely to be so. The previous most sensitive search for GMSB with low neutralino lifetimes ($\tau_{\widetilde{\chi}_1^0} \ll 1$ ns) was done using Run II data from the DØ experiment, which set a limit

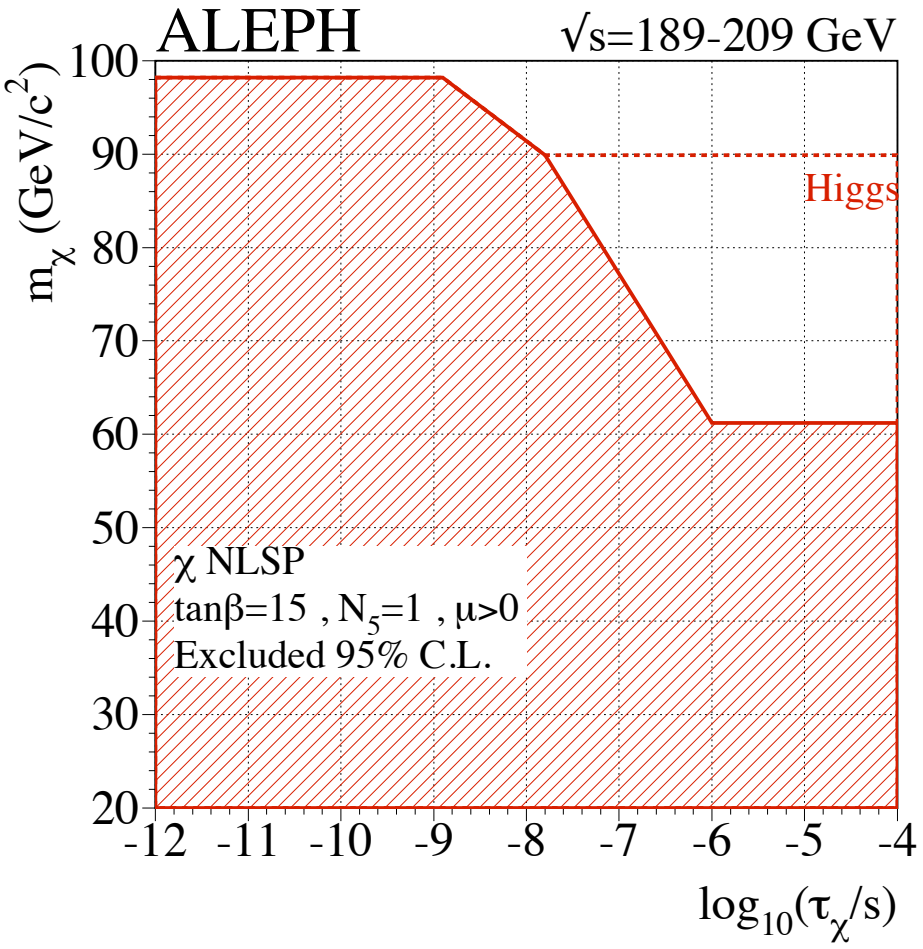

FIG. 6: The 95% C.L. exclusion region for GMSB searches with the ALEPH detector at LEP [18] as a function of the $\widetilde{\chi}_1^0$ mass and lifetime for the SPS 8 choice of parameters [31]. The shaded region is from direct searches for a GMSB $\widetilde{\chi}_1^0$ up to $\tau_{\widetilde{\chi}_1^0} \sim 10$ ns using pointing techniques, and from indirect searches for sleptons and charginos for longer $\widetilde{\chi}_1^0$ lifetimes. The dashed line shows the indirect upper exclusion limit on the $\widetilde{\chi}_1^0$ from searches for the Higgs boson; $\widetilde{\chi}_1^0$ masses of less than 90 GeV/c^2 in GMSB models are excluded. There are comparable limits from other LEP collaborations [18] but they are unpublished as of this writing.

on $m_{\tilde{\chi}_1^0} > 125$ GeV/c^2 [21].

In 2006 CDF extended its searches to include those for long-lived $\widetilde{\chi}_1^0$'s (1 ns< $\tau_{\tilde{\chi}_1^0}$ <10 ns) by searching for events where one of the neutralinos decayed with a macroscopic decay length but in the detector, while the other was allowed to leave the detector [19]. This was done by looking for events with a single photon that arrived with a delayed time at the detector (relative to expectations), using a new photon timing detector [42]. This search was done by requiring the delayed arrival of a photon, at least one jet (from a gaugino decay to the $\widetilde{\chi}_1^0$), and $\not\!\!E_T$. The search found 2 events using 570 pb^{-1} of data, which was consistent with the background estimate of 1.3±0.7 events. This search produced the most stringent limits on GMSB for nanosecond lifetimes and large masses of the $\widetilde{\chi}_1^0$'s. Figure 7 shows the exclusion region in the $\widetilde{\chi}_1^0$ lifetime vs. mass plane with a mass reach of 101 GeV/c^2 at $\tau_{\tilde{\chi}_1^0}$ =5 ns.

The most recent published search using the CDF in the $\gamma\gamma$+$\not\!\!E_T$ final state was with 202 pb^{-1} of data [20] in 2005. That search yielded zero observed events with two photons and $\not\!\!E_T$> 45 GeV on a background of 0.27±0.12. It produced a limit of $m_{\tilde{\chi}_1^0} > 93$ GeV/c^2, assuming the SPS 8 model and a $\widetilde{\chi}_1^0$ lifetime of much less than 1 ns, as shown in Figure 8-(a). There has been more than 10 times the amount of data collected since then, thus, we are in a position to significantly extend our sensitivity.

Since the search presented in this thesis covers more collected data, 2.6 fb^{-1} vs. 0.2 fb^{-1}, and the authors have gained more experience we focus on a number of improvements based on the dominant limitations from the previous Run II searches. In the preceding search the dominant background was due to SM $\gamma\gamma$ and γ+jet production where one jet fakes a photon, and in both cases the $\not\!\!E_T$ is due to a detector mismeasurement. We now have improved methods to reject these events while retaining our sensitivity to SUSY events. However, as we do a better and better job of rejecting mismeasurements, other backgrounds become important. In particular,

events from electroweak production that produce neutrinos, and thus real $\not\!\!E_T$, become important. Finally, non-collision backgrounds become a larger fraction of the background and need to be dealt with more carefully. All of these are described in the next section.

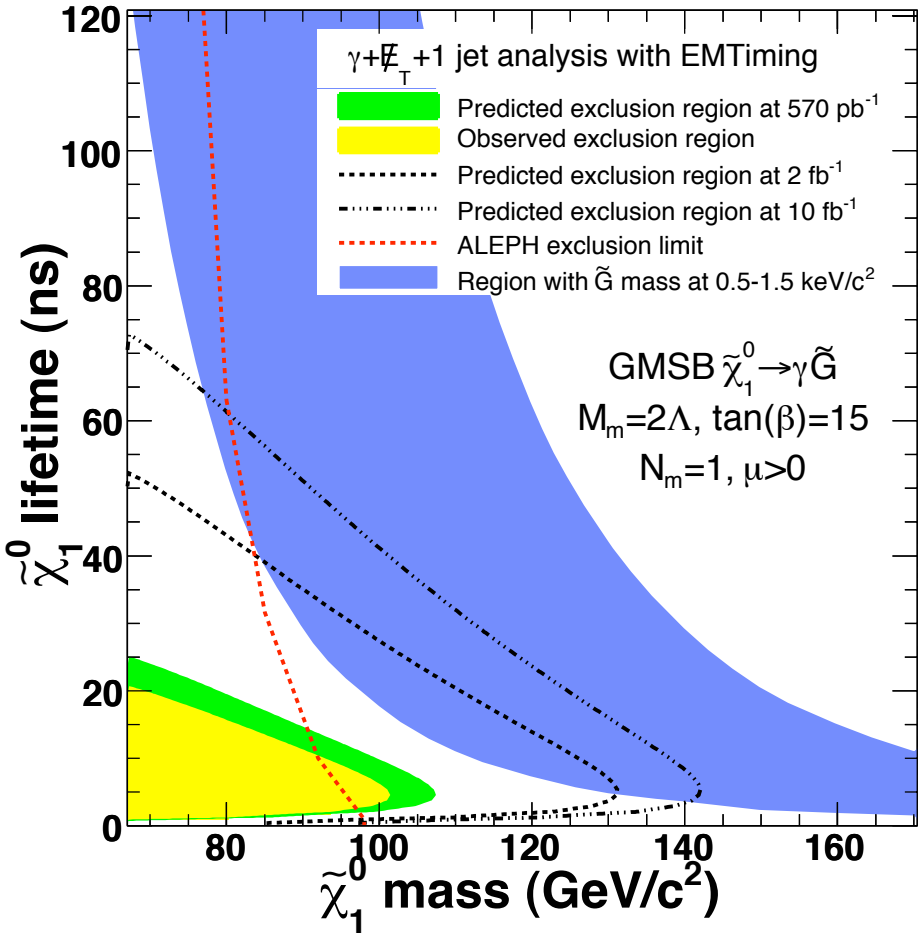

FIG. 7: The predicted and observed exclusion region from the delayed photon search in the $\gamma+\not\!\!E_T$+jet final state, taken from Ref. [19], along with cosmology favored region and the exclusion limit from ALEPH/LEP [18]. The $\widetilde{\chi}_1^0$ mass is excluded up to 101 GeV/c^2 for $\tau_{\widetilde{\chi}_1^0} = 5$ ns. The black dashed lines show the expected limits for searches with higher luminosities of 2 and 10 fb^{-1}, respectively. Note that there is an uncovered region below about a nanosecond for masses above 100 GeV/c^2.

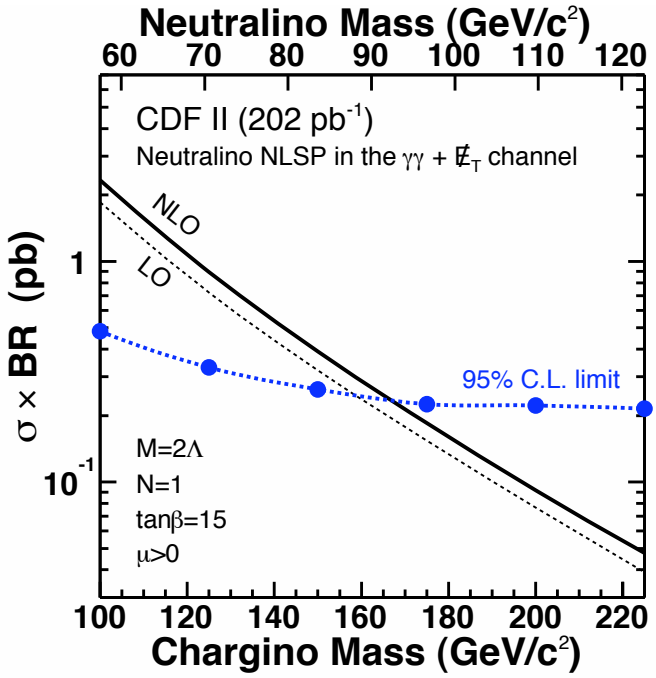

(a)

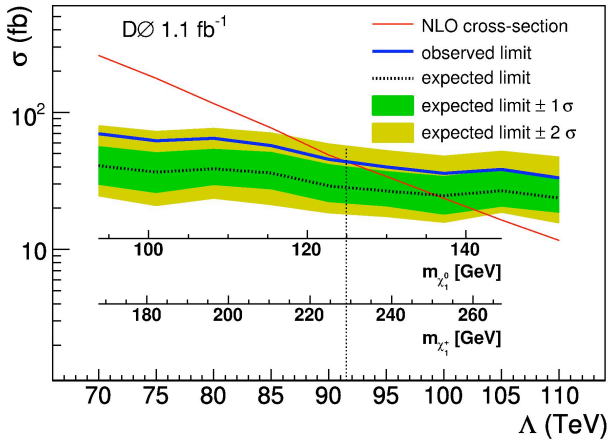

(b)

FIG. 8: In (a) the 95% C.L. upper limits on the total production cross section times branching ratio versus $m_{\tilde{\chi}_1^\pm}$ and $m_{\tilde{\chi}_1^0}$ for the light gravitino scenario using the SPS 8 parameters with $\tau_{\tilde{\chi}_1^0} \ll 1$ ns [31] from the CDF search for GMSB with $\gamma\gamma + \not\!\!E_T$ and 0.2 fb^{-1} of data [20]. The lines show the experimental limit and the LO and NLO theoretically predicted cross sections. The $m_{\tilde{\chi}_1^0} < 93$ GeV/c^2 was excluded. A similar search for GMSB with $\tau_{\tilde{\chi}_1^0} \ll 1$ ns from DØ using 1.1 fb^{-1} of data [21] is shown in (b). All values with $m_{\tilde{\chi}_1^0} < 125$ GeV/c^2 were excluded.

D. Overview of the Search

This analysis is designed to extend our search sensitivity to low-lifetime neutralinos GMSB with higher masses. For this reason we focus on the $\gamma\gamma + \not\!\!E_T$ final state [17] with $m_{\tilde{\chi}_1^0} > 100$ GeV/c^2 and a lifetime of $\tau_{\tilde{\chi}_1^0} \ll 1$ ns, but interpret our results for the higher lifetime regimes since the same analysis is sensitive for $\tau_{\tilde{\chi}_1^0} \lesssim 2$ ns. This also makes it complimentary to the single delayed photon search [19]. In addition to the two photons and $\not\!\!E_T$ in the event we also take advantage of the other high energy final state SM particles expected to be in the event from the cascade decays from $\widetilde{\chi}_1^{\pm}$ and/or $\widetilde{\chi}_2^0$ down to the $\widetilde{\chi}_1^0$.

The analysis strategy is to study a large number of high energy proton-antiproton collisions and select all the collisions that produce two photons in our data and search them for the presence of indications that they are supersymmetric in origin. The dominant source of two photon events are from QCD type interactions. Specifically, the main backgrounds sources are dominated by $\gamma\gamma$, $\gamma j \rightarrow \gamma\gamma_{fake}$ and $jj \rightarrow \gamma_{fake}\gamma_{fake}$, where j is a jet, and in this case is misidentified by the detector as a photon, which is labeled γ_{fake}. The subset of events with $\gamma\gamma + \not\!\!E_T$ are typically from QCD with fake $\not\!\!E_T$, electroweak events with real $\not\!\!E_T$ (e.g., $W\gamma \rightarrow e\nu\gamma \rightarrow \nu\gamma_{fake}\gamma$ where the electron is misidentified as a photon, again γ_{fake}) and non-collision backgrounds such as cosmic rays and beam related interactions.

The new features of our analysis to improve over the last $\gamma\gamma + \not\!\!E_T$ search with 202 pb^{-1} [20] are the following:

- Use a new *Met Resolution Model* (METMODEL) [43] to improve the rejection of events with no intrinsic $\not\!\!E_T$ such as QCD production of $\gamma\gamma$.

- Use the EMTiming system [42] to reject non-collision backgrounds from cosmic rays muons interacting the detector material and accelerator-related back-

grounds ("beam halo").

- Include a more complete set of backgrounds from electroweak sources.
- Simplify and re-optimize the analysis due to more direct ways of rejecting backgrounds and include the additional final state particles in the event as part of the optimization process to separate SUSY from SM sources.
- Investigate the sensitivity for models where the $\widetilde{\chi}_1^0$ lifetime becomes significantly different than 0 ns. Expand it to estimate the sensitivity for $\tau_{\tilde{\chi}_1^0} \lesssim 2$ ns.
- Use 13 times the data (2.6 fb^{-1}).

The analysis begins by examining sets of interactions from collision events with two photon candidates in the detector that surrounds the collision point. All events are required to pass photon identification requirements as well as non-collision background rejection requirements. This set of requirements defines our preselection sample.

We perform an *a priori* analysis in the sense that we do not look at ("blind") the signal region until after we have completely defined the final event requirements based on the expected GMSB event rate ("signal") and background expectations alone. The final signal region is defined to be the subset of events that pass the presample requirements as well as the final optimization requirements. These requirements are designed to select events with significant $\not\!\!E_T$ and identify the presence of a large amount of energy deposited in the detector that would indicate the production and decay of heavy supersymmetric particles. By tuning the values of these requirements we optimize the rejection of the remaining backgrounds while retaining acceptance for our signal. The methods for determining the number of signal events and the number of expected background events in the signal region are based on a combination of

data and Monte Carlo (MC) simulation techniques and allow for a large variety of potential final sets of requirements for a wide variety of different neutralino mass and lifetime values. We optimize our search for models with $\tau_{\tilde{\chi}_1^0} \ll 1$ ns decays and estimate our sensitivity for models with $\tau_{\tilde{\chi}_1^0} \lesssim 2$ ns. As shown in Figure 7 there is an uncovered region below about a ns. We thus extend the limits beyond the current $\widetilde{\chi}_1^0$ mass and lifetime region and towards the cosmologically favored $\widetilde{G}$ mass region $0.5 < m_{\widetilde{G}} < 1.5$ keV/c^2 where the $\widetilde{G}$ could be a dark matter candidate [15].

The results of the full analysis presented here have been approved by the CDF Collaboration and were published in Phys. Rev. Lett. in January of 2010 [44].

E. Outline of the Dissertation

The outline of this dissertation is as follows: Chapter II describes the experimental apparatus including the Fermilab Tevatron proton-antiproton ($p\bar{p}$) accelerator complex and the Collider Detector at Fermilab (CDF), which is a large, powerful multi-purpose particle detector that surrounds the $p\bar{p}$ collision and is used to identify the final state particles and their 4-momenta. Chapter III describes how the final state photons from GMSB events are identified and measured. We use the standard identification techniques with minor, customized modifications for our purposes. Also motivated and described in Chapter IV are the measurement of the $\not\!\!E_T$ in the detector and the other final state observables including jets (the final observables from quarks, gluons and hadronic τ decays) and the measurement of a global event property, known as H_T, which is an effective measurement of the total energy of all the objects (photons, jets and $\not\!\!E_T$) in the event. Chapter V discusses the set of preliminary requirements to identify $\gamma\gamma$ events and describes the data sample of events selected. Chapter VI describes our techniques of quantitatively estimating the probability of $\not\!\!E_T$ just being

from a fluctuation of the measurement uncertainty. This new technique is known as METMODEL and it measures the significance of the $\not\!\!E_T$ measurement. The various background sources, as well as the methods to estimate their rates of passing the final requirements, are described in Chapter VII. Chapter VIII describes the MC simulation of GMSB events and the systematic uncertainties on the rates at which they are produced as well as the rates at which they pass our final set of requirements. The optimization procedure and the expected sensitivity are described in Chapter IX. Chapter X discusses the data in the final signal region and compares to background expectations. Finally, Chapter XI concludes with the final results and a discussion of future prospects for complimentary analyses with more data.

CHAPTER II

THE FERMILAB TEVATRON, THE CDF DETECTOR, TRIGGERS AND MONTE CARLO EVENT SIMULATION

This chapter both describes the parts of the experimental apparatus that are indispensable for this analysis as well as their simulation. The Tevatron is a circular particle accelerator that produces and collides proton-antiproton beams at the Fermi National Accelerator Laboratory (Fermilab) in Batavia, Illinois. During the time the data for this analysis was collected and analyzed it was the highest energy particle collider in the world [1]. The CDF detector, which surrounds the collision point with its subsystems, is used to identify and record the trajectories and energies of long-lived particles such as electrons, photons and hadrons. The subsystem that are relevant to this analysis are the calorimeters, including the timing system in the electromagnetic calorimeter, and the central charged particle tracking chamber which are described in the following subsections. The results from these subsystems are fed to a custom set of systems which allow us to select ("trigger on"), in real time, diphoton candidates from millions of collisions that occur every second. This set of events is then analyzed offline and searched for the presence of evidence of collisions that are supersymmetric in origin.

This analysis relies heavily on the use of Monte Carlo (MC) event generation for both signal and background processes which is followed by a full detector simulation and event reconstruction. We, therefore, describe MC event simulation after a discussion of the various experimental apparatus descriptions.

---

[1] The Large Hadron Collider (LHC) at the European Organization of Nuclear Research (CERN) had collisions at 2.36 TeV on Dec 14th, 2009.

A. The Fermilab Tevatron

The Tevatron accelerator complex [45, 46] is a superconducting synchrotron of 1 km radius. An aerial view of the Fermilab site is shown in Figure 9-(a). As shown in Figure 9-(b) at the first stage it has a proton source, that consists of a Pre-accelerator that negatively ionizes hydrogen (H^-) and a Linac that accelerates the ions and then passes them through carbon foil for electron removal. A Booster then accelerates the protons to an energy around 8 GeV and gathers them into "bunches". The proton bunches are then transferred into the Main Injector which is a bigger synchrotron. To load the protons into the Tevatron, the Main Injector accelerates 7 proton bunches to 150 GeV and combines them into a single bunch. This process is repeated 36 times to get 36 bunches. Separately, protons are also accelerated by the Main Injector to 120 GeV and directed to hit a nickel target to produce a wide range of secondary particles including many antiprotons. The antiprotons are then collected and decelerated ("debunched") and stochastically cooled and transferred to an Accumulator, where the antiprotons are accumulated. Then the Main Injector accelerates them to 150 GeV and combines them into 4 bunches. This process is repeated 9 times to get 36 bunches. Finally the 36 bunches of protons and antiprotons are sent ("injected") into the Tevatron main ring [45] where both particle types are accelerated from 150 GeV to 980 GeV. Also shown in Fig. 9-(b) are the Recycler that is used to store unused antiprotons returned from the Tevatron and the Switchyard that controls the 120 GeV beam to a number of final destinations, e.g. fixed target experiments.

Each of the 36 proton and antiproton "bunches" typically contains $\sim 3 \cdot 10^{11}$ and $\sim 3 \cdot 10^{10}$ particles, respectively. They counter-rotate in the Tevatron ring during data taking ("a store") and collide with a center of mass energy of 1.98 TeV on average

(a)

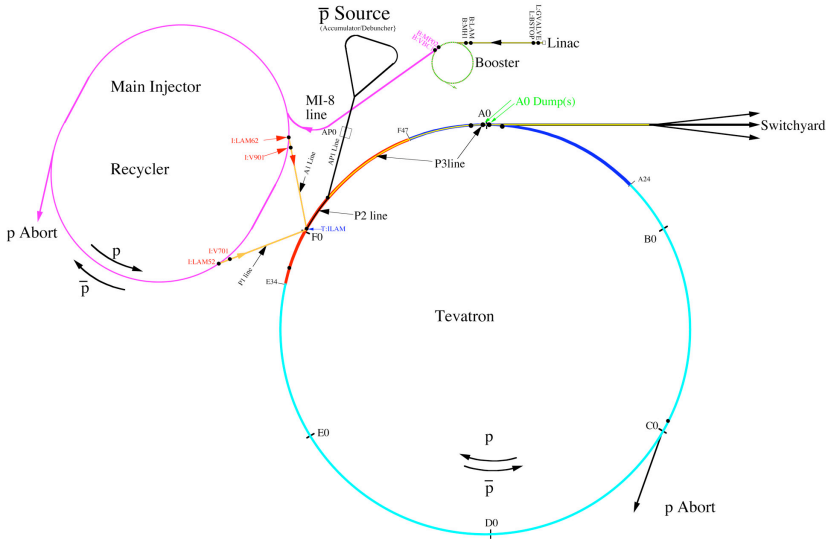

(b)

FIG. 9: An aerial view of the Fermilab accelerator complex with the Main Injector in the foreground and the Tevatron in the back (a) taken from Ref [47]. The bottom figure, (b), shows the Fermilab accelerator chain [45] in detail. The CDF detector is situated at the BØ point.

every 396 ns at each of the two focus points, BØ and DØ in Figure 9. These points are surrounded by the CDF and the DØ detectors, respectively. The smallest data-taking unit is a "run" which is defined by a uninterrupted time interval as part of a store for which no change in detector setup or data-acquisition occurred.

Since the bunches have finite extent in both the longitudinal (along the beam line) and the transverse profile, a description of the collision distribution in the interaction region is well approximated by Gaussian distributions with a typical RMS of 30 cm along the beam (z) and 30 μm in the transverse direction (x-y). The interaction time variation is also Gaussian with an RMS of $\sim$1.28 ns. The average number of collisions per bunch crossing varies between 0.4-4.4 [48].

The number of collisions per bunch crossing, the instantaneous luminosity, is measured using gaseous Cherenkov luminosity counters (CLC) [49] to estimate the amount of collision data. Two modules of 48 counters each are situated along the p and the $\bar{p}$ direction at $3.7 < |\eta| < 4.7$ (see the definition of the η with the CDF coordinate system in next section). As the number of $p\overline{p}$ interactions in a bunch crossing follows Poisson statistics the instantaneous luminosity is determined by the inelastic cross section ($\sigma_{in} \sim 60$ mb) and the measured fraction of empty bunch crossings. The systematic error on the integrated luminosity is estimated to be 6% [49]. The integrated luminosity for the data used in this analysis was 2.59 ± 0.16 fb^{-1}, which corresponds to approximately 1.6×10^{14} collisions to be sorted through for evidence of Supersymmetry.

B. The CDF Detector

The CDF detector for the data taking period 2002-2008 ("CDF II") [50] is an azimuthally and forward-backward symmetric, general-purpose magnetic spectrometer.

Figure 10 shows a photograph of the detector and a schematic drawing of the major detector components. A detailed description can be found in [51, 52].

The CDF coordinate system defines the proton beam direction to be the positive z direction, and the azimuthal angle ϕ is measured around the beam axis. The polar angle θ is measured with respect to the positive z direction. The pseudorapidity η is defined as $\eta = -\ln\tan(\theta/2)$. The transverse components of particle energy (E) and momentum ($\vec{p}$) are conventionally defined as projections onto the plane transverse to the beam line, $E_T = E\sin\theta$ and $p_T = |\vec{p}|\sin\theta$.

A 1.4 T magnetic field along the z-direction is generated by a superconducting solenoid of 1.5 m radius and 4.8 m length and contains the tracking detectors to measure charged particle trajectories. The calorimetry and muon detectors are located outside the solenoid to further provide particle identification and energy measurements.

The CDF detector is a well understood measuring instrument and there exist standardized identification criteria for photons, electrons, muons, taus, b-quarks, and other standard model particles. The identification criteria for the objects we use most in this analysis, like photons, are described in Chapters III and IV. Techniques to remove non-collision backgrounds such as muons from cosmic rays and beam-related effects that interact in the detector are discussed in Chapter V. Next we describe the detector elements directly related to this analysis.

1. The Tracking Systems

The innermost portion of the detector consists of a set of tracking detectors designed to measure the momenta and charge of charged particles using their measured paths and curvatures in a magnetic field. Where the particle trajectories are projected to intersect at the beam line allows for the reconstruction of both the time and position

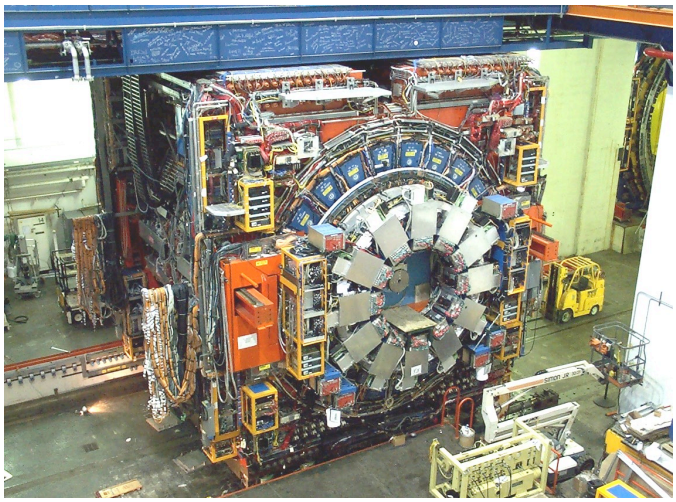

(a)

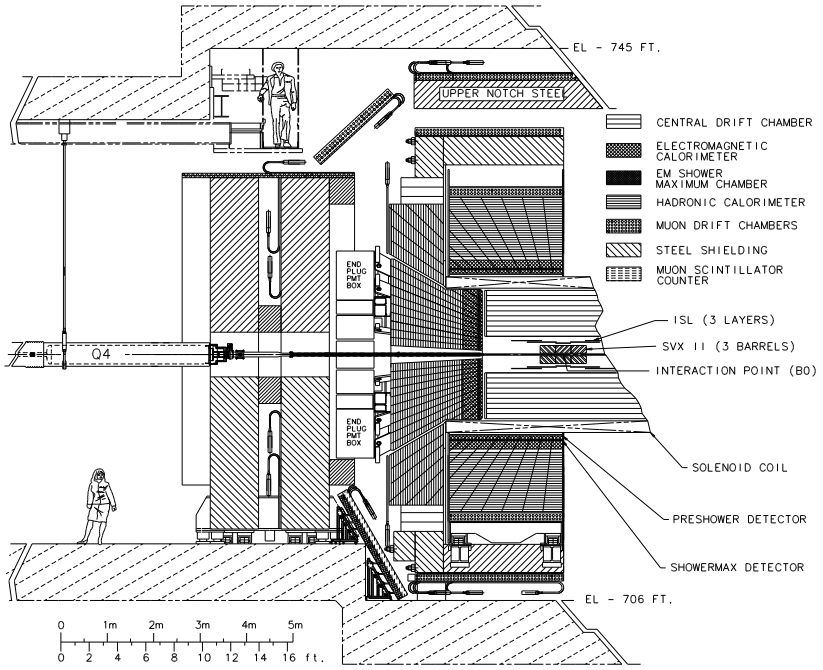

(b)

FIG. 10: A photograph [45] (a) and a side view [51] (b) in 2-dimensional projection of the CDF II detector. This analysis mainly uses the calorimeter systems for photon identification and timing, with the EMTiming system in the EM part. The tracking chambers are also used to reject electron backgrounds.

of the primary interaction (the vertex for an event) as well as any secondary vertices due to decays of long-lived particles coming from the primary collision. The tracking system includes two detectors: the Silicon VerteX detector (SVX II) and the Central Outer Tracker (COT). Figure 11 shows end views of the SVX II and a section of the COT end plate.

The SVX II is the component of the CDF II detector closest to the beam line. It provides a precise determination of the track position in the transverse plane via r-ϕ tracking and is used as part of the measurement of the momentum and vertex measurements in conjunction with the COT. There are three separate silicon microstrip subdetectors. At the smallest radius there is a single-sided silicon strip detector mounted on the beam pipe and called Layer 00 (L00) [53]. The SVX II [54], a replacement for the Run I version, has five layers of double-sided silicon arranged in 12 wedges of 15° between a radius of 2.44 cm and 10.6 cm. In the z-direction each layer is split into three 29 cm cylindrical "barrels" of 12 wedges each. The intermediate silicon layer (ISL) detector [55] surrounds the SVX II. It is 175 cm long and extends the tracking coverage to the region of $|\eta| < 1.9$. It is also structured into three barrels of twelve wedges each. The central barrel has one layer of silicon at a radius of 22 cm, and the outer barrels have two layers at 20 and 28 cm, respectively. There are a total of 722,432 channels in the eight layers of SVX II. While the silicon systems are usually used in conjunction with the tracking of the COT to search for tracks and they allow for full 3D standalone tracking of charged particles even without a COT track seed. The SVX II+ISL has a single hit resolution of 20 μm.

Just outside the SVX II is the central outer tracker. The COT is a cylindrical, 310 cm long [56], open cell drift chamber covering the radii from 43.3 cm to 132.3 cm. The COT reconstructs charged particle trajectories and momenta in the region $|\eta| < 1$. The COT chamber is filled with a 50-50 Argon-Ethane gas mixture with a small

admixture of isopropyl alcohol and oxygen, which has maximum drift time of 100 ns (which is small compared to the 396 ns bunch spacing). The chamber contains 96 layers of sense wires grouped into eight "superlayers" (4 axial and 4 stereo) of 12 wires each that run approximately parallel to the beam line. Each wire is 40 μm in diameter and made of gold-plated tungsten and run between the two endplates. In total there are 30,240 wires. The superlayers alternate between purely axial wires that run parallel to the beam line, and stereo wires tilted by 3° with respect to the beam line. The two different kinds of layers allow particle trajectories to be reconstructed in 3D. Each superlayer is divided in ϕ into cells with 12 wires each, and each making 35° angle with respect to radial lines from the z-axis as shown in Figure 11-(b). The number of cells increases from 168 for the first superlayer to 480 at the eighth (last or outer) one to maintain the same wire density with increasing radius. With a hit resolution of 140 μm it measures the track momentum with a resolution of $\sigma(p_T)/p_T^2 \approx 0.3\%(\mathrm{GeV}/c)^{-1}$ [52], and the track z position at the beam line with a typical resolution of 0.22 cm. The time information of each hit allows for a timing measurement of the track along the trajectory and is used to derive the time that the particle was produced, t_0. The track t_0 has an approximate resolution of 0.27 ns for well measured tracks.

Trajectories in the COT are used to draw a path in the SVX II and look for SVX II hits which can be attached to the trajectory. This can give a better measurement of the particle trajectory. The combined system (SVX II+COT) results in $\sim$30 μm resolutions for z_0 and $\sigma(p_T)/p_T^2 \approx 0.17\%(\mathrm{GeV}/c)^{-1}$ for the p_T measurement resolution. Since there is no timing information from the SVX II it does not improve the t_0 measurement.

In all events the tracks are used to create a set of vertices. In this analysis we will require the presence of a well measured vertex that was produced along the beam

line indicating the primary collision between the proton and antiproton (known as a primary vertex), which is likely the source of the photon and $\not\!\!E_T$ candidates. Since the photon is neutral there is no associated track with it and we cannot be sure we are selecting the true collision point. Thus, in this analysis we select the primary vertex to be the one that produces the highest total p_T of charged tracks, the highest $\sum p_T$, in the event and use a number of techniques, such as checking to see which produces the smallest $\not\!\!E_T$, to reduce the potential problems this can cause. This vertex is used to determine the polar angle, θ, of any final state particle. The transverse energy, E_T, of each calorimeter tower is calculated according to this vertex using $E_T = E \sin\theta$. This will also be used in measuring the E_T of final state objects, including the $\not\!\!E_T$.

2. The Calorimeters

The CDF calorimeters [51] are located outside of the tracking volume, cover the region $|\eta| < 3.6$, and are used to measure the energy and direction of the particles at large distances from the collision point. The sampling calorimeters have a sandwich-like structure with layers of absorber, lead or iron, and active layers of scintillator. They consist of an electromagnetic (EM) compartment followed by a hadronic (HAD) compartment and are divided into a central portion that surrounds the solenoid coil ($|\eta| < 1.1$) and a pair of end-plugs that cover from outside the central region to an angle close to the beam line ($1.1 < |\eta| < 3.6$). The calorimeters are segmented into projective geometry[2] "towers". Most towers cover 15° in ϕ and between 0.10 to 0.13 units in η.

Different particles deposit their energies in different ways in the two calorimeters. Electrons and photons mostly interact and deposit all their energy in the EM calorime-

[2]The division between towers always point at the center of the detector, $z = 0$.

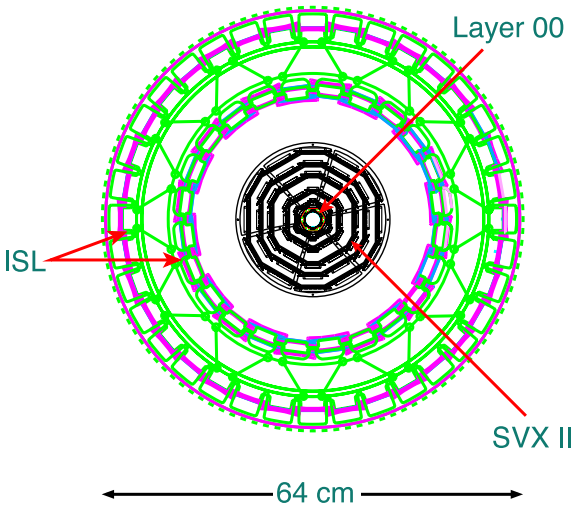

(a)

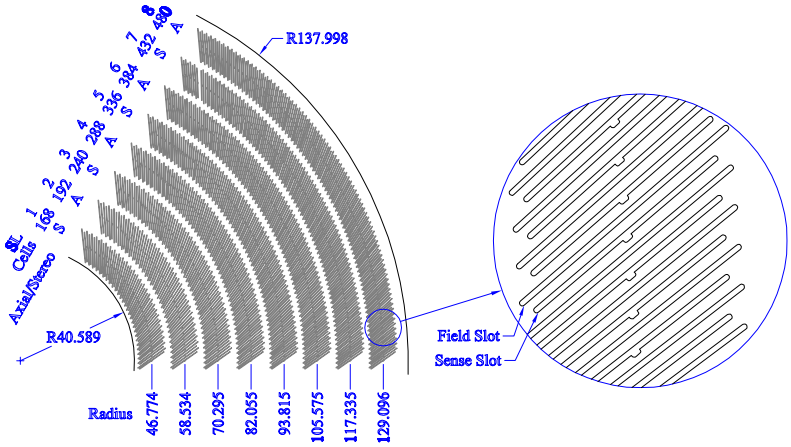

(b)

FIG. 11: In (a) is an end-view of the silicon detector. The innermost layer (L00) is attached to the beam pipe, and is surrounded by five concentric layers of silicon wafers (SVX II). The outmost layers are the intermediate silicon layers (ISL), which sit just inside the outer tracking chamber. In (b) end-view of a section of a central outer tracker (COT) end plate. The COT consists of eight concentric "superlayers", separated azimuthally into cells, each containing 12 sense wires and sandwiched by field sheets. The end plates contain precision-machined slots where each cell's sense wires and field sheets are held under tension. The radius at the center of each superlayer is shown in cm.

ter. Upon reaching the front face of the calorimeter, they start to interact with the heavy material in the calorimeter in ways which produce a cascade, or "shower", of electrons, positrons and photons which are detected and measured as they deposit energy in the various components of the detector. These electrons and photons lose energy mainly through the process of electromagnetic showering that consists of cycles of bremsstrahlung and pair production, and is characterized by the radiation length, X_0, which is the average distance a particle must travel in order for $1/e$ of its original energy to remain. The central EM calorimeter (CEM), shown in Fig. 12, uses 23 alternating lead and polystyrene scintillator layers of $\sim$5 mm thickness each and has a total of 21 radiation lengths. The electromagnetic shower reaches its maximum profile between 4-7 radiation lengths. Hadrons, on the other hand, typically lose their energy through inelastic nuclear interactions, forming hadronic cascades in material. The nuclear interaction length is much longer than X_0 due to the smaller interaction cross section. So hadrons mostly pass through the EM calorimeter and deposit most of their energy in the hadronic calorimeters, which are outside the EM calorimeter. Muons lose only a small amount of their energy in either calorimeter since they only interact via ionization. Thus, electrons and photons can be separated from hadronic particles by virtue of the fact that they deposit the overwhelming majority of their energy in the EM calorimeter, while hadronic particles deposit significant amount of energy in both. Muons can be identified by having deposited small amounts of both and by having continued on through to detectors located outside the calorimeters.

The calorimeters measure the energy of the photons, electrons and hadronic particle using sampling techniques. The energy is proportional to the total number of particles created in an electromagnetic shower or hadronic cascade. The EM calorimeter contains the majority of the particles created in an electromagnetic shower cascade, although there is some leakage of the shower into the hadronic calorimeter.

The light produced by the charged particles interacting in the various layers of the scintillator is collected by two phototubes on opposing sides of each tower for readout. The light output is proportional to the total energy. This system, along with the readout system, has an energy resolution of $13.5\%/\sqrt{E_T} \oplus 2\%$.

A photon is identified as an energy deposition in one EM calorimeter tower ("a seed tower") with only a small amount of leakage ("shoulder") into an adjacent tower of the same wedge in η (same ϕ wedge). A set of one seed and its two adjacent shoulder towers in η is referred to as an "EM cluster" and constitutes a photon candidate. Within the CEM, a proportional strip and wire chamber (Central Electron Strips, CES) at $\sim 6X_0$, corresponding to the shower maximum of electrons and photons, measures the transverse position and profile of the beam, as shown in Figure 12. Then, the CES in this tower is searched for a cluster and, if found, the centroid of the CES profile is used to determine the position of the photon. The typical shower profile of promptly produced electrons or photons is Gaussian with a width of 1.5-2.0 cm. The resolution of the position measurement is typically 2 mm for 50 GeV/c electrons.

The central hadronic (HAD) calorimeter has the same tower/wedge geometry as the EM but uses iron instead of lead. It typically measures "sprays" of hadronic particles from the collision, known as "jets", with an energy resolution of approximately $\sim 0.1E_T + 1.0$ GeV [57]. The plug calorimeters are also sampling scintillator calorimeters. The EM part has an energy resolution of $16\%/\sqrt{E_T} \oplus 1\%$, and the HAD part has an energy resolution of $74\%/\sqrt{E_T} \oplus 4\%$. During beam operations the calorimeter systems integrate the energy deposited in each tower over an integration window time of 128 ns around the collision time which collects over 95% of the energy deposited which we correct for.

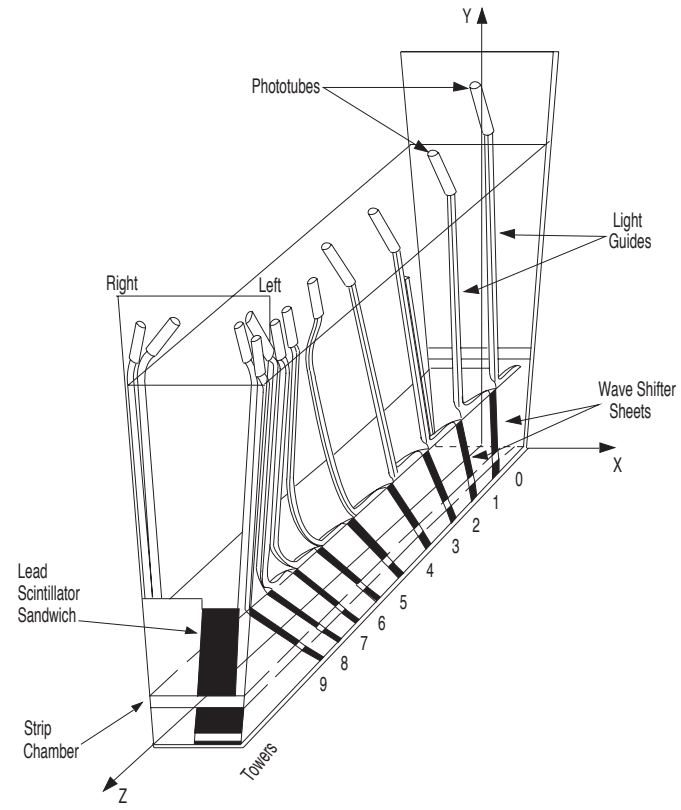

(a)

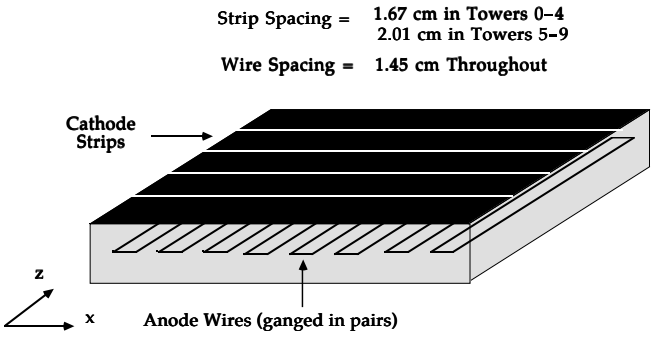

(b)

FIG. 12: In (a) is a schematic drawing of a wedge in the central calorimeter, including the EM and CES subsystem. In (b) is a schematic drawing of the CES subsystem showing strips and wires taken from Ref [45].

3. The EMTiming System

In addition to measuring the energy and direction of the particles from the collision, the calorimeters also record the time of arrival of the particles. This information is used to help reject photon candidates and other particles that might be from sources other than from the primary collision. The EMTiming system [42] was partially built in response to the $ee\gamma\gamma\not\!\!E_T$ candidate event from CDF in Run I [13], in particular to verify whether EM clusters in future events were from the primary collision; one of the photons and the plug electron in this event had no arrival time information and it was speculated that they were from cosmic ray sources. It is particularly useful in this analysis to reject events with cosmic ray or beam-related background sources and do so in a way that allows us to estimate their rate of occurrence. The timing system covers the central and plug region of the calorimeter, $|\eta| < 2.1$, and produces a timing readout. The hadronic calorimeter also has timing with a threshold of $\sim$2 GeV, but it is not used in this analysis.

As shown Fig. 13-(a) the photon arrival time in the calorimeter is measured using the electronic signal from the energy of the EM shower. As the shower develops in the calorimeter the scintillator lights from the particle interactions travel in the scintillator and are routed to photomultiplier tubes (PMTs), which effectively convert the energy deposited into an analog signal, as shown in Fig 13-(b). The EMTiming system attaches to the output of two PMTs on opposite sides of each tower in the CEM detector as shown in Fig. 12-(a). This signal is sent to an amplifier shaper discriminator (ASD) that converts the analogue signal to a digital signal, which is sent to time-to-digital converters (TDCs) for a time measurement that is then read out by the data acquisition system. The system is 100% efficient for tower energies above $\sim$3 GeV in the CEM with an "intrinsic" system timing resolution of 0.5 ns [42].

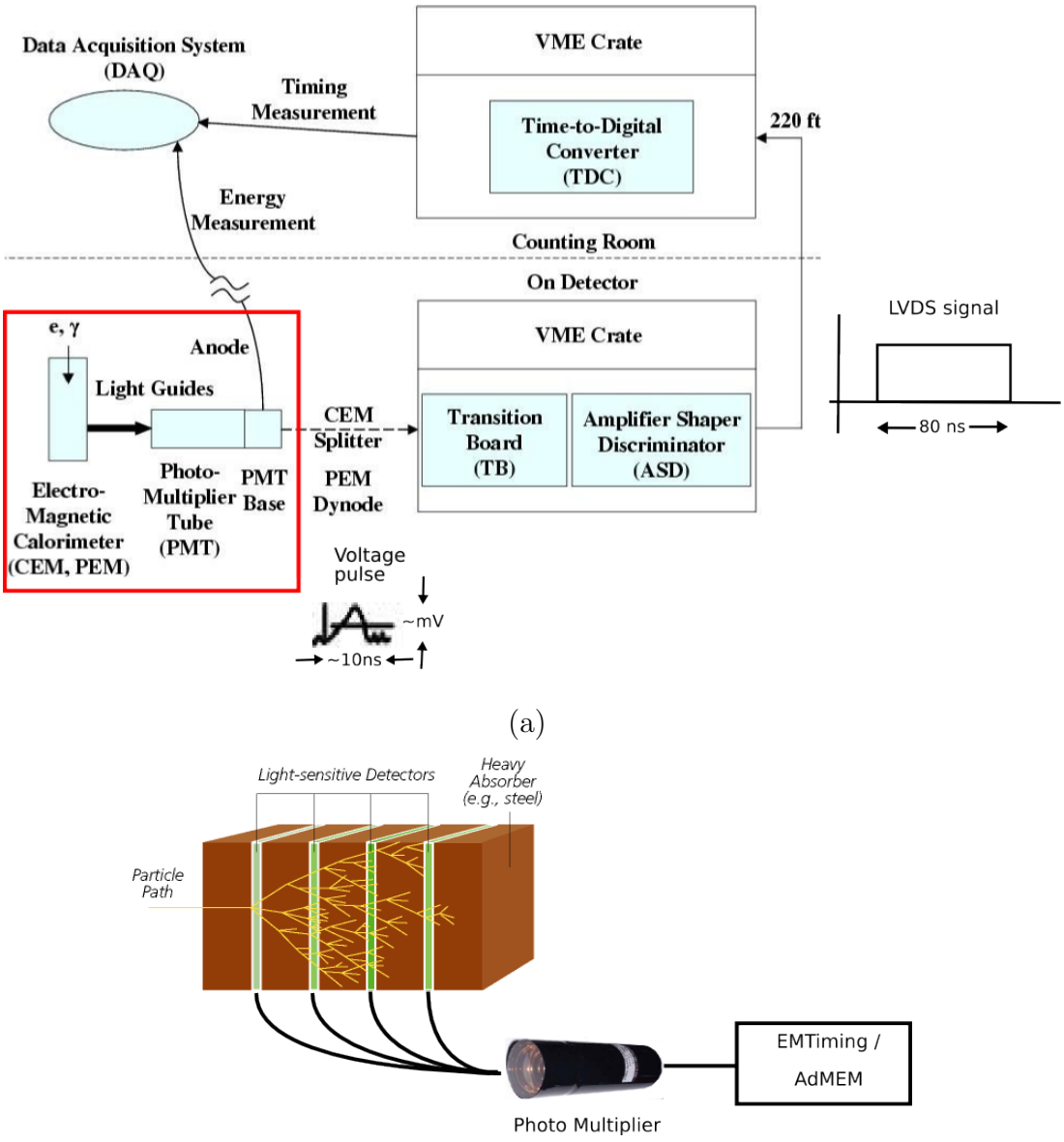

FIG. 13: In (a) is a schematic diagram of the EMTiming system including the pulse descriptions. The pulse from the PMT in the CEM gets inverted due to the inductive splitter. Note that the tower example in (b) does not show the CES.

C. Trigger: Generic Description

Collisions occur at the center of the CDF detector every 396 ns. The necessary rejection rate is roughly $10^6 : 1$, as only about 100 events per second can be written to tape, since the average logging rate is $\sim$23 MB/s. The challenging task of selecting $\gamma\gamma$ candidate events from the millions of other types of collisions is done using a three level selection "trigger" system [51]. The levels are referred to as Level 1 (L1), Level 2 (L2) and Level 3 (L3), respectively. The first two levels consist of special-purpose, custom built hardware, allowing for a gradual reduction of the event rate to < 50 kHz out of L1 and down to 300 Hz out of L2. For L1 and L2 each subdetector system is read out separately and an overall decision is made based on the observations in that single detector. After L2 accepts an event, the data from all the detector systems is combined into a single event recorded by an event "builder" [58] and passed to L3. Level 3 is a farm of computers that filters the datastream coming from the event builder down to about 100 events per second and sends them for data storage. The system is designed so that the operation results in a minimal or no loss of important data (no dead time).

At each level there are a number of different trigger paths that correspond to accepting different types of physics events. The relevant trigger paths for this analysis will be described in Chapter V. Here we only describe the basic elements of the trigger system that are important to us.

L1 picks up events from every beam crossing and performs some simple hardware reconstruction. This time it takes for L1 to analyze an event is $\sim$4 μs. L1 has access to the energy measurements for the calorimeter "trigger tower", defined as groups of two physical towers adjacent in η. This tower segmentation is used only at L1 and L2; in all other parts of the text the term "tower" always refers to a physical tower

unless specified otherwise.

Both L1 and L2 have access to the measurement of missing transverse energy, $\not\!\!E_T$. L2 performs the same reconstruction algorithm as L1 but with greater accuracy and a longer decision time of $\sim$20 μs. It also performs clustering of energy in adjacent trigger towers, which allows a better energy measurement.

L3 allows further refinement of the selection by running a smaller version of the offline photon and $\not\!\!E_T$ reconstruction algorithms. These will be described in more detail in Chapters III and IV. There are about 200 separate paths or combinations of L1, L2 and L3 triggers that are implemented at L3. About 5% of the events that pass L3 are selected to monitor the quality of data taking and functionality of the detector systems in real time at the CDF control room.

D. Monte Carlo Event Simulation

Due to the complexity of the detector systems, MC methods provide the only possible way to accurately model the observables for GMSB signal production predictions, as will be described in Chapter VIII. We also depend on MC predictions for many of the background estimation processes. A full generation-simulation-reconstruction chain is fulfilled by the standard CDF MC tools [59].

The full simulation chain begins by running an event generator which uses theoretical differential cross section formulae, random number generation, initial and final state radiation and hadronization mechanisms. This is sent to a special particle decayer package to produce possible outcomes of physics processes such as the decays of the hadrons. The result for each generated event is a list of particles that would enter the detector volume including their kinematics and their relationships to the primary collision particles. We typically use PYTHIA [38] as a MC generator, as it provides

a well understood description of our backgrounds and GMSB signal processes. The number of events simulated is proportional to the integrated luminosity. Effects of the instantaneous luminosity during different data taking conditions are simulated by adding extra collisions, known as Min-Bias events [60], which are also generated using PYTHIA.

After an event is generated, a full simulation of the interactions of the final state particles with the detector is simulated using a GEANT-based detector simulation, often called *cdfSim* [61]. Different versions of the simulation correspond to different data taking conditions and are calibrated using collision data. The detector simulation process begins with the random picking of the primary vertex location according to the beam parameters. The simulation performs step-by-step particle propagation using GEANT through the detector medium following a detailed geometrical representation of CDF II. This enables the creation of detector hits using particle position and energy loss in each step. The results of this procedure are finally converted into the raw data format that is the same as coming from the real detectors and data. This simulated raw data can then be processed and analyzed using the same techniques as used in real data. The output has been shown to do an excellent approximate simulation of the production and reconstruction of physical processes in our detector. The identification of photons, and other particles, in the event is discussed next.

CHAPTER III

PHOTON IDENTIFICATION

This chapter describes the identification of photons, the primary object in this search. It begins with a review of the standard CDF photon identification (ID) procedures and criteria as well as two additional, customized requirements that remove backgrounds that are particularly important to our search. Photons are identified using the central region of the CDF detector, $|\eta| < 1.0$, which contains both calorimeters and tracking chambers for robust identification. The calorimeters are used to distinguish between photons produced as part of the $p\bar{p}$ collision and those which are produced in the decay of hadrons, such as $\pi^0 \to \gamma\gamma$, or non-collision sources. The tracking systems are used to provide additional rejection against jets of hadrons as well as against electrons which are the other primary background as they shower in the EM calorimeter in a manner that is virtually identical to photons. To ensure that events are well measured and allow the full capability of the calorimeter and tracking chambers to be used in the identification of photons we only consider candidates in the fiducial region of the EM calorimeter.

A. Standard Photon Identification Variables

The CDF detector has been identifying photons for over 20 years so the ID criteria are well established and standardized. A photon deposits most of its energy in the EM calorimeter, so the primary identification searches for a large amount of energy deposited in an EM calorimeter tower. Since the dominant backgrounds are from electrons and $\pi^0 \to \gamma\gamma$ from jets, additional requirements are placed to reject them in a way that retains a high efficiency for real photons. For example, we require that there only be a small fraction of additional energy deposited in the hadronic tower behind

it to reject hadronic jets. We also require that there be a large amount of energy deposited in the CES and that it have a shower profile in the CES which is consistent with being from a single shower. We also require that there be no reconstructed track in the COT pointing to the cluster of energy in the tower, which would have indicated that the particle hitting the calorimeter was charged (or was associated with a charged particle). We also separate prompt photons from photons which are the decay products of hadrons, which are typically associated with other hadrons in jets and would make the photon "non-isolated". Thus, we require all photons in our sample to be isolated. This section briefly describes the high-E_T photon ID criteria; Ref. [62] lists sources that contain good reviews. All the criteria are summarized in Table IV.

At CDF we typically consider photons that deposit their energy in the central, $|\eta| < 1.0$, portion of the detector as it is the best instrumented for our purposes. Photons are identified as an energy deposition in up to three calorimeter towers in η and one tower in ϕ where the seed tower exceeds 3 GeV. We also require a matching cluster of energy in the CES in the same seed tower that is also used to determine the position of the photon. In order for a photon to be considered, we require that it be deposited in a portion of the calorimeter such that it is likely to be well measured and its shower to be fully contained. This region is called the fiducial region and is defined to be near the center of each tower, within 21 cm of the tower center in r-ϕ ($|X_{\rm CES}| < 21$ cm). A similar requirement in z is $9 < |Z_{\rm CES}| < 230$ cm [63]. The fraction of the CEM covered is $\sim 80\%$. The photon E_T is calculated from the summed energy of the three towers in the cluster (including the seed tower) and $\sin\theta$ is calculated with respect to the highest-$\Sigma p_{\rm T}$ vertex and the position in the CES.

TABLE IV: The photon selection requirements used to identify high-E_T, isolated photon candidates. These are the standard requirements with the addition of a customized electron rejection algorithm known as "Phoenix" rejection as well as a PMT asymmetry requirements.

The Standard Photon ID and Isolation Requirements	
detector	$\lvert\eta\rvert < 1.0$
E_T	≥ 13 GeV
fiduciality	$\lvert X_{\rm CES}\rvert \leq 21$ cm
	9 cm $\leq \lvert Z_{CES}\rvert \leq 230$ cm [63]
χ^2_{CES}	$\leq$20
$E_{\rm Had}/E_{\rm Em}$	$\leq 0.055+0.00045\times E$
E^{iso}_{cal}	$\leq 0.1\times E_T$ if $E_T<$20 GeV or
	$\leq 2.0+0.02\times(E_T-20)$
track isolation	$\leq 2.0+0.005\times E_T$
$N3D$ tracks in cluster	≤ 1
track P_T if $N3D=1$	$\leq 1.0+0.005\times E_T$
2nd CES cluster energy	$\leq 0.14\times E_T$ if $E_T<$18 GeV
	$\leq 2.4+0.01\times E_T$ if $E_T\geq$18 GeV
Additional Photon ID Requirements	
"Phoenix"	Reject photons matched to a "Phoenix" track
PMT Asymmetry	$\mathrm{A_P} = \frac{\lvert E_{\rm PMT1}-E_{\rm PMT2}\rvert}{E_{\rm PMT1}+E_{\rm PMT2}} < 0.6$

The identification and isolation variables are:

- $\chi^2_{\rm CES}$: The photon shower shape is measured at shower maximum by the strip chamber and wire chamber components of the CES in both the x and z directions as shown in Figure 12-(b). This is compared to the expected shape as measured from test beam data using a χ^2 test. This is particularly helpful in rejecting π^0's that decay via $\gamma\gamma$ where both photons deposit energy very near each other because of their large boost.

- Hadronic Leakage ($E_{\rm Had}/E_{\rm Em}$): Photons leave most of their energy in the EM portion of the calorimeter. The ratio of energy deposited in the hadronic part of the towers in the cluster to that in the electromagnetic part helps separate photons from jet backgrounds. The upper limit rejects these backgrounds from jets that usually deposit most of their energy in the hadronic part. Since higher energy photons are more likely to deposit some energy in the hadronic component this requirement scales with photon energy.

- E^{iso}_{cal}: Photons from heavy neutralino decays are likely to be spatially separated from other particles from the collisions. By way of comparison, photons from the decays of hadrons are often parts of jets and not isolated in space. To reject photons from hadron decays (which are often from jets) we create a calorimeter isolation variable that takes the sum of the energy of all EM and HAD towers within a cone of 0.4 in $\eta-\phi$ space, $\sqrt{\Delta\eta^2+\Delta\phi^2}=0.4$, centered on the photon and subtracts off the energy of the photon cluster, $E^{iso}_{raw}=E^{0.4}-E^{\gamma}$. This variable is then corrected to take into account the location of the photon within the calorimeter and subtract-off an average amount of energy to take into account potential energy leakage into the ϕ-cracks between the towers, $E^{location}_{corr}$. If there are additional reconstructed vertices it is expected that particles from

those collisions deposit an additional 356.3 MeV, on average, energy per tower from the underlying event. This contribution is subtracted for each additional vertex before the final requirement is made: $E_{cal}^{iso} = E^{0.4} - E^{\gamma} - E_{corr}^{location} - N_{vtx} \cdot$ 0.3563 GeV.We require E_{cal}^{iso} to be less than 2.0 GeV for $E_T^{\gamma} > 20\ GeV$, but becomes less restrictive with higher photon E_T to retain efficiency or to be less than $0.1 \times E_T^{\gamma}$ for $E_T^{\gamma} < 20$ GeV.

- Track rejection: Since electrons shower in the calorimeter in a manner that is almost identical to that for photons, the primary way to reject this background is by identifying the track from the charged particle's trajectory. If a track points to the photon cluster it is allowed to have a p_T of at most 1 GeV/c. This helps reject electrons, but since there can be stray tracks pointing at the photon the efficiency is retained by allowing a single track ($N3D = 1$) with a small p_T.

- Track isolation: In the same way we reject hadrons using isolation in the calorimeter, we require photons to be isolated in the tracking chamber. The Σp_{T} of all tracks coming from the vertex associated to the photon's position in the calorimeter within a cone of 0.4 around the seed tower, is required to be less than 2 GeV/c, but becomes less restrictive with higher photon E_T to retain efficiency.

- 2nd CES cluster rejection: If a photon is due to a $\pi^0 \rightarrow \gamma\gamma$ decay, there should be a second photon that can be identified in the CES. The CES of the seed tower is searched for the presence of a 2nd cluster. If one is found, the lower energy one is required to be less than 2.34 GeV, becoming less restrictive with higher photon E_T. We note that this requirement becomes less effective for high energy photons as the two photons from boosted π^0 decays are typically very colinear.

We note again at this point that this procedure is well established for identifying photons that come from the beam line. However, photons that are the decay products of neutralinos that travel a significant distance from the beam line before decaying, as shown in Figure 14, can alter the distribution of the $\chi^2_{\rm CES}$ for photons [19]. For this reason, only low lifetimes of the $\widetilde{\chi}^0_1$ are considered in this analysis since the detector simulation does not simulate $\chi^2_{\rm CES}$ correctly for a high incident angle photons from $\widetilde{\chi}^0_1$'s [19]. To avoid this problem we only consider the the $\widetilde{\chi}^0_1$'s lifetimes up to 2 ns where this problem is not an issue.

The next sections describe two additional photon ID requirements that are designed to reject instrumental backgrounds and electrons that could otherwise be misidentified as photons. Without their rejection, they would constitute a substantial background to our final state.

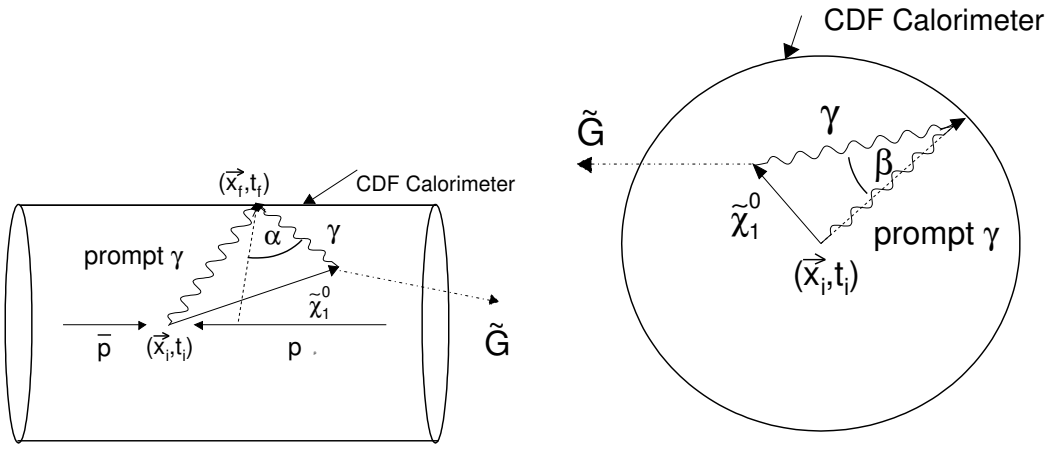

(a) (b)

FIG. 14: The production and decay of a long-lived neutralino into a photon and a gravitino. The incident angles (α and β) of the photon at the face of the calorimeter, relative to the expected direction from the center of the detector, are large when a photon comes from a long-lived $\widetilde{\chi}^0_1$ compared to a prompt photon. This causes the χ^2_{CES} variable to be different from expectations.

B. PMT Spikes

In the CEM an energy deposition is identified as a large amount of charge measured from the output of the two PMTs that collect light from the scintillator in the calorimeter. However, a high voltage breakdown in the PMT, known as a "spike", which is unrelated to an energy deposited in the calorimeter, can fake an energy deposit which can be misidentified as a photon. This instrumental effect can mimic photons if they overlap with a low energy deposit from an unrelated collision sources. Such an occurrence can produce false photon candidates that are uncorrelated with the collision and thus erroneously create corresponding missing energy. Since photons from the collision will approximately deposit the same amount of energy in each PMT (i.e., the same amount of light will be collected on both sides of the scintillator from each tube) these PMT spikes can be separated from real photon deposits by considering the asymmetry of the two energy measurements of the PMTs of a tower:

$$\mathrm{A_P} = \frac{|E_{\mathrm{PMT1}} - E_{\mathrm{PMT2}}|}{E_{\mathrm{PMT1}} + E_{\mathrm{PMT2}}} \tag{3.1}$$

where E_{PMT1} and E_{PMT2} are the energies as reported by PMT 1 and 2, respectively. Figure 15 compares photon candidates from both real photons and spikes to real electrons from $W \rightarrow e\nu$ events selected using a special trigger, described in Table V. The photon and spike candidates pass the PMT-enriched $\gamma + \not\!\!E_T$ sample identification requirements given in Table VI, while the electrons are required to pass the requirements of Table VII and the $W \rightarrow e\nu$ sample requirements are given in Table VIII. A comparison shows that PMT spikes cause a high PMT asymmetry and can be efficiently ($\sim$100%) rejected by requiring $\mathrm{A_P} < 0.6$. While most events with PMT spikes have a high asymmetry, their asymmetry magnitude is mainly less than 1 because of spurious deposits of energy from unrelated particles. The rate of this background,

after this requirement, is negligible and this requirement has a rejection power of ∼100%. Thus, this source will be neglected in the background estimate. We note, for completeness, that this requirement is more than 99.9% efficient as measured from the W sample.

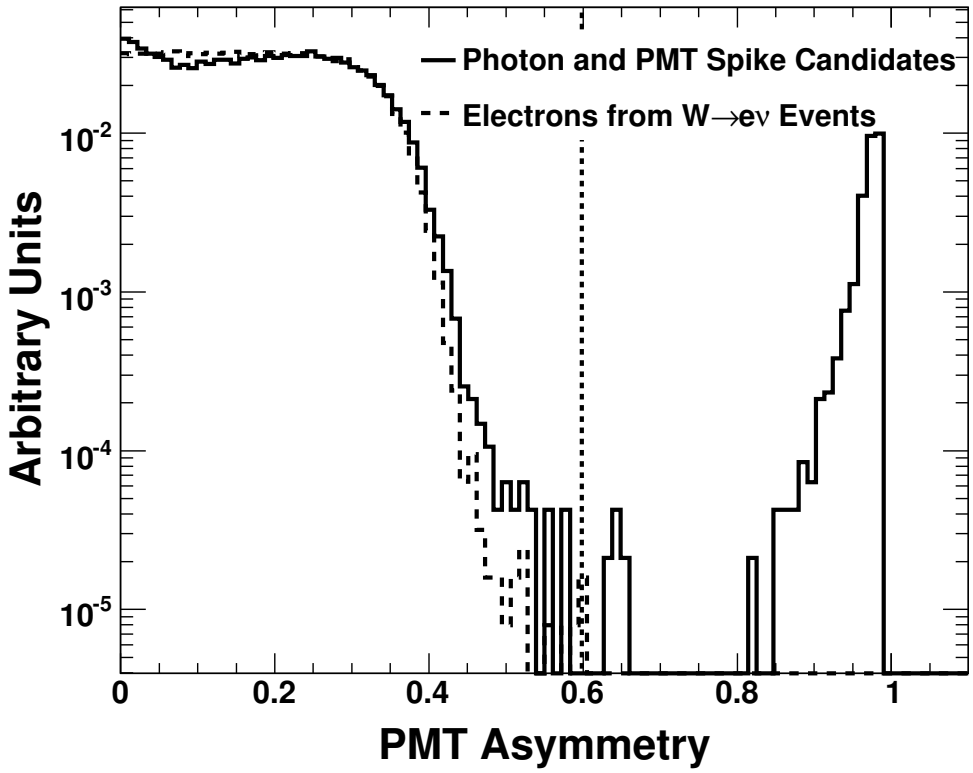

FIG. 15: A comparison of the PMT asymmetry, A_P, for a photon+$\not\!\!E_T$ sample that contains both PMT spikes and real photons, and a sample of electron from $W \to e\nu$ events. PMT spikes can be effectively removed by requiring the asymmetry to be less than 0.6.

TABLE V: The trigger requirements used to create the $\gamma + \not\!\!E_T$ and $W \rightarrow e\nu$ sample used to study the PMT asymmetry in electrons, photons and PMT spikes. This trigger is known as the W_NOTRACK trigger for historical reasons. Note also that all trigger E_T's at all three levels are calculated using $z = 0$.

	W_NOTRACK
L1	Single tower $E_T > 8$ GeV, $\lvert\eta\rvert < 3.6$
	Single tower $E_{\rm Had}/E_{\rm Em} < 0.125$
	$\not\!\!E_T > 15$ GeV
	$\sum E_T > 1$ GeV
L2	Single EM cluster $E_T > 20$ GeV, $\lvert\eta\rvert < 1.0$
L3	Single EM cluster $E_T > 25$ GeV, $\lvert\eta\rvert < 1.0$
	Single cluster $E_{\rm Had}/E_{\rm Em} < 0.125$
	$\not\!\!E_T > 25$ GeV

TABLE VI: The PMT-enriched $\gamma + \not\!\!E_T$ sample selection requirements. This sample is selected using the W_NOTRACK trigger given in Table V. The photon identification requirements are identical to those of Table IV, but with higher photon $E_T > 30$ GeV and a looser $E_{\rm Had}/E_{\rm Em} < 0.125$ requirements denoted with an *, except that the two additional requirements (PMT and Phoenix) are not required. Also the trigger, $\not\!\!E_T$ and vertex requirements are added and denoted with an †. The $\not\!\!E_T$ will be defined in next chapter.

The PMT-enriched $\gamma + \not\!\!E_T$ selection requirements	
trigger	W_NOTRACK trigger†
detector	$\lvert\eta\rvert < 1.0$
E_T*	≥ 30 GeV
fiduciality	$\lvert X_{\rm CES}\rvert \leq 21$ cm
	9 cm $\leq \lvert Z_{CES}\rvert \leq 230$ cm [63]
$E_{\rm Had}/E_{\rm Em}$*	0.125
E_{cal}^{iso}	$\leq 0.1\times E_T$ if $E_T<20$ GeV or
	$\leq 2.0+0.02\times(E_T - 20)$
track isolation	$\leq 2.0 + 0.005 \times E_T$
$N3D$ tracks in cluster	≤ 1
track P_T if $N3D = 0$	$\leq 1.0+0.005\times E_T$
2nd CES cluster energy	$\leq 2.4+0.01\times E_T$
$\not\!\!E_T$†	> 30 GeV
vertex requirement†	$N_{\rm vx} \geq 1$ with $z_{\rm vx} < 60$ cm

TABLE VII: The standard ("tight") requirements used to identify isolated electrons. Since we will also be considering electrons selected with a looser set of requirements later in this document (higher efficiency, smaller purity) the "loose" electron ID requirements are also given. They are identical to the tight electron ID requirements except for the requirements denoted with an *. Note that "Q" is the charge of the electron. All the variables are the same as those used to measure photons. Appendix A describes the electron-only ID variables that have not been used to identify photons.

The Standard Electron ID Requirements	
detector	$\lvert\eta\rvert < 1.0$
E_T	≥ 20 GeV
fiduciality	$\lvert X_{\rm CES}\rvert \leq 21$ cm
	9 cm $\leq \lvert Z_{CES}\rvert \leq 230$ cm [63]
track p_T	≥ 10 GeV
track $\lvert z_0\rvert$	≤ 60 cm
COT axial segments with $N_{hits} \geq 5$	≥ 3
COT stereo segments with $N_{hits} \geq 5$	≥ 2
track E/p if $p_T \leq 50$ GeV*	≤ 2.0
$Lshr$*	≤ 0.2
$\chi^2_{CES\ Strip}$*	≤ 10
Δz_{CES}*	≤ 3 cm
signed Δx_{CES}*	-3 cm$\leq Q \cdot \Delta x_{CES} \leq 1.5$ cm
$E_{\rm Had}/E_{\rm Em}$	$\leq 0.055 + 0.00045 \times E$
E^{iso}_{cal}	$\leq 0.1 \times E_T$

TABLE VIII: The identification requirements for use in selecting electrons from $W \rightarrow e\nu$ events. Appendix A describes the matching requirements.

The Requirements for Selecting the $W \rightarrow e\nu$ Sample
W_NOTRACK trigger in Table V
The tight electron ID requirements in Table VII
$\not\!\!E_T > 30$ GeV
Vertex requirements: $\sum p_T > 2$ GeV, $N_{\rm trk} > 2$ and $\lvert z_{\rm vx}\rvert < 60$ cm
Electron track-vertex matching: $\lvert z_{\rm trk} - z_{\rm vx}\rvert < 2$ cm and $\lvert t_{\rm trk} - t_{\rm vx}\rvert < 1.3$ ns

C. Customized Electron Rejection: Phoenix Tracking

Since $W\gamma \to e\nu\gamma \to \gamma\gamma_{fake} + \not\!\!E_T$ sources are an important background to the $\gamma\gamma + \not\!\!E_T$ final state, additional electron rejection techniques are needed. This section describes an additional photon identification requirement designed to suppress events where an electron is misidentified as a prompt photon candidate. This can occur, for example, when an electron has a catastrophic bremsstrahlung in the detector material before the COT chamber [64]. Such electrons, as charged particles, however, are likely to have left energy deposits in the silicon detector. By looking in the silicon for the presence of these hits along the path between the calorimeter deposit and the vertex we can sometimes find evidence of a charged particle. This algorithm, for historical reasons, is known as "Phoenix tracking" [65]. The algorithm reconstructs the trajectories of electrons without requiring hits in the COT as shown in Figure 16.

The approach is similar to the standard tracking algorithms in which reconstructed COT tracks are projected into the silicon and hits in a narrow road around the trajectory are considered for addition to the fit. In the same way, the Phoenix algorithm uses information from the calorimeter and the vertex position to project into the silicon and performs a standalone silicon track reconstruction, considering both the electron and positron hypothesis. A photon candidate will be rejected if it has a Phoenix track reconstructed. The standard rate at which electrons pass the standard photon ID requirements is 1.5±0.1%; after the addition of the Phoenix rejection requirements it is reduced to 0.4±0.2% (although it is E_T dependent). Because of the possibility of stray tracks being identified by this algorithm and causing prompt photons to fail this requirement, the efficiency of this requirement is $91.5 \pm 0.4\%$ for real photons.

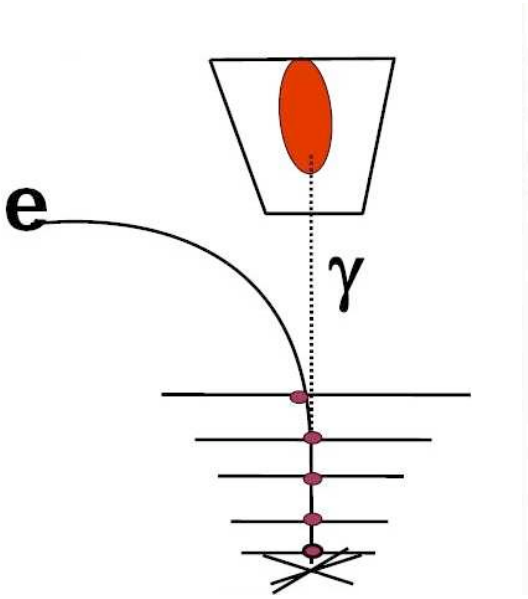

FIG. 16: The method of identifying electrons from their hits in the silicon detector (black solid lines).

D. Photon Identification Summary

The final efficiency for identifying two isolated, promptly produced photons is defined to be the ratio of all true photons that hit the fiducial part of the detector passing all photon identification requirements to the total number of events that have both photons hitting the fiducial part. It is measured to be $74.3 \pm 0.4\%$ from MC and is largely consistent with the the efficiency for identifying a single photon which is estimated to be $86.0 \pm 0.3\%$ [66]. We note that with all the requirements the probability of a jet faking an isolated photon is $0.3 \pm 0.1\%$ at $E_T^{\rm jet} = 10$ GeV and is falling as a function of E_T [67] and the probability of an electron faking an isolated photon is $0.4 \pm 0.2\%$ and is also falling as a function of E_T. Both effects are simulated in MC and taken into account in our background estimation techniques.

CHAPTER IV

MISSING TRANSVERSE ENERGY, UNCLUSTERED ENERGY, JETS AND TOTAL TRANSVERSE ENERGY

This chapter describes the remaining other objects that are central to our search: missing transverse energy, unclustered energy, jets and total transverse energy. The missing transverse energy is defined as an energy imbalance in the calorimeter and it is an experimental signature of neutrinos or new particles, like the gravitino, that do not interact significantly with the detector material. The $\not\!\!E_T$, however, can be mimicked by a simple energy mismeasurement or misreconstruction in SM events. We refer to this as "fake" $\not\!\!E_T$. Fluctuations or mismeasurements of jet energy are the most common source of such fake $\not\!\!E_T$. Thus, the more energy in the event the more likely it is to have a large amount of measured $\not\!\!E_T$. For these reasons, we describe both the energy measurement in the event and how it is broken into both a clustered component, which is what we call jets, and unclustered energy. We then talk about the jet measurement, the ways we correct their measurement and how we use these corrections to get a better measurement of the $\not\!\!E_T$.

Events with two photons from SM sources with no intrinsic $\not\!\!E_T$ can have a large measured $\not\!\!E_T$, fake $\not\!\!E_T$, from two major sources. There are large energy measurement fluctuations in the calorimeter, and event reconstruction pathologies such as picking the "wrong" vertex where one or both photon candidates are coming from a vertex other than the highest $\sum P_T$ primary vertex. A similar pathology is when tri-photon events are produced and one of the photons does not deposit its energy in the calorimeter (it is lost). More details of these pathological sources are described in Section VII.A.2 where we describe methods to correct for them and/or reduce their impact on our search.

We begin with a more complete description of the missing transverse energy measurement. Then we describe jets and unclustered energy, which will also be heavily used in correcting and modeling the $\not\!\!E_T$ resolution in Chapter VI. Finally, we end this chapter with describing the measurement of the total transverse energy, H_T.

A. Missing Transverse Energy

In proton-antiproton interactions the collision occurs with approximately no momentum in the plane transverse to the collision[1]. By conservation of momentum the vector sum of the transverse momenta of the final state particles is approximately zero. Particles that do not interact with the calorimeter can be inferred from the transverse energy imbalance of the detected, outgoing particles of a collision.

The measured missing transverse energy, $\not\!\!E_T$, is defined as the negative of the vector sum of the transverse energy measured in all calorimeter towers with $|\eta| < 3.6$. It is calculated relative to the highest-Σp_{T} vertex z-position, taking into account the x and y coordinates of the vertex. We refer to this value as $\not\!\!E_T{}^{raw}$. To improve the resolution, and to reduce the number of events with large fake $\not\!\!E_T$, the $\not\!\!E_T$ is corrected to account for the detector response for each reconstructed jets with $E_T > 15$ GeV. This procedure will be described after we describe the jet measurements.

There are both non-collision and collision sources that can cause $\not\!\!E_T$. SM neutrinos will leave the detector and produce significant $\not\!\!E_T$, and gravitinos, if they exist, are also expected to produce real significant $\not\!\!E_T$. Another source of significant $\not\!\!E_T$ can come from non-collision backgrounds. While the transverse energy of all produced particles is expected to be conserved in collisions, this is not true for non-collision

[1] As the momentum in the z direction of the protons and antiprotons is shared among its constituents ("partons"), the total momentum of the colliding partons is not known.

backgrounds that can produce energy deposits of the calorimeter; this will be described in detail in Section VII.C. In some sense this $\not\!\!E_T$ is fake since it is not from the collision, but it is real in the sense that it is not due to a mismeasurement of the energy deposited. On the other hand, mismeasurements of deposits of energy can give the appearance of $\not\!\!E_T$ in the detector. For QCD ($\gamma\gamma$, γj, and jj) events there are, in principle, no high E_T particles from these collisions that do not interact with the detector. In principle they produce minimal $\not\!\!E_T$, assuming perfect measurements. However, they can have large fake $\not\!\!E_T$ due to energy loss or mismeasurement in the calorimeter. We will refer to any source of $\not\!\!E_T$ that is not from high energy, weakly interacting particles as fake $\not\!\!E_T$.

While large values of fake $\not\!\!E_T$ from energy fluctuation are rare, there are so many events with no true $\not\!\!E_T$ that this is one of the biggest backgrounds in $\gamma\gamma$ events. Historically, the way to identify events with high energy, non-interacting particles in the final state was to require a large amount of $\not\!\!E_T$. Since only a small fraction of QCD events have a large measured value of $\not\!\!E_T$ this has been effective. However, the amount of fake $\not\!\!E_T$ due to mismeasurements is highly correlated with the amount and location of energy deposited energy in the detector. Since we are looking for events with large amount of energy, a more powerful, less biased technique is needed. For these reasons we compare the measured $\not\!\!E_T$ to the typical expectations based on the amount and location of the energy deposited. Thus, we consider the significance of the measured $\not\!\!E_T$, rather than its absolute value, to separate events with mismeasured $\not\!\!E_T$ from events with real $\not\!\!E_T$. This will be described in Chapter VI.

B. Jets, Jet Corrections and Corrected $\not\!\!E_T$

The term "jet" typically refers to the hadronization of a high energy quark or gluon that is produced in the $p\bar{p}$ collision. Since, at CDF, jets are identified as clusters of energy in the calorimeter this definition generically includes the reconstruction of the hadronic decays of a τ-lepton [68] and/or the energy deposited from electrons or photons. Algorithmically, jets are identified as clusters of energy in the calorimeter, using the standard jet-cone algorithm [69] with a search-cone radius $R = \sqrt{\Delta\phi^2 + \Delta\eta^2} = 0.4$. Calorimeter towers are grouped within 0.4 in $\eta - \phi$ space ("0.4 cone") around any single "seed" tower with $E_{_T} > 1$ GeV, and the energy and cluster centroid are calculated using all calorimeter towers within the 0.4 cone. The cluster centroid is calculated and the cone is moved to be centered on the centroid. This process is iteratively recalculated until convergence. Jets with an overlap of >50% are merged. The E_T is calculated based on the energy and location of the centroid of the jet in the calorimeter and the location of the primary vertex. Since the primary goal of the jet energy measurement is to determine the energy of the particle that originally produced it, see Figure 17, the energy measured directly in the calorimeter is corrected for a number of effects. In addition, these corrections help reduce the amount of mismeasurements of the energy of jet which are, in turn, used to correct the measurement of the $\not\!\!E_T$.

The jet energy corrections at CDF are standardized and have been used with great success for many years [70]. They are divided into different groups to accommodate different effects that can distort the measured jet energy. These include a) the response of the calorimeter to different particles, non-linear response of the calorimeter to the particle energies and uninstrumented regions of the detector, and b) effects like the fraction of the energy radiated outside the jet clustering algorithm

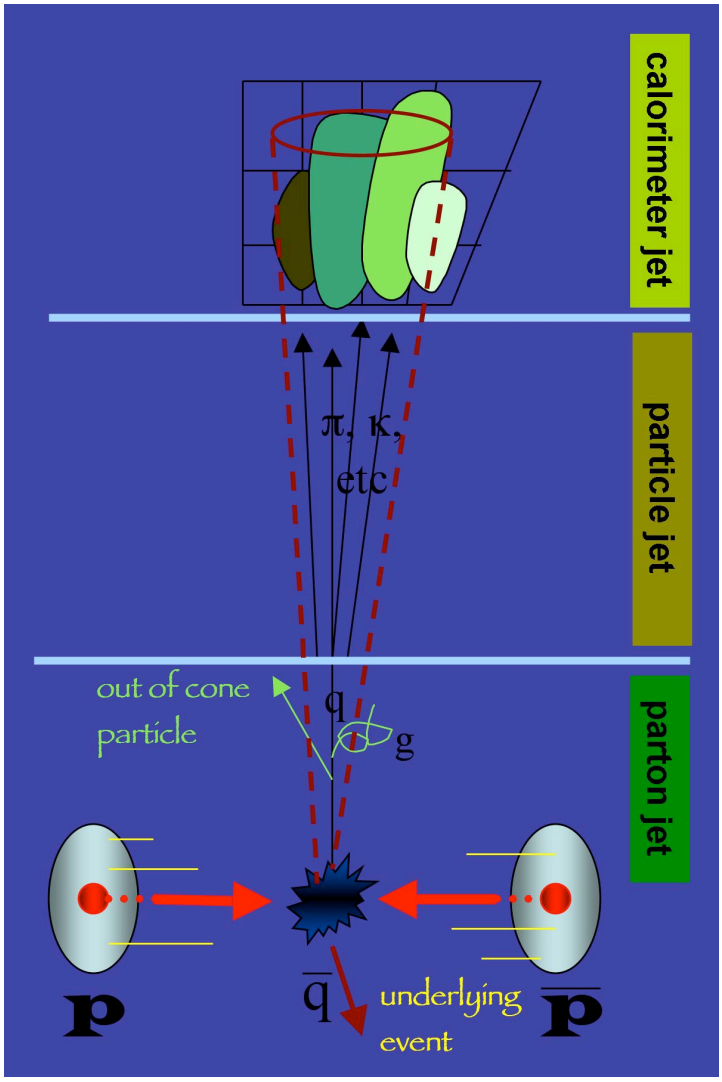

FIG. 17: A schematic of calorimeter (top), particle (middle), and parton (bottom) jet, showing also out-of-cone radiation.

cone. After these corrections the typical jet energy resolution is $\sim 64\%/\sqrt{p_T} \oplus 4\%$. More details on some of the effects that we correct for are described in Appendix B. Unless otherwise stated, only jets with $E_T > 15$ GeV and $|\eta| < 3.0$ are considered.

Since one of the biggest sources of fake $\not\!\!E_T$ is jet energy mismeasurement we reduce this effect by correcting the raw $\not\!\!E_T$ for the improved jet energy measurement. The correction due to all the jets is given by:

$$\vec{\not\!\!E}_T^{\,corr} = \vec{\not\!\!E}_T^{\,raw} - \sum^{jets} (\vec{E}_T^{raw} - \vec{E}_T^{corr}) \tag{4.1}$$

where $\vec{\not\!\!E}_T^{\,corr}$ is the missing E_T corrected for all the jets, $\vec{\not\!\!E}_T^{\,raw}$ is the missing E_T before the correction, and $\vec{E}_T^{corr}$ ($\vec{E}_T^{raw}$) is the jet E_T after (before) the jet energy correction described above. From here on out when we refer to the $\not\!\!E_T$ for an event we will only be talking about $|\vec{\not\!\!E}_T^{\,corr}|$.

C. Unclustered Energy

Figure 18 shows different types of interactions in the $p\bar{p}$ collision as well as additional collisions that produce energy in the event that is not part of a reconstructed cluster. We refer to this energy as the unclustered energy, $\sum E_T^{uncl}$. While jets come from the portion of the proton-antiproton collision that produces a "hard" parton scattering with large transverse momentum, p_T, the unclustered energy comes from the other particles that originate from the two outgoing partons as well as initial and final state radiation and particles that originate from the breakup of the proton and antiproton bunch ("beam-beam remnants"). Everything except the outgoing hard scattered objects, and the initial and final state radiation are known as the "underlying event". Also it is possible that multiple parton scattering contributes to the unclustered energy as shown in Figure 18-(b).

The activity of the underlying event and additional interactions in the same bunch crossing produce the unclustered energy. The $\sum E_T^{uncl}$ for each event is estimated by taking the total measured transverse energy in the event (measured tower-by-tower in the same way as the $\not\!\!E_T$, but using a scalar sum, and assuming the collision came from the position of the highest $\sum p_T$ vertex) and subtracting the transverse energies of all reconstructed photons, electrons, and jets:

$$\sum E_T^{uncl} = \sum E_T^{tower} - \sum E_T^{jet} - \sum E_T^{\gamma} - \sum E_T^{ele} \tag{4.2}$$

where the photons are identified using the criteria of Table IV and the electrons are identified using the criteria of Table VII.

D. Total Transverse Energy

Now that we have a good definition of the photon E_T, the jet E_T and the $\not\!\!E_T$, we are in a position to describe our last important object: the total transverse energy, H_T, for an event. The H_T is defined as a scalar sum of the transverse energies of all identified objects as follows:

$$H_T = \sum E_T^{\gamma} + \sum E_T^{ele} + \sum E_T^{jet} + \not\!\!E_T. \tag{4.3}$$

The H_T is an important variable because it is highly correlated with the mass of any SUSY particles produced. For example, they would produce large E_T photons and large $\not\!\!E_T$ from the neutralino decays. They would also produce large E_T particles in addition to the decay products of the $\widetilde{\chi}_1^0$ as part of the $\widetilde{\chi}_2^0$ and $\widetilde{\chi}_1^{\pm}$ decays as shown in Figure 4. In SPS 8 these would be taus, but in other, similar models, they could be other SM particles, like quarks or electrons, that would be identified as clusters of energy in the detector (jets). In the interests of model-independence we just simply

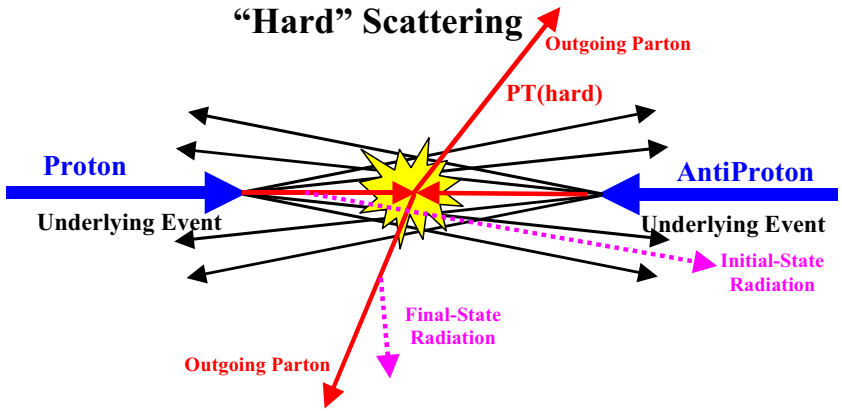

(a)

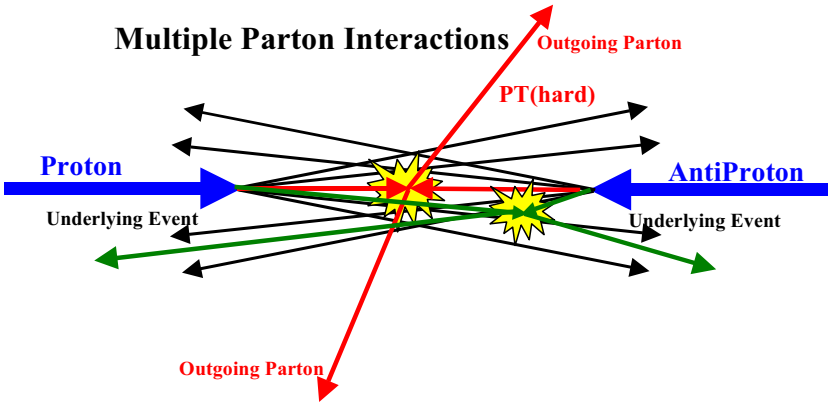

(b)

FIG. 18: In (a) is an illustration of a proton-antiproton collision in which a "hard" parton scattering produces a set of outgoing partons with large transverse momentum, p_T (hard). The resulting event contains particles that originate from the two outgoing partons (plus initial and final state radiation) and particles that come from the breakup of the proton-antiproton ("beam-beam remnants"). The "underlying" event is everything except the two outgoing hard scattered particles and consists of the beam-beam remnants. As shown in (b) it is possible that multiple parton scattering contributes to the underlying event. In addition to the hard parton-parton scattering, there can be a second "semi-hard" parton-parton scattering that contributes particles to the underlying event. Operationally, we consider the clustered portion of the event separately from the unclustered energy.

measure the total transverse energy of the photons, $\not\!\!E_T$ and jets and include electrons, if any are observed that pass the requirements listed in Table VII.

According to GMSB models, new physics is expected to appear at large energy scales and may reveal itself in an anomalous rate of $\gamma\gamma + \not\!\!E_T$ events with large values of $H_{_T}$ compared to SM expectation.

CHAPTER V

TRIGGERS, DATASETS AND EVENT PRESELECTION

Since the $\gamma\gamma + \not\!\!E_T$ analysis provides the best sensitivity for $\widetilde{\chi}_1^0$'s with low lifetimes and large masses this chapter describes the selection of $\gamma\gamma$ candidate events with an eye towards the final analysis where we take experimental limitations into consideration. There are three major sources of background for $\not\!\!E_T$ in $\gamma\gamma$ candidate events. They are:

- QCD events with fake $\not\!\!E_T$

  These types of events can arise from a number of sources: a) direct production of $\gamma\gamma$, $\gamma j \rightarrow \gamma\gamma_{fake}$, and $jj \rightarrow \gamma_{fake}\gamma_{fake}$ events where the $\not\!\!E_T$ arises due to normal resolution variations in the energy measurements in the calorimeter.

  b) large fake $\not\!\!E_T$ due to event reconstruction pathologies such as wrong vertex events where one or both photon candidates are coming from a vertex other than the highest $\sum p_T$ primary vertex, causing a systematic mismeasurement of the $\not\!\!E_T$ or other pathologies such as tri-photon events with a lost photon that creates the fake $\not\!\!E_T$.

- Electroweak events with real $\not\!\!E_T$

  a) charged leptonic decays of 1) $W\gamma\gamma$ and $Z\gamma\gamma$ events where both photons are real and the $\not\!\!E_T$ is from a neutrino produced in W decays, but lost leptons in Z's; 2) $W\gamma j$ and $Z\gamma j$ events where the jet fakes a photon and the $\not\!\!E_T$ is the same as in the previous case; 3) Wjj and Zjj events where both photon candidates are fake photons; 4) $t\bar{t}$ production and decay where the photons are produced from radiation from internal fermion lines or are from jets or electrons which fake the photon signature.

b) neutral leptonic channels: $Z\gamma\gamma \rightarrow \nu\bar{\nu}\gamma\gamma$, $Z\gamma j \rightarrow \nu\bar{\nu}\gamma\gamma_{fake}$ or $Zjj \rightarrow \nu\bar{\nu}\gamma_{fake}\gamma_{fake}$.

- Non-collision events:

  a) PMT spikes that overlap with soft particles, e.g. π^0, from the collision.

  b) cosmic ray muons that bremsstrahlung in the calorimeter and create one or more fake photons.

  c) beam related backgrounds ("beam halo") that produce one or more fake photons that are not related to the collision.

More details on each of these backgrounds, and rate at which they pass the selection requirements, are described in Chapter VII.

With these backgrounds in mind we describe our two-stage event selection process. First, we create an inclusive $\gamma\gamma$ sample, where we select any events with two photon candidates passing our photon ID and isolation requirements. We also require that it has a well measured vertex and does not have any specific properties that indicate a pathological reconstruction. This sample is defined as our "preselection" sample. In the second stage, a subset of this presample is chosen using selection requirements that are optimized for sensitivity to retain signal and reject backgrounds. This chapter describes the triggers used to select diphoton events for this search. Then the full set of event preselection criteria are motivated with an eye on the expectation of what GMSB events would look like. A full description of their simulation is given in Chapter VIII and forms the starting point for an optimization of the sensitivity to the GMSB signal, which is done in Chapter IX.

A. Triggers and Datasets

For this analysis events are selected from the subset of events that by pass one of four different sets of 3-level trigger requirements. These four trigger "paths" are summarized in Tables IX and X. Each set of requirements is slightly different, and has different advantages and limitations, but when the outputs are combined they are very efficient for our signal. They are known as the DIPHOTON_12, DIPHOTON_18, PHO_50 and PHO_70 triggers. To summarize their requirements, the first two triggers require two photons. The DIPHOTON_12 trigger allows candidate events with two photons with E_T as low as 12 GeV, but requires that each photon be isolated (using calorimeter isolation requirements similar to, but not the same as those described in Chapter III, [71]) in order to reduce the rate. Since these requirements can be inefficient, the DIPHOTON_18 trigger allows two photon candidate events to enter the data stream if they are both above 18 GeV without any isolation requirement. Since the photon ID requirements at the trigger level include a $\chi^2_{\rm CES}$ cut, and this value is slightly different online and offline (and inefficient at high E_T), we allow events into our sample if they pass a trigger if there is even a single photon in the event with $E_T > 50$ GeV without an isolation requirement or $E_T > 70$ without a $E_{\rm Had}/E_{\rm Em}$ requirement. These triggers are known as the PHO_50 and PHO_70 triggers. We next describe these requirements in more detail at each trigger level.

For all the trigger paths, at L1, events are required to have an energy deposit in a single EM calorimeter trigger tower (two adjacent physical towers in η) [72] that received a deposit of more than 8 GeV and has $E_{\rm Had}/E_{\rm Em} < 0.125$ to help reject hadronic jets, unless $E_T > 14$ GeV. At L2 the diphoton triggers require two EM clusters [71] with $|\eta| < 3.6$ and $E_T > 10$ GeV ($E_T > 16$ GeV), and $E_{\rm Had}/E_{\rm Em} < 0.125$ with (without) an isolation requirement for the DIPHOTON_12 (DIPHOTON_18)

trigger. The single photon triggers at L2 requires an EM cluster to have $E_T > 40$ GeV ($E_T > 70$ GeV) with $E_{\rm Had}/E_{\rm Em} < 0.125$ (no $E_{\rm Had}/E_{\rm Em}$) for the PHO_50 (PHO_70) triggers. At L3 the diphoton triggers do an EM clustering algorithm and require two EM clusters to have $E_T > 12$ GeV ($E_T > 18$ GeV) with $\chi^2_{\rm CES} < 20$ and isolation (no isolation) for the DIPHOTON_12 (DIPHOTON_18) trigger. As mentioned in Section III.A this trigger path already requires the $\chi^2_{\rm CES}$ requirement and limits our search sensitivity to long-lifetime neutralinos. The single photon triggers require only a single EM cluster to have $E_T > 50$ GeV ($E_T > 70$ GeV) with $E_{\rm Had}/E_{\rm Em} < 0.125$ unless $E > 200$ GeV ($E_{\rm Had}/E_{\rm Em} < 0.2+0.001E$ unless $E > 100$ GeV) for the PHO_50 (PHO_70) triggers.

In this analysis we consider data from the data-taking period after the EMTiming system became fully functional (Dec 7th, 2004, run number 190851), and until the spring shutdown of 2008 (April 16th, 2008, run number 216005). The integrated luminosity is measured using the Cherenkov Luminosity Counters. To ensure data quality a standard set of subsystems are required to be fully functional during data taking. We require the following systems to be good: CAL, SMX, COT [73]. After these requirements the data correspond to an integrated luminosity of 2.59 ± 0.16 fb^{-1} [74].

B. Event Preselection

In this subsection we describe the full set of offline preselection requirements. These include the photon requirements, the vertex requirements as well as non-collision and instrumental backgrounds rejection requirements.

Diphoton candidate events are selected from the subsample of events that pass any one of the four triggers. The two highest E_T ("leading") photons are required

TABLE IX: The diphoton triggers used in the selection of the diphoton sample. We only require an event to pass one of the four trigger paths described in this table or Table X. Note that while the L3 cluster isolation is basically the same as in offline, as described in Chapter III the L2 cluster isolation is calculated differently [71]. Note also that all trigger E_T's and isolations at all three levels are calculated using $z = 0$.

	DIPHOTON_12
L1	Single tower $E_T > 8$ GeV, $\|\eta\| < 3.6$
	Single tower $E_{\rm Had}/E_{\rm Em} < 0.125$ unless $E_T > 14$ GeV
L2	Two EM clusters $E_T > 10$ GeV, $\|\eta\| < 3.6$
	Both clusters $E_{\rm Had}/E_{\rm Em} < 0.125$
	Both L2 clusters isolation < 3 GeV or $< 0.15E_T$
L3	Two EM clusters $E_T > 12$ GeV, $\|\eta\| < 3.6$
	Both clusters $E_{\rm Had}/E_{\rm Em} < 0.055 + 0.00045E$ or $E_T > 200$ GeV
	Both L3 clusters isolation < 2 GeV or $< 0.10E_T$
	$\chi^2_{\rm CES} < 20$
	DIPHOTON_18
L1	Single tower $E_T > 8$ GeV, $\|\eta\| < 3.6$
	Single tower $E_{\rm Had}/E_{\rm Em} < 0.125$ unless $E_T > 14$ GeV
L2	Two EM clusters $E_T > 16$ GeV, $\|\eta\| < 3.6$
	Both clusters $E_{\rm Had}/E_{\rm Em} < 0.125$
L3	Two EM clusters $E_T > 18$ GeV, $\|\eta\| < 3.6$
	Both clusters $E_{\rm Had}/E_{\rm Em} < 0.055 + 0.00045E$ or $E_T > 200$ GeV
	$\chi^2_{\rm CES} < 20$

TABLE X: To help ensure that signal events are in our sample with 100% efficiency, we allow the event to come on either one of the triggers in Table IX or on one of the PHO_50 or PHO_70 triggers that are described here.

	PHO_50
L1	Single tower $E_T > 8$ GeV, $\|\eta\| < 3.6$
	Single tower $E_{\rm Had}/E_{\rm Em} < 0.125$ unless $E_T > 14$ GeV
L2	Single EM cluster $E_T > 40$ GeV, $\|\eta\| < 3.6$
	Single cluster $E_{\rm Had}/E_{\rm Em} < 0.125$
L3	Single EM cluster $E_T > 50$ GeV, $\|\eta\| < 3.6$
	Single cluster $E_{\rm Had}/E_{\rm Em} < 0.125$ unless for $E > 200$ GeV
	PHO_70
L1	Single tower $E_{\rm Had} + E_{\rm Em} > 10$ GeV, $\|\eta\| < 3.6$
	Single tower $E_{\rm Had}/E_{\rm Em} < 0.125$ unless $E_T > 14$ GeV
L2	Single EM cluster $E_T > 70$ GeV, $\|\eta\| < 3.6$
	No $E_{\rm Had}/E_{\rm Em}$ requirements
L3	Single EM cluster $E_T > 70$ GeV, $\|\eta\| < 3.6$
	Single cluster $E_{\rm Had}/E_{\rm Em} < 0.2 + 0.001E$ unless $E > 100$ GeV

to be in the central part of the calorimeter, $|\eta| \leq 1.0$, be in the fiducial part, have $E_T^\gamma > 13$ GeV, and pass the standard photon ID and isolation requirements, with the two additional ID requirements in Table IV described in Section III.A. When we consider these and the other, final offline requirements, as described in the rest of this Section, and using the MC techniques described in Section II.D we estimate that GMSB events that would pass all the final requirements are 100% likely to also pass the trigger requirements; said differently we estimate that they would have been written to disk by the trigger with 100% efficiency. More details on trigger efficiency and luminosity effects on the GMSB signal acceptance are described in Appendix C.

Since we only want to consider events that are well measured, only events where the diphoton candidates pass one of the trigger requirements as well as the photon ID and isolation requirements make it into our sample. We also require them to have: (a) a high quality vertex for the event, (b) no evidence of being from a non-collision source, and (c) no evidence of being an event from instrumental backgrounds. We next describe these selection requirements in more detail.

1. Vertex Requirements

To reject against non-collision events we require a high quality collision vertex, and to help maintain the projective nature of the calorimeter we require it to have $|z| \leq$ 60 cm. If there is more than one vertex reconstructed in the event, the E_T of all calorimeter objects (individual towers, photons, electrons, jets and $\not\!\!E_T$) are calculated with respect to the highest $\sum p_T$ vertex. In some cases this algorithm chooses the wrong vertex, for example, when a $\gamma\gamma$ pair is produced by one interaction and overlaps with a more energetic, second interaction that produces the highest $\sum p_T$ vertex.

A wrong vertex choice results in a mis-measurement of the E_T of both photon candidates, thus it causes fake $\not\!\!E_T$. Although this mis-measurement is small in most

cases, sometimes it can give a very large value of fake $\not\!\!E_T$ if the two vertices are far apart or if the photons are very energetic. Fortunately, this effect can be easily corrected for most events by a vertex re-assignment procedure. For every event we calculate the photon E_T for every vertex with $|z| \leq$60 cm and correct the $\not\!\!E_T$ for this difference. If it produces a smaller $\not\!\!E_T$ value we take these new values of the photon E_T and $\not\!\!E_T$, and use then these values instead of the primary vertex values in the kinematic calculations used in the final event selection[1]. This procedure minimizes the fake $\not\!\!E_T$ in events with the wrong vertex choice. The effect is shown in Figure 19 for a sample of 41,402 events that pass the photon ID requirements in Table IV and the vertex requirement ($z > 60$ cm) where we plot the difference of $\not\!\!E_T$, $\Delta\not\!\!E_T = \not\!\!E_T{}^{\rm old} - \not\!\!E_T{}^{\rm new}$, where $\not\!\!E_T{}^{\rm old}$ and $\not\!\!E_T{}^{\rm new}$ are before and after vertex swap, respectively. The changes are mostly small, but in some cases they are as large as ∼20 GeV. This well defined algorithm is used for signal and background calculations with identical procedures. As a result of this procedure some photons fall below the $E_T^\gamma \geq$13 GeV threshold and are removed from the final sample. Events that start with $E_T^\gamma <$13 GeV are not added back. The standard vertex requirements, with vertex re-assignment, are listed in Table XI.

[1]This algorithm is different than just choosing a vertex with the lowest $\not\!\!E_T$ since we only correct the photon E_T for a different vertex and use the other objects E_T based on the highest $\sum p_T$ vertex.

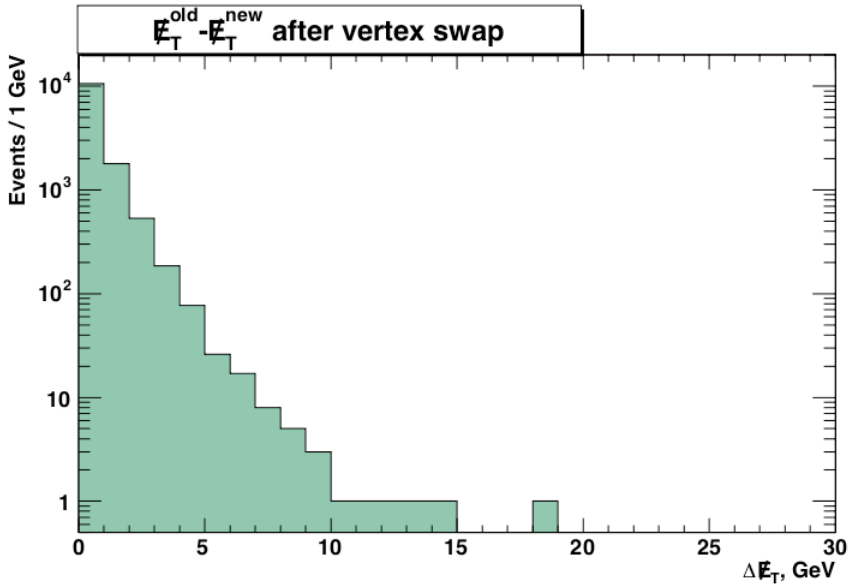

FIG. 19: Change in $\not\!\!E_T$ after passing the photon ID and isolation requirements given in Table IV and the vertex re-assignment in Table XI. Note that this value is always positive since we always select the smaller $\not\!\!E_T$ after reassignment.

TABLE XI: Summary of the vertex requirements and vertex re-assignment algorithms.

Vertex Requirements
At least one vertex with $\lvert z\rvert \leq$60 cm
The highest $\sum p_T$ vertex is selected as a primary vertex
For events with multiple vertices:
Calculate the photon E_T and $\not\!\!E_T$ for every vertex with $\lvert z\rvert \leq$60 cm
Correct only the photon E_T for this change (and the $\not\!\!E_T$ for the photon E_T)
Take these new values of the photon E_T and the $\not\!\!E_T$ if the $\not\!\!E_T$ is smaller

2. Non-Collision Rejection Requirements

We next describe the additional requirements placed on the sample to reduce the contamination of non-collision events. In particular, they are designed to remove backgrounds from beam related and cosmic ray sources where either a single or double photon-like signature produces the photons and/or $\not\!\!E_T$.

a. Beam Halo Rejection

Beam related backgrounds arise from particles, such as muons, which are created in interactions between the proton beam and material near the beam pipe upstream of the CDF detector [19]. They then travel parallel to the beam and thus form a "halo" around it. Backgrounds from them are known as beam halo backgrounds. As illustrated in Figure 20-(a) they travel roughly parallel to the original proton beam and can traverse the HAD and/or EM calorimeters where they have minimum ionizing interactions. While they typically leave a small amount of energy in multiple towers, they can deposit significant energy in a single tower that can mimic a photon. Figure 20-(b) shows the energy deposits of all calorimeter towers with $|\eta| < 4$ in a grid in η-ϕ space from an example beam halo event with no collision vertex; EM energy deposits are indicated in pink, hadronic in blue. Clearly visible is the tower with the photon candidate and the trail of energy deposits in towers along the z direction of the same wedge. For geometric reasons these photon candidates are typically located in the same wedge, mostly $|\phi| < 15°$. A beam halo "photon" typically arrives a few ns earlier than prompt photons, again for geometric reasons [19]. However, while the rate is lower, the photon candidate can also have a T_γ of $\sim$18 ns, where T_γ is the EMTiming recorded value without vertex time, or time of flight corrections [42], and multiples later and earlier, if the muon was created by a satellite proton bunch [19].

The dominant background from this source is when a beam halo source creates both photon candidates that overlap with a second collision from the bunch crossing; single γ beam halo overlapping a SM γ event has been shown to be negligible [43].

To suppress contributions due to this background, events are rejected if both photons are identified as beam halo candidates, using the beam halo ID requirements in Table XII, and separated by $|\Delta\phi| < 30^\circ$ (within neighboring wedges). These events are required to have energy deposits in multiple towers of the same wedge by the beam halo particle candidate as it travels roughly parallel to the beam pipe.

TABLE XII: Summary of the requirements used to identify photons from beam halo sources. For more detail see Ref. [19, 43]. Events are rejected if both photons are identified as beam halo candidates and are separated by $|\Delta\phi| < 30°$. Note that seedWedge is the number of CEM towers with $E_T > 0.1$ GeV (calculated with respect to $z = 0$) in the same wedge as the beam halo candidate, NHadPlug is the number of Plug HAD towers with $E_T > 0.1$ GeV in the same wedge as the beam halo candidate. The variable seedWedgeHadE is sum of the energy deposited in all of the hadronic towers from the same wedge as beam halo candidate. Note that this requirement on this quantity scales with both the number of observed vertices as well as the number of CEM towers.

A photon is identified as being from Beam Halo if	
Requirements	values
seedWedge	>9
NHadPlug	>2
seedWedgeHadE	$< [0.4 + (0.019(N_{vx} - 1) + 0.013)\text{seedWedge}]$ GeV
wedge number	0 or 23 ($\|\phi\| < 15°$)

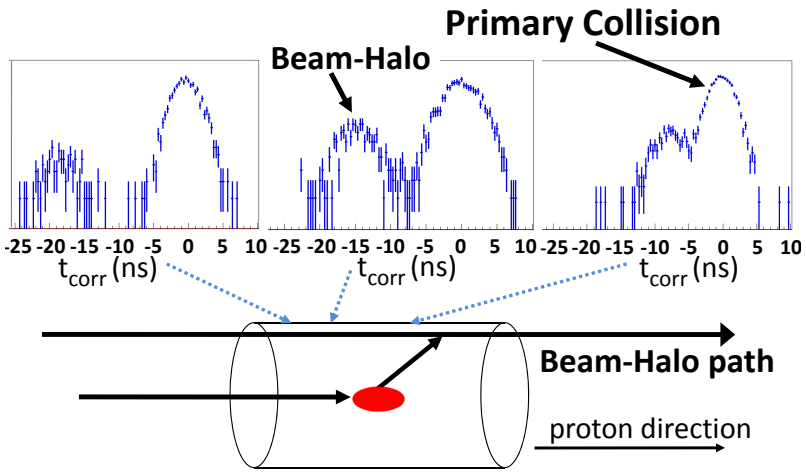

(a)

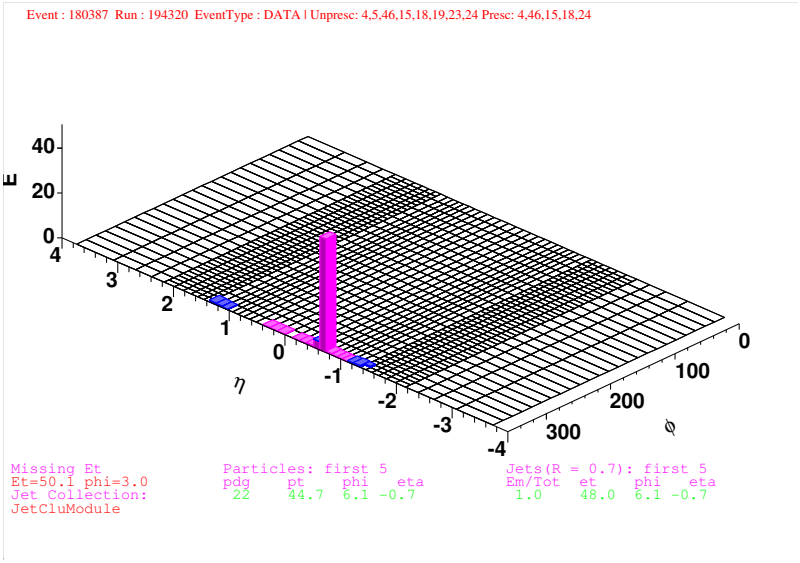

(b)

FIG. 20: In (a) is an illustration of beam halo type events. The beam halo path is indicated with an arrow and is along the path of the proton direction. A comparison of the time distributions of prompt collision events and beam halo "photons" that arrive at three example towers in the calorimeter shows that it is harder to separate them the further tower lies in beam halo direction. In (b) the energy deposit of all calorimeter towers with $|\eta| < 4$ in a grid in η-ϕ space from an example beam halo candidate event with no collision. Beam halo tends to deposit energy in a series of towers in the same wedge along the z direction.

b. Cosmic Ray Rejection

It is believed that cosmic rays produce EM clusters that are misidentified as photons either from bremsstrahlung as they traverse the magnet, or from a catastrophic interaction with the EM calorimeter [19]. This also can help fake the $\gamma\gamma + \not\!\!E_T$ signature. Figure 21 shows an event with a reconstructed photon candidate that has likely been produced by a cosmic ray particle. As cosmic ray sources interact with the detector and produce a photon randomly in time, their time distribution is flat over the full energy integration window range of 132 ns around the collision [19]. Figure 22 shows the "corrected" arrival time (corrected for average path length) distribution for cosmic ray events, which are selected from the $\gamma + \not\!\!E_T$ sample that pass the requirements in Table VI except we have added the PMT rejection requirement, but removed the reconstructed vertex.

If the cosmic ray created both photons then the difference in arrival time of the first and second photons from cosmic rays is also proportional to the spatial separation between these two photons; photons from collision events arrive at the calorimeter almost coincidentally in time. Thus, to suppress contributions from cosmic ray sources, we use the EMTiming system to apply timing requirements and compare their timing to a sample of $Z \rightarrow e^+e^-$ events. The $Z \rightarrow e^+e^-$ sample is created by selecting events with two electrons of opposite charge and 85 GeV/c^2 $< M_{e^+e^-} <$ 97.5 GeV/c^2 to be consistent with the measured Z mass of 91 GeV/c^2. Both electrons are required to pass the standard loose electron ID and isolation requirements in Table VII; Table XIII gives the full event requirements. There are 12,477 events in this sample. These timing requirements separately reject an event if either photon is more than 4σ, where $\sigma_{\rm T} = 1.665$ ns as measured in $Z \rightarrow e^+e^-$ events as shown in Figure 23. Similarly, the event is rejected if the two photons are well separated in time; specifically if

$|\Delta T_{\gamma\gamma} = T_{\gamma 1} - T_{\gamma 2}| > 4\sigma_{\Delta T}$, where $\sigma_{\Delta T} = 1.021$ ns as measured in the same sample of $Z \rightarrow e^+e^-$ events (again see Figure 23). The cosmic ray rejection requirements are listed in Table XIV.

TABLE XIII: The $Z \rightarrow e^+e^-$ sample selection requirements.

The Requirements for Selecting the $Z \rightarrow e^+e^-$ Sample
Both electrons passing the requirements in Table VII
Z mass requirement with two opposite signs of electrons:
$85 \text{ GeV}/c^2 < M_{e^+e^-} < 97.5 \text{ GeV}/c^2$
$\lvert z_{\text{vx}} \rvert < 60$ cm
$\not\!\!E_T$ cleanup requirements given in Table XV

TABLE XIV: Summary of the EMTiming requirements used to remove cosmic ray events. T_γ is the EMTiming recorded value without vertex time, or time of flight corrections [42].

An event is identified as a cosmic ray if
Either $\lvert T_{\gamma 1} \rvert$ or $\lvert T_{\gamma 2} \rvert > 4\sigma_T$, where $\sigma_T = 1.665$ ns
or $\lvert \Delta T_{\gamma\gamma} = T_{\gamma 1} - T_{\gamma 2} \rvert > 4\sigma_{\Delta T}$, where $\sigma_{\Delta T} = 1.021$ ns

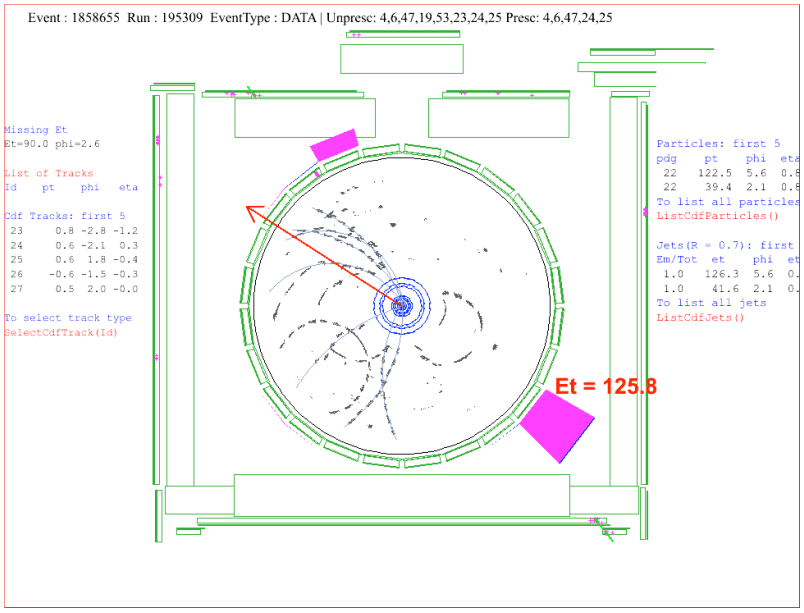

(a)

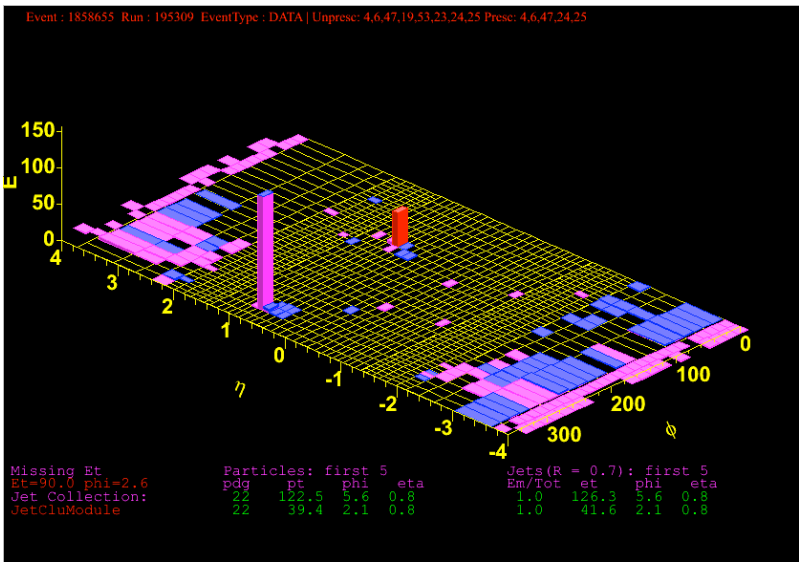

(b)

FIG. 21: A view in the r-ϕ plane (a) along the beam direction and the calorimeter towers in the η-ϕ plane (b) for a cosmic ray background candidate. Note that (a) shows no tracks associated with photons, indicating that this is a non-collision event.

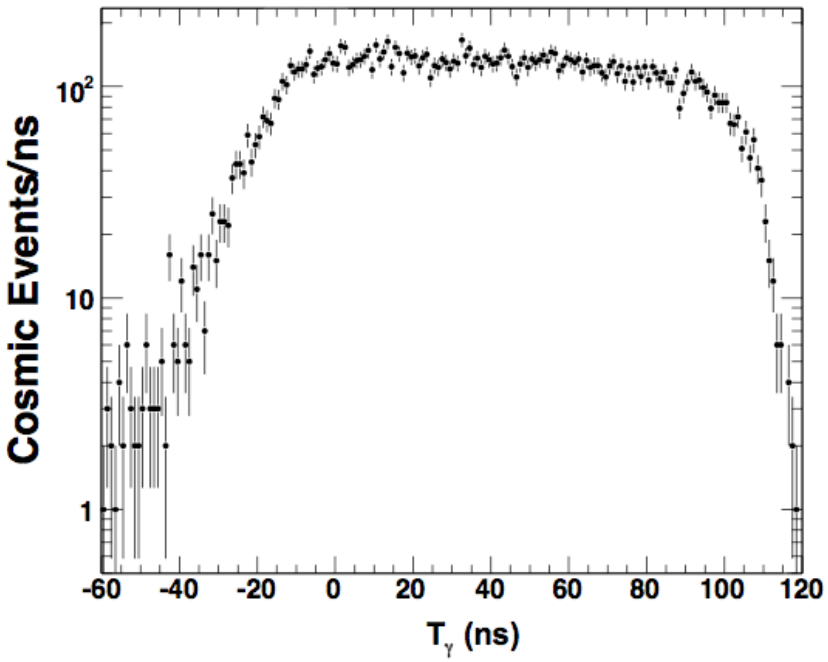

FIG. 22: The corrected time, T_γ, for cosmic ray background in the $\gamma + \not\!\!E_T$ sample selected using the requirements in Table VI, but with the PMT rejection requirement and no reconstructed vertex. Note that the number of events falls off rapidly towards the edges of the energy integration windows on both size of 0 ns.

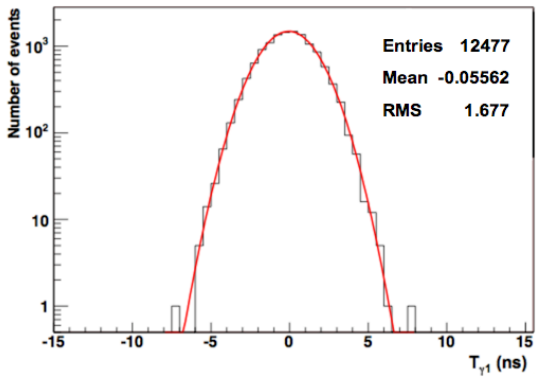

(a)

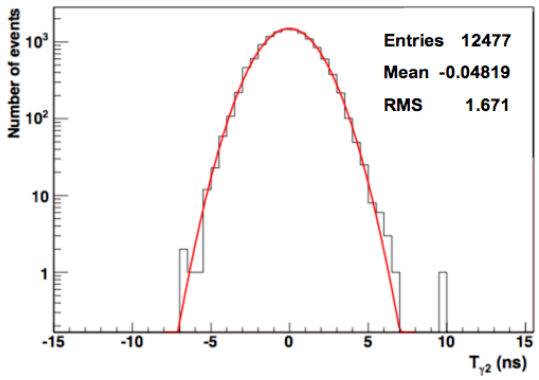

(b)

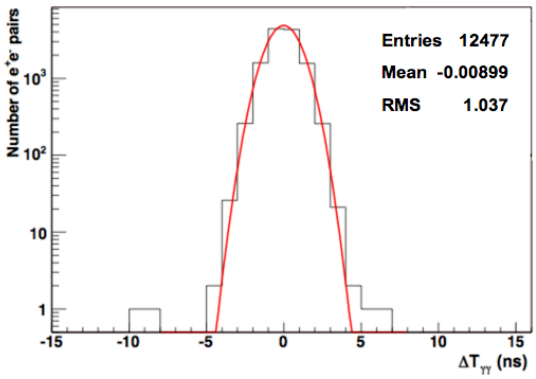

(c)

FIG. 23: Timing resolution for the first electron (a) and the second electron (b) from $Z \to e^+e^-$ data events, selected using the requirements in Table XIII. Bottom plot (c) shows a resolution for the difference between the arrival times of the two electrons.

3. $\not\!\!E_T$ Cleanup Requirements

The last set of requirements are to remove events where the $\not\!\!E_T$ is likely to be due to a severe energy mismeasurement (not due to a fluctuation of the measurement) of a photon in the calorimeter. Photons with the second highest E_T that either has very few tracks (N_{trk}) or deposit energy in a small number of calorimeter towers (N_{twr}), can be severely mismeasured and thus cannot be reconstructed as a photon if they are located close to the calorimeter cracks at $\eta\sim0$ and $|\eta|\sim1.1$. Such cases include when a photon (or π^0) is partially lost in the cracks. When the photon hits an edge of CES chamber close to the crack ($|X_{\rm CES}(\gamma2)|$ >18.5 cm) it leaves the signature of a jet mostly in HAD calorimeter ($EmFr$ <0.3) and thus, the photon is reconstructed as a jet with small number of tracks. Therefore, we remove events where the azimuthal angle between $\not\!\!E_T$ and the second-highest E_T photon or a jet is $|\Delta\phi(\not\!\!E_T - \gamma2)| < 0.3$ or if any jet points to the uninstrumented regions of the calorimeter. The full set of $\not\!\!E_T$ "cleanup" requirements are listed in Table XV.

TABLE XV: Summary of the $\not\!\!E_T$ cleanup cuts. Note that misreconstructed photons can be identified as jets where the number of calorimeter towers in the jet, N_{twr}, and the number of tracks in the jet, N_{trk}, are small. Also the fraction of the energy in the EM towers divided by the total energy of the jet, $EmFr$, is small.

Case	The event is removed if
For 2nd photon with $\Delta\phi(\not\!\!E_T - \gamma2)$ <0.3	$\|\eta(\gamma2)\|$ >1.0 or $\|\eta(\gamma2)\|$ <0.1 or $\|X_{CES}(\gamma2)\|$ >18.5 cm
For any jet ($\|\eta_{det}(jet)\|$ <2.5, E_T >5 GeV, N_{twr} <10, N_{trk} <5) with $\Delta\phi(\not\!\!E_T - jet)$ <0.3	$EmFr$ >0.875 and $\|\eta_{det}(jet)\|$ <1.1 or $EmFr$ <0.3 and ($\|\eta(jet)\|$ <0.1 or $\|\|\eta(jet)\| - 1.15\|$ <0.05)

C. Summary of the Preselection Requirements

After all the requirements in Tables IV-XV the $\sim 10^{16}$ collisions considered by the CDF detector have been reduced to a preselection sample that consists of 38,053 events. Table XVI gives a summary of the event reduction as a function of the requirements as they are applied sequentially.

TABLE XVI: Summary of the $\gamma\gamma + \not\!\!E_T$ presample selection requirements and the event sample reduction. The trigger requirements are given in Tables IX and X, the photon ID and isolation, Phoenix and PMT requirements are described in Table IV, the vertex requirements and vertex swap procedure are described in Table XI, the beam halo rejection requirements are described in Table XII, the cosmic rejection requirements are given in Table XIV and the $\not\!\!E_T$ cleanup cuts are given in Table XV.

Requirements	Signal sample (events passed)
Trigger and photon ID and isolation requirements with $\lvert\eta\rvert < 1.1$ and $E_T > 13$ GeV	45,275
Phoenix rejection	41,418
PMT spike rejection	41,412
Vertex requirements	41,402
$E_T^{swap} > 13$ GeV after vertex swap	39,719
Beam Halo rejection	39,713
Cosmic rejection (EMTiming requirements)	39,663
$\not\!\!E_T$ cleanup	38,053

CHAPTER VI

METMODEL: A $\not\!\!E_T$ RESOLUTION MODEL

Since SUSY particles are expected to produce both a large amount of $\not\!\!E_T$ and a large amount of clustered energy (H_T) we will need a sophisticated understanding of the $\not\!\!E_T$. Since we will require the presence of a large amount of deposited energy we need additional techniques to separate events with large energy and fake $\not\!\!E_T$ from large energy and real $\not\!\!E_T$. This can be achieved if we consider the significance of the measured $\not\!\!E_T$, $\not\!\!E_T$-significance, rather than its absolute value, which requires an understanding of the $\not\!\!E_T$ resolution as a function of the energy deposited in the calorimeter.

While large values of fake $\not\!\!E_T$ from energy fluctuation are rare, there are so many events with no true $\not\!\!E_T$ that this is one of the biggest backgrounds in $\gamma\gamma$ events. Historically, the way to identify events with high energy, non-interacting particles in the final state was to require a large amount of $\not\!\!E_T$. Since only a small fraction of QCD events have a large measured value of $\not\!\!E_T$ this has been effective. However, the amount of fake $\not\!\!E_T$ due to mismeasurements is highly correlated with the amount of energy deposited energy in the detector. Since we are looking for events with large amount of energy, a more powerful, less biased technique is needed. Since the overwhelming majority of events are slightly mismeasured we have developed a new model of the resolution of the measurement which we call METMODEL [43]. This predicts the shape of fake $\not\!\!E_T$ distribution due to fluctuations in energy measurements in the calorimeter and calculates its significance on an event-by-event basis. We define the quantity of $\not\!\!E_T$-significance as a dimensionless number based on the METMODEL. This new modeling takes into account a detailed understanding of how each jet in the event (clustered energy) as well as all the unclustered particles interact in the detector.

The previous version of the significance used at CDF [75], defined as $\not\!\!E_T/\sum E_T$

where $\sum E_T$ is the total energy measured in the detector, is useful, but it is insufficient. Its effectiveness is limited because it does not take into account important effects like the number of jets and how and where they deposit energy in the detector. The $\not\!\!E_T$-significance we calculate is based on the simple assumption that fluctuations in energy measurements of the jets and unclustered energy are different, but when combined separately well model the dominant sources of fake $\not\!\!E_T$. With this assumption we can calculate the probability that the observed $\not\!\!E_T$ is significant.

The individual contributions of each of these components to fake $\not\!\!E_T$ can be modeled, on average, by varying their energy distributions ("smearing") according to the corresponding energy resolutions of the measured objects. Jets are the dominant source of fake $\not\!\!E_T$ because they contain most of the energy and because they are collimated sprays of energetic particles in a certain direction, which can cause large energy measurement fluctuations in that direction. The unclustered energy, on the other hand, tends to be smaller and uniformly spread in the calorimeter. Therefore, the portion of $\not\!\!E_T$ due to this source is usually small.

The resolution of the $\not\!\!E_T$ is an unusual quantity. Typically, when a quantity is measured it can be well described by its mean value and its RMS. The RMS often describes the resolution. The $\not\!\!E_T$ distribution, however, for events with no intrinsic $\not\!\!E_T$ is different in that it is not Gaussian. Rather, it is the measurement of the missing energy in the x and y directions separately and these are then added in quadrature. That being said, the missing energy distribution in the x-direction is essentially a Gaussian with a mean centered at zero (assuming a well calibrated detector) and an RMS that is given by the resolution. The same is true with the y-direction. Knowing the mean and RMS's of these two distributions allows us to determine the expected $\not\!\!E_T$ distribution assuming no mean, true $\not\!\!E_T$. When we describe the $\not\!\!E_T$ resolution we mean the RMS of the x and y direction measurements. Both are a function of the jet

activity and the unclustered energy in the event.

We begin with a measurement of how the detector responds to both jets and the unclustered energy and how we create what we call the energy resolution functions. With these resolution functions we can calculate the overall mean offset and resolution of the $\not\!\!E_T{}^x$ and $\not\!\!E_T{}^y$ separately on an event-by-event basis. This allows for a prediction of the distribution of expected $\not\!\!E_T$ measurement when there is no "true" $\not\!\!E_T$ in the event. Essentially we can calculate a probability distribution function, $\mathcal{P}(\not\!\!E_T)$, for the event. We can use this probability along with a Monte Carlo pseudo-experiment method to estimate the distribution of the expected $\not\!\!E_T$ and its correlation with H_T in events. Similarly, we can use it with integration techniques, to quickly calculate a $\not\!\!E_T$-significance for the event.

In the next sections we describe how we measure the contributions of the unclustered and jet energies to the $\not\!\!E_T$ resolution functions separately. We then continue with a description of how these resolution functions are combined. We begin with a description of the measurement of the resolution due to the unclustered energy because it is easier to explain.

A. The $\not\!\!E_T$ Resolution Function due to Unclustered Energy

The $\not\!\!E_T$ resolution due to the unclustered energy is measured and checked using two independent sets of data events from SM sources where there is expected to be no significant source of real $\not\!\!E_T$. These are a sample of photon+jet events and a sample of $Z \to e^+e^-$ events since both samples can be selected without the presence of a jet. The photon+jet sample is selected as having all the same properties of the diphoton sample, but where one of the photon candidates does not pass all the photon criteria in Table IV, yet does pass a "loose" photon-like set of photon requirements. The loose

photon ID requirements are listed in Table XVII. The full set of sample requirements are given in Table XVIII. We call this the $\gamma\gamma$ control sample. There are 52,229 events in this sample. Unlike the $\gamma\gamma$ control sample a set of $Z \rightarrow e^+e^-$ events, selected using Table XIII, have essentially no contamination from non-collision backgrounds thus making this sample ideal[1] for testing techniques to evaluate the resolution for QCD background with fake $\not\!\!E_T$. The downside to this sample is that it has lower statistics.

TABLE XVII: Summary of the standard loose photon ID requirements used to create the $\gamma\gamma$ control sample. Note that the requirements that are different from the standard photon ID and isolation requirements in Table IV are indicated with a *. Also we do not require the PMT asymmetry and Phoenix rejection requirements.

Cuts	Loose photon ID requirements
detector	$\lvert\eta\rvert < 1.0$
E_T	≥ 13 GeV
fiduciality	$\lvert X_{\rm CES}\rvert \leq 21$ cm
	9 cm $\leq \lvert Z_{CES}\rvert \leq 230$ cm [63]
$\chi^2_{\rm CES}$	$\leq$20
$E_{\rm Had}/E_{\rm Em}$*	$\leq$0.125
E^{iso}_{cal}*	$\leq 0.15\times E_T$ if $E_T<20$ GeV or
	$\leq 3.0+0.02\times(E_T-20)$
track isolation*	≤ 5 GeV
$N3D$ tracks in cluster	≤ 1
track P_T if $N3D=1$*	$\leq 0.25\times E_T$
2nd CES cluster energy*	no cut

[1]This is only true for low $\not\!\!E_T$ region since WW, WZ and ZZ process can significantly contribute large, real $\not\!\!E_T$.

TABLE XVIII: The $\gamma\gamma$ control sample selection requirements. There are 52,229 events in the sample. Note that any events where both photons pass the tight photon ID requirements in Table IV are rejected from this sample.

The Requirements for Selecting the $\gamma\gamma$ Control Sample
Both photons pass the requirements in Table XVII
At least one photon fails the requirements in Table IV
The event passes all other preselection requirements in Table XVI

We start by looking at the subsample of 42,334 events with no jets in the $\gamma\gamma$ control sample, $N_{jet}(E_T > 15 \text{ GeV}) = 0$, to isolate and measure the contribution of the unclustered energy to the $\not\!\!E_T{}^x$ and $\not\!\!E_T{}^y$ resolutions. Since, as we will see, the calorimeter energy resolution in the x and y directions grows linearly as a function of $\sqrt{\sum E_T^{uncl}}$ (defined according to Equation 4.2) we break the $\not\!\!E_T$ into the distributions of both x and y components of the $\not\!\!E_T$ for events with no jets into eight separate bins of $\sqrt{\sum E_T^{uncl}}$. The $\not\!\!E_T{}^x$ and $\not\!\!E_T{}^y$ distribution, which we call a probability distribution function, is shown for a single bin of $\sum E_T^{uncl}$ in Figure 24 and is well described by a two Gaussian fit where the second Gaussian helps describe the probability of observing a large energy value of $\not\!\!E_T{}^x$ or $\not\!\!E_T{}^y$ tails and which, overall, does a better job of describing the distribution. The probability distribution function, $\mathcal{P}_{uncl}^{\not\!\!E_T{}^{x,y}}\left(\sqrt{\sum E_T^{uncl}}\right)$, due to the unclustered energy is thus given by

$$\mathcal{P}_{uncl}^{\not\!\!E_T{}^{x,y}}\left(\sqrt{\sum E_T^{uncl}}\right) = Norm_1 \cdot Gauss_1(mean_1, \sigma_1) + Norm_2 \cdot Gauss_2(mean_2, \sigma_2) \tag{6.1}$$

where $Gauss_1$ and $Gauss_2$ refer to the two Gaussians fit to the distribution, and the $mean_i$, σ_i, and $Norm_i$ of two Gaussians are measured for each bin of $\sqrt{\sum E_T^{uncl}}$ from the individual fits of $\not\!\!E_T{}^x$ and $\not\!\!E_T{}^y$ distributions, as shown in Figure 24. Since we

assume the two Gaussian's have the same means we take $mean_1 = mean_2 = mean$. We allow the two RMS's to be different and take $\sigma_2 = scale \cdot \sigma_1 = scale \cdot \sigma$ due to intrinsic calorimeter effects (e.g., particles lose some energy in the calorimeter cracks), and do the normalizations so that only a single normalization term is used. Rewriting we take:

$$\mathcal{P}_{uncl}^{\not\!\!E_T{}^{x,y}}\left(\sqrt{\sum E_T^{uncl}}\right) = \frac{Gauss(mean,\sigma) + Norm \cdot Gauss(mean, scale \cdot \sigma)}{1 + Norm} \quad (6.2)$$

where the $\frac{1}{1+Norm}$ term normalizes the $\mathcal{P}_{uncl}^{\not\!\!E_T{}^{x,y}}\left(\sqrt{\sum E_T^{uncl}}\right)$ to 1. We find the parameters we have chosen vary smoothly as a function of $\sqrt{\sum E_T^{uncl}}$, see Figure 24, and we parameterize them as:

$$\begin{aligned} mean &= p_0 + p_1 \sum E_T^{uncl} \\ \sigma &= p_0 + p_1 \sqrt{\sum E_T^{uncl}} \\ scale &= p_0 + p_1 \sqrt{\sum E_T^{uncl}} \\ Norm &= p_0 \end{aligned} \quad (6.3)$$

where all p_0 and p_1 are different for each equation.

The default set of parameters is obtained from the $\gamma\gamma$ control sample since it has higher statistics. The results of similar parameterizations in fits to the data $Z \to e^+e^-$ sample are used as an alternative set of parameters to study the associated systematic variations. We do not observe any significant difference in the parameterization of the $\not\!\!E_T$ resolution due to unclustered energy between $Z \to e^+e^-$ and our $\gamma\gamma$ control samples in data. The resulting fits and their uncertainties are given in Table XIX. More examples and details, including studies with MC simulations that show similar results, can be found in Ref [76].

TABLE XIX: The parametrization of the $\not\!\!E_T{}^x$ and $\not\!\!E_T{}^y$ resolutions due to the unclustered energy for the $\gamma\gamma$ control and $Z \to e^+e^-$ samples. Note that the uncertainties are only the statistical uncertainties from the fits. The parameters given refer to the formulation given in Eq 6.3. There is no significant difference between the measurements from the two different control samples.

Parameters	$\gamma\gamma$ control sample	$Z \to e^+e^-$ sample
$mean_{\not\!\!E_T{}^x}$	$p_0 = -0.022 \pm 0.057$	$p_0 = -0.048 \pm 0.057$
	$p_1 = 0.0065 \pm 0.0008$	$p_1 = 0.0067 \pm 0.0007$
$mean_{\not\!\!E_T{}^y}$	$p_0 = -0.016 \pm 0.038$	$p_0 = -0.017 \pm 0.053$
	$p_1 = 0.0038 \pm 0.0003$	$p_1 = 0.0032 \pm 0.0007$
$\sigma_{\not\!\!E_T{}^x}$	$p_0 = 0.82 \pm 0.25$	$p_0 = 1.03 \pm 0.36$
	$p_1 = 0.372 \pm 0.031$	$p_1 = 0.371 \pm 0.042$
$\sigma_{\not\!\!E_T{}^y}$	$p_0 = 0.60 \pm 0.25$	$p_0 = 1.04 \pm 0.32$
	$p_1 = 0.387 \pm 0.022$	$p_1 = 0.389 \pm 0.034$
$scale_{\not\!\!E_T{}^x}$	$p_0 = 2.16 \pm 0.17$	$p_0 = 1.94 \pm 0.11$
	$p_1 = -0.064 \pm 0.020$	$p_1 = -0.051 \pm 0.013$
$scale_{\not\!\!E_T{}^y}$	$p_0 = 1.99 \pm 0.17$	$p_0 = 2.19 \pm 0.16$
	$p_1 = -0.046 \pm 0.020$	$p_1 = -0.079 \pm 0.019$
$Norm_{\not\!\!E_T{}^x}$	$p_0 = 0.180 \pm 0.022$	$p_0 = 0.281 \pm 0.076$
$Norm_{\not\!\!E_T{}^y}$	$p_0 = 0.147 \pm 0.036$	$p_0 = 0.235 \pm 0.078$

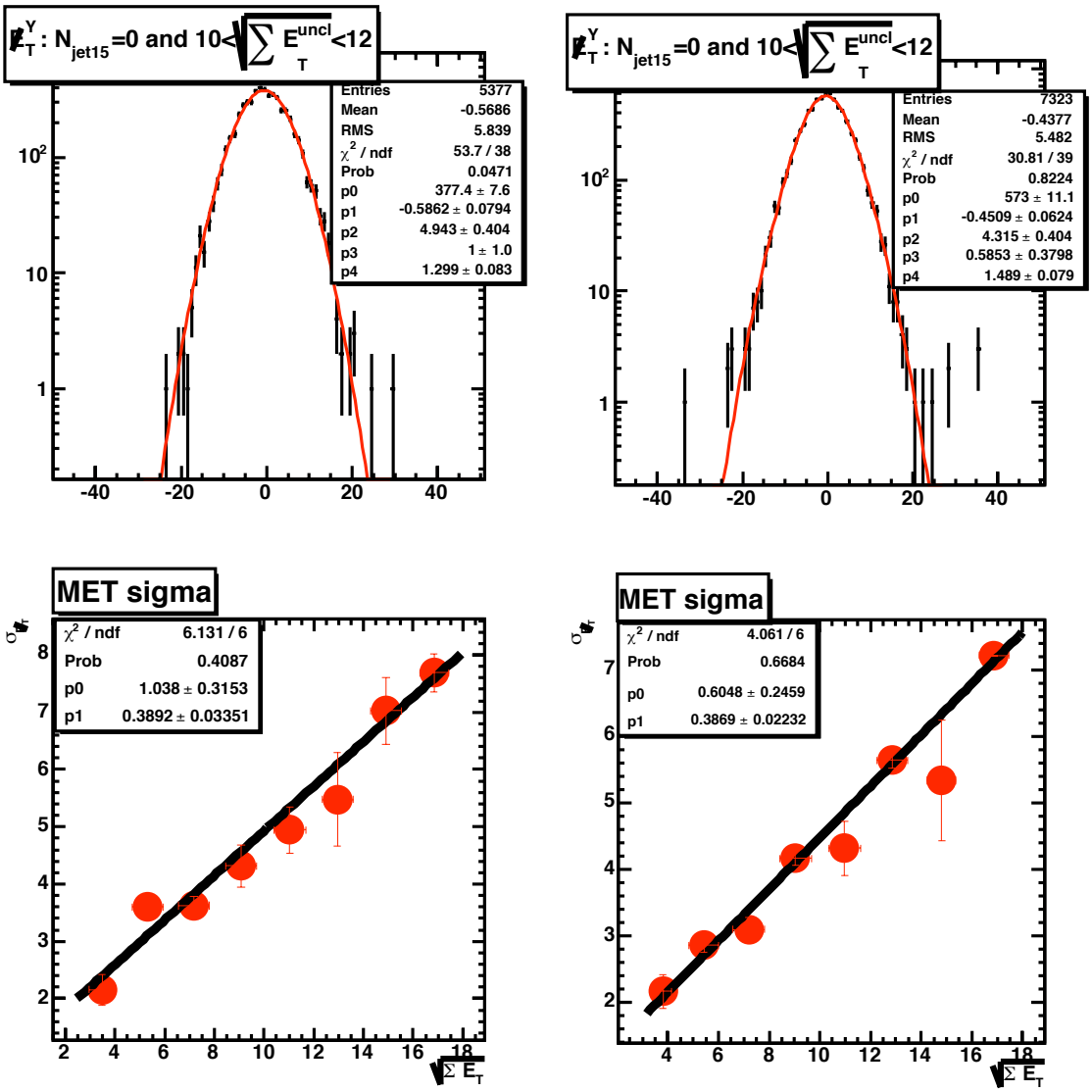

(a) (b)

FIG. 24: Example of the measurements of the $\not\!\!E_T$ parameterization methods due to unclustered energy. The top figures show a two-Gaussian fit of the $\not\!\!E_T{}^y$ distribution for the $Z \rightarrow e^+e^-$ control data (a) and the the $\gamma\gamma$ control data (b) sample events from one of the bins in $\sqrt{\sum E_T^{uncl}}$. The bottom figures demonstrate how the width, σ, of the leading Gaussian depends on the $\sqrt{\sum E_T^{uncl}}$. On both plots, points are data and curves are the fit functions.

B. The $\not\!\!E_T$ Resolution Function due to Jets

To account for the contribution of the measurements of jets to the $\not\!\!E_T$ resolution we measure the detector response to jets as a function of both jet energy (E) and pseudo-rapidity (η). To do this we simulate samples of dijet [77] and Z-jet [78] events using the PYTHIA [38] MC with the GEANT-based detector simulation [61] because data samples such as our $\gamma\gamma$ control sample cannot provide hadron level jet energy information, which is needed to fully measure the jet energy resolution. In each simulated event, jets are reconstructed before they hit the detector (*hadron* jet) and after the detector simulation (*detector* jet) by using the same cone clustering algorithm at both levels (again see Figure 17). We define the jet energy resolution (JER) measurement to be

$$JER = \frac{E^{det}}{E^{had}} - 1 \tag{6.4}$$

where E^{det} is the measured jet energy in the detector and E^{had} is the simulated hadron level jet energy. For this study we consider clusters of energy with both E^{det} and E^{had} greater than 3 GeV which is well below the 15 GeV threshold and require that both jets are matched within a cone of $R(\phi, \eta) < 0.1$ of each other. This definition of JER accounts for detector effects such as energy lost in the calorimeter cracks, and minimizes the dependence of the resolution on the effects of initial and final state radiation (see Section VIII.C.1.b).

Since the JER is a strong function of jet energy and η we break the data into a number of different subsamples or "bins". Each bin is in increments of 5 GeV in jet energy and $\Delta\eta$=0.2 bins in η[2]. A set of examples are shown in Figure 25. Each distribution is fit using a linear combination of a Gaussian and a Landau [79]

[2]We have 14 η-bins of size of 0.2 in the range $|\eta| < 2.8$ and one bin for $2.8 < |\eta| < 3.6$.

function. The jet energy resolution probability distribution function, $\mathcal{P}_{JER}(E^{jet}, \eta)$, is then described as:

$$\mathcal{P}_{JER}(E^{jet}, \eta) = \frac{Landau(mean_1, \sigma_1) + Norm \cdot Gauss(mean_2, \sigma_2)}{1 + Norm} \tag{6.5}$$

where both the mean and σ of the Gaussian and Landau distributions are measured with the PYTHIA dijet MC sample. Here we use a Landau instead of a Gaussian because it better fits the tails of the distributions. Examples of fits are also shown in Figure 25, which illustrate that this fit function successfully describes the jet energy resolution in a wide range of jet energies. It is also important to mention that we use the same functional form for all η-bins, but with the parameters measured for each η-bin. From the individual fits for each (E^{jet},η)-bin, a relative normalization ($Norm$) and parameters of a Gaussian ($mean$ and σ) and Landau($mean$ and σ) fits are obtained. These parameters are fit as a function of E^{jet} for each η-bin with the following functions:

$$\begin{aligned} mean_i &= p_0 + p_1 E^{jet} + \frac{p_2}{E^{jet}} \\ \sigma_i &= \sqrt{\frac{p_0}{E^{jet}} + p_1} \\ Norm_i &= \frac{p_0 + p_1\sqrt{E^{jet}}}{E^{jet}} + p_2 \end{aligned} \tag{6.6}$$

where each i refers to a different η-bin. This provides a smooth parameterization of JER for all reconstructed jets with $E^{jet} > 3$ GeV and $|\eta| < 3.6$. The results of the JER parametrization for $i = 3$ ($0.4 < |\eta| < 0.6$) are shown in Table XX. The full results are given in Ref [76].

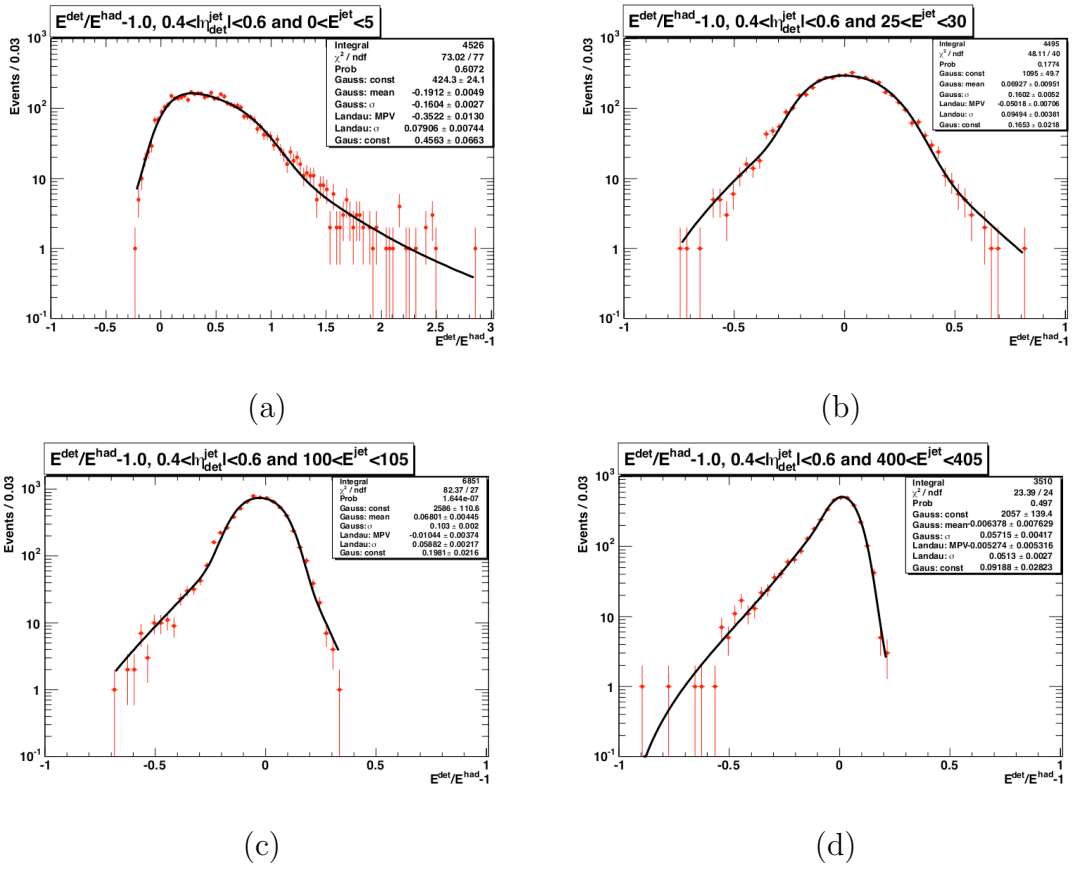

FIG. 25: Examples of the jet energy resolution fits from the PYTHIA dijet sample, using a linear combination of Gaussian and Landau functions for two different jet energy bins, but with $0.4 < |\eta| < 0.6$: 0 GeV$<E^{jet}<$5 GeV (a), 25 GeV$<E^{jet}<$30 GeV (b), 100 GeV$<E^{jet}<$105 GeV (c) and 400 GeV$<E^{jet}<$405 GeV (d).

TABLE XX: The METMODEL parametrization of the JER for $i = 3$ ($0.4 < |\eta| < 0.6$) measured with PYTHIA dijet MC sample. For the full set of parameters see Ref [76].

Parameters	Gauss	Landau
$mean_3$	$p_0 = 0.1006 \pm 0.0024$	$p_0 = 0.0105 \pm 0.0018$
	$p_1 = (-2.018 \pm 0.084)10^{-4}$	$p_1 = (-3.77 \pm 0.58)10^{-5}$
	$p_2 = -0.69 \pm 0.13$	$p_2 = -1.860 \pm 0.097$
σ_3	$p_0 = 0.656 \pm 0.010$	$p_0 = 0.1396 \pm 0.0051$
	$p_1 = (3.007 \pm 0.087)10^{-3}$	$p_1 = (2.272 \pm 0.038)10^{-3}$
$Norm_3$	$p_0 = -19.3 \pm 1.1$, $p_1 = 5.67 \pm 0.26$, $p_2 = -0.161 \pm 0.014$	

C. Prediction of the Fake $\not\!\!E_T$ Distribution

The METMODEL is not designed to predict the exact value of the fake $\not\!\!E_T$ in each event. Instead, it predicts the expected shape of the fake $\not\!\!E_T$ based on the energy resolution probability distribution functions as described in the previous section. Specifically, for each data event, we can produce a probability density function, $\mathcal{P}(\not\!\!E_T)$, of all possible values of the fake $\not\!\!E_T$ by taking into account the variation of the energies of the unclustered energy and jet energy according to Equations 6.2 and 6.5. For a sample of events we can sum up these individual $\mathcal{P}(\not\!\!E_T)$ distributions for all events to obtain a shape for the full sample. We will use this probability density function to simulate an expected $\not\!\!E_T$ distribution using pseudo-experiments and a $\not\!\!E_T$-significance using integration techniques.

Generating pseudo-experiments is very useful to help determine the final selection requirements as they provide a simulated sample of events to test the final sample selection requirements on. Algorithmically, we simulate pseudo-experiments for each event individually using the unclustered energy in the event as well as the E and η of all the observed jets. For each pseudo-experiment, a list of all reconstructed jets with $E_T > 3$ GeV and $|\eta| < 3.0$ in an event is formed and their energies are "smeared" using an MC method according to $\mathcal{P}_{JER}(E^{jet}, \eta)$ as described above (the angles are assumed to stay the same). If the smeared jet energy, E_T^{smear}, is above the 15 GeV threshold, the contribution of that jet to the fake $\not\!\!E_T$ is calculated: $\vec{\not\!\!E}_T{}^{jet} = \vec{E}_T^{meas} - \vec{E}_T^{smear}$. The unclustered energy is also recalculated based on E_T^{smear} of each jet to avoid double-counting when one of the jets with $E_T < 15$ GeV has $E_T^{smear} > 15$ GeV. Thus, we subtract these jets from the unclustered energy. We also add a jet back in if the jet with $E_T > 15$ GeV has $E_T^{smear} < 15$ GeV. Then we randomly generate the expected $\not\!\!E_T{}^x$ and $\not\!\!E_T{}^y$ contributions due to the measured unclustered energy

deposited in the calorimeter according to the resolution probability function given by Eq. 6.2. We label this contribution $\vec{\not\!\!E}_T^{\,uncl}$. Finally, we take a vector sum of all the individual $\not\!\!E_T$ components due to the unclustered energy and from each of the jets with $E_T^{smear} > 15$ GeV to obtain the final prediction of the fake $\not\!\!E_T$ as the following:

$$\vec{\not\!\!E}_T^{\,pred} = \sum \vec{\not\!\!E}_T^{\,jet} + \vec{\not\!\!E}_T^{\,uncl}. \tag{6.7}$$

An example where we run 1000 pseudo experiments for a single $\gamma\gamma$ data sample event that passes the preselection requirements given in Table XVI is shown in Figure 26. The results of the predicted $\not\!\!E_T$ distribution are compared with the measured $\not\!\!E_T$ distribution in MC samples without intrinsic $\not\!\!E_T$ in Figure 27 which shows the predicted and measured distributions for the PYTHIA $\gamma\gamma$ and PYTHIA $Z \rightarrow e^+e^-$ samples after the preselection requirements in Table XVI and shows how well the METMODEL works. We note that the number of pseudo-experiments per event controls the precision of our predictions. While ideally we would run millions of simulations per event, we only use 10 pseudo-experiments per event because our data samples have tens of thousands of events. Similarly, we must run multiple different pseudo-experiments per event to generate systematic variations. This has been shown to have negligible effect on our search sensitivity. We next consider an integration method to calculate the $\not\!\!E_T$-significance.

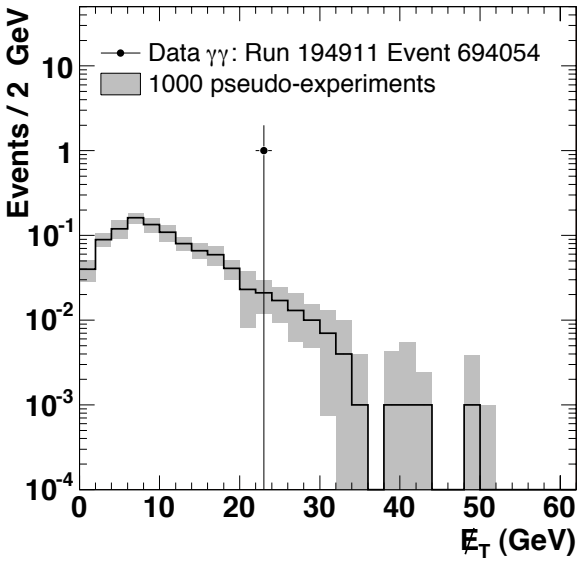

(a)

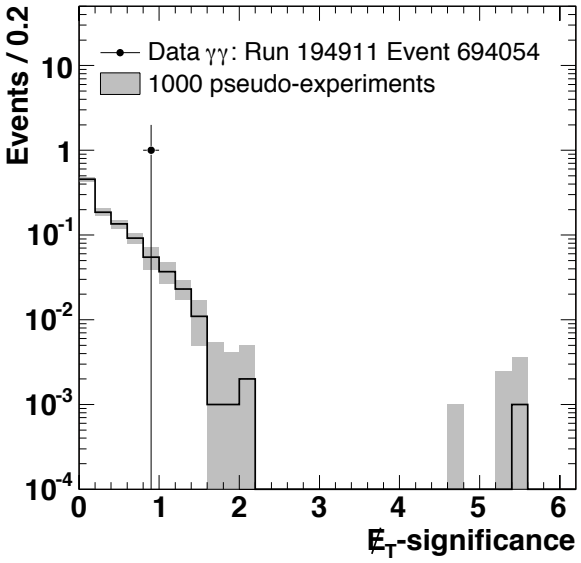

(b)

FIG. 26: Examples of the expected $\not\!\!E_T$ as generated pseudo-experiments (top) and $\not\!\!E_T$-significance (bottom) distributions for one of the $\gamma\gamma$ sample events. Note that the $\not\!\!E_T$-significance will be defined in Equation 6.9. The shaded regions in both plots are statistical uncertainty only from the pseudo-experiments.

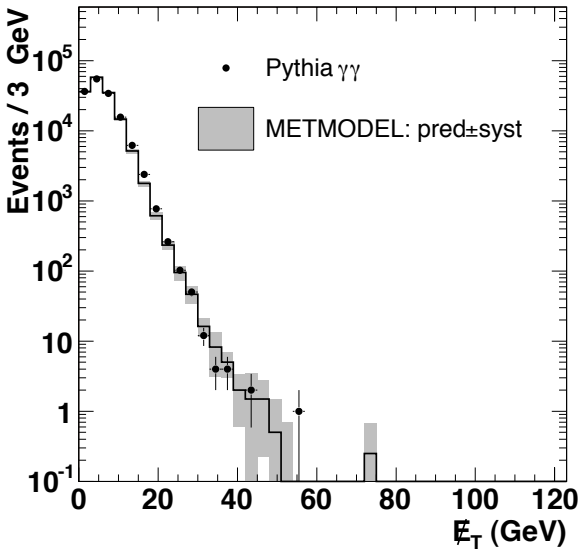

(a)

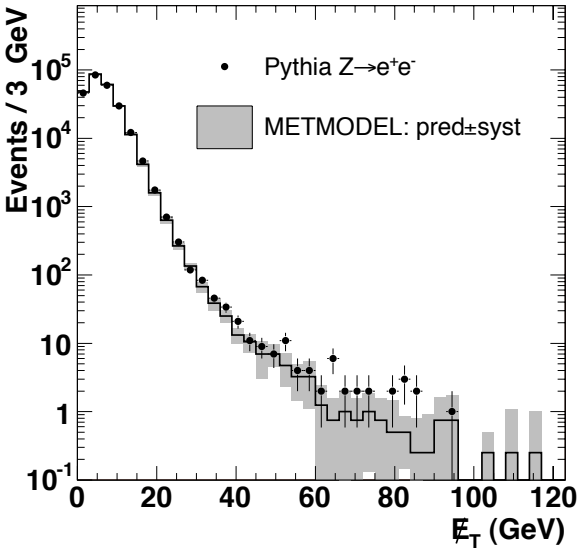

(b)

FIG. 27: Examples of the METMODEL predictions for the $\not\!\!E_T$ distributions in simulations of $\gamma\gamma$ (top) and $Z \to e^+e^-$ (bottom) events using the PYTHIA MC that pass the requirements of Table XVI. These events do not have intrinsic $\not\!\!E_T$. This shows how simple fluctuations in energy measurements can result in the fake $\not\!\!E_T$ as large as 100 GeV. Both distributions are well described by the METMODEL predictions in the entire range of the observed $\not\!\!E_T$ until $\not\!\!E_T > 60$ GeV which are due to pathologies as described in Section V.B.

D. $\not\!\!E_T$-significance

A powerful way to use the resolution functions is to create a significance of the observed $\not\!\!E_T$. While there are a number of ways to define significance, we choose a value which is simple to use in searches. Supposing our data sample has no intrinsic $\not\!\!E_T$, we define the true $\not\!\!E_T$-significance to have a simple shape defined by an *a priori*.

$$\frac{dN}{dx} = \mathrm{N_{event}} \cdot ln(10) \cdot 10^{-x} \tag{6.8}$$

where $x = \not\!\!E_T$-significance and $\mathrm{N_{event}}$ is the number of events in a sample. The shape of this true $\not\!\!E_T$-significance has one important property: if all events in a data sample were to have only fake $\not\!\!E_T$ due to energy mismeasurements, then $\mathrm{N_{event}} \cdot 10^{-\mathrm{cut}}$ events would pass a requirement of $\not\!\!E_T$-significance>*cut*. For example, a $\not\!\!E_T$-significance requirement of 2, 3, and 4 allows ∼1.0%, ∼0.1%, and ∼0.01% of events respectively, as shown in Figure 28. We thus define the $\not\!\!E_T$-significance to be

$$\not\!\!E_T\text{-significance} = -\log_{10}\left(1 - \int_0^{\not\!\!E_T{}^{\mathrm{meas}}} \mathcal{P}(\not\!\!E_T)\, d\not\!\!E_T\right) \tag{6.9}$$

where $\not\!\!E_T{}^{\mathrm{meas}}$ is the measured $\not\!\!E_T$ for an event. While the calculation of $\mathcal{P}(\not\!\!E_T)d\not\!\!E_T$ is straightforward from the resolution functions, it is a non-trivial function. In the limit of infinite number of pseudo-experiments, we can estimate Equation 6.9 using the following:

$$\not\!\!E_T\text{-significance} = -\log_{10}\left(1 - \frac{\sum(\not\!\!E_T{}^{\mathrm{pseud}} < \not\!\!E_T{}^{\mathrm{meas}})}{\sum(\text{all pseudo experiments})}\right) \tag{6.10}$$

where $\not\!\!E_T{}^{\mathrm{pseud}}$ is the generated fake $\not\!\!E_T$ from the pseudo-experiments. While the $\not\!\!E_T$-significance defined by Equation 6.10 takes into account all of the correlations between jets and the observed $\not\!\!E_T$, a significant operational drawback is that it requires generating a large number of pseudo-experiments (e.g., $> 10^6$ pseudo-experiments for

$\not\!\!E_T$-significance= 6).

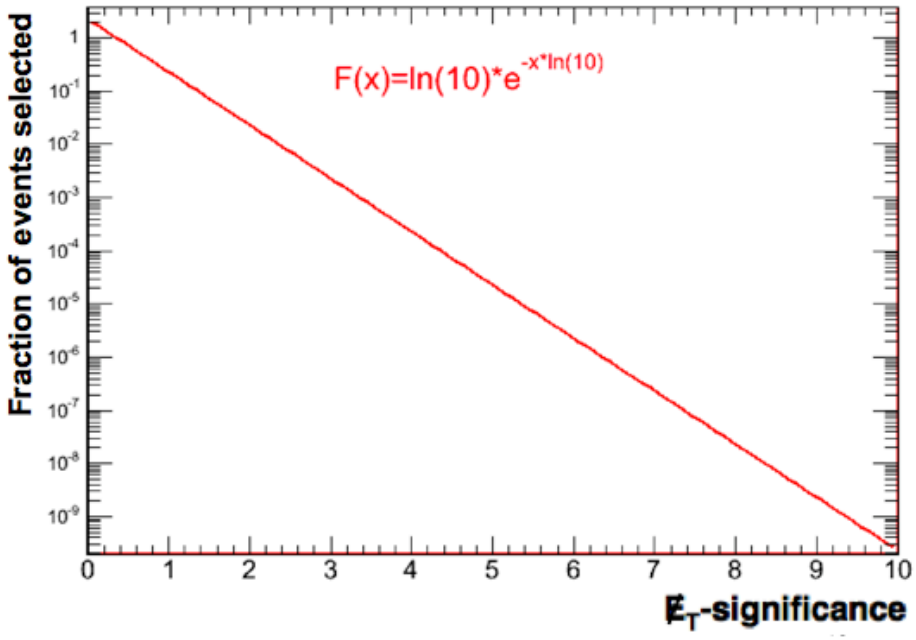

FIG. 28: The perfect prediction of the $\not\!\!E_T$-significance where energy measurement fluctuations in events that have no intrinsic $\not\!\!E_T$ create fake $\not\!\!E_T$. This is an *a priori* distribution of $\frac{dN}{dx} = \mathrm{N_{event}} \cdot ln(10) \cdot 10^{-x}$.

To overcome this problem we use a simplified approach and calculate an upper limit on the $\not\!\!E_T$-significance by doing a simplified integration of the resolution functions ("raw" $\not\!\!E_T$-significance) and then correct this limit for known limitations of the integration method ("corrected" $\not\!\!E_T$-significance). For each event there are $n = 2 + N_{\mathrm{jet}}$ components of the resolution functions; 2 from the x and y components of the unclustered energy, and one from the energy variation for each jet, N_{jet}. Note that we only consider the energy variation in the jet and not the variation in the directionality of the jet. Since it is non-trivial to calculate this n-dimensional integral explicitly to create a $\mathcal{P}(\not\!\!E_T)$, we calculate the product of n 1-dimensional integrals.

Each integral is designed to overestimate the probability of observing a fluctuation which would be equal to or larger than the observed value of $\not\!\!E_T$ in this event from the x and y components of the unclustered energy and the jets, if any, separately. This is an approximation since the probability for only one component to make the fluctuation go above the measured value while keeping all other constants provides an estimate of the upper limit on the "true" $\not\!\!E_T$-significance, which we would obtain if we were to calculate the n-dimensional integral explicitly. After multiplying the probability from each separately, we then correct.

The raw $\not\!\!E_T$-significance is calculated according to following formula:

$$\text{raw } \not\!\!E_T\text{-significance} = -\log_{10}(\widetilde{\mathcal{P}}_{uncl}\widetilde{\mathcal{P}}_{jets}) \tag{6.11}$$

where $\widetilde{\mathcal{P}}_{uncl}$ is the probability of observing the fluctuation from the unclustered energy contribution to $\not\!\!E_T$ resolution and $\widetilde{\mathcal{P}}_{jets}$ is the probability for the jet contribution to cause the $\not\!\!E_T$ to go above the measured $\not\!\!E_T$ value. The two are calculated separately and we then take the product of the two. The value of $\widetilde{\mathcal{P}}_{uncl}$ is given by

$$\widetilde{\mathcal{P}}_{uncl} = \prod_{i=x,y}\left(1 - \int_{-\not\!\!E_T{}^{i,meas}}^{\not\!\!E_T{}^{i,meas}} \mathcal{P}_{uncl}^{\not\!\!E_T{}^{i}}(\sqrt{\sum E_T^{uncl}})\, d\not\!\!E_T{}^{i}\right) \tag{6.12}$$

where $\mathcal{P}_{uncl}^{\not\!\!E_T{}^{i}}(\sqrt{\sum E_T^{uncl}})$ are the probability functions of observing the $\not\!\!E_T{}^{x}$ and $\not\!\!E_T{}^{y}$ values for an observed value of the $\sum E_T^{uncl}$ of the event. The limits of integration represent the measured $\not\!\!E_T{}^{x}$ and $\not\!\!E_T{}^{y}$ components of the $\not\!\!E_T$.

The contribution of the probability of the jet energy mismeasurements to fake the $\not\!\!E_T$ is calculated by assuming that the direction of the jet remains the same, but that the single jet energy fluctuates to create the entire $\not\!\!E_T$. To take into account the direction in which the jet points we consider the case where the difference between the observed energy of the jet and the fluctuated energy, due to variations in the resolution

function, caused the $\not\!\!E_T$. Taking into account the direction we are interested in the case when

$$(E_T^{had} - E_T^{det}) \cos\Delta\phi \geq \not\!\!E_T \tag{6.13}$$

where E_T^{had} is the measured energy of the jet in the event, E_T^{det} is the fluctuated value of the jet E_T and $\Delta\phi$ is the azimuthal angle between the jet and the measured $\not\!\!E_T$. Using the definition of the JER in Equation 6.4 (and adding the $\sin\theta$ term to the numerator and denominator) we find

$$\begin{aligned} JER = \frac{E_T^{det}}{E_T^{had}} - 1 = \frac{E_T^{det} - E_T^{had}}{E_T^{had}} \\ \longrightarrow E_T^{det} - E_T^{had} = E_T^{had} \cdot JER. \end{aligned} \tag{6.14}$$

Combining with Equation 6.13 we find

$$E_T^{had} \cdot JER_{max} \cdot \cos\Delta\phi \geq \not\!\!E_T \tag{6.15}$$

where JER_{max} is the variation required to produce the observed $\not\!\!E_T$ from a fluctuation of this jet. We then solve to find

$$JER_{max} \geq \frac{\not\!\!E_T}{E_T^{had} \cos\Delta\phi}. \tag{6.16}$$

We can then integrate the probability of observing the JER from -1, given in Equation 6.5, to the JER that produces the $\not\!\!E_T$. Since the jet can point either towards or away from the $\not\!\!E_T$ we consider the two cases of $\cos\Delta\phi > 0$ or $\cos\Delta\phi < 0$. To calculate the contribution to the raw significance from each jet, $\widetilde{\mathcal{P}}_{jet}^{i}$, we use the following equations:

$$\begin{aligned} \widetilde{\mathcal{P}}_{jet}^{i} &= \int_{-1}^{JER_{max}^{i}} \mathcal{P}_{JER}(E_i^{jet}, \eta_i)\, d(JER), \quad \text{if} \quad \cos\Delta\phi_i < 0, \\ \text{or} \quad \widetilde{\mathcal{P}}_{jet}^{i} &= \left(1 - \int_{-1}^{JER_{max}^{i}} \mathcal{P}_{JER}(E_i^{jet}, \eta_i)\, d(JER)\right), \quad \text{if} \quad \cos\Delta\phi_i > 0, \end{aligned} \tag{6.17}$$

where $\mathcal{P}_{JER}(E_i^{jet}, \eta_i)$ is the probability of observing a fluctuation energy to a value JER (given in Equation 6.5) for the measured values of E_i^{jet} and η_i for the jet, and JER_{max}^i is taken according to Equation 6.16 for jet i. We find the probability for all the jets by taking the product of the probability using

$$\widetilde{\mathcal{P}}_{jets} = \prod_{i=0}^{N_{jets}} \widetilde{\mathcal{P}}_{jet}^i. \tag{6.18}$$

This integration method provides an approximation to the $\not\!\!E_T$-significance from the jets alone and is combined with the contribution from the unclustered energy according to Equation 6.11 to create the raw $\not\!\!E_T$-significance.

By construction, since the raw $\not\!\!E_T$-significance represents an upper limit on the true $\not\!\!E_T$-significance, the true $\not\!\!E_T$-significance will also always be less than or equal to the predicted value of the raw $\not\!\!E_T$-significance. While we calculate the raw $\not\!\!E_T$-significance on an event-by-event basis, we can correct the raw $\not\!\!E_T$-significance for all events using a simple set of functional forms for events with zero jets, 1 jet or more than 1 jet. We begin with throwing pseudo-experiments where we randomly smear the unclustered and jet energies according to their resolution probability functions as given in Eqs. 6.2 and 6.5 for a MC sample of $\gamma\gamma$ events [81] that pass the requirements in Table XVI where we have split the sample into events with no jets, one jet and more than one jet to generate high statistics. This generates multiple values of fake $\not\!\!E_T$ for each event. We then calculate the raw significance of each generated $\not\!\!E_T$ just as we do for a data event. The result is shown in Figure 29. By counting the fraction of events that pass a value of a particular raw $\not\!\!E_T$-significance we can determine the relationship between the raw $\not\!\!E_T$-significance and what is expected from a true $\not\!\!E_T$-significance. We calculate the corrected $\not\!\!E_T$-significance for an event using the relationship between a raw $\not\!\!E_T$-significance value and corrected $\not\!\!E_T$-significance value for this sample using

the following relationship:

$$\sum N_{event}(\text{raw } \not\!\!E_T\text{-significance} > \text{raw } \not\!\!E_T\text{-significance cut}) \tag{6.19}$$
$$= N_{event} \cdot 10^{-(\text{true } \not\!\!E_T\text{-significance} > \text{true } \not\!\!E_T\text{-significance cut})}.$$

For example, for the sample with one jet we see that 0.1% of the events have raw $\not\!\!E_T$-significance > 6. Thus, we say events with a raw $\not\!\!E_T$-significance of 6 have a corrected $\not\!\!E_T$-significance corresponding to 0.1% which is a corrected $\not\!\!E_T$-significance of 3. The relationship between the corrected $\not\!\!E_T$-significance is shown in Figure 29 and is different for events with no jets, one jet and more than one jet. Effectively, for every event we calculate the energy resolution functions and calculate the raw $\not\!\!E_T$-significance and then use the relationships given in Figure 29 and from that look-up the value of the corrected significance. It is this value of the corrected $\not\!\!E_T$-significance that we refer to as the $\not\!\!E_T$-significance through the rest of this document. The $\not\!\!E_T$-significance distribution for our simulated $\gamma\gamma$ sample before and after the correction are shown in Figure 30.

In summary, the E_T and η of every jet in an event, the unclustered energy and the measured $\not\!\!E_T$ allow us to calculate the raw significance of the measured $\not\!\!E_T$ on an event-by-event basis. This variable is then readily converted into an analogous variable that can be used in a simple way such that we can simply make a $\not\!\!E_T$-significance requirement and calculate the fraction of QCD type events that would pass it. This will be particularly useful in Section VII.A when we do the optimization process. Similarly, it allows us to predict the $\not\!\!E_T$-significance distribution for any set of events using pseudo-experiment techniques where we simulate the $\not\!\!E_T$, H_T and $\not\!\!E_T$-significance for events.

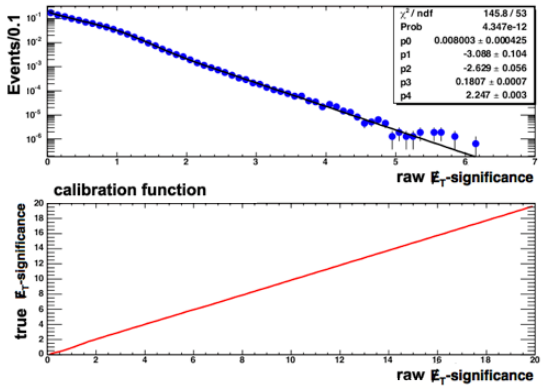

(a)

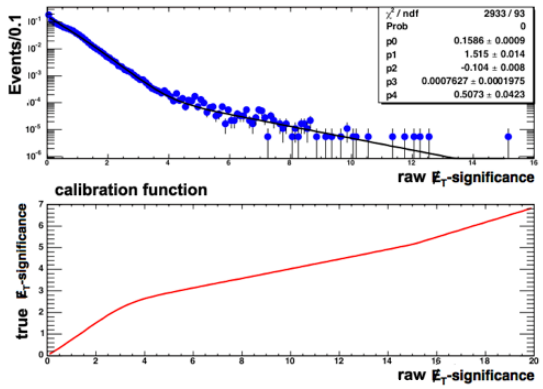

(b)

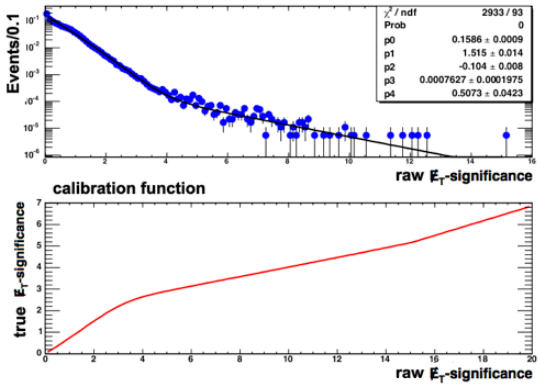

(c)

FIG. 29: An example of the $\not\!\!E_T$-significance calibration for PYTHIA $\gamma\gamma$ events that pass the requirements in Table XVI with $N_{\rm jet} = 0$ (a), $N_{\rm jet} = 1$ (a) and $N_{\rm jet} > 1$ (c). Each top plot shows raw $\not\!\!E_T$-significance distribution and bottom plot shows the relationship between the corrected $\not\!\!E_T$-significance and the raw $\not\!\!E_T$-significance.

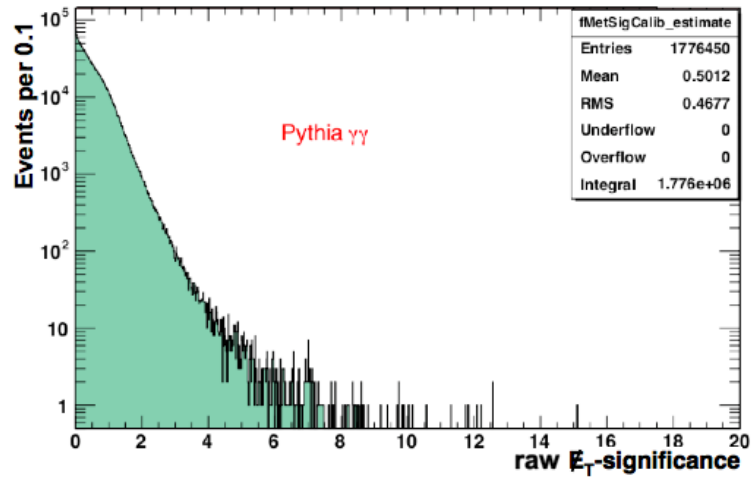

(a)

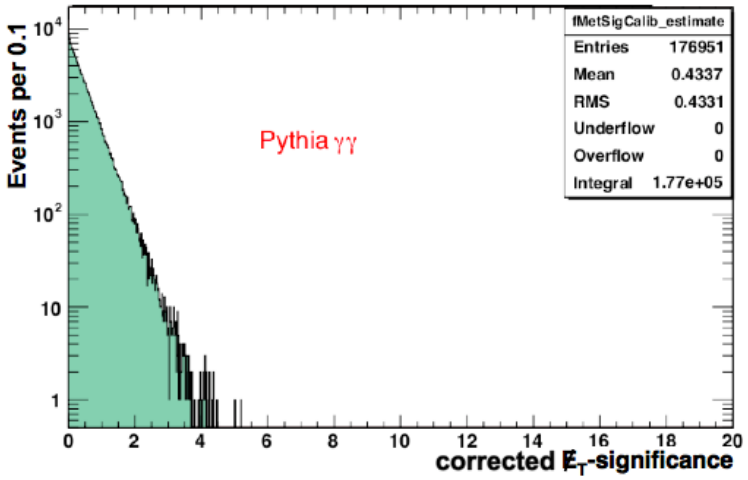

(b)

FIG. 30: The raw and corrected $\not\!\!E_T$-significance distributions for a sample of diphoton events simulated using the PYTHIA MC before (a) and after (b) the $\not\!\!E_T$-significance correction. Note that all pathologies described in Section V.B are explicitly removed from the sample using methods in Ref [43].

CHAPTER VII

BACKGROUNDS AND THEIR ESTIMATIONS

As previously described, the dominant source of two photon events are from QCD type interactions. Specifically, the main backgrounds sources are dominated by $\gamma\gamma$, $\gamma j \rightarrow \gamma\gamma_{fake}$ and $jj \rightarrow \gamma_{fake}\gamma_{fake}$. The subset of events with $\gamma\gamma + \not\!\!E_T$ are typically from QCD with fake $\not\!\!E_T$, electroweak events with real $\not\!\!E_T$ and non-collision backgrounds such as cosmic rays and beam related interactions.

The "final signal region" for this analysis is defined by the subsample of preselection events that also pass a set of optimized, final kinematic requirements. In this chapter we describe in more detail the backgrounds that can mimic the GMSB events in the $\gamma\gamma + \not\!\!E_T$ final state and still pass the final requirements. The final analysis is a counting of the observed number of events that pass the final event selection criteria in the data and a comparison to the expectations from background sources and the number expected from signal sources. The final set of selection criteria is thus chosen from an optimization that is based on a balance between the number of events expected from backgrounds and the numbers expected from signal.

The methods for determining the number of background events for a number of different potential selection criteria are based on an understanding of what the expected distributions look like as a function of these variables. The methods for determining the number of expected background events in the signal region are based on a combination of data and Monte Carlo and allow for a large variety of potential final sets of requirements. These estimates are used, in conjunction with the expectations from GMSB, described in Chapter VIII, as part of the optimization procedure which is described in Chapter IX. We note in advance of the optimization description that the observables that provide the best separation between signal and background are

the variables: $\not\!\!E_T$-significance, H_T, and $\Delta\phi(\gamma_1, \gamma_2)$. We will show the distributions for each background separately, after the preselection requirements. Similar distributions for GMSB will be shown in Chapter VIII.

A. QCD Backgrounds with Fake $\not\!\!E_T$

We start by describing the QCD backgrounds and the techniques used to predict the number of expected events in the signal region after all kinematic requirements. These backgrounds come in two different categories; fake $\not\!\!E_T$ due to energy measurement fluctuations in the calorimeter as estimated using our METMODEL ($\mathrm{N}_{\mathrm{signal}}^{\mathrm{METMODEL}}$), and fake $\not\!\!E_T$ due to pathologies ($\mathrm{N}_{\mathrm{signal}}^{\mathrm{PATH}}$) such as picking the wrong vertex in events where the true collision did not create a vertex, or from tri-photon events with a lost photon. The total QCD background prediction in the signal region, $\mathrm{N}_{\mathrm{signal}}^{\mathrm{QCD}}$, is given by

$$\mathrm{N}_{\mathrm{signal}}^{\mathrm{QCD}} = \mathrm{N}_{\mathrm{signal}}^{\mathrm{METMODEL}} + \mathrm{N}_{\mathrm{signal}}^{\mathrm{PATH}}. \tag{7.1}$$

The next subsections describe how each is estimated in more detail.

1. Energy Measurement Fluctuations in the Calorimeter

Standard Model QCD events, $\gamma\gamma$, $\gamma j \rightarrow \gamma\gamma_{fake}$, and $jj \rightarrow \gamma_{fake}\gamma_{fake}$, are the dominant sources of events in the diphoton preselection sample and a major background for $\gamma\gamma + \not\!\!E_T$. Energy measurement fluctuations in the calorimeter occur in every event, but lead to considerable values of fake $\not\!\!E_T$ only in a small fraction of cases. However, large cross sections for these processes make them one of the largest backgrounds. As mentioned in Chapter VI we evaluate the $\not\!\!E_T$-significance for every event and use this variable to select events. Thus, our goal is to model the QCD expectations in the signal for large values of $\not\!\!E_T$-significance for a large variety of potential final selection

requirements.

$N_{signal}^{METMODEL}$, the QCD contribution of the background with fake $\not\!\!E_T$ that passes the kinematic requirements due to normal measurement variations, is predicted using the data and METMODEL. To estimate the expected $\not\!\!E_T$-significance for a data sample, the jets and unclustered energy for each event in the sample that pass the other kinematic requirements are considered. For each data event 10 pseudo-experiments[1] are thrown to generate a fake $\not\!\!E_T$, H_T, and calculate the significance of the measured $\not\!\!E_T$. Then the number of events in the pseudo-experiments that pass our $\not\!\!E_T$-significance and other kinematic requirements, N_{signal}^{pseudo}, is counted. This number, divided by the number of pseudo-experiments, $N_{pseudo} = 10$, gives $N_{signal}^{METMODEL}$. In this way the $\not\!\!E_T$-significance distribution is predicted for lots of kinematic requirement combinations. The expected $\not\!\!E_T$ and $\not\!\!E_T$-significance distributions for QCD backgrounds are shown in Figure 31 for the preselection sample.

The systematic uncertainty on the number of events above a $\not\!\!E_T$-significance requirement is evaluated by comparing the METMODEL predictions with the default set of model parameters to predictions obtained with the parameters deviated by $\pm\sigma$ as described in Sections VI.A and VI.B. In total we consider 10 sources of systematic uncertainties on the METMODEL predictions that can be grouped into three categories: 1) differences in the unclustered energy parameterization between the $\gamma\gamma$ control sample and $Z \to e^+e^-$ event sample; 2) uncertainties on the four parameters of unclustered energy parameterization given in Table XIX; 3) uncertainties on the five parameters of the *JER* parameterization given in Table XX. The systematic uncertainty is then taken to be the RMS of these 10 different variations from the

[1]More than 10 pseudo-experiments, such as 100 or 1000, etc., are possible, but not realistic due to matter of CPU time and total time restrictions. As will be clear later, we must run many pseudo-experiments for a number of different configurations to estimate the systematic uncertainties.

10 pseudo-experiments. The total uncertainty is obtained by adding the statistical uncertainty on the number of pseudo-experiments passing the kinematic requirements and these 10 individual sources of systematic uncertainties in quadrature.

2. Event Reconstruction Pathologies

A source of QCD background that is unaccounted for by the METMODEL is QCD diphoton production with event reconstruction pathologies. For example, a $\gamma\gamma$ pair is produced by a QCD interaction and a pair of jets is produced in a separate collision which produces the highest $\sum p_T$ vertex, and causes the event to have a very large $\not\!\!E_T$-significance. As described in Section V.B.1, this effect can usually be fixed by the vertex re-assignment procedure. However, there are situations when the vertex swap procedure cannot identify large fake $\not\!\!E_T$. This happens, for example, when the $\gamma\gamma$ interaction does not produce a reconstructed vertex at all. The METMODEL will not be able to account for this background since this effect is not due to an energy measurement fluctuation.

A second example of QCD events whose contribution to the $\gamma\gamma + \not\!\!E_T$ signature is not estimated by the METMODEL are events with three photon candidates but one photon is lost in the calorimeter. The cross section of this process is very small. However, the probability to lose one of the photons in any one of the calorimeter cracks is on the order of $\sim$10% or more [80], so that the probability to lose one of the photon candidates in a potential tri-photon event can be $\sim$30% or larger.

To obtain the prediction for all events reconstruction pathologies from QCD sources at the same time, we model $\gamma\gamma$ kinematics and event reconstruction using a PYTHIA $\gamma\gamma$ sample [81], with large statistics. Additional jets and photons are produced as part of the simulation in the form of initial and final state radiation. We then normalize the number of events in the $\gamma\gamma$ MC sample that pass all the

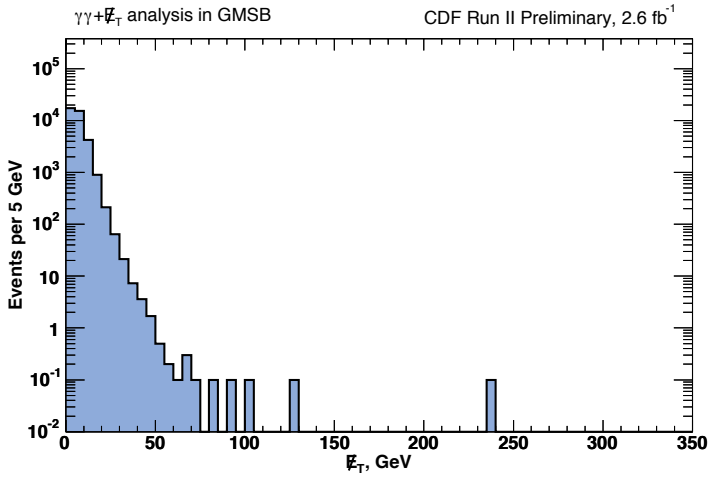

(a)

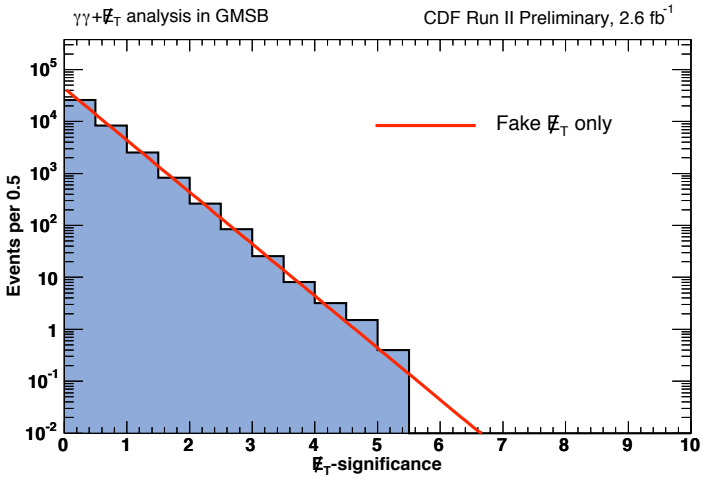

(b)

FIG. 31: The QCD background predictions of the $\not\!\!E_T$ and $\not\!\!E_T$-significance using the METMODEL for the events in the presample. The red solid line in (b) shows the perfect prediction of fake $\not\!\!E_T$ from energy measurement fluctuations only having no intrinsic $\not\!\!E_T$. In this case, the perfect prediction of $\not\!\!E_T$-significance has a simple *a priori* distribution of $dN/dx = N_{event} \times ln(10) \times 10^{-x}$, where x is $\not\!\!E_T$-significance.

presample selection requirements, described in Table XVI, to the number of events observed in the $\gamma\gamma$ data presample. This scale factor, $\mathrm{SF_{QCD}}$, takes into account γj and jj contributions, but assumes the rate at which pathologies occur is the same for $\gamma\gamma$, γj and jj contributions. It further assumes the rates of electroweak and non-collision sources of events in the presample are small, which is checked later to be a good assumption. We subtract off the expectations for energy mismeasurement fluctuations in the MC using the METMODEL to avoid double counting. The final prediction of these QCD backgrounds is given by

$$\mathrm{N_{signal}^{PATH}} = (\mathrm{N_{signal}^{PATH-MC}} - \mathrm{N_{signal}^{MM-MC}}) \cdot \mathrm{SF_{QCD}} \tag{7.2}$$

where $\mathrm{N_{signal}^{PATH-MC}}$ is the number of reconstructed PYTHIA MC $\gamma\gamma$ events that pass the final set of kinematic requirements after optimization (see Chapter IX), including the $\not\!\!E_T$-significance requirement, and $\mathrm{N_{signal}^{MM-MC}}$ is the estimated rate of energy measurement fluctuation events passing the final kinematic requirements. The $\mathrm{N_{signal}^{MM-MC}}$ is estimated by

$$\mathrm{N_{signal}^{MM-MC}} = \mathrm{N_{signal}^{no\ \not\!\!E_T\text{-significance}}} \cdot \mathrm{R^{exp}_{\not\!\!E_T\text{-significance}}} \tag{7.3}$$

where $\mathrm{N_{signal}^{no\ \not\!\!E_T\text{-significance}}}$ is the number of events in the MC that pass all the kinematic requirements except the $\not\!\!E_T$-significance requirement, and $\mathrm{R^{exp}_{\not\!\!E_T\text{-significance}}}$ is the expected rate for events to pass the $\not\!\!E_T$-significance requirement using Equation 6.8. The scale factor, $\mathrm{SF_{QCD}}$, is taken to be equal to the ratio of the number of events passing the preselection requirements in data (the presample is dominated by QCD), $\mathrm{N_{presample}^{QCD-Data}}$, and in the MC sample, $\mathrm{N_{presample}^{QCD-MC}}$. The number of events that pass the preselection requirements for data ($\mathrm{N_{presample}^{QCD-Data}}$) and MC ($\mathrm{N_{presample}^{QCD-MC}}$) are 38,053 and

283,554 respectively. The $\mathrm{SF_{QCD}}$ is then given by

$$\mathrm{SF_{QCD}} = \frac{\mathrm{N}^{\mathrm{QCD-Data}}_{\mathrm{presample}}}{\mathrm{N}^{\mathrm{QCD-MC}}_{\mathrm{presample}}} = \frac{38,053}{283,554} = 0.134 \pm 0.007 \ \ \text{(stat.only)}. \tag{7.4}$$

In advance of the final optimization requirements we show the expected $\not\!\!E_T$, $\not\!\!E_T$-significance, H_T and $\Delta\phi(\gamma_1, \gamma_2)$ distributions for the $\gamma\gamma$ MC sample passing the preselection requirements in Figure 32. The tails in Figure 32-(b) for the $\not\!\!E_T$-significance are long and, as expected, are dominated by tri-photon and wrong vertex events.

The systematic uncertainties on this background prediction include the uncertainty on the scale factor and the uncertainty due to MC-data differences in the unclustered energy parameterization and the jet energy scale. To get the systematic uncertainty on the unclustered energy parametrization from the METMODEL we deviate the default set of parameters by $\pm\sigma$, as described in the previous section. For the systematic uncertainty on the jet energy scale we allow shifting the jet energy scale up or down by $\pm\sigma$, following the standard procedure at CDF [48]. An additional systematic uncertainty due to the fact that the presample includes other pathologies (see, for example, Figure 31), is overestimated to be 5% and is taken in quadrature with the other errors. The total uncertainty is estimated by adding the statistical uncertainty, which is taken to be $\sqrt{\mathrm{N}^{\mathrm{PATH-MC}}_{\mathrm{signal}}}$, and these systematic uncertainties in quadrature.

3. Combined QCD Results

After estimating both classes of QCD backgrounds, the expected kinematic distributions for the combined QCD sources, after the preselection requirements, are shown in Figure 33.

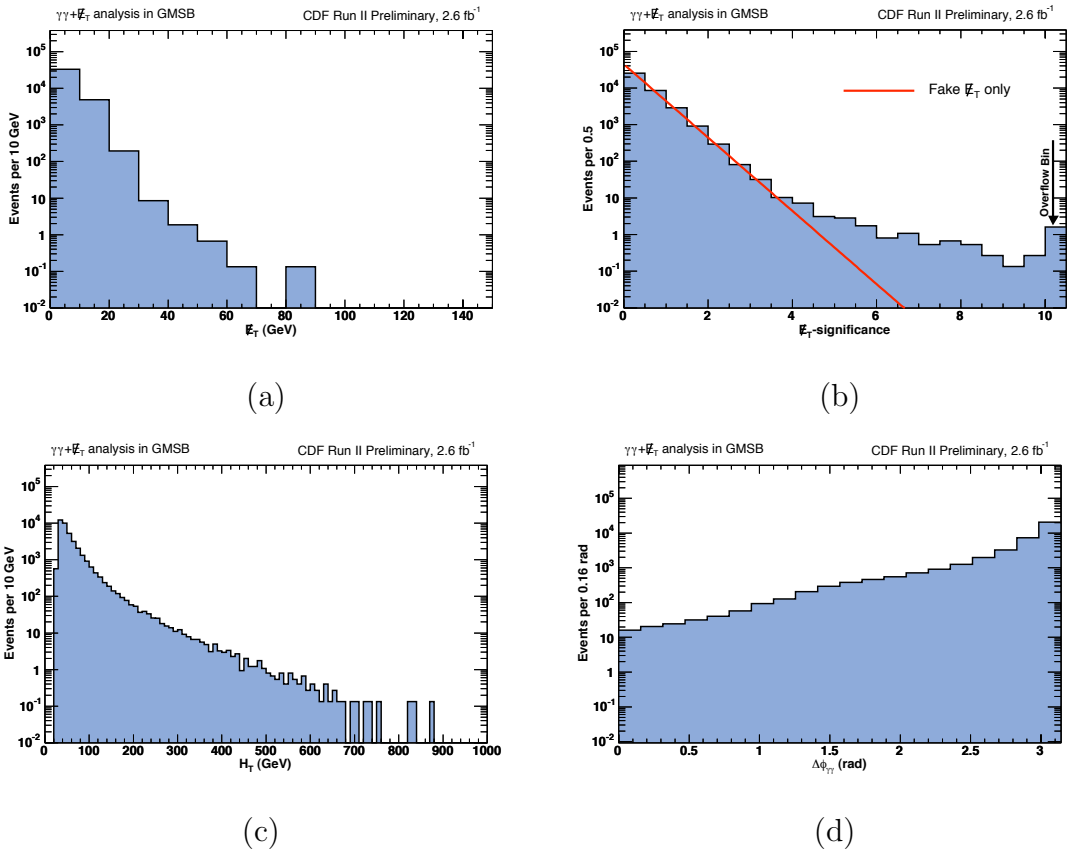

FIG. 32: The $\not\!\!E_T$, $\not\!\!E_T$-significance, H_T, and $\Delta\phi(\gamma_1, \gamma_2)$ distributions for the PYTHIA $\gamma\gamma$ MC sample after the preselection requirements, but normalized by the $\mathrm{SF_{QCD}}$ scale factor. The tails in the $\not\!\!E_T$-significance are long, but the overall rate of this process is low.

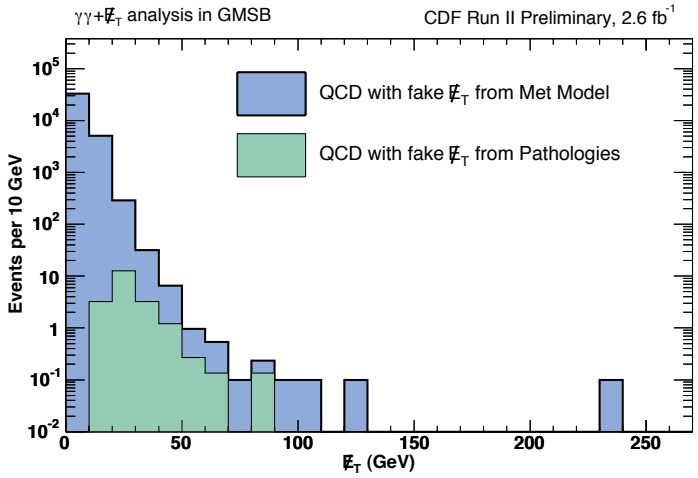

(a)

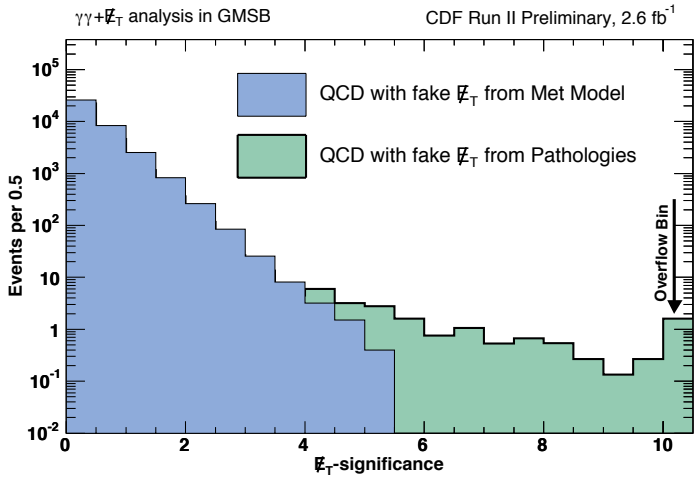

(b)

FIG. 33: The combined QCD background predictions after the preselection requirements. (a) and (b) show $\not\!\!E_T$ and $\not\!\!E_T$-significance distributions, respectively. Note that the $\Delta\phi(\gamma_1, \gamma_2)$ and H_T distributions are not given as they are highly correlated with the $\gamma\gamma$ presample. The $\not\!\!E_T$ and $\not\!\!E_T$-significance samples, after those requirements in the final selection, are modeled using the METMODEL.

B. Electroweak Backgrounds with Real $\not\!\!E_T$

Electroweak processes involving the production and decay of W's and Z's are the most common source of real and significant $\not\!\!E_T$ in $p\bar{p}$ collisions since they produce neutrinos in the final state as well as produce leptons in their decays that can be lost in the detector. The background rate from decays into both charged and neutral leptons is estimated using a combination of Monte Carlo and data samples [38, 82].

There are four ways to get diphoton candidates in electroweak events: 1) from $W\gamma\gamma$ and $Z\gamma\gamma$ events where both photons are real; 2) from $W\gamma j$ and $Z\gamma j$ events where a jet fakes a photon; 3) from Wjj and Zjj events where both jets fake photons; and 4) $t\bar{t}$ production and decay where photons are from initial and final radiation or from jets or electrons that fake photons. As will be seen, the dominant electroweak background in the presample is $W\gamma \rightarrow e\nu\gamma \rightarrow \nu\gamma\gamma_{fake}$ production and decay. Production and decay of $Z\gamma j \rightarrow \nu\nu\gamma\gamma_{fake}$ events are the dominant electroweak background in our analysis after all kinematic requirements.

To estimate the contribution from each electroweak backgrounds we use a combination of the MC samples and data. Each source is simulated using an MC sample which is normalized to its production cross sections, k-factors (see Section I.B.2.d) and branching fractions. This allows us to normalize all sources to each other. Then an overall normalization factor is used to take into account Data-MC differences by using the measured and predicted rate of events with an electron and a photon in the final state.

To simulate $W\gamma$ and $Z\gamma$ processes we use the BAUR MC [82] to evaluate contributions from both $W/Z+\gamma$, $W/Z+\gamma\gamma$ and $W\gamma/Z\gamma+j$ for the charged decay modes and ISR/FSR to add the extra photon or jet. Inclusive production of W, Z and $t\bar{t}$ are simulated using the PYTHIA [38] (see Section II.D) to obtain the contribution

from Wjj and Zjj events where both photon candidates are fakes and $t\bar{t}$ events. To avoid overlaps between the BAUR and PYTHIA simulated samples, we filter out events from the PYTHIA samples where photons reconstructed in the detector are matched to photons from either quark ISR or lepton FSR. Also an inclusive PYTHIA $Z(\nu\bar{\nu})\gamma$ sample with ISR/FSR [83] is used to estimate contributions from neutral leptonic decays.

The electroweak background predictions are given by counting the number of simulated events from each of the MC samples, labeled i through n, with the following equation:

$$\mathrm{N}^{\mathrm{EWK}}_{\mathrm{signal}} = \sum_{i=0}^{n} \mathrm{N}^{\mathrm{EWK-MC}}_{\mathrm{signal},i} \cdot \mathrm{SF}_i \cdot \left(\frac{\mathrm{N}^{\mathrm{Data}}_{e\gamma,\mathrm{signal}}}{\mathrm{N}^{\mathrm{MC}}_{e\gamma,\mathrm{signal}}} \right) \tag{7.5}$$

where $\mathrm{N}^{\mathrm{EWK-MC}}_{\mathrm{signal},i}$ is the number of events in the sample passing all the final kinematic requirements from MC sample i, for each electroweak source. The scale factor, SF_i, normalizes each electroweak background to its production cross section and includes its k-factor. To minimize the dependence of our predictions on potential Data-MC differences (trigger efficiencies, acceptance and ID efficiencies, modeling of ISR/FSR, PDF uncertainties, luminosity uncertainties, etc.), we select the $e\gamma$ sample using the requirements listed in Table XXI. We then normalize the total electroweak background estimate to data by comparing the rate of the number of $e\gamma$ events observed in the data that pass all signal kinematic requirements, $\mathrm{N}^{\mathrm{Data}}_{e\gamma,\mathrm{signal}}$, to the expected number of events predicted using the MC's, $\mathrm{N}^{\mathrm{MC}}_{e\gamma,\mathrm{signal}}$. To minimize differences between the simulation of $e\gamma$ and $\gamma\gamma$ events, electrons are required to satisfy the photon-like ID requirements listed in Table XXII. The MC prediction is calculated using the following equation:

$$\mathrm{N}^{\mathrm{MC}}_{e\gamma,\mathrm{signal}} = \sum_{i=0}^{n} \mathrm{N}^{\mathrm{MC}}_{e\gamma,\mathrm{signal},i} \cdot \mathrm{SF}_i \tag{7.6}$$

where $\mathrm{N}^{\mathrm{MC}}_{e\gamma\ \mathrm{signal},i}$ is the number of $e\gamma$ events in each MC sample passing all the re-

TABLE XXI: The $e\gamma$ presample selection requirements. A total of 1,921 data events pass all these requirements.

The Requirements for Selecting the $e\gamma$ Sample
Passing one of the triggers in Tables IX and X
An electron that passes the photon-like electron ID requirements in Table XXII
The $\gamma\gamma$ preselection requirements in Table XVI, but one photon candidate needs to fail the photon ID requirements, but pass the requirements in Table XXII

quirements in Table XVI as well as the final optimization requirements. All sources (i) that contribute to the $e\gamma$ sample are normalized to their production cross sections and include their k-factors using the SF_i. Here, and later, we will refer to the ratio of $\left(\frac{\mathrm{N}^{\mathrm{Data}}_{e\gamma,\mathrm{signal}}}{\mathrm{N}^{\mathrm{MC}}_{e\gamma,\mathrm{signal}}}\right)$ as the global electroweak normalization factor. After the preselection requirements the global electroweak scale factor is given as follows:

$$\frac{\mathrm{N}^{\mathrm{Data}}_{e\gamma,presample}}{\mathrm{N}^{\mathrm{MC}}_{e\gamma,presample}} = \frac{1,921}{2,463} = 0.78 \pm 0.02 \text{ (stat. only)} \tag{7.7}$$

where we take into account statistical errors on all the $e\gamma$ sources. The numerical values of the scale factors in Eqs. 7.5 and 7.6 are calculated using

$$\mathrm{SF}_i = \frac{\sigma_i \cdot \mathrm{k}_i \cdot \mathcal{L}}{\mathrm{N}^{\mathrm{EWK}\ (e\gamma)}_{\mathrm{sample},i}} \tag{7.8}$$

where for each source i σ_i is production cross section, k_i is the k-factor, $\mathcal{L}$ is the luminosity (2.6 fb^{-1}) and $\mathrm{N}^{\mathrm{EWK}\ (e\gamma)}_{\mathrm{sample},i}$ is the number of simulated electroweak $\gamma\gamma$ ($e\gamma$) events. The results are summarized in Table XXIII.

The uncertainty on the electroweak backgrounds are dominated by the $e\gamma$ normalization factor uncertainty because there are not many events in the data that pass all the final kinematic requirements. This value includes the data and MC statistical

TABLE XXII: The photon-like electron ID requirements used to make the $e\gamma$ data set in data and MC. The requirements that are different from the standard photon ID and isolation, given in Table IV, are indicated with an *. Also, no additional requirements in Table IV such as PMT spikes and Phoenix rejection requirements are added. The electron variables, denoted with a †, are described in appendix A.

The Standard Photon-like Electron ID Requirements	
detector	$\lvert\eta\rvert < 1.0$
Conversion*†	No
E_T	$\geq$ 13 GeV
fiduciality	$\lvert X_{\rm CES}\rvert \leq 21$ cm
	9 cm $\leq \lvert Z_{CES}\rvert \leq 230$ cm [63]
$\chi^2_{\rm CES}$	≤ 20
$E_{\rm Had}/E_{\rm Em}$	$\leq 0.055 + 0.00045 \times E$
E^{iso}_{cal}	$\leq$0.1$\times E_T$ if E_T<20 GeV or
	$\leq$2.0+0.02$\times(E_T - 20)$
$N3D$ tracks in cluster*	1 or 2
E/P of 1st track*†	0.8$\leq E/P \leq$1.2 if $P_T < 50$ GeV
	no cut if $P_T \geq 50$ GeV
2nd track P_T if $N3D = 2$*	$\leq$1.0+0.005$\times E_T$
track isolation	$\leq 2.0 + 0.005 \times E_T$
2nd CES cluster energy	$\leq$0.14$\times E_T$ if E_T<18 GeV
	$\leq$2.4+0.01$\times E_T$ if $E_T \geq$18 GeV
$\Delta z = \lvert z_{trk} - z_{vx}\rvert$*†	$\lvert\Delta z\rvert \leq 3$ cm

TABLE XXIII: The calculation of the scale factors for the individual electroweak backgrounds. Note that the scale factors for $W(\mu)$ no-ISR/FSR and $Z(\mu)$ no-ISR/FSR are listed twice. For these two samples only parts of the samples were used in the $e\gamma$ counting experiment as they are low rate processes.

Background Source	Cross Section σ_i(pb)	k-factor k_i	MC events $N^{EWK}_{sample,i}$	MC-to-Data SF SF_i
$W(e\nu)+\gamma$	32.0	1.36	1,775,122	0.0635
$W(\mu\nu)+\gamma$	32.0	1.34	1,836,273	0.0605
$W(\tau\nu)+\gamma$	32.0	1.34	1,824,182	0.0609
$Z(ee)+\gamma$	10.3	1.36	9,258,132	0.0039
$Z(\mu\mu)+\gamma$	10.3	1.36	9,214,135	0.0040
$Z(\tau\mu)+\gamma$	10.3	1.36	9,196,501	0.0040
$Z(\nu\bar{\nu})+\gamma$	2.5	1.4	8,766,307	0.0010
$W(e\nu)$ no ISR/FSR	1,960	1.4	33,815,147	0.210
$W(\mu\nu)$ no ISR/FSR	1,960	1.4	23,058,663	0.308
			(10,166,426)	(0.699)
$W(\tau\nu)$ no ISR/FSR	1,960	1.4	24,057,340	0.296
$Z(ee)$ no ISR/FSR	355	1.4	22,986,333	0.056
$Z(\mu\mu)$ no ISR/FSR	355	1.4	14,704,660	0.0876
			(10,203,233)	(0.126)
$Z(\tau\tau)$ no ISR/FSR	355	1.4	33,278,066	0.0387
$t\bar{t}$ (incl.)	6.7	N/A	7,430,826	0.0023

uncertainties as well as differences in MC modeling. The other systematic uncertainty comes from the fact that part of the $e\gamma$ data sample is not from real electron sources. If a π^0 in a jet fakes an electron it will not bremsstrahlung the way that real electrons do, so they fake photons at a lower late. This effect is estimated by comparing results for a default value of the E/p requirement ($0.8 < E/p < 1.2$) and a deviated value of the E/p requirement ($E/p < 2.0$) for variation of scale factor as a function of the requirements. As a check we look at the systematic variation of the scale factor as the final kinematic requirements are varied. The variations are consistent with the other methods. The total uncertainties also include the MC statistical uncertainties and uncertainties on the normalization factors added in quadrature.

The expected $\not\!\!E_T$, $\not\!\!E_T$-significance, $H_{_T}$ and $\Delta\phi(\gamma_1, \gamma_2)$ distributions for the electroweak backgrounds in the presample are shown in Figure 34.

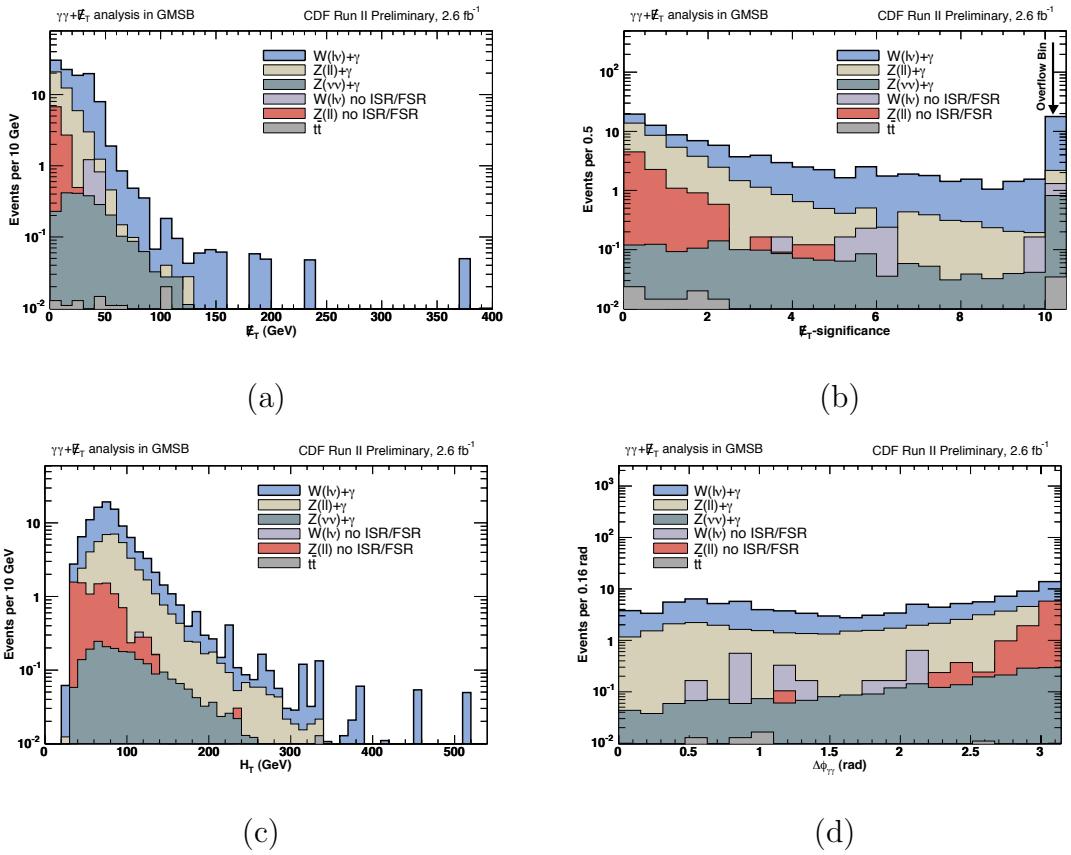

FIG. 34: The electroweak background predictions after the preselection requirements. (a), (b), (c), and (d) show the $\not\!\!E_T$, $\not\!\!E_T$-significance, H_T, and $\Delta\phi(\gamma_1, \gamma_2)$ distributions respectively. Here we have normalized each background to the others using Table XXIII, but used a global scale factor of 0.78 from Equation 7.7 for the full sample of events that pass the preselection requirements.

C. Non-Collision Backgrounds

Non-collision backgrounds to the $\gamma\gamma + \not\!\!E_T$ background come from PMT spikes, beam halo and cosmic rays sources where either a single or double photon-like signature comes from the non-collision source. Because these events do not originate from beam-beam interactions, they can be a source of spurious $\not\!\!E_T$ that is correctly identified by the METMODEL as being very significant. It was shown in Ref. [43] that other sources of spurious energy in $\gamma\gamma$ events are negligible. These non-collision backgrounds are estimated using the data. We estimate the non-collision background events in the signal region using extrapolation techniques and the measured efficiencies of the non-collision rejection requirements given in Tables XIV and XII.

PMT spikes, while not rare, do have a distinct signature (see Ref. [19]) and our PMT asymmetry requirement removes them very efficiently. Therefore, we do not explicitly evaluate this background and take the number of remaining PMT spikes backgrounds events to be zero. We next discuss beam halo and cosmic rays.

1. Beam Halo

Muons from beam halo can fake photon candidates as they pass through the calorimeter [19]. Because such events are not related to a hard interaction and usually appear only in one calorimeter wedge. The dominant background from this source is when the beam halo muon(s) produce both photons. Events with a single beam halo candidate overlapping with a SM event such as $\gamma + jet$ event, as previously mentioned, have been estimated previously to be negligible and we have ignored them here [43].

To study beam halo contributions to the $\gamma\gamma + \not\!\!E_T$ final state after the beam halo rejection procedure, listed in Table XII, we create a sample of events ("a beam halo enriched $\gamma\gamma$ sample") which are mostly beam halo. These events are used to predict

the shape of the kinematic distributions as well as their correlations so we can predict how many events will pass all the kinematic requirements. To predict the expected number of beam halo events after all final requirements we use estimation techniques to take into account differences between our beam halo enriched sample and the final signal sample. The numeric calculation of these differences are known as "correction" factors or "scale" factors.

The beam halo enriched sample is selected as having two "loose" photon candidates passing the requirements of Table XVII, where each photon is also identified as beam halo using the requirements in Table XII. To increase the number of events in our sample we do not require a vertex because there is no correlation between the presence of a beam halo event and a collision event that produces a vertex. The same is true for the EMTiming requirements. The full set of requirements used to select the beam halo enriched sample are given in Table XXIV. There are a total of 13 events, $N^{BH}_{control}$, in the beam halo enriched sample and their kinematic distributions in the final signal region are shown in Figure 35. To take into account the difference between our final signal sample and the beam halo sample we also correct for a number of effects.

To use this sample to predict the number of events in the signal region, we consider how many events pass the final kinematic requirements, described in Chapter IX. We then multiply by the measured rate at which these events pass the kinematic requirements as well as the rate they pass the ID and isolation, vertex and timing requirements. Since not all beam halo events that are produced make their way into our enriched beam halo sample, we correct for this effect using the estimated rate at which they fail our requirements. We estimate the number of events from beam halo

sources in the final $\gamma\gamma + \not\!\!E_T$ signal region, after all requirements, to be:

$$N^{BH}_{signal} = N^{BH}_{control} \cdot R^{BH}_{ID,VX,T} \cdot R^{BH}_{kinematic} \cdot \frac{1}{\epsilon_{BH}} \tag{7.9}$$

where $R^{BH}_{ID,VX,T}$ is the rejection factor that takes into account the rate at which the photon ID and isolation, vertex and timing requirements reject beam halo events, $R^{BH}_{kinematic}$ is the rejection factor that estimates the rate at which beam halo events pass the kinematic requirements, and $\frac{1}{\epsilon_{BH}}$ takes into account the fraction of beam halo events that are not in our sample. The first rejection factor, $R^{BH}_{ID,VX,T}$, is estimated by

$$R^{BH}_{ID,VX,T} = \frac{N^{BH-control}_{ID,VX,T}}{N^{BH}_{control}} = \frac{1}{13} \tag{7.10}$$

where $N^{BH-control}_{ID,VX,T} = 1$ is the number of events in the control sample that also pass the photon ID and isolation requirements, vertex requirements and the EMTiming requirements. The $R^{BH}_{kinematic}$, rejection factor for the final kinematic requirements is estimated by

$$R^{BH}_{kinematic} = \frac{N^{BH-control}_{kinematic}}{N^{BH}_{control}} = \frac{N^{BH-control}_{kinematic}}{13} \tag{7.11}$$

where $N^{BH-control}_{kinematic}$ is the number of events in the control sample that also pass the final kinematic requirements described in Chapter IX. To normalize to the lost rate of beam halo events in our sample we use the measured rate at which the beam halo identification requirements select beam halo sources of photons, R_{BH}. This is measured to be 90% [76]. We thus take

$$\frac{1}{\epsilon_{BH}} = \frac{(1 - R_{BH})}{R_{BH}} = \frac{1 - 0.9}{0.9} = 0.11. \tag{7.12}$$

The final expected number of beam halo events in the signal region that pass the final

kinematic requirements is given by

$$\begin{aligned} N^{BH}_{signal} &= N^{BH}_{control} \cdot R^{BH}_{ID,VX,T} \cdot R^{BH}_{kinematic} \cdot \frac{1}{\epsilon_{BH}} \\ &= 13 \cdot \frac{1}{13} \cdot \frac{N^{BH-control}_{kinematic}}{13} \cdot 0.11 \\ &= N^{BH-control}_{kinematic} \cdot (0.008) \\ &= N^{BH-control}_{kinematic} \cdot SF_{BH} \end{aligned} \tag{7.13}$$

where $SF_{BH} = 0.008 \pm 0.008$ (stat. only).

The uncertainty on the beam halo estimation is dominated by the statistical uncertainty on the number of events after all kinematic requirements in the beam halo control sample, $N^{BH-control}_{kinematic}$. The other major source of uncertainty is due to the uncertainty on the fraction of beam halo events that pass the vertex, ID and EMTiming requirements.

TABLE XXIV: Summary of the requirements used to select the beam halo enriched sample. A total of 13 events pass these requirements.

The Beam Halo Enriched Sample Selection Requirements
Passing one of the triggers in Tables IX and X
Two photons passing the loose photon ID requirements in Table XVII
No vertex requirements
No EMTiming requirements
Two photons identified by the Beam Halo ID requirements listed in Table XII
$\not\!\!E_T$ >20 GeV

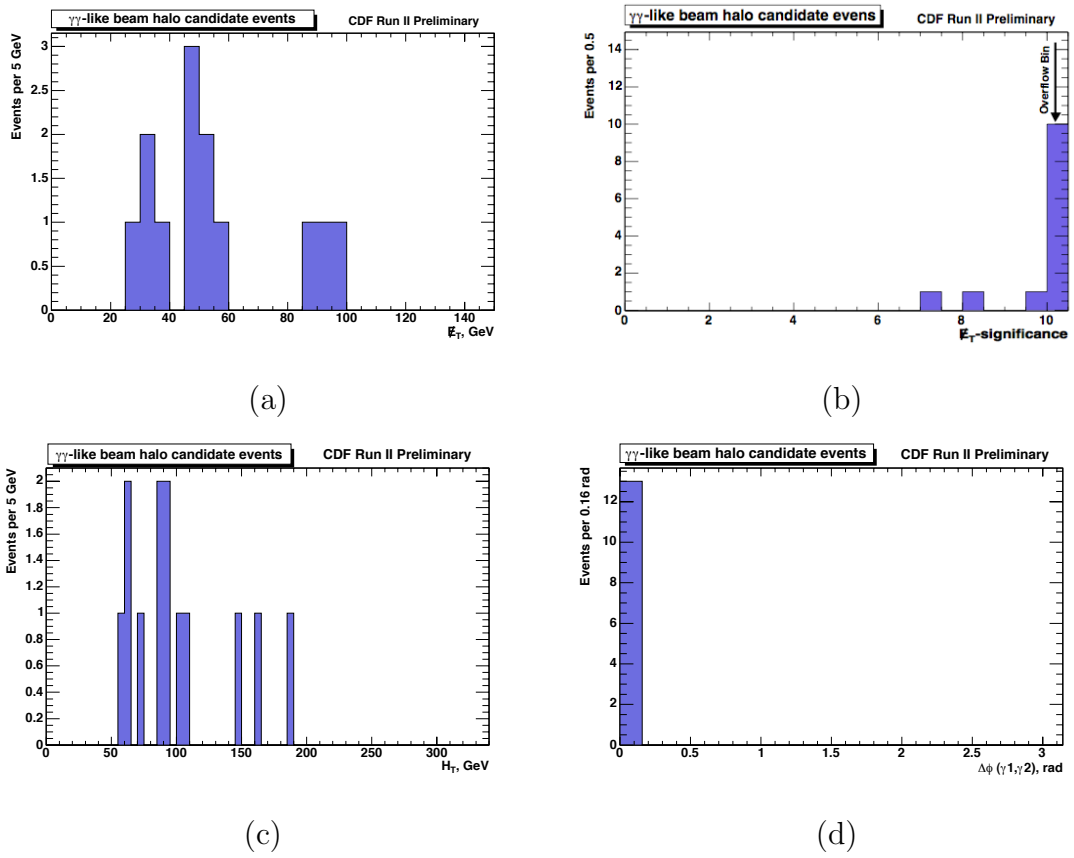

FIG. 35: The $\not\!\!E_T$, $\not\!\!E_T$-significance, H_T and $\Delta\phi(\gamma_1, \gamma_2)$ distributions for the 13 events in the $\gamma\gamma$ beam-halo enriched sample. Events are selected using the requirements in Table XXIV. As expected these events have large $\not\!\!E_T$-significance. They have small $\Delta\phi(\gamma_1, \gamma_2)$ by construction.

2. Cosmic Rays

A cosmic ray muon that traverses the detector can also help fake the $\gamma\gamma + \not\!\!E_T$ signature. These events can mostly be rejected based on their time of arrival in the calorimeter; cosmics are not correlated in time with collisions, and therefore their arrival time distribution is roughly flat as shown in Figure 22. In addition to using the EMTiming system to remove contamination due to cosmic rays (see the requirements in Table XIV), similar techniques to those above are used to evaluate the remaining contribution after the kinematic requirements.

A cosmic ray enriched sample of $\gamma\gamma + \not\!\!E_T$ candidate events is created by selecting events with two photons passing the loose photon ID requirements in Table XVII, but failing the timing requirements. Specifically, at least one of the photon candidate must have $|\mathrm{T}_\gamma| > 25$ ns. That way all cosmic ray sources are taken into account; both photons from the same cosmic ray, each photon from a different cosmic ray, and one photon which comes from a cosmic ray and one from the collision. To increase the sample statistics events are not required to pass our vertex requirements. The full set of requirements are given in Table XXV. This produces a sample of 40 cosmic ray events, $\mathrm{N}^{\mathrm{CR}}_{\mathrm{control}}$. All 40 events are used as a template for the kinematic distributions, as shown in Figure 36, from which the kinematic rejection fraction, $\mathrm{R}^{\mathrm{CR}}_{\mathrm{kinematic}}$, is obtained.

We use estimation techniques that are similar to those used to estimate the beam halo background rate to take into account differences between our cosmic ray enriched sample and the final signal sample. We estimate the expected number of cosmic ray events in the signal region, using the following equation:

$$\mathrm{N}^{\mathrm{CR}}_{\mathrm{signal}} = \mathrm{N}^{\mathrm{CR}}_{\mathrm{control}} \cdot \mathrm{R}^{\mathrm{CR}}_{\mathrm{kinematic}} \cdot \mathrm{R}^{\mathrm{CR-window[25,120]}}_{\mathrm{ID,VX}} \cdot \mathrm{R}^{\mathrm{CR}}_{\Delta\mathrm{T}} \tag{7.14}$$

TABLE XXV: Summary of the requirements used to select the cosmic ray enriched sample. A total of 40 events pass these requirements.

The Cosmin Ray Enriched Sample Selection Requirements
Passing one of the triggers in Table IX and X
Two photons passing the loose photon ID requirements in Table XVII
No vertex requirements
$\lvert T_{\gamma_1}\rvert$ or $\lvert T_{\gamma_2}\rvert > 25$ ns

where $\mathrm{R}_{\mathrm{ID,VX}}^{\mathrm{CR-window[25,120]}}$ is the rejection factor to estimate the rate at which cosmic ray events have both photons passing the photon ID and the vertex requirements. This factor takes into account the extrapolation from the control timing window, [25,120] ns, into signal timing window, [4·σ_T,-4·σ_T] ns. The $\mathrm{R}_{\Delta\mathrm{T}}^{\mathrm{CR}}$ term is used to estimate the rate at which cosmic ray events pass a cut on $\Delta\mathrm{T}_{\gamma\gamma}$ between arrival time of two photons. The first rejection factor, $\mathrm{R}_{\mathrm{kinematic}}^{\mathrm{CR}}$, is estimated by

$$\mathrm{R}_{\mathrm{kinematic}}^{\mathrm{CR}} = \frac{\mathrm{N}_{\mathrm{kinematic}}^{\mathrm{CR-control}}}{\mathrm{N}_{\mathrm{control}}^{\mathrm{CR}}} = \frac{\mathrm{N}_{\mathrm{kinematic}}^{\mathrm{CR-control}}}{40} \tag{7.15}$$

where $\mathrm{N}_{\mathrm{kinematic}}^{\mathrm{CR-control}}$ is the number of events in the control sample that pass the final kinematic requirements defined in Chapter IX. To estimate $\mathrm{R}_{\mathrm{ID,VX}}^{\mathrm{CR-window[25,120]}}$, we count the number of events in the control region timing window [25,120] ns that pass the photon ID and vertex requirements and extrapolated into the signal region timing window [-4·σ_T,4·σ_T] ns, where $\sigma_T = 1.665$ ns, using the observed flat timing distribution [19] shown in Figure 37. The $\mathrm{R}_{\mathrm{ID,VX}}^{\mathrm{CR-window[25,120]}}$ term is estimated by:

$$\begin{aligned} \mathrm{R}_{\mathrm{ID,VX}}^{\mathrm{CR-window[25,120]}} &= \frac{\mathrm{N}_{\mathrm{ID,VX}}^{\mathrm{CR-window[25,120]}}}{\mathrm{N}_{\mathrm{control}}^{\mathrm{CR}}} \cdot \frac{(4\cdot\sigma_T - (-4\cdot\sigma_T))\mathrm{ns}}{(120-25)\mathrm{ns}} \\ &= \frac{7}{40} \cdot \frac{(4\cdot 1.665 - (-4\cdot 1.665))\mathrm{ns}}{(120-25)\mathrm{ns}} = 0.025 \end{aligned} \tag{7.16}$$

where $N_{ID,VX}^{CR-window[25,120]} = 7$ is the number of events that pass the photon ID and vertex requirement where either photon has the arrival time in the range [25,120] ns. The last rejection fraction, $R_{\Delta T}^{CR}$, for the $\Delta T_{\gamma\gamma}$ cut between arrival time of two photons, is given by

$$R_{\Delta T}^{CR} = \frac{N_{\Delta T}^{CR-ID,VX}}{N_{control}^{CR}} = \frac{1}{40} \tag{7.17}$$

where $N_{\Delta T}^{CR-ID,VX} = 1$ is the number of events that pass the photon ID and vertex requirements with $\Delta T_{\gamma\gamma} < 5 \cdot \sigma_{\Delta T}$ ns between arrival times of both photons, where $\sigma_{\Delta T} = 1.021$ ns[84]. Putting it all together, the final expected number of cosmic ray events in the signal region that pass the final kinematic requirements is given by

$$\begin{aligned} N_{signal}^{CR} &= N_{control}^{CR} \cdot R_{kinematic}^{CR} \cdot R_{ID,VX}^{CR-window} \cdot R_{\Delta T}^{CR} \\ &= 40 \cdot \frac{N_{kinematic}^{CR-control}}{40} \cdot 0.025 \cdot \frac{1}{40} \\ &= N_{kinematic}^{CR-control} \cdot (0.001) \\ &= N_{kinematic}^{CR-control} \cdot SF_{CR} \end{aligned} \tag{7.18}$$

where $SF_{CR} = 0.001 \pm 0.001$. (stat. only) is taken.

The uncertainties are dominated by statistical uncertainty on the number of identified cosmics events in the various subsamples.

After estimating the beam halo and cosmic ray backgrounds, the expected kinematic distributions for the combined non-collision backgrounds in the presample are shown in Figure 38.

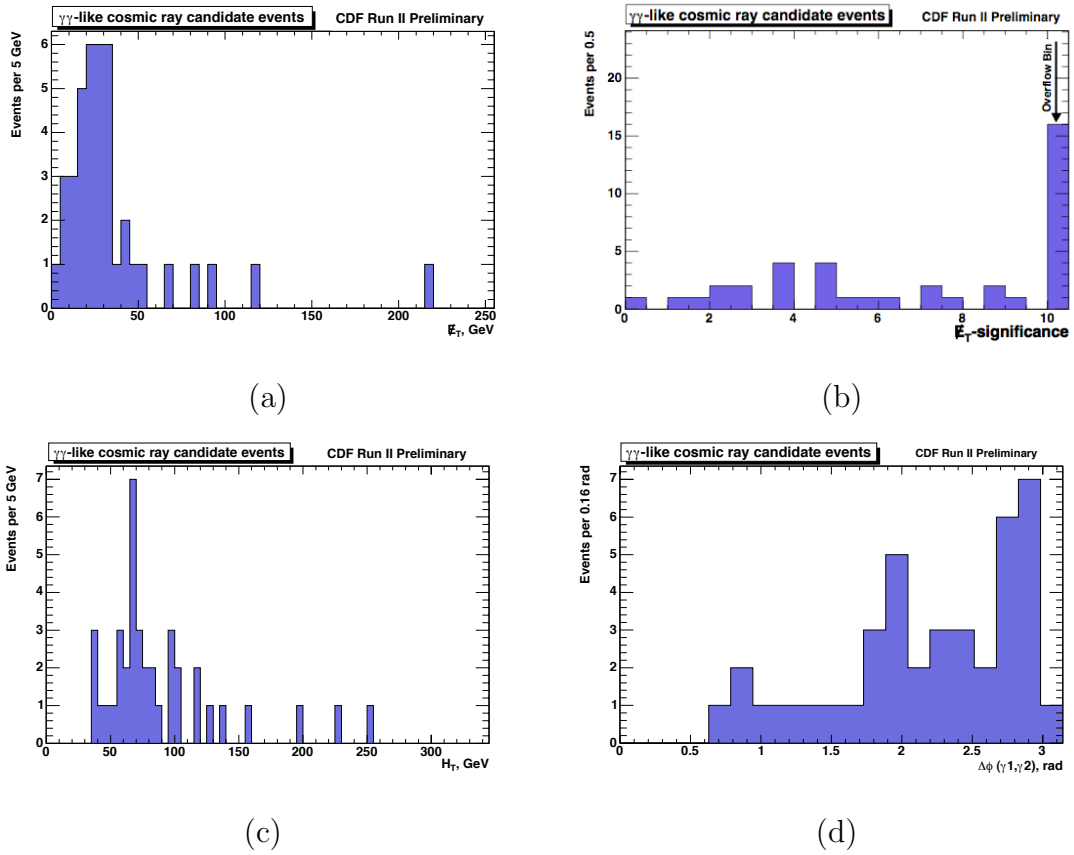

FIG. 36: The $\not\!\!E_T$, $\not\!\!E_T$-significance, H_T and $\Delta\phi(\gamma_1, \gamma_2)$ distributions for the 40 $\gamma\gamma$ candidate events in the cosmic ray enriched sample. Events are selected using the requirements in Table XXV.

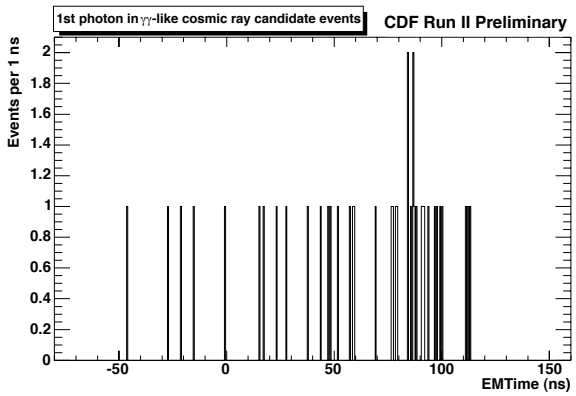

(a)

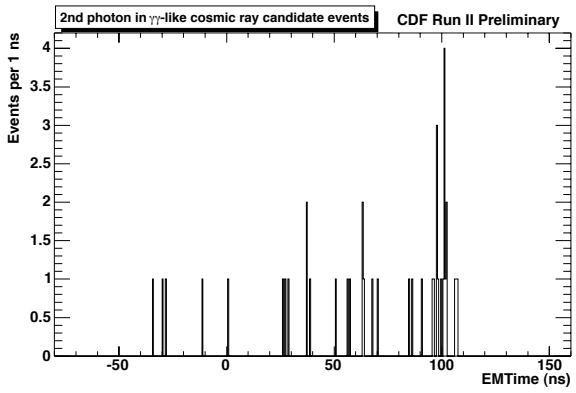

(b)

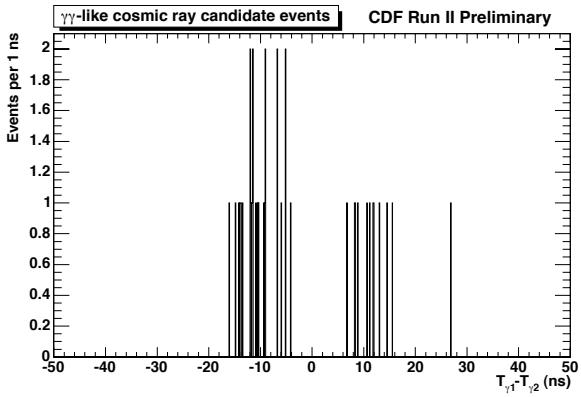

(c)

FIG. 37: The EMTiming distributions for the first and second photons in (a) and (b) for the 40 observed $\gamma\gamma$-like cosmic events selected using the requirements in Table XXV. Figure (c) shows the $\Delta T_{\gamma\gamma} = T_{\gamma 1} - T_{\gamma 2}$ between the arrival times of the two photons.

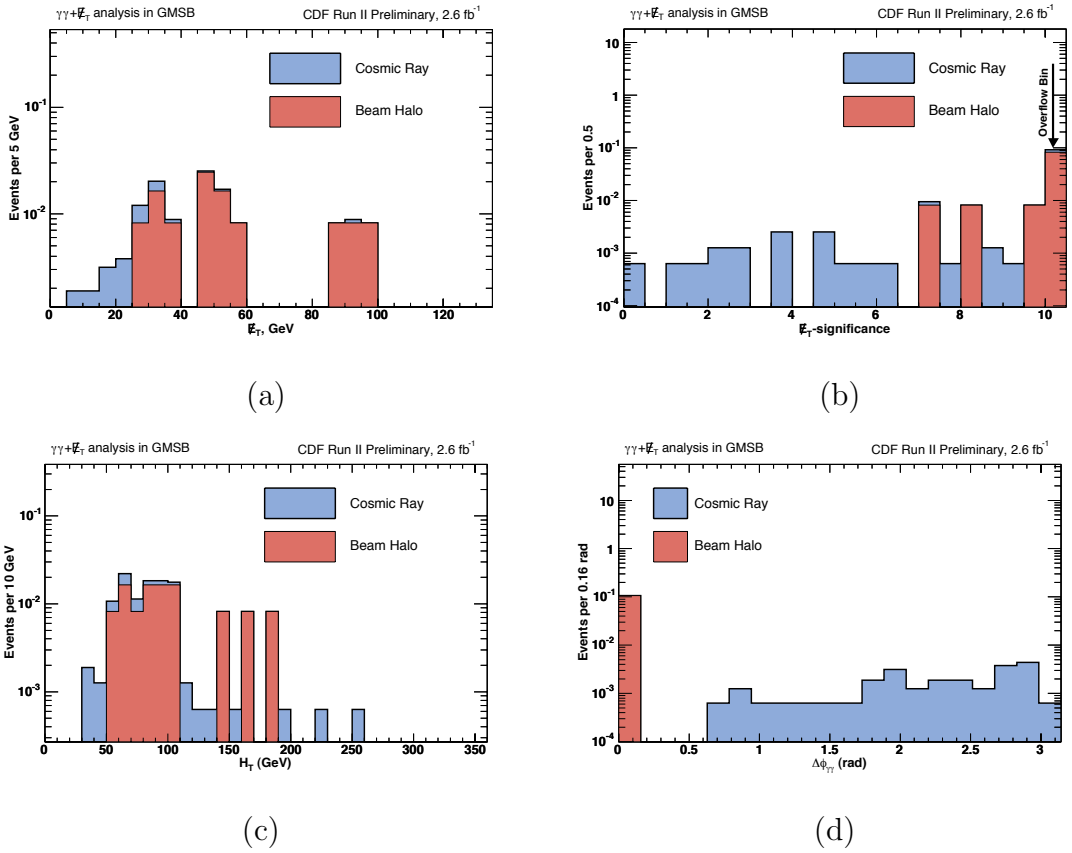

FIG. 38: The non-collision background predictions after the preselection requirements, but with beam halo and cosmic ray normalized by SF_{BH} and SF_{CR} respectively. (a), (b), (c) and (d) show the $\not\!\!E_T$, $\not\!\!E_T$-significance, H_T and $\Delta\phi(\gamma_1, \gamma_2)$ distributions respectively.

D. Background Summary

After considering all the backgrounds, the expected kinematic distributions for all the backgrounds in the presample, normalized to expectations, are shown in Figure 39. The $\not\!\!E_T$-significance in Figure (b) shows the clear separation between the QCD (99.7%) and electroweak (0.3%) backgrounds showing the power of the background estimation techniques and understanding level of the data sample. The data in the presample is well described by the background predictions alone. Note that events at large $\not\!\!E_T$-significance=10 in Figure (b) are overflow bins.

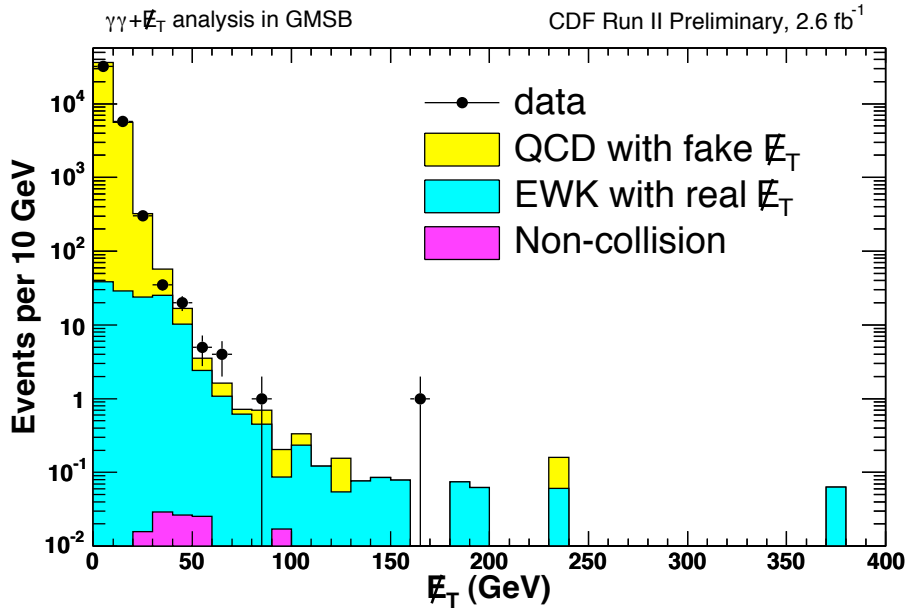

(a)

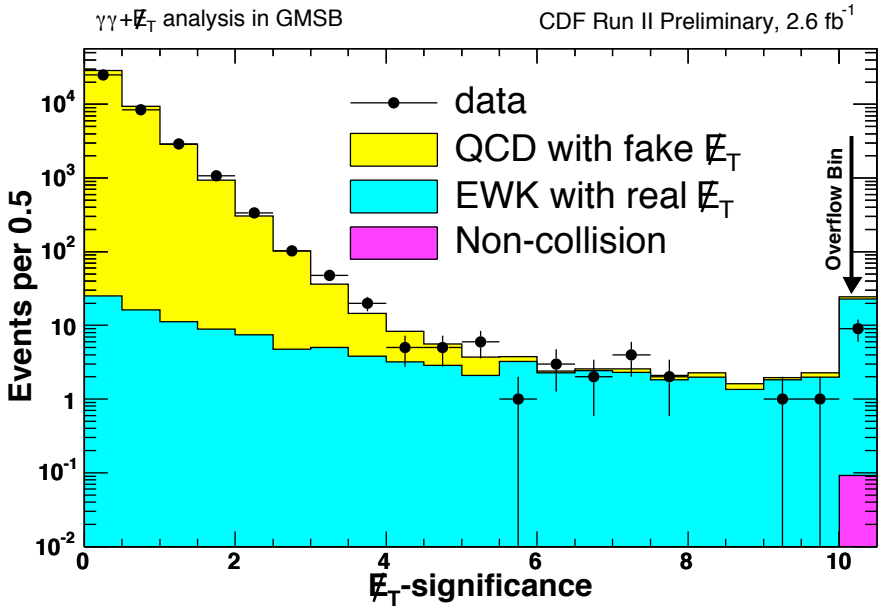

(b)

FIG. 39: The $\not\!\!E_T$ (a) and $\not\!\!E_T$-significance (b) predictions after the preselection requirements along with the data. Note that events with $\not\!\!E_T$-significance=10 in Figure (b) are overflow bins.

CHAPTER VIII

ACCEPTANCE FOR GMSB MODELS AND SYSTEMATIC UNCERTAINTIES

As there are no real GMSB events available a MC simulation is used to mimic both the event production and decay as well as the detector response. This allows for an estimation of our sensitivity to various GMSB model parameters for a variety of different search strategies and final event requirement configurations. Events from all SUSY processes are simulated, including those which may not have direct sensitivity, to maximize the sensitivity which we define to be expected 95% confidence level (C.L.) cross section limit in the no-signal scenario [40]. This chapter describes why this is a strong estimator of the sensitivity, how it is calculated and how we estimate the values of the important quantities that go into calculating it. Of particular importance is the acceptance which is the fraction of all produced SUSY events that are reconstructed by the detector and pass all our event selection criteria. In addition to describing how it is estimated we also describe and estimate the various sources of systematic uncertainty.

A. Overview: Search Sensitivity, Acceptance and Cross Section Limits

A search for "new" physics, such as supersymmetry, at the Tevatron typically involves the comparison of observables in an experiment where the signal and background processes are predicted to be different. The number of signal events that will pass all our selection requirements is given by:

$$N_{\text{signal}} = \mathcal{L} \cdot \sigma_{prod} \cdot A_{\text{signal}} \tag{8.1}$$

where the $\mathcal{L}$ is the total integrated luminosity (2.59 ± 0.16 fb^{-1}), the σ_{prod} is the GMSB signal production cross section and A_{signal} is the fraction of all SUSY events

that are reconstructed in the detector and pass all the event selection requirements. The total production cross section, for our SPS 8 model line, is mostly a function of the $\widetilde{\chi}_1^{\pm}$ and $\widetilde{\chi}_2^0$ mass. However, since this is a linear function of the $\widetilde{\chi}_1^0$ mass we use the $m_{\tilde{\chi}_1^0}$ as our independent variables to parametrize the production cross section as described in Chapter I, Section I.B.2.d. The acceptance is a function of the mass of the neutralino, the lifetime of the neutralino, our detector and the final selection criteria. That being said, a full estimation of our sensitivity also depends on the systematic error on the values in Eq. 8.1.

For a fixed detector configuration the total event acceptance for our signal is a strong function of the mass and lifetime of the $\widetilde{\chi}_1^0$ we estimate it using a MC method. As the $m_{\tilde{\chi}_1^0}$ rises it has more and more energy to transfer into the final state particles energies. This makes the acceptance rise. As the lifetime rises, more and more of the neutralinos will leave the detector before they decay into photons making the acceptance drop. The final event requirements are based on the preselection requirements discussed in Section V.B and on a subsequent set of requirements determined by the optimization described in Chapter IX. Quantitatively, we estimate the A_{signal} using our MC sample as:

$$A_{\text{signal}}(\%) = \frac{N_{\text{events}}^{\text{passing all requirements}}}{N_{\text{events}}^{\text{total produced}}} \tag{8.2}$$

where $N_{\text{events}}^{\text{passing all requirements}}$ is the number of simulated events that pass all the preselection and final optimization requirements.

Since the final observable in this search is the number of observed events in the signal region in the data, N_{obs}, it is useful to quote results based on that. In particular, we expect the number of events in the signal region to be given by

$$N_{\text{obs}} = N_{\text{signal}} + N_{\text{bkg}} \tag{8.3}$$

where $N_{\rm bkg}$ is the number of background events (estimated in the previous chapter). Since we observe $N_{\rm obs}$ and calculate $N_{\rm bkg}$ for a set of requirements we can see if there is any evidence for a value of $N_{\rm signal}$ which is statistically and systematically different than zero. If it is not observed to be different from zero, it is useful to set a limit on the amount of new physics events from SUSY. It is further useful to remove the detector specific sensitivity from this measurement, $A_{\rm signal}$, and report a limit on the number of produced events (which takes into account the acceptance). Further taking into account the known luminosity we can report a limit on the production cross section via:

$$\sigma_{\rm prod} = \frac{N_{\rm signal}}{\mathcal{L} \cdot A_{\rm signal}}. \tag{8.4}$$

In this analysis the sensitivity is estimated in the form of expected 95% Confidence Level (C.L.) upper cross section limits [85]. The 95% C.L. cross section upper limit, σ_{95}, is set by comparing the observed number of events in the data that pass the final kinematic requirements after subtracting the expected backgrounds from the non-signal sources and assuming there are no signal events in the data. The 95% C.L. upper limit on the cross section is a number used in the occurrence of a non-observation of signal events to describe a limit on the amount of signal that could be hidden our data but we do not have sensitivity to. Said differently, we exclude all cross sections above a certain amount with 95% C.L. By comparing the expected production cross section to the observed 95% C.L. limit we exclude any model where $\sigma_{\rm prod} > \sigma_{95}$. More details of this process are described in Chapter IX.

Since we have the luminosity and production cross section, we next give more detail on the estimation of the signal acceptance. It shows the methods to find the GMSB signal acceptance to pass various sets of requirements, both as a function of the $\widetilde{\chi}_1^0$ mass and lifetime. After that we will discuss the sources of uncertainty on the

acceptance as well as the uncertainty on the production cross section.

B. Simulated Acceptance for GMSB signal

To estimate the sensitivity for GMSB models we simulate MC samples in the mass-lifetime range, 75 GeV $\leq m_{\tilde{\chi}_1^0} \leq$ 150 GeV and $\tau_{\tilde{\chi}_1^0} \leq$ 2 ns [86, 87]. For non-zero lifetimes of the $\widetilde{\chi}_1^0$ we also simulate the EMTiming system [88]. These regions are chosen to cover from below the current limits in mass (see Figure 7) to masses up to and including where we will be sensitive. Similarly, we will consider lifetimes only up to 2 ns because of the photon identification issues mentioned in Chapter III. For each simulated GMSB mass-lifetime combination the particle masses and the production cross sections are calculated with the ISASUGRA package interfaced with the PYTHIA [89]. The acceptance is the number of simulated events that pass all the requirements divided by the number simulated as given in Eq. 8.2. The statistical uncertainty is estimated based on the number of simulated events passing our final kinematic requirements. The number of simulated events for each GMSB MC samples is thus chosen such that their statistical uncertainty is $\sim$1% to make it negligible to the combined systematic uncertainty which, as will be discussed later in this chapter, is $\sim$8%.

The acceptance is calculated for each GMSB mass-lifetime combination based on the preselection requirements and the final kinematic requirements. The breakdown of events passing each of the selection requirements for an example GMSB point at $m_{\tilde{\chi}_1^0} = 140$ GeV and $\tau_{\tilde{\chi}_1^0} \ll 1$ ns is shown in Table XXVI. For completeness we have included the results for the final event selection, determined in Chapter IX. Figure 40 shows the $\not\!\!E_T$, $\not\!\!E_T$-significance, H_T and $\Delta\phi(\gamma_1, \gamma_2)$ distributions for GMSB signal MC after the preselection requirements which show that these quantities are expected to

be very different from the expected distributions of the backgrounds.

TABLE XXVI: Summary of the event reduction for a GMSB example point in the $\gamma\gamma$+$\not\!\!E_T$ final state. We have included the final, optimized requirements for completeness.

Requirement	Events passed	A_{signal} (%) ($m_{\tilde{\chi}_1^0}$=140 GeV and $\tau_{\tilde{\chi}_1^0} \ll 1$ ns)
Events simulated	133330	100.0
Two EM Objects and $\lvert z_{vx}\rvert < 60$ cm	124771	93.6
Standard photon ID requirements with $\lvert\eta\rvert < 1.0$ and $E_T > 13$ GeV	18270	13.7
Phoenix and PMT Rejection	17625	13.2
Beam Halo and Cosmic Rejection	17612	13.2
$E_T^{swap} > 13$ GeV after vertex swap and $\not\!\!E_T$ Cleanup	17049	12.8
$\not\!\!E_T$-significance>3	12610	9.5
H_T>200 GeV	11913	8.9
$\Delta\phi(\gamma_1, \gamma_2) < \pi - 0.35$	10395	7.8

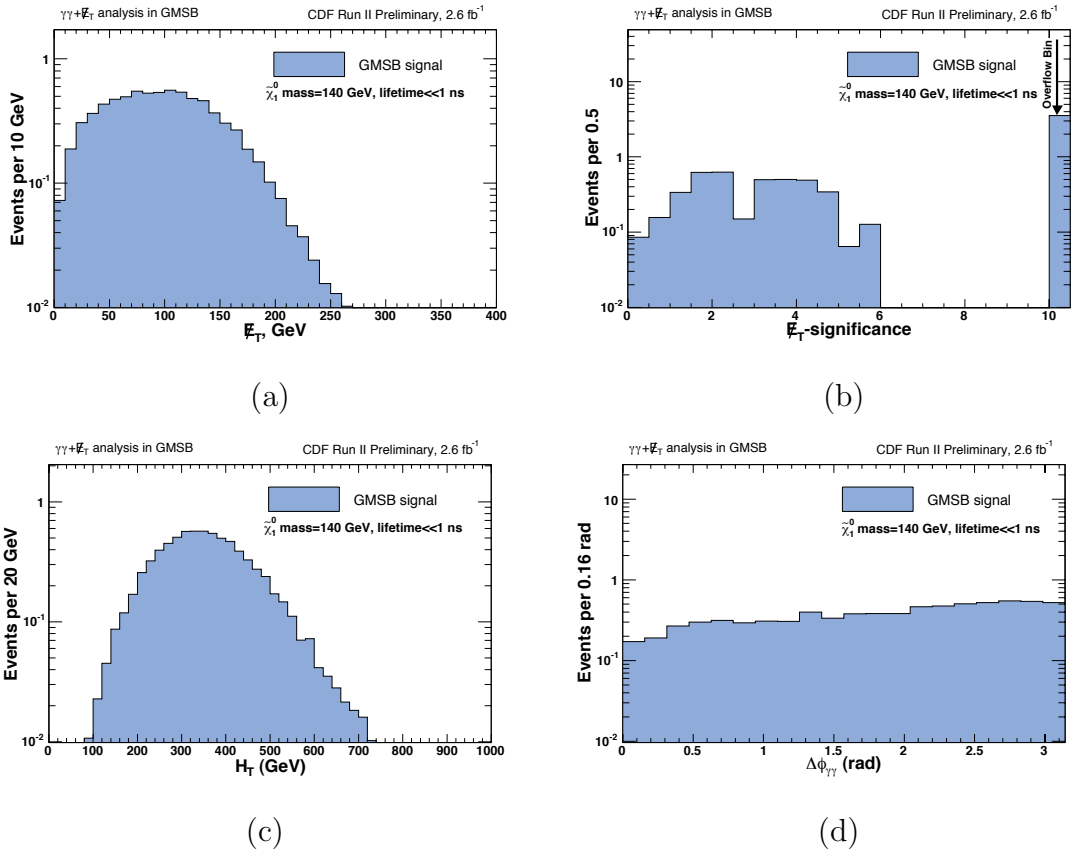

FIG. 40: The $\not\!\!E_T$, $\not\!\!E_T$-significance, H_T and $\Delta\phi(\gamma_1, \gamma_2)$ distributions for a GMSB signal point with $m_{\tilde{\chi}_1^0} = 140$ GeV/c^2 and $\tau_{\tilde{\chi}_1^0} \ll 1$ ns using the full MC simulation, but after the preselection requirements. The amount of data is normalized by the NLO cross section and luminosity. In Figure (b) there are a subset of events with low $\not\!\!E_T$-significance (< 7) due to the fact that while the non-interacting particles are highly energetic, they might not have small η, or there are two (or more) that point in opposite directions and cancel each other out, giving small $\not\!\!E_T$. The second region, which are essentially all in the the overflow bins at 10, is due to events with large $\not\!\!E_T$.

C. Estimation of the Systematic Uncertainties

Since we have defined the sensitivity of the search to be equal to the expected 95% C.L. cross section limits, a proper sensitivity estimate must take into account the uncertainties on the trigger, luminosity, background and acceptance. As mentioned in Section V.A (more detail in Appendix C), with our combination of triggers and high E_T photons we take a trigger efficiency of 100% with negligible error [90]. The systematic uncertainty on the luminosity is measured separately to be 6% [49]. The systematic uncertainty on the number of background events in the signal region is determined from our understanding of both the collision and non-collision sources, as described in Chapter VII. The background uncertainty is evaluated for every set of requirements in the optimization procedure. The acceptance uncertainties used in the cross section limits are described in the subsections below. Similarly, the uncertainty on the theoretical production cross sections are estimated in the subsections below. The results are summarized in Table XXVII for an example GMSB point of $m_{\tilde{\chi}_1^0} = 140$ GeV and $\tau_{\tilde{\chi}_1^0} \ll 1$ ns. All uncertainties are consistent with the GMSB diphoton and delayed photon in Ref. [19, 20] unless otherwise noted. The systematic uncertainty is taken to be constant for all masses.

TABLE XXVII: Summary of the systematic uncertainties on the acceptance and production cross section for an example GMSB point at $m_{\tilde{\chi}_1^0} = 140$ GeV and $\tau_{\tilde{\chi}_1^0} \ll 1$ ns. In the limit calculators (see Chapter IX) we get the full limit from taking into account the systematic uncertainties on both the production cross section and the acceptance in quadrature to get a 10.6% uncertainty on the "acceptance" [85].

Source of Uncertainty	Relative Systematic Uncertainty (%)
Acceptance:	
Efficiency of the Diphoton ID and Isolation Requirements	5.4
Initial and Final State Radiation	3.9
Jet Energy Scale	1.6
$\not\!\!E_T$-significance parametrizations	0.7
Parton Distribution Functions	0.4
Total	6.9
Cross section:	
Parton Distribution Functions	7.6
Renormalization scale (Q^2)	2.6
Total	8.0

1. Acceptance Uncertainties

There are a number of effects that can cause our estimate of the acceptance to be systematically misestimated. For example, if the photon ID efficiency is lower than what the MC simulates this will cause more photons to pass the requirements which, in turn, causes the acceptance to be overestimated. We next look at the dominant sources of uncertainty and describe how each is estimated and how the variation in each effect translates into an uncertainty on the acceptance. They are identified here, in order of decreasing magnitude.

a. Photon ID and Isolation Efficiency

The photon ID and isolation variables are imperfectly modeled in *cdfSim* [61], but have been measured to be correct on average. Thus, we do not correct the acceptance and only use the the measured uncertainty on the photon ID and isolation efficiency. Using the results of [91], we take a systematic uncertainty of 1.8% for the photon ID and 2.0% for the isolation efficiencies and add them in quadrature for a total of 2.7% uncertainty per photon. Since there are two photons we take the total systematic uncertainty to be $2 \times 2.7\% = 5.4\%$. This represents an improvement over the 202 pb^{-1} result [20] due to improved understanding of the detector.

b. Initial and Final State Radiation

Initial state radiation (ISR), caused by a gluon radiating from an incoming parton, or final state radiation (FSR) from an outgoing jet, can both make the E_T spectrum of the final state particles harder or softer than expected without radiation. This can cause extra jets in the final state or can cause the photon, the jets or the $\not\!\!E_T$ to be systematically more or less likely to pass the kinematic requirements. These effects

are included as part of the event simulation, but their rate and magnitude are not perfectly understood or modelled. To estimate the corresponding uncertainty on the acceptance we use the standard CDF procedure by varying the Sudakov parameters as described in [92]. Doing so we find a variation in the acceptance, taken to be the systematic uncertainty, of 3.9%.

c. Jet Energy Scale

Since we allow jets with a corrected $E_T > 15$ GeV to be counted in our $H_{_T}$ and $\not\!\!E_T$-significance calculations we have studied the change in acceptance if the jet energy is mismeasured. The sensitivity in the final event selection depends on how often signal events have jets that are around the energy threshold. The standard procedure at CDF [93] varies each correction factor independently by $\pm 1\sigma$. The resulting variation on the acceptance is 1.6%.

d. $\not\!\!E_T$-significance Parametrization and Calibration

The $\not\!\!E_T$-significance calibrations for data and MC are slightly different due to the fact that the unclustered energy parametrizations are measured to be slightly different (See Figures 10 and 16 in Ref. [76]). To estimate the magnitude of this uncertainty on the acceptance we compare the acceptance using the most different sets and find the variation on the acceptance to be 0.7%, which we take as the uncertainty.

e. Parton Distribution Functions

In a typical proton and antiproton collision it is mostly a single subparticle of the (anti-)proton, a parton (quark or gluon), that participates in the hard collision and produces a high center-of-mass energy event. The momentum fraction, described by parton distribution functions (PDFs), that is carried by each of the partons in the

proton or antiproton is not perfectly understood. This affects both the rate at which a process happens (the production cross section) and the kinematics of the outgoing final state particles (the acceptance of the event selection criteria).

To estimate how this uncertainty translates into an uncertainty on the acceptance, we use the standard technique. For each simulated event the MC generator calculates the momentum fraction of the colliding parton using a standardized "PDF-set" by the `CTEQ` collaboration (`CTEQ-5L`) [94]. For this task we use a special "error" set of 20 uncertainty pairs of `CTEQ-6M`. This set is based on $\pm 1\sigma$ deviations of a diagonalized set of 20 parameters which have their most likely values tuned using a fit to experimental data. We calculate the full event selection acceptance variations for all 40 "error" PDFs. The variations are taken with respect to the central best-fit PDF. All the variations are summed up in quadrature according to a special prescription [94] to obtain the positive and negative uncertainties on the acceptance. For the example GMSB point we get a relative uncertainty of $+0.3\%$ -0.4% on the acceptance. The larger value is taken to estimate the uncertainty conservatively.

2. Production Cross Section Uncertainties

The production cross section uncertainty is dominated by the uncertainty on the PDFs.

a. Parton Distribution Functions

Using the same methods in subsection VIII.C.1.e, but considering the total production cross section calculation for the example GMSB point, the variation is measured to be taken of $+7.6\%$ -7.3% of the cross section. To be conservative the larger value is taken to be the uncertainty. As expected, this uncertainty is a little bit bigger than that reported in the delayed photon analysis ($\sim 5.9\%$ for $m_{\tilde{\chi}_1^0} = 100$ GeV [19]) since

the example point in this analysis uses a heavier mass.

b. Renormalization Scale

While the dominant GMSB production mechanisms are via electroweak processes like those shown in Figure 4, the probability that QCD processes occur via gluon emission and higher-order loops depends sensitively on the energy scale at which the process happens. In PYTHIA [38] events are generated using a fixed renormalized (q^2) scale of $\hat{s}$. However, the NLO cross section, which is calculated with PROSPINO2 [95] for the systematic studies only[1], varies as a function of the renormalization scale. The variation of the NLO production cross section observed by changing the scale from $0.25 \cdot q^2$ to $4 \cdot q^2$ is calculated to be 2.6% for the example GMSB point.

3. Summary of Systematic Uncertainties

All systematic errors are combined in quadrature to give 6.9% on the acceptance and 8.0% on the production cross section. These are combined in quadrature to give a total systematic uncertainty of 10.6% used in the limit calculators for the "acceptance". The individual results are given in Table XXVII.

[1]Elsewhere we use the PYTHIA and k-factors to calculate the NLO cross sections.

CHAPTER IX

OPTIMIZATION AND EXPECTED SEARCH SENSITIVITY

In this chapter we describe the methods to estimate and optimize the expected search sensitivity. Now that the background estimation methods are determined and the signal acceptance is available for a given set of requirements, along with their uncertainties, an optimization procedure can be readily employed. Using only general requirements we can conduct a robust and partially model independent search. We optimize the values of the requirements before unblinding the signal region in the next chapter,

A. Optimization Requirements

As previously mentioned we have chosen the $\not\!\!E_T$-significance, $H_{_T}$, and $\Delta\phi(\gamma_1, \gamma_2)$ variables for our final optimization requirements. In this section we describe in more detail why we chose these requirements, and then show the optimization procedure using them. Note that many other requirements were considered, including the magnitude of the $\not\!\!E_T$, $\Delta\phi(\gamma 1, \not\!\!E_T)$, $\Delta\phi(\gamma 2, \not\!\!E_T)$, $\Delta\phi(jet, \not\!\!E_T)$, $E_T^{\gamma 1}$, $E_T^{\gamma 2}$ and N_{jets} (number of jets), but these yield negligible gain and add additional systematic uncertainties if they were added to the three already chosen; none is a better replacement for the ones we have. Our primary requirements are:

- $\not\!\!E_T$-significance:

  As described in Section VII.A, this requirement is very effective at separating between events with no intrinsic $\not\!\!E_T$ and those events with real $\not\!\!E_T$. As such it gets rid of most of the QCD background with fake $\not\!\!E_T$ and large H_T but is very efficient for GMSB signal.

- $H_{_T}$:

  In GMSB production heavy gaugino pair-production dominates, and the gauginos decay to light, but high E_T, final state particles via cascade decays. Thus, GMSB signal has lots of $H_{_T}$ compared to SM backgrounds, which are dominated by QCD and electroweak backgrounds which do not have lots of high E_T objects.

- $\Delta\phi(\gamma_1, \gamma_2)$:

  The dominant electroweak backgrounds with two photons, significant $\not\!\!E_T$ and large $H_{_T}$ are from $W\gamma$ events where the photon has high E_T and is typically recoiling against $W \rightarrow e\nu \rightarrow \gamma_{fake} + \not\!\!E_T$. This scenario is readily rejected because the gauge boson decay is highly boosted, which makes the two photon candidates in the final state mostly back-to-back. Also, the remaining QCD background with $\gamma\gamma + \not\!\!E_T$ with large $H_{_T}$ are from events with a pair of high E_T photons where the wrong vertex is selected, the right vertex is not found, and the photons are mostly back-to-back. In this case the $\not\!\!E_T$ is fake and comes from having picked the wrong vertex. Even after the vertex swap procedure, this background is still significant. The $\Delta\phi(\gamma_1, \gamma_2)$ requirement effectively reduces both these backgrounds as the two photons in GMSB signal have no reason to be back-to-back (see Figures 4 and 40) and so efficiently pass this requirement.

B. Optimization and Setting Limits

There are many ways to estimate the search sensitivity. We have chosen to estimate the search sensitivity to be equal to the expected 95% C.L. upper cross section limits [96] in the no-signal assumption. This chapter will talk about how we set limits on cross sections, using the definitions from Equations 8.2 and 8.4 from last chapter,

and how to get expected limits based on expectations from background and signal predictions. This method is particularly useful as it provides an effective balance between signal and background, does not depend on the magnitude of a signal if there is one, and effectively takes into account the systematic errors when deciding on a set of final requirements.

The sensitivity is estimated on the acceptance for the full set of GMSB production diagrams [40], and is done for all the considered GMSB parameter points. With a background prediction and an acceptance, it is straightforward to determine the expected cross section limit for each set of possible event requirements, and choose the one that minimizes the expected cross section limit [96]. It is this set of requirements which optimizes the sensitivity. This can be done for each value of the GMSB $\widetilde{\chi}_1^0$ mass and lifetime parameters. If no signal is observed, then by comparing the predicted production cross section with the 95% C.L. limit, we exclude those mass and lifetime combinations that have a production cross section that is above the exclusion cross section limit, after also taking into account the production cross section uncertainties. Similarly, if we assume no signal we can predict the probability of getting various results and we can get expected limits. Since the optimized set of requirements for each mass and lifetime combination are slightly different, we checked to see if a single choice of final state requirements is robust enough to be applied throughout the parameter space for simplicity. Since it does, we choose the single combination that optimizes the mass limit in the $\tau_{\tilde{\chi}_1^0} \ll 1$ ns scenario. This prescription has been shown to be as effective as optimizing for the case with the assumption that there will be signal observed. The difference between these two assumptions is small compared to the variation between the variation of optimal selection requirements for different mass-lifetime combinations.

We begin with a description of how a 95% C.L. cross section upper limit is

calculated, and how it is readily extended to calculate an expected 95% C.L. cross section upper limit. We then talk about how this expected limit changes as a function of the final selection requirements. In an experiment such as ours, after a set of final event requirements are selected, this uniquely determines the number of background events expected, and the acceptance. A certain number of events is observed in the data, $N_{\rm obs}$, and this is compared with background and if no signal is observed then a 95% C.L. limit is set on the amount of production cross section. We next detail that process, and move on to extending it for the case where we can estimate the expected sensitivity before looking at the data.

For a fixed integrated luminosity of $\mathcal{L} = 2.59 \pm 0.16$ fb^{-1} and an observed number of events in the data, $N_{\rm obs}$, and assuming no signal the 95% C.L. upper limit on the production cross section, we can find the number of signal events that would produce more than the observed number of events 95% of the time. The mean number events from a hypothetical signal is given by $\mu_{\rm exp}(\sigma) = N_{\rm bkg} + \sigma \cdot \mathcal{L} \cdot A_{\rm signal}$. The production cross section that produces this number of events is known as $\sigma_{95}(N_{\rm obs})$ and is determined using the following equation which takes into account the statistical fluctuations of the backgrounds and any expected signal (ignoring systematic errors for now).

$$0.95 = 1 - \sum_{n=0}^{N_{\rm obs}} \text{Poisson}(n, \mu_{\rm exp}(\sigma_{95})) \tag{9.1}$$

where the Poisson$(N_{\rm obs}, \mu_{\rm exp})$ is the normalized Poisson probability to observe n events when $\mu_{\rm exp}$ are expected. To take into account the systematic errors and calculate the full cross section limit, we use the standard Bayesian limit calculation tool [85] using a flat prior for the cross section and Gaussian priors for the signal acceptances, backgrounds and luminosity to take into account the systematic uncertainties of each.

The expected 95% C.L. cross section limit, $\sigma_{95}^{\rm exp}$, can be calculated from the $\sigma_{95}(N_{\rm obs})$ if we assume no signal and allow $N_{\rm obs}$ to vary according to the Poisson variations in the backgrounds alone, $N_{\rm obs}^{\rm pseudo}$. The expected limit is thus a function of the selection requirements and is readily determined by a simple expansion of our procedure. Since the cross section limit is a function of the background and acceptance, which are a function of the selection requirements ("cuts") we can calculate the cross section limit if we make the no-signal assumption where $\mu_{\rm exp} = N_{\rm bkg}({\rm cut})$. Then the expected number of observed events is just given by Poisson($N_{\rm obs}^{\rm pseudo}, N_{\rm bkg}({\rm cut})$). The value of $\sigma_{95}^{\rm exp}({\rm cut})$ is calculated from $\sigma_{95}(N_{\rm obs}^{\rm pseudo}, {\rm cut})$ in the no signal scenario and takes into account all possible outcomes of the pseudo-experiments, determined by their relative Poisson probability. To summarize, we take:

$$\sigma_{95}^{\rm exp}({\rm cut}) = \sum_{N_{\rm obs}^{\rm pseudo}=0}^{\infty} \sigma_{95}(N_{\rm obs}^{\rm pseudo}, {\rm cut}) \cdot {\rm Poisson}(N_{\rm obs}^{\rm pseudo}, N_{\rm bkg}({\rm cut})) \tag{9.2}$$

$${\rm RMS}^2({\rm cut}) = \sum_{N_{\rm obs}^{\rm pseudo}=0}^{\infty} (\sigma_{95}(N_{\rm obs}^{\rm pseudo}, {\rm cut}) - \sigma_{95}^{\rm exp}({\rm cut}))^2 \cdot {\rm Poisson}(N_{\rm obs}^{\rm pseudo}, N_{\rm bkg}({\rm cut})) \tag{9.3}$$

Thus, we have the expected 95% C.L. cross section upper limit as a function of the final selection criteria. For each GMSB point the set of requirements that produces the minimum expected cross section limit, Min($\sigma_{95}^{\rm exp}({\rm cut})$), defines our set of optimal requirements for that mass and lifetime combination. The expected exclusion region is defined by the region where the production cross section is above the expected 95% C.L. cross section limit. The expected mass/lifetime limit is where the two cross. To find the optimal set of criteria we consider a simple grid search where we vary our three requirements over the region: $0 \leq \not\!\!E_T$-significance ≤ 10 in steps of 1, $0 \leq H_{_T} \leq 400$ GeV in steps of 25 GeV, and $2.44 \leq \Delta\phi(\gamma_1, \gamma_2) \leq 3.14$ rad in steps of

0.05 rad.

After the optimization procedure we find that the values of $\not\!\!E_T$-significance >3, H_T>200 GeV and $\Delta\phi(\gamma_1, \gamma_2)<\pi - 0.35$ rad maximize the mass limit for $\tau_{\tilde{\chi}_1^0} \ll 1$ ns. As an illustration that the optimization minimizes the expected cross section limit in all three variables, Figures 41-(a), (c) and (e) show the expected limit for a GMSB example point at $m_{\tilde{\chi}_1^0} = 140$ GeV/c^2 and $\tau_{\tilde{\chi}_1^0} \ll 1$ ns as a function of a requirement while keeping all other requirements fixed at the optimized values around the mass limit. Indicated in green is the 8.0% uncertainty-band on the production cross section. In yellow we show the expected statistical variation in the cross section limit using the data in Table XXVIII and the RMS definition in Eq. 9.3. As previously mentioned, we decided to use a single set of requirements before we open the box based on the expectation that they will yield the largest expected exclusion region without significant loss of sensitivity[1] to lower mass or higher lifetime scenarios.

With these requirements we predict a total of 1.38±0.44 of background events with 0.92±0.37 from electroweak sources with real $\not\!\!E_T$, 0.46±0.24 from QCD with fake $\not\!\!E_T$ and $0.001^{+0.008}_{-0.001}$ from non-collision sources. Table XXIX shows the raw numbers and calculations for the individual electroweak background rates to pass the optimal requirements. They are summarized in Table XXX. The global electroweak scale factor is estimated to be 1.31 ± 0.47 for the final optimal requirements[2]. Note that we calculate the electroweak global scale factor for each different set of requirements and its distribution is shown in Figure 42. The single dominant electroweak contribution

[1]This has been shown in the delayed photon analysis [19]. In that analysis we lost less than 4% of sensitivity in the cross section limits by using one fixed set of requirements. There was no loss of exclusion region area.

[2]$0.47 = \sqrt{0.44^2 + (1.57 - 1.41)^2}$ (see Table XXIX), where we take the difference between the value of 1.41 ± 0.44 (stat. only), using Eq. 7.8, with a default value of E/p and the value of 1.57 ± 0.43 (stat. only) with a deviated value of E/p, after the optimal requirements.

is $Z\gamma j \rightarrow \nu\nu\gamma\gamma_{fake}$ which produces a total of 0.26±0.08 events. From the Table XXX, the combined rate of $Z\gamma j \rightarrow l^+_{lost} l^-_{lost} \gamma\gamma_{fake}$ dominates since most $W \rightarrow l\nu$ processes are rejected by the $\Delta\phi(\gamma_1, \gamma_2)$ requirement (see Section IX.A). The QCD background contributions are given in Tables XXXI and are dominated by energy measurement fluctuations in the $\not\!\!E_T$, estimated using the METMODEL to have a rate of 0.40±0.22 events. The non-collision background calculations are shown in Table XXXII and are dominated by cosmics which have a rate of 0.001±0.001. Table XXXIII provides the final summary.

Table XXXIV shows the expected cross section limits, acceptance and production cross sections for each GMSB point simulated, along with the predicted backgrounds. Figures 41-(b), (d) and (f) show the distributions of each optimization variable normalized to the number of expected events, while holding all other variables at optimized requirements ("N-1 distribution"). Compared are the background distribution before unblinding the signal region and the expected signal in the signal region for an example GMSB point at $m_{\tilde{\chi}^0_1} = 140$ GeV/c^2 and $\tau_{\tilde{\chi}^0_1} \ll 1$ ns. Taking into account the errors, we estimate the acceptance to be (7.80±0.54)%. In the next section, the signal region is unblinded and limits are set on GMSB models.

Note that we do not perform a separate optimization for non-zero lifetimes as described in Section VIII.B. Rather, the sensitivity of the analysis is simply estimated for these scenarios for lifetimes up to 2 ns. The expected results are given in Table XXXIV.

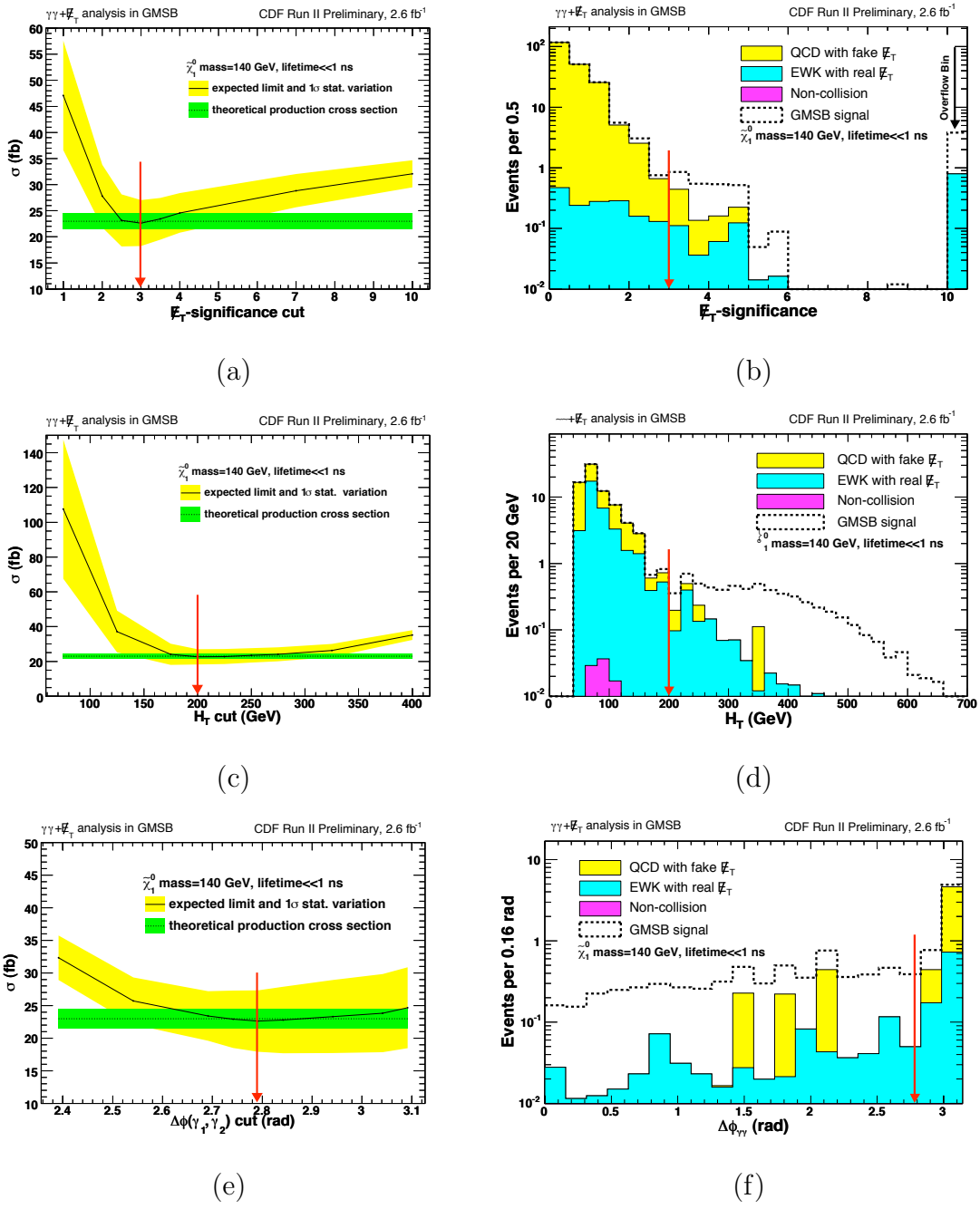

FIG. 41: The expected 95% C.L. cross section limit as a function of the $\not\!\!E_T$-significance (a), H_T (c) and $\Delta\phi(\gamma_1, \gamma_2)$ (e) requirements for a GMSB example point ($m_{\tilde{\chi}_1^0} = 140$ GeV/c^2 and $\tau_{\tilde{\chi}_1^0} \ll 1$ ns). All other requirements are held at their optimized values. The optimal cut is where the expected cross section is minimized. Indicated in yellow is the RMS (See Eqn. 9.3) and in green is the 8.0% uncertainty-band for the production cross section (see Table XXVII). The N-1 predicted kinematic distributions after the optimized requirements are shown in Figures (b), (d) and (f). The red arrows indicate the value of the final requirement.

TABLE XXVIII: The 95% C.L. cross section limit as a function of the hypothetically observed number of events, after the optimization requirements. The Poisson probability for this number of events is based on the background expectation of 1.38 events. The acceptance and cross section limit are calculated for an example GMSB point of $m_{\tilde{\chi}_1^0} = 140$ GeV/c^2 and $\tau_{\tilde{\chi}_1^0} \ll 1$ ns. The expected limit and its variation are calculated as shown in [96] with Eqs. 9.2 and 9.3. With these numbers we find an expected cross section limit of 22.1 fb with an RMS on the limit of 7.6 fb.

$N_{\rm obs}^{\rm pseudo}$	Probability	$\sigma_{95}(N_{\rm obs}^{\rm pseudo})$ (fb)
0	0.252	15.1
1	0.347	20.7
2	0.240	26.8
3	0.110	33.4
4	0.038	40.3
5	0.002	48.2

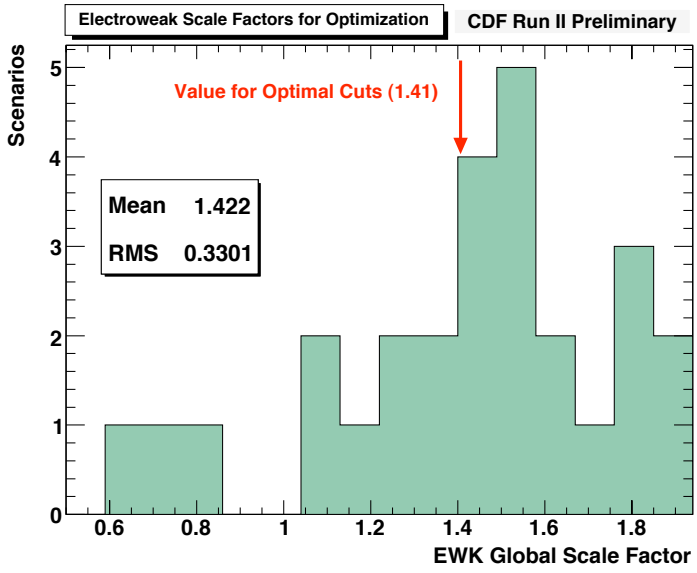

FIG. 42: The electroweak global scale factor distributions for each different set of cuts considered in our optimization procedure. Note that the optimal point is near the mean of the distribution, consistent with no bias in the optimization. The RMS is consistent with uncertainties on the expectation from the E/p variation (see Section VII.B).

TABLE XXIX: The expected rates, and the calculations to get them, for the electroweak backgrounds after all the optimal requirements ($\not\!\!E_T$-significance > 3.0, $H_T > 200$ GeV and $\Delta\phi(\gamma_1, \gamma_2) < \pi - 0.35$). The SF_i scale factors are defined in Equation 7.8 and are taken from Table XXIII. All errors are statistical only unless noted otherwise. The final electroweak global scale factor with E/p variations is estimated for each different set of optimal requirements. Figure 42 shows the variation of the electroweak global scale factor for a number of different optimization requirements. These results are summarized in Table XXX.

Background Source	SF_i	EWK $\gamma\gamma + \not\!\!E_T$ signal		$0.8 < E/p < 1.2$ for $e\gamma$		$0.0 < E/p < 2.0$ for $e\gamma$	
		MC Events	$\mathrm{N}^{\mathrm{EWK-MC}}_{\mathrm{signal},i} \cdot \mathrm{SF}_i$	MC Events	$\mathrm{N}^{\mathrm{MC}}_{e\gamma,\mathrm{signal},i} \cdot \mathrm{SF}_i$	MC Events	$\mathrm{N}^{\mathrm{MC}}_{e\gamma,\mathrm{signal},i} \cdot \mathrm{SF}_i$
$W(e\nu) + \gamma$	0.064	1	0.064±0.064	83	5.270±0.578	99	6.286±0.632
$W(\mu\nu) + \gamma$	0.060	0	0.00±0.060	0	0.00±0.060	0	0.00±0.060
$W(\tau\nu) + \gamma$	0.061	1	0.061±0.061	3	0.183±0.105	3	0.183±0.105
$Z(ee) + \gamma$	0.004	3	0.012±0.007	64	0.252±0.031	76	0.299±0.034
$Z(\mu\mu) + \gamma$	0.004	35	0.138±0.023	5	0.020±0.009	8	0.032±0.011
$Z(\tau\tau) + \gamma$	0.004	25	0.099±0.020	93	0.368±0.038	129	0.511±0.045
$Z(\nu\bar{\nu}) + \gamma$	0.0010	183	0.183±0.013	0	0.00±0.001	0	0.00±0.001
$W(e\nu)$ no ISR/FSR	0.210	0	0.00±0.035	4	0.84±0.42	5	1.05±0.47
$W(\mu\nu)$ no ISR/FSR	0.308 (0.699)	0	0.00±0.051	0	0.00±0.699	0	0.00±0.699
$W(\tau\nu)$ no ISR/FSR	0.296	0	0.00±0.049	0	0.00±0.296	0	0.00±0.296
$Z(ee)$ no ISR/FSR	0.056	0	0.00±0.056	1	0.056±0.056	1	0.056±0.056
$Z(\mu\mu)$ no ISR/FSR	0.088 (0.126)	0	0.00±0.088	0	0.00±0.126	0	0.00±0.126
$Z(\tau\tau)$ no ISR/FSR	0.039	1	0.039±0.039	1	0.039±0.039	1	0.039±0.039
$t\bar{t}$ (incl.)	0.0023	25	0.058±0.012	621	1.453±0.058	739	1.729±0.064

Continued on next page...

Table XXIX – Continued

Background Source	SF_i	EWK $\gamma\gamma + \not{E}_T$ signal		$0.8 < E/p < 1.2$ for $e\gamma$		$0.0 < E/p < 2.0$ for $e\gamma$	
		MC Events	$N^{EWK-MC}_{signal,i} \cdot SF_i$	MC Events	$N^{MC}_{e\gamma,signal,i} \cdot SF_i$	MC Events	$N^{MC}_{e\gamma,signal,i} \cdot SF_i$
$\sum_{i=0}^{n} N^{EWK-MC}_{signal,i} \cdot SF_i$			0.65±0.15				
$N^{MC}_{e\gamma,signal} = \sum_{i=0}^{n} N^{MC}_{e\gamma,signal,i} \cdot SF_i$					8.49±1.06		10.18±1.11
$N^{Data}_{e\gamma,signal}$				12		16	
$\frac{N^{Data}_{e\gamma,signal}}{N^{MC}_{e\gamma,signal}}$				1.41±0.44		1.57±0.43	
The Final EWK Prediction N^{EWK}_{signal} $= \sum_{i=0}^{n} N^{EWK-MC}_{signal,i} \cdot SF_i \cdot \left(\frac{N^{Data}_{e\gamma,signal}}{N^{MC}_{e\gamma,signal}} \right)$		=(0.65±0.15)×(1.41±0.47)					
		0.92±0.21±0.30 (Expected Rate±Stat±Sys)					

TABLE XXX: Summary of the scaled electroweak background estimations after optimization, taken from Table XXIX. Note that we assumed that all the systematic errors are not correlated in their combination.

Background Source	Expected Rate±Stat±Sys
$W(l\nu)+\gamma$	0.176±0.149±0.059
$Z(ll)+\gamma$	0.351±0.044±0.117
$Z(\nu\nu)+\gamma$	0.26±0.03±0.08
$W(l\nu)$ no ISR/FSR	0.0±0.111±0.001
$Z(ll)$ no ISR/FSR	0.055±0.096±0.018
$t\bar{t}$	0.082±0.017±0.027
EWK combined	0.92±0.21±0.30

TABLE XXXI: Summary of the QCD background estimations after optimization. The normalized prediction of the number of events from event reconstruction pathologies is given by $N_{signal}^{PATH} = (N_{signal}^{PATH-MC} - N_{signal}^{MM-MC}) \cdot SF_{QCD}$. To avoid double counting the number of events from energy mismeasurements predicted by the METMODEL it is taken to be $N_{signal}^{MM-MC} = N_{signal}^{no\ \not{E}_T-significance} \cdot R_{\not{E}_T-significance=3}^{exp} = 527 \cdot 0.001$, where $R_{\not{E}_T-significance=3}^{exp} = 0.1\%$, using Equation 6.8, as described in Section VII.A.1. The METMODEL prediction is given by $N_{signal}^{METMODEL} = \frac{N_{signal}^{pseudo}}{N_{pseudo}} = \frac{4}{10} = 0.40 \pm 0.20$ (stat. only). See Section VII.A for a description of the systematic errors.

Background Source	Scale Factor SF_{QCD}	MC Events $N_{signal}^{PATH-MC}$	METMODEL Pred. N_{signal}^{MM-MC}	Normalized Pred. $N_{signal}^{PATH\ /\ METMODEL}$
Pathology	0.134±0.007	1	0.527	0.063±0.092±0.003
METMODEL				0.40±0.20±0.10
Total QCD				0.46±0.22±0.10

TABLE XXXII: Summary of the non-collision background estimations after optimization. The normalized prediction of the beam halo/cosmic ray background rate is given by $N_{signal}^{i} = N_{kinematic}^{i-control} \cdot SF_i$, where i=beam halo or cosmic ray, described in Section VII.C.

Background Source (i)	Total Rejection Fraction (SF_i)	Events Passed ($N_{kinematic}^{i-control}$)	Normalized Pred. (N_{signal}^{i})
Beam Halo	0.008±0.008	0	0.0+0.008±0.001
Cosmic Rays	0.001±0.001	1	0.001±0.001±0.001
Non-Collision			$0.001^{+0.008}_{-0.001} \pm 0.001$

TABLE XXXIII: Summary of the combined background estimations after optimization. Note that the small asymmetric uncertainty is ignored in the total calculation. We have assumed that all the errors are uncorrelated in their combination.

Background Source	Expected Rate±Stat±Sys
Electroweak	0.92±0.21±0.30
QCD	0.46±0.22±0.10
Non-Collision	$0.001^{+0.008}_{-0.001} \pm 0.001$
Total	1.38±0.30±0.32

TABLE XXXIV: The acceptance and expected cross section limits for various simulated GMSB points for the final selection requirements. For completeness both the expected and observed number of events and cross section limits from Chapter IX are included. Note the same analysis is used for all masses and lifetimes up to 2 ns.

$m_{\tilde{\chi}_1^0}$ (GeV/c^2)	$\tau_{\tilde{\chi}_1^0}$ (ns)	Acceptance (%)	Background	σ_{95}^{exp} (fb)	σ_{95}^{obs} (fb)	$\sigma_{95}^{\text{prod}}$ (fb)
70	$\ll 1$	2.04±0.43		81.92	57.20	
70	1	1.85±0.18		90.92	62.99	999.9
70	2	1.41±0.14		124.5	86.30	
80	$\ll 1$	4.29±0.43		40.83	28.22	
80	1	3.71±0.37		45.59	31.51	524.6
80	2	2.82±0.28		60.02	41.48	
90	$\ll 1$	5.12±0.51		32.76	22.65	
90	1	4.42±0.44	Total: 1.38±0.44	38.32	26.48	286.8
90	2	3.48±0.34	(0 observed)	48.60	33.59	
100	$\ll 1$	6.74±0.67		25.12	17.36	
100	1	6.40±0.64	EWK: 0.92±0.37	26.46	18.29	169.0
100	2	4.93±0.49	QCD: 0.46±0.24	34.25	23.67	
110	$\ll 1$	7.08±0.71	Non-Collision:	23.88	16.53	99.47
110	1	7.06±0.71	$0.001^{+0.008}_{-0.001}$	23.95	16.54	
120	$\ll 1$	7.21±0.72		23.97	26.24	
120	2	5.64±0.56		29.97	20.71	58.38
130	$\ll 1$	7.86±0.79		21.90	14.84	
130	1	8.05±0.80		21.40	14.49	36.23
130	2	5.95±0.60		28.44	19.67	
140	$\ll 1$	7.80±0.78		22.62	15.11	
140	1	7.87±0.79		21.94	14.87	22.97
140	2	6.08±0.61		27.86	19.26	
150	$\ll 1$	7.95±0.79		21.25	14.67	14.54

CHAPTER X

DATA, CROSS SECTION LIMITS AND FINAL RESULTS

In this chapter the optimized requirements found in Chapter IX are applied to the data and the signal region is unblinded. No events are observed, consistent with the background expectation of 1.38 ± 0.44 events. This chapter sets cross section limits and shows the exclusion region as a function of $m_{\tilde{\chi}_1^0}$ and $\tau_{\tilde{\chi}_1^0}$ for GMSB models. Expectations for future running are presented in the next chapter.

A. The Data

After all the kinematic requirements listed in Chapter IX there are no events observed in the data. There is a good agreement between the background prediction and the number of events observed. Figures 43-45 show the N-1 kinematic distributions for the background and signal expectations along with the data. The data appears to be well modeled by the background prediction alone.

B. Cross Section Limits and the GMSB Exclusion Region

Figure 46 shows the predicted and observed cross section limits along with the NLO production cross sections and errors (see Table XXVII) as a function of the $\widetilde{\chi}_1^0$ mass at $\tau_{\tilde{\chi}_1^0} \ll 1$ ns and as a function of the $\widetilde{\chi}_1^0$ lifetime at $m_{\tilde{\chi}_1^0} = 140$ GeV/c^2. Indicated in green is the 8.0% uncertainty-band on the production cross section. In yellow we show the expected variation in the expected cross section limit using the results from Table XXVIII and the RMS definition in Eq. 9.3. Since the number of observed events is below expectations the observed limits are slightly better than the expected limits. The $\widetilde{\chi}_1^0$ mass reach, based on the predicted (observed) number of events

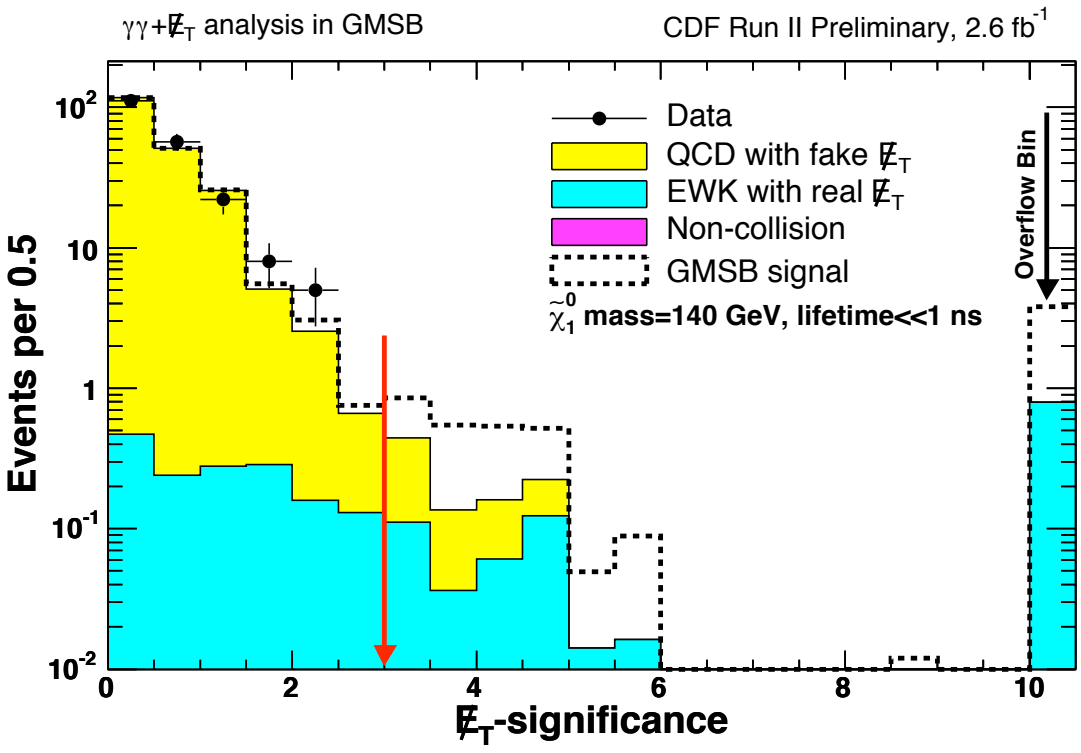

FIG. 43: The same N-1 plot for the $\not\!\!E_T$-significance as Figure 41-(a), but including the data. The $\not\!\!E_T$-significance variable is plotted through the whole region while holding other variables at the optimal cuts. There is no evidence for new physics and the data is well modeled by backgrounds alone.

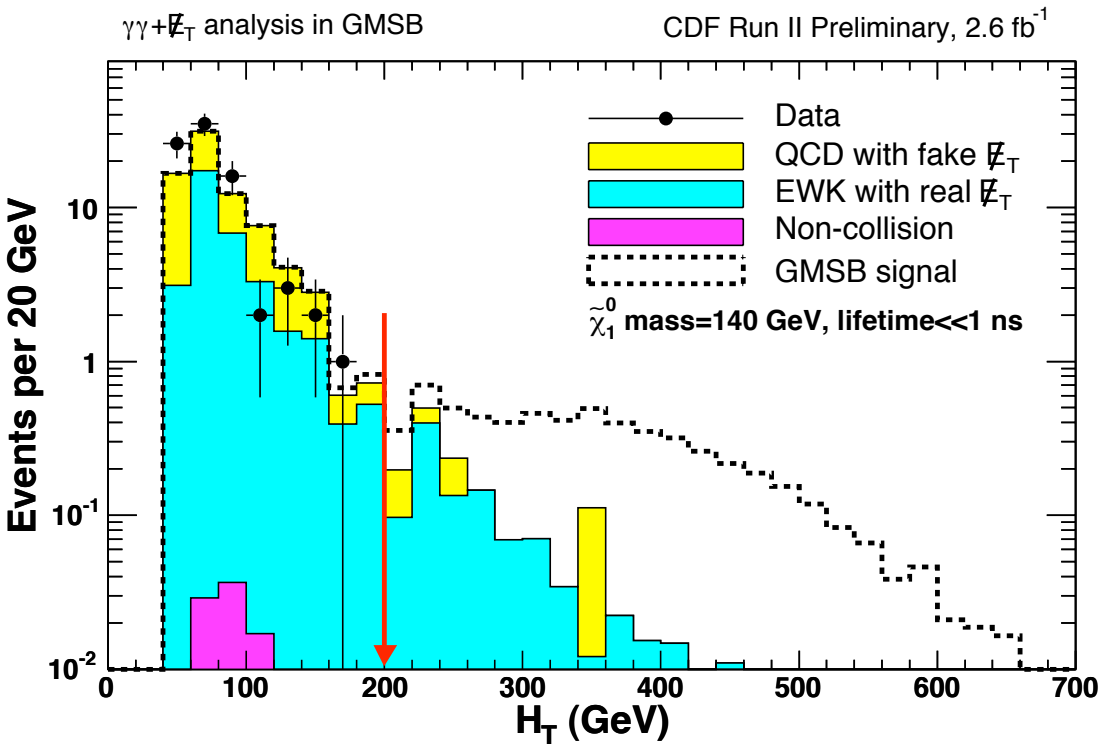

FIG. 44: The same N-1 plot for the H_T as Figure 41-(c), but including the data. The H_T variable is plotted through the whole region while holding other variables at the optimal cuts. There is no evidence for new physics and the data is well modeled by backgrounds alone.

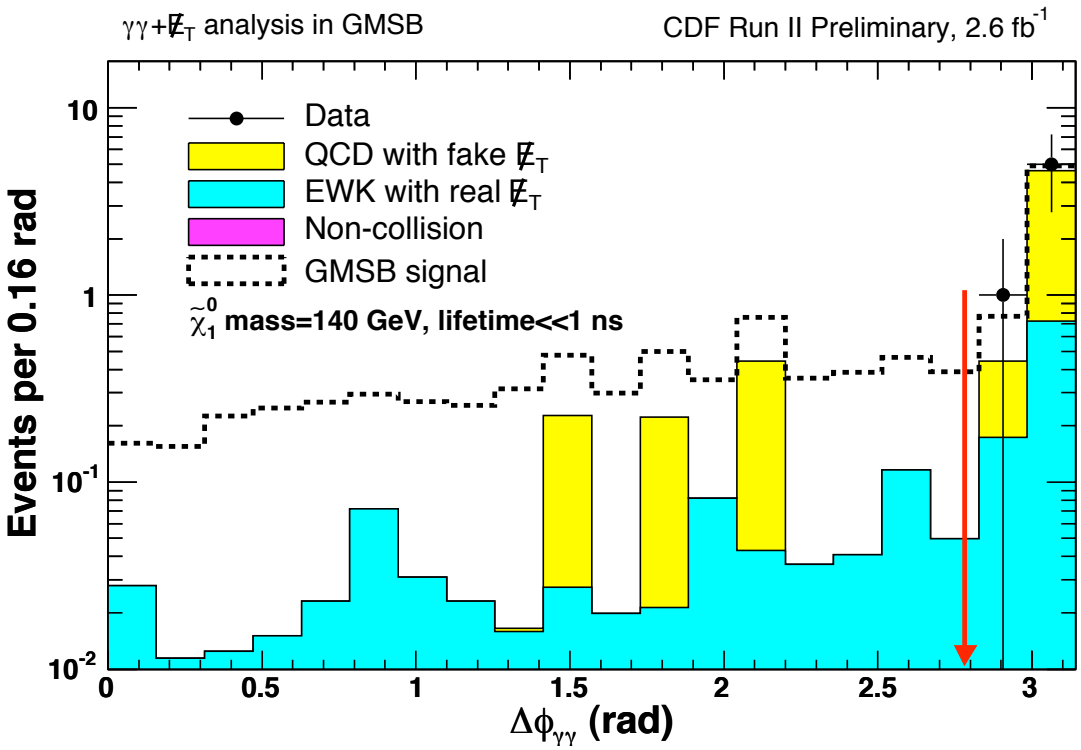

FIG. 45: The same N-1 plot for the $\Delta\phi(\gamma_1, \gamma_2)$ as Figure 41-(e), but including the data. The $\Delta\phi(\gamma_1, \gamma_2)$ variable is plotted through the whole region while holding other variables at the optimal cuts. There is no evidence for new physics and the data is well modeled by backgrounds alone.

is 141 GeV/c^2 (149 GeV/c^2), at a lifetime below 1 ns. Lifetimes above 2 ns are not considered for the reasons mentioned in Section VIII.A as well as the expectation that most of the parameter space in high lifetimes there should be excluded by searches in single delayed photon analysis [17, 19]. Fig. 47 shows the 95% C.L. NLO exclusion region as a function of mass and lifetime of $\widetilde{\chi}_1^0$ using the fixed choice of cuts from the optimization for both for the predicted and observed number of background events. These limits extend the reach beyond the delayed photon results [19], well beyond those of DØ search at $\tau_{\tilde{\chi}_1^0} \ll 1$ ns [21] and the limits from ALEPH/LEP [18]. They are currently the world's best.

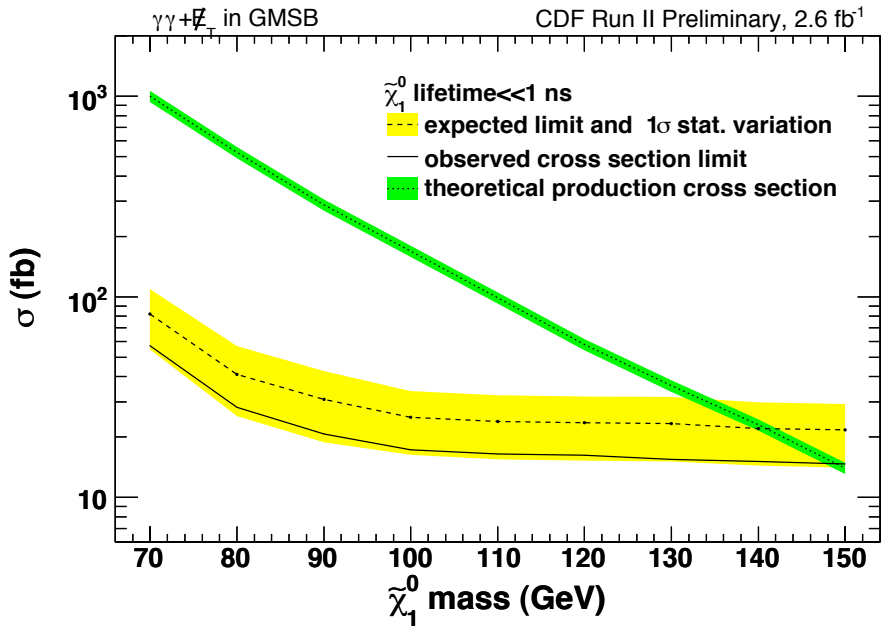

(a)

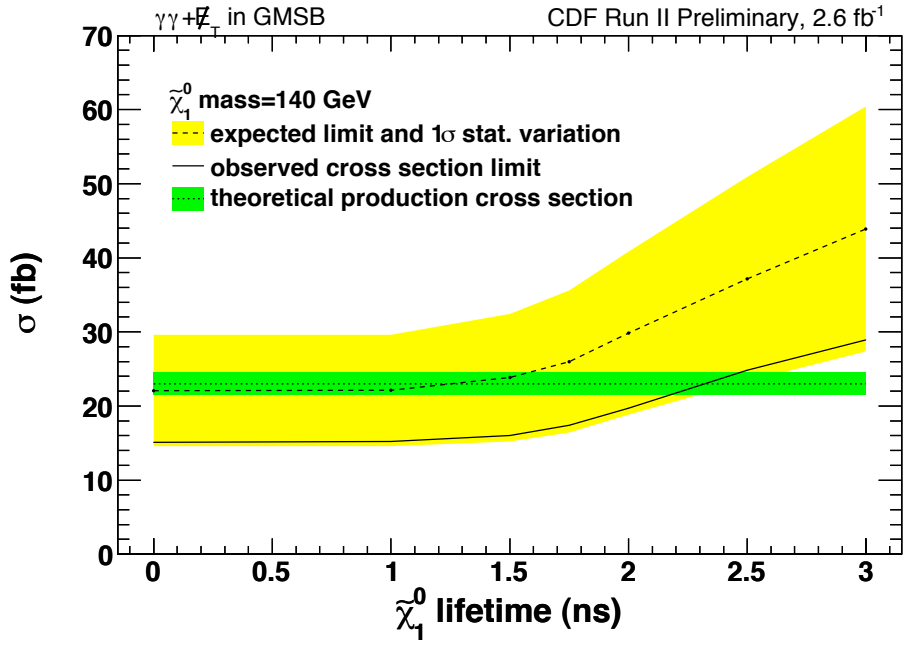

(b)

FIG. 46: The predicted and observed cross section limits as a function of the $\tilde{\chi}_1^0$ mass at $\tau_{\tilde{\chi}_1^0} \ll 1$ ns (a) and as a function of the $\tilde{\chi}_1^0$ lifetime at a mass of 140 GeV/c^2 (b). Indicated in yellow is the RMS variation on the expected cross section limit and in green is the 8.0% uncertainty-band for the production cross section (see Table XXVII).

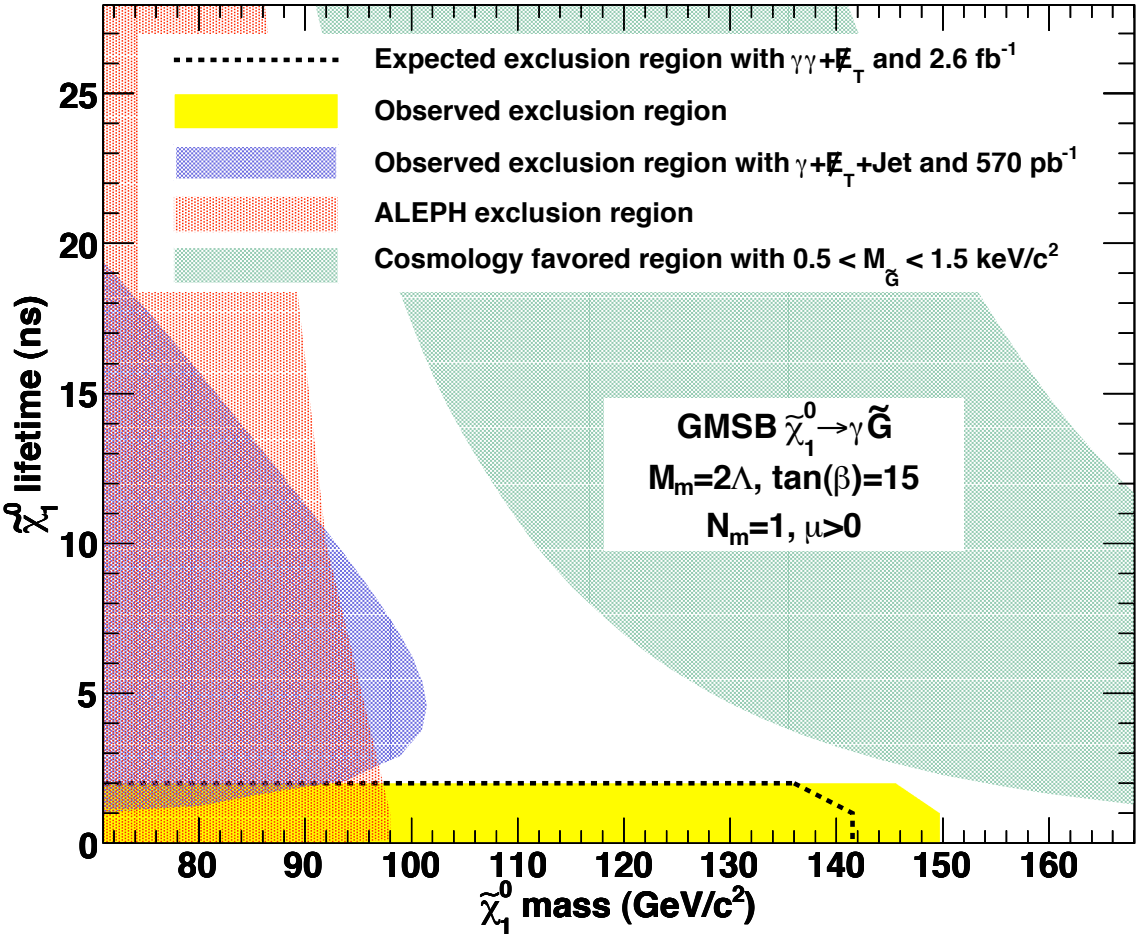

FIG. 47: The predicted and observed exclusion region along with the limit from ALEPH/LEP [18] and the $\gamma + \not\!\!E_T + jet$ delayed photon analysis [19]. We have a mass reach of 141 GeV/c^2 (predicted) and 149 GeV/c^2 (observed) at the lifetime up to 1 ns. The green shaded band shows the parameter space where $0.5 < m_{\tilde{G}} < 1.5$ keV/c^2, which is favored in cosmologically consistent models [35].

CHAPTER XI

CONCLUSION

A. Summary of the Search

This dissertation has presented a search for supersymmetry with gauge mediated SUSY breaking in a sample of $\gamma\gamma + \not\!\!E_T$ events from $p\bar{p}$ collisions at $\sqrt{s} = 1.96$ TeV using the CDF II detector. This analysis is optimized for the search for high mass, low lifetime neutralinos, as expected in cosmology favored regions. This analysis is a significant improvement over previous searches and it has the further advantage that it considers non-negligible lifetimes of the $\widetilde{\chi}_1^0$. The experimental improvements such as selecting candidate events using a $\not\!\!E_T$-significance and rejecting events with the new EMTiming system and a full optimization procedure shows a significant impact on the sensitivity. Using 2.59 fb^{-1} of data collected during 2004-2008 at the Fermilab Tevatron no events were found, which is consistent with the background estimate of 1.38 ± 0.44 events. Since there is no evidence for new physics we have set cross section limits and made an exclusion region for a gauge mediated supersymmetry model with $\widetilde{\chi}_1^0 \to \gamma\widetilde{G}$ in the $\widetilde{\chi}_1^0$ lifetime vs. mass plane, with a mass reach of 149 GeV/c^2 for $\widetilde{\chi}_1^0$ lifetime up to 1 ns. These results significantly extend the world sensitivity to these models beyond all other previous searches [18, 20, 21].

This exclusion region is also approaching an important region of parameter space where the $\widetilde{G}$ is predicted to be thermally produced in the early universe with a mass of 0.5-1.5 keV/c^2 as described in Section I.B.2.c.

B. Future Prospects

To investigate the prospects of a search at higher luminosity we calculate the expected cross section limits assuming all backgrounds scale linearly with luminosity while their uncertainty fractions remain constant. Figure 48 shows the predicted exclusion region for a luminosity of 10 fb^{-1}. For higher lifetimes, above $\sim$2 ns, the next generation delayed photon analysis will extend the sensitivity taken from Ref. [19]. At that point we expect these results will be combined for completeness. Another improvement that future versions of this analysis could employ would be to remove the χ^2_{CES} requirement so the sensitivity we can be more readily extended to higher lifetimes. However, this would require that another trigger, like the one used in the delayed photon search, as it did not have this requirement on it.

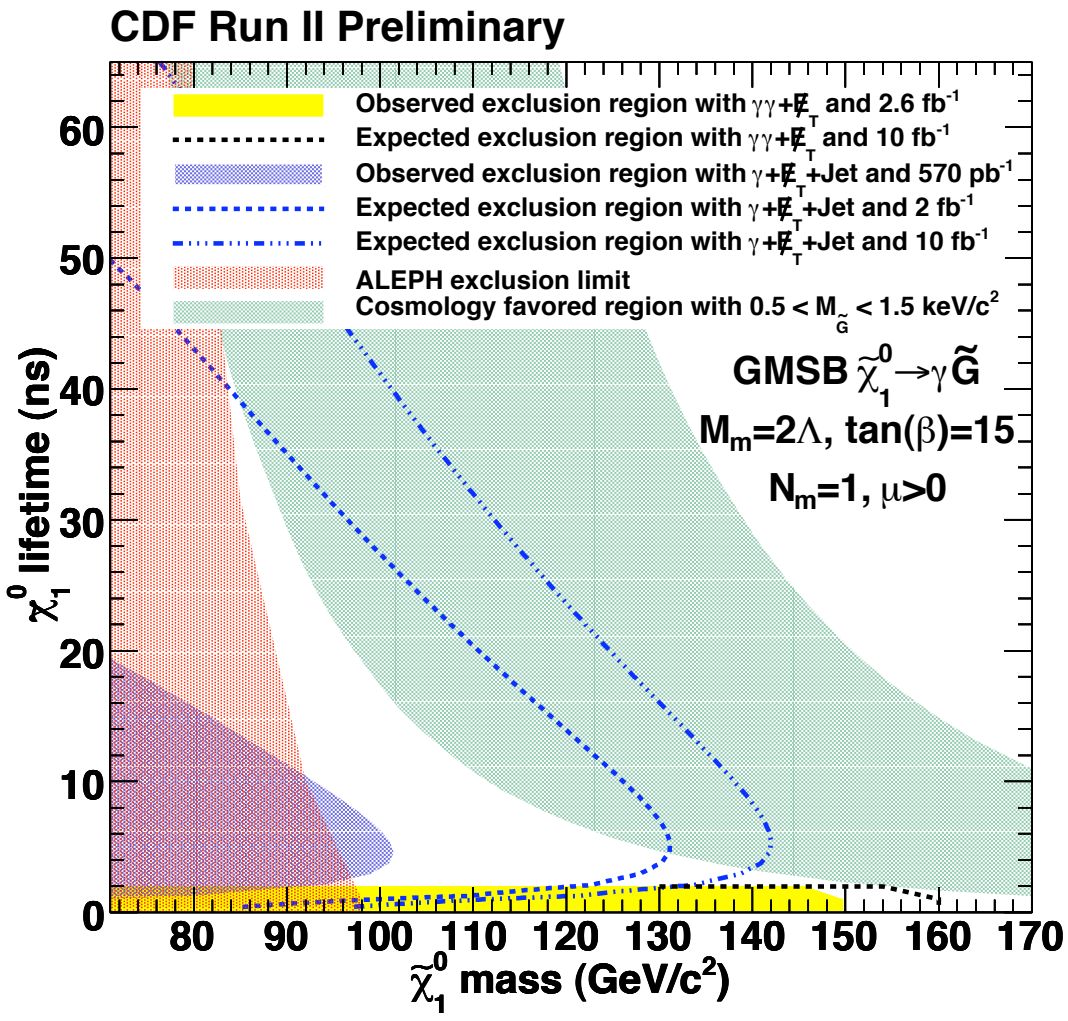

FIG. 48: The black dashed line shows the prediction of the exclusion region limit after a scaling of the background prediction and the uncertainties for a luminosity of 10 fb^{-1}, which is the expected full CDF Run II data taking. The blue dashed lines show the prediction of the exclusion region limits from the delayed photon analysis for a luminosity of 2 fb^{-1} and 10 fb^{-1}, respectively, as taken from Ref. [19] and the red region is taken from ALEPH/LEP limits [18].

REFERENCES

[1] S. Weinberg, *The Quantum Theory of Fields* (Cambridge Univ. Pr., Cambridge, UK, 1995-2000), Vols. 1-3.

[2] P. W. Higgs, Phys. Rev. Lett. **13**, 508 (1964), F. Englert and R. Brout, Phys. Rev. Lett. **13**, 321 (1964).

[3] S. Weinberg, Phys. Rev. D **13**, 974 (1976), Phys. Rev. D **19**, 1277 (1979); E. Gildener, Phys. Rev. D **14**, 1667 (1976); L. Susskind, Phys. Rev. D **20**, 2691 (1979).

[4] S. Weinberg, in *Gauge Theories and Modern Field Theory*, edited by R. Arnowitt and P. Nath (MIT Press, Cambridge, Massachusetts, 1976).

[5] M. Veltman, Acta Phys. Polon. B **8**, 475 (1977).

[6] R. Dashen and H. Neuberger, Phys. Rev. Lett. **50**, 1897 (1983); K. Wilson, Phys. Rev. B **4**, 3184 (1971).

[7] S. Weinberg, Phys. Rev. Lett. **36**, 294 (1976); S. Coleman and S. Weinberg, Phys. Rev. D **7**, 188 (1973).

[8] B. W. Lee, C. Quigg and H. B. Thacker, Phys. Rev. D **16**, 1519 (1977).

[9] For a good review of supersymmetry, see, for example, S. P. Martin, arXiv:hep-ph/9709356; H. P. Nilles, Phys. Rept. **110**, 1 (1984); H. E. Haber and G. L. Kane, Phys. Rept. **117**, 75 (1985).

[10] C. Amsler *et al.* (Particle Data Group), Phys. Lett. B **667**, 1 (2008).

[11] G. Hinshaw *et al.*, Astrophys. J. Suppl. **180**, 225-245 (2009).

[12] At CDF, and other collider experiments, the collision occurs with no momentum in the plane transverse to the collision. By conservation of momentum the vector sum of the momenta of the final state particles must be zero in the transverse plane. Since the energies of most final state particles are measured by the detector, any imbalance of energy could indicate the presence of a particle, such a neutrino, which does not interact with the detector. This imbalance is known as missing transverse energy ($\not\!\!E_T$).

[13] D. Toback, Ph.D thesis, University of Chicago, FERMILAB-THESIS-1997-36 (1997); F. Abe, *et al.* (CDF Collaboration), Phys. Rev. Lett. **81** 1791 (1998); F. Abe, *et al.* (CDF Collaboration), Phys. Rev. D **59** 092002 (1999).

[14] S. Dimopoulos, S. Thomas, and J. Wells, Nucl. Phys. B **488**, 39 (1997); S. Ambrosanio, G. Kribs, and S. Martin, Phys. Rev. D **56**, 1761 (1997); G. Giudice and R. Rattazzi, Phys. Rep. **322**, 419 (1999); S. Ambrosanio, G. Kane, G. Kribs, S. Martin, and S. Mrenna, Phys. Rev. D **55**, 1372 (1997).

[15] C. H. Chen and J. F. Gunion, Phys. Rev. D **58**, 075005 (1998).

[16] See, for example, M. Strassler and K. Zurek, Phys. Lett. B **651**, 374 (2007); M. Strassler and K. Zurek, arXiv:hep-ph/0607160.

[17] D. Toback and P. Wagner, Phys. Rev. D **70**, 114032 (2004).

[18] A. Heister *et al.* (ALEPH Collaboration), Eur. Phys. J. C **25**, 339 (2002); A. Garcia-Bellido, Ph.D. thesis, Royal Holloway University of London (2002) (unpublished), arXiv:hep-ex/0212024; also see L3 Collaboration, arXiv:hep-ex/0611010; G. Abbiendi *et al.* (OPAL Collaboration), Proc. Sci. HEP2005 346 (2006); J. Abdallah *et al.* (DELPHI Collaboration), Eur. Phys. J. C **38**, 395 (2005).

[19] P. Wagner, Ph.D thesis, Texas A&M University, FERMILAB-THESIS-2007-14 (2007); A. Abulencia *et al.* (CDF Collaboration), Phys. Rev. Lett. **99**, 121801 (2007); T. Aaltonen *et al.* (CDF Collaboration), Phys. Rev. D **78**, 032015 (2008).

[20] D. Acosta *et al.* (CDF Collaboration), Phys. Rev. D **71**, 031104 (2005).

[21] V. Abazov *et al.* (DØ Collaboration), Phys. Lett. B **659**, 856 (2008).

[22] J. Scherk and J. Schwarz, Nucl. Phys. B **81**, 118 (1974).

[23] S. Weinberg, Phys. Rev. D **26**, 287 (1982); G. R. Farrar and S. Weinberg, Phys. Rev. D **27**, 2732 (1983); S. Dawson, Nucl. Phys. B **261**, 297 (1985).

[24] S. Dimopoulos, M. Dine, S. Raby, S. Thomas and J. Wells, Nucl. Phys. Proc. Suppl. A **52**, 38 (1997).

[25] See for example, R. Arnowitt and P. Nath, arXiv:hep-ph/9708254 and references therein.

[26] N. Vittorio and J. Silk, Astrophys. Journal, Part 2-Letters to the Editor **285**, L39-L43 (1984).

[27] J. L. Feng and T. Moroi, Phys. Rev. D **58**, 035001 (1998).

[28] U. Sarid and S. Thomas, Phys. Rev. Lett. **85**, 1178 (2000).

[29] S. Schael *et al.*, Eur. Phys. J. C **47**, 547 (2006).

[30] G. W. Bennett *et al.* (Muon $(g-2)$ Collaboration), Phys. Rev. Lett. **92**, 161802 (2004); S. Baek, P. Ko and W. Song, J. High Energy Phys. **03**, 054 (2003).

[31] We follow B. C. Allanach *et. al.*, Eur. Phys. J. C **25**, 113 (2002), The parameters $c_{\rm Grav}$ (gravitino mass factor) and Λ (supersymmetry breaking scale) are allowed to vary.

[32] H. Pagels and J. R. Primack, Phys. Rev. Lett. **48**, 223 (1982); D. N. Spergel *et al.*, Astrophys. J. Suppl. **148**, 175 (2003).

[33] S. Khalil, C. Munoz and E. Torrente-Lujan, New J. Phys. **4**, 27 (2002); A. Arbey and F. Mahmoudi, Phys. Lett. B **669**, 46 (2008).

[34] T. Moroi, H. Murayama, and M. Ynmaguchi, Phys. Lett. B **303**, 289 (1993).

[35] P. Bode, J. Ostriker and N. Turok, Astrophys. J. **556**, 93 (2001).

[36] J. Feng, Phys. Rev. D **70**, 075019 (2004), and references therein.

[37] M. Carena *et al.*, Rev. Mod. Phys. **71**, 937 (1999).

[38] T. Sjöstrand *et al.*, Comput. Phys. Commun. **135**, 238 (2001). We use version 6.216.

[39] W. Beenakker *et al.*, Phys. Rev. Lett. **83**, 3780 (1999).

[40] P. Simeon and D. Toback, J. Undergrad. Research in Phys. 20, 1 (2007).

[41] B. Abbott *et al.* (DØ Collaboration), Phys. Rev. Lett. **80**, 442 (1998).

[42] M. Goncharov *et. al.*, Nucl. Instr. Meth. A**565**, 543 (2006).

[43] T. Aaltonen *et al.* (CDF Collaboration), submitted to Phys. Rev. D. (arXiv:0910.5170).

[44] T. Aaltonen *et al.* (CDF Collaboration), Phys. Rev. Lett. **104**, 011801 (2010).

[45] Tevatron Accelerator Division, "Operations Rookie Books," http://www-bdnew.fnal.gov/operations/rookie_books/rbooks.html.

[46] Fermilab Beams Division, Run II Handbook (1998), http://www-bd.fnal.gov/runII/index.html.

[47] Fermilab Visual Media Services, Graphic Arts Gallery, http://www-visualmedia.fnal.gov (accessed 2009).

[48] A. Bhatti *et al.*, Nucl. Instrum. Methods Phys. Res., Sect. A **566**, 375 (2006).

[49] J. Elias *et al.*, Nucl. Instrum. Methods Phys. Res., Sect. A **441**, 366 (2000); D. Acosta *et al.*, Nucl. Instrum. Methods Phys. Res., Sect. A **461**, 540 (2001); S. Klimenko, J. Konigsberg and T. M. Liss, FERMILAB-FN-0741 (2003); The systematic uncertainty on the luminosity is measured with major contributions from the uncertainties on the CLC acceptance from the precision of the event generator and the detector simulation and the event generator and is standard for all measurements done with the CDF detector.

[50] CDF Run IIb detector upgrade projects, http://www-cdf.fnal.gov/run2b.html.

[51] R. Blair *et al.* (CDF Collaboration), FERMILAB-PUB-96-390-E.

[52] D. Acosta *et al.* (CDF Collaboration), Phys. Rev. D **71**, 032001 (2005).

[53] C. S. Hill *et al.* (CDF Collaboration), Nucl. Instrum. Meth. A **530**, 1 (2004).

[54] A. Sill *et al.* (CDF Collaboration), Nucl. Instrum. Meth. A **447**, 1 (2000).

[55] A. A. Affolder *et al.* (CDF Collaboration), Nucl. Instrum. Meth. A **453**, 84 (2000).

[56] A. A. Affolder *et al.* (CDF Collaboration), Nucl. Instrum. Meth. A **526**, 249 (2004).

[57] See, for example, F. Abe *et al.* (CDF Collaboration), Phys. Rev. Lett. **68**, 1104 (1992). For a discussion of the jet energy measurements, see T. Affolder *et al.*

(CDF Collaboration), Phys. Rev. D **64**, 032001 (2001). For a discussion of standard jet correction systematics, see Ref. [48].

[58] G. Gomez-Ceballos *et al.*, Nucl. Instrum. Meth. A **518**, 522 (2004).

[59] S. D'Auria *et al.*, CDF Report No. CDF-NOTE-7055 (2004), unpublished.

[60] R. Field, CDF Report No. CDF-NOTE-8876 (2007), unpublished.

[61] The standard GEANT-based detector simulation [R. Brun *et al.*, CERN-DD/EE/84-1 (1987)] is used. For more details on the *cdfSim*, see http://www-cdf.fnal.gov/cdfsim/cdfsim_main.html.

[62] Y. Liu, Ph.D. thesis, Universitè de Genéve, FERMILAB-THESIS-2004-37 (2004).

[63] The two towers that cover the region $75^\circ < \phi < 90^\circ$ and $0.77 < \eta < 1.0$ contain the solenoid cooling pipe ("chimney") are also excluded.

[64] A. Abulencia *et al.* (CDF Collaboration), Phys. Rev. D **75** 112001 (2007).

[65] D. Acosta *et al.* (CDF Collaboration), Phys. Rev. D **71** 051104 (2005).

[66] C. Group, R. Culbertson and J. Ray, CDF Report No. CDF-NOTE-9429 (2008), unpublished.

[67] A. Goshaw *et al.*, CDF Report No. CDF-NOTE-6838 (2004), unpublished.

[68] τ-leptons can decays into lighter leptons for example via $\tau^\pm \to e^\pm \nu_e \nu_\tau$ or $\tau^\pm \to \mu^\pm \nu_\mu \nu_\tau$ ("leptonically"), or into one or more pions as $\tau^\pm \to \pi^\pm \nu_\tau$ or $\tau^\pm \to \pi^\pm \pi^\mp \pi^\pm \nu_\tau$ (hadronically). While there are more efficient ways at CDF to identify hadronic taus (see A. Safonov, Nucl. Phys. Proc. Suppl.**144**, 323 (2005)), they can also be identified as jets, see Ref. [57].

[69] F. Abe *et al.* (CDF Collaboration), Phys. Rev. D **45**, 1448 (1992).

[70] T. Aaltonen *et al.* (CDF Collaboration), Phys. Rev. D **79**, 052007 (2009).

[71] B. Blair *et al.*, CDF Report No. CDF-NOTE-5788 (2001), unpublished.

[72] Trigger towers encompass $0.2 \times 15^\circ$ in $\eta - \phi$ space.

[73] For experts only, this is the good run list v.23 from the CDF *Photon* group. Note that SMX stands for Shower Maximum: the point in a calorimeter at which the particle shower is expected to be at a maximum. A position detector palced there improves resolution of the calorimeter clusters.

[74] For experts only, this is periods 1 to 17 and the integrated luminosity is obtained from the offline database and scaled by the 1.019 correction factor.

[75] See, for example, D. Acosta *et al.* (CDF Collaboration), Phys. Rev. Lett. **94**, 211801 (2005).

[76] R. Culbertson, M. Goncharov and A. Pronko, CDF Report No. CDF-NOTE-9184 (2008).

[77] We use "cdfpstn:pydjmb18" dataset;
http://www-cdf.fnal.gov/internal/physics/qcd/qcdmc5/.

[78] We use "cdfpstn:pyzjt20" dataset;
http://www-cdf.fnal.gov/internal/physics/qcd/qcdmc5/.

[79] The Landau distribution function is defined as $Landau(x) = \frac{1}{2\pi i}\int_{c-i\infty}^{c+i\infty} e^{s\ln s + xs}\, ds$, where c is a positive real number. For numerical purposes it is more convenient to use the equivalent from of the integral, $Landau(x) = \frac{1}{\pi}\int_0^\infty e^{-t\ln t - xt}\sin(\pi t)\, dt$, where both t and s are unitless.

[80] This is an educated guess based on a fact that the CEM ϕ-cracks alone account for $\sim$8% of the CEM area. This number is not used in the analysis, rather it is just given as a value that indicates to the reader the magnitude that this is an important background.

[81] We use "cdfpstn:gx0s1g" dataset; http://www-cdf.fnal.gov/internal/physics/photon/docs/mclist.html.

[82] U. Baur, T. Han, and J. Ohnemus, Phys. Rev. D **48**, 5140 (1993); U. Baur, T. Han, and J. Ohnemus, *ibid.* **57**, 2823 (1998); The $W\gamma$ and $Z\gamma$ processes are simulated using the leading-order BAUR event generator with a k-factor fixed at 1.36. Initial and final state radiation (resulting in additional jets or photons), underlying event, and additional interactions are simulated using PYTHIA [38].

[83] We require the photon to have the $E_T > 7$ GeV and $|\eta| < 1.5$ to generate $Z(\nu\bar{\nu}) + \gamma$ sample.

[84] $4 \cdot \sigma_{\Delta \mathrm{T}}$ is used, but since no events are found in this region it is extended to $5 \cdot \sigma_{\Delta \mathrm{T}}$ to overestimate this background.

[85] T. Junk, Nucl. Instrum. Methods A **434**, 435 (1999).

[86] We use the PYTHIA [38] event generator with the GEANT-based detector simulation, *cdfSim*, of *cdfsoft* release 6.1.4 with default settings. The full GMSB model is simulated with the setting MSEL=39 [38].

[87] The detector calibrations of data taking periods from p1 to p13 are used and all GMSB MC samples are properly simulated with tune-A and Min-Bias to implement multiple collision with underlying events effects.

[88] M. Goncharov, V. Krutelyov, D. Toback and P. Wagner, CDF Report No. CDF-NOTE-7928 (2006), unpublished.

[89] F. Paige and S. Protopopescu, BNL Report BNL38034, 1986; F. Paige, S. Protopopescu, H. Bear and X. Tata, hep-ph/0001086. Version 7.64 is used to generate the SUSY masses.

[90] M. Dorigo and S. Yu, CDF Report No. CDF-NOTE-9533 (2009), unpublished.

[91] C. Group, R. Culbertson and J. Ray, CDF Report No. CDF-NOTE-9429 (2008), unpublished; M. McFarlane, H. Bachacou, J. Nielsen and W. Yao, CDF Report No. CDF-NOTE-7682 (2005).

[92] CDF Joint Group Agenda, Procedures for Estimating Uncertainties due to Initial and Final State Radiation, http://www-cdf.fnal.gov/internal/physics/joint_physics/agenda/20050527-minutes.html (accessed 2009).

[93] CDF Jet and Energy Resolution Group, http://www-cdf.fnal.gov/internal/physics/top/jets/corrections.html (accessed 2009).

[94] O. Gonzalez and C. Rott, CDF Report No. CDF-NOTE-7051 (2005), unpublished; J. Pumplin *et al.*, J. High Energy Phys. **0207**, 012 (2002); J. Huston *et al.*, J. High Energy Phys. **0310**, 046 (2003).

[95] W. Beenakker, R. Hopker, M. Spira, and P. M. Zerwas, Nucl. Phys. B **492**, 51 (1997).

[96] E. Boos, A. Vologdin, D. Toback, and J. Gaspard, Phys. Rev. D **66**, 013011 (2002).

[97] S. Kopp, Int. J. Mod. Phys. A **10**, 4413 (1995); M. Coca and E. Halkiadakis, CDF Report No. CDF-NOTE-6580 (2004), unpublished.

APPENDIX A

THE ELECTRON IDENTIFICATION VARIABLES

Electrons in the central calorimeter are identified using methods which are similar to those used to identify photons. We listed the identification of electrons using two different sets of requirements in Tables VII and XXII. The calorimeter cluster requirements (fiduciality, energy isolation, transverse profile $\chi^2_{\rm CES}$ test, ratio of hadronic to EM energy) are similar and the E_T measurement is identical to photons (see Section III.A). Since photons and electrons will produce different distributions of these variables and others in this appendix we describe in more detail the variables used that are not part of the photon ID criteria or ones that are used differently. For a good description of electron identification see Ref [97]. They are:

- The $E_{\rm Had}/E_{\rm Em}$ requirements are typically tighter for electrons than for photons as electrons can start showering earlier than photons into the EM calorimeter.

- A lateral sharing variable, $Lshr$, compares the energy that the electron candidate deposits in neighboring towers (in η) in the same wedge to that expected from test beam data to help discriminate it from hadronic showers. This variable is not used for photons since there is no track to positively identify the incident angle of the photon at the face of the calorimeter.

- The highest-p_T track that is extrapolated to the CES position is compared to the measured position of the shower max. Electrons criteria typically include requirements that the position be within 3 cm in z (Δz) and a charge dependent distance in (r, ϕ) (Δx) of the CES shower position due to the bending of the particle trajectory in the magnet field.

- The track must have at least three axial and stereo superlayers with greater than 5 hits to ensure a good track quality.

- The E/p requirement matches the track momentum to the calorimeter energy to reduce the misidentification due to conversions of $\gamma \to e^+e^-$.

- The track is required to originate from the most probable collision region, $|z_{\rm trk} - z_{\rm vx}| < 2$ cm and $|t_{\rm trk} - t_{\rm vx}| < 1.3$ ns, as well as be less than 60 cm away from the center of the detector, $|z_{\rm trk}| < 60$ cm.

- Electrons coming from photon conversion are removed. The conversion algorithm looks for a pair of opposite sign tracks with $|\Delta x| < 0.2$ cm and $|\Delta \cot\theta| < 0.04$.

The standard versions of both the tight and loose ID requirements are summarized in Table VII in Section III.B. The photon-like electron ID requirements for $e\gamma$ samples are described in Table XXII in Section VII.B.

APPENDIX B

MORE ON THE JET ENERGY SCALE

In this appendix we describe the various corrections to the jet energy measurements that were described in Chapter IV in more detail. We also discuss the sources of systematic error as they are important in our evaluations of the $\not\!\!E_T$ resolution as well as in the systematic error on the acceptance. We describe the mean measurement of the jets as well as how we estimate the systematic uncertainties on the jet energy measurement. This discussion follows those of Ref. [57].

- η-dependency (relative energy corrections): corrects for the calorimeter response near the gaps at $\eta = 0$ and $\eta = 1.1$ and the response difference between the central and plug calorimeters. The η-dependent corrections are introduced to minimize the η-dependence of the calorimeter response. The systematic uncertainty varies with the E_T of the jet between 0.5% and 2.5% in the region $|\eta| < 2.1$.

- Multiple interactions: corrects for the energy from additional collisions in the same event ("pile-up") that is deposited in the 0.4 cone of the jet cluster. After the correction an uncertainty on the slope of 150 MeV remains per additional vertex.

- Absolute energy scale: transforms the jet energy measured in the calorimeter into the energy corresponding to the original particles in the jet. The uncertainties are estimated using the differences between MC and data, in particular the calorimeter response to single particles (∼3%), differences in hadronization modelling between MC's (PYTHIA [38], BAUR [82], etc.) (1%) and stability of the calorimeter calibrations (0.5%).

- Underlying event: corrects for jet energy that falls into the cone that is not from the jets, but is rather from spectator quarks and initial state QCD radiation. The uncertainty is not well understood and different MC generators give different results. We take differences in MC generators of up to 28% are taken as systematic uncertainty which corresponds to ≈ 0.11 GeV for a cone size of 0.4.

- Energy out-of-cone (OOC): corrects for radiation and hadronization effects that can cause a fraction of the jet energy to be deposited outside the jet reconstruction cone of 0.4. These are detector independent and corrected for on-average. Differences between MC and data are taken as systematic uncertainty. They are $\sim$3% at $\sim$15 GeV, decreasing with increasing E_T.

APPENDIX C

TRIGGER EFFICIENCY AND LUMINOSITY EFFECTS ON THE ACCEPTANCE

A. Trigger Efficiency for GMSB Signal

In this analysis diphoton candidate events are selected from the subsample of events that pass any one of the four triggers, described in Tables IX and X. If they did not pass one of the four triggers, this would introduce an inefficiency in our analysis and make our search less sensitive. Therefore it is important to estimate the fraction of our GMSB signal events that would pass the combination of the four triggers, after the final kinematic requirements. Figure 49 shows the E_T distributions of both photons in GMSB MC signal after the final kinematic requirements. With the combination of four triggers (see Section V.A) we see that over 99% of the events with photons with the second highest have $E_T > 13$ GeV. For this reason a trigger efficiency is taken of 100% with negligible error [90].

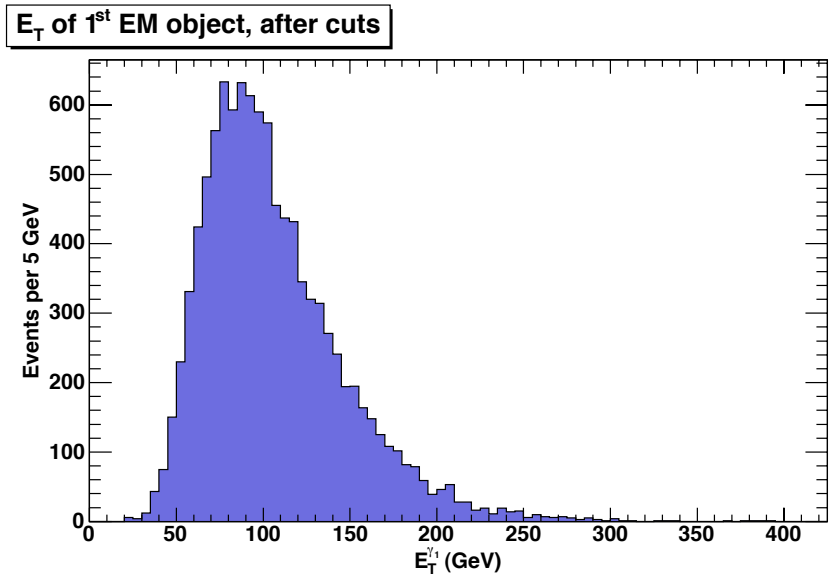

(a)

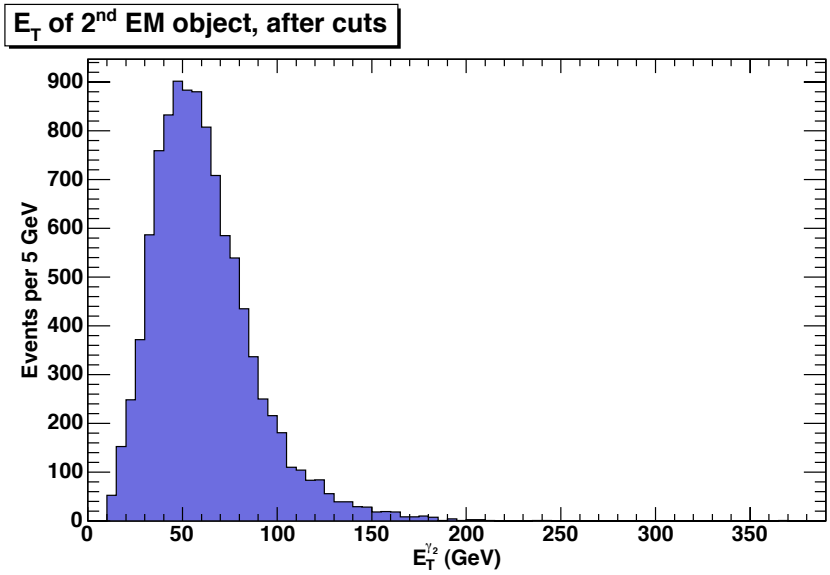

(b)

FIG. 49: The photon E_T distributions for GMSB signal with $m_{\tilde{\chi}_1^0} = 140$ GeV/c^2 and $\tau_{\tilde{\chi}_1^0} \ll 1$ ns after the final kinematic requirements. We note that more than 99% of our isolated diphoton candidates are well above our $E_T > 13$ GeV threshold. This is important because it means that our trigger paths, which requires two photons above 13 GeV, is 100% efficient when taken in conjunction with the other triggers.

B. Luminosity Effects on the Acceptance

The GMSB signal acceptance is estimated using a "run condition-dependent" MC simulation that takes into account the different detector responses for different data taking periods ("run period")[1]. To check that our our signal acceptance does not have any significant dependence on the instantaneous luminosity or other such effects we calculate the acceptance for the different portions of the data taking period to see if and how they vary. Figure 50 shows the acceptance curve as a function of data taking period. While the linear fit finds a small slope, we note that it is consistent with zero (flat) slope within statistical errors. We observe no acceptance dependence on the luminosity, thus we ignore additional systematics due to the fact that we have not simulated the data taking conditions for the last 30% of the data taking which have, on average, higher instantaneous luminosity. Note that most points are above the final acceptance for the whole run periods, (7.8±0.8)%, but the preponderance of the luminosity is in the later run periods.

[1]We use run periods 1 to 13 only.

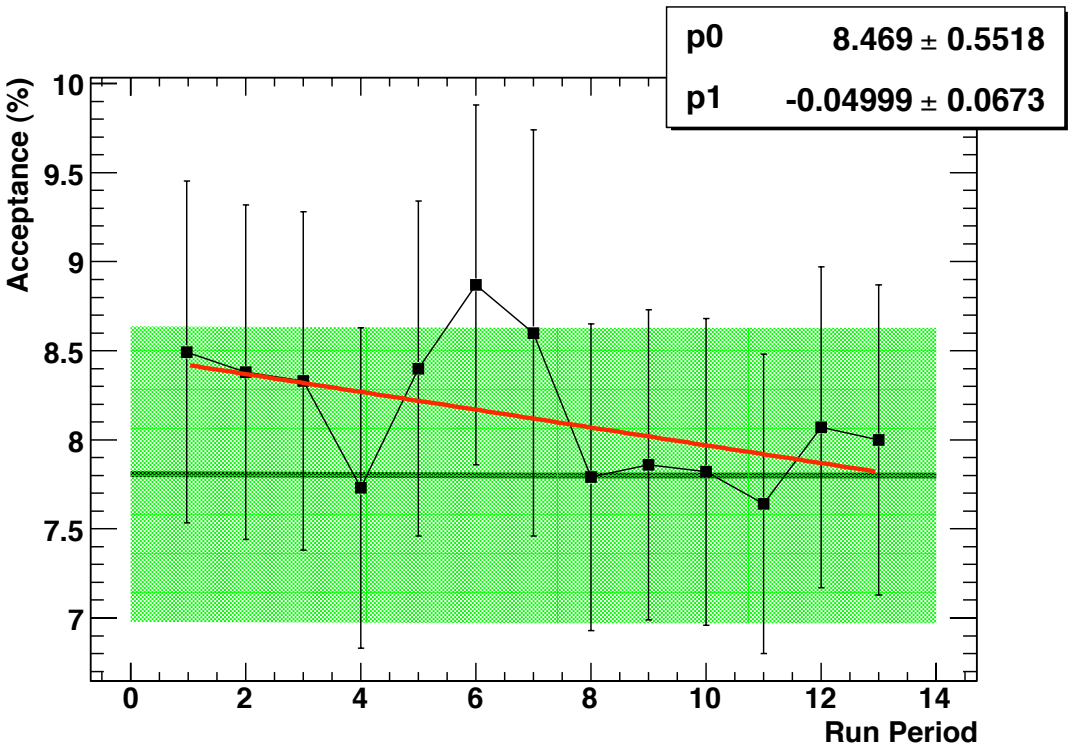

FIG. 50: The signal acceptance as a function of luminosity with only statistical errors. Each data taking period (run period) is effectively about $1/13^{\text{th}}$ of the first part of the data, but with more luminosity for later run periods. The slope (red solid line) from a linear fit has a small slope, but it is consistent with zero within uncertainty. The green solid band indicates the total signal acceptance, (7.8±0.8)%, as described in Chapter IX. Note that the mean value of the fitted value is not equal to 7.8% because the points do not reflect equal amounts of data taking; more of the data is in later data taking periods.

APPENDIX D

PRL FIGURES

Here we show the figures that were published in the PRL that corresponds to this analysis [44]. Note that they are the same content as Figures 39-(b), 43-(c), 46, and 47, but with PRL formatting. We have included the captions as they appear in PRL.

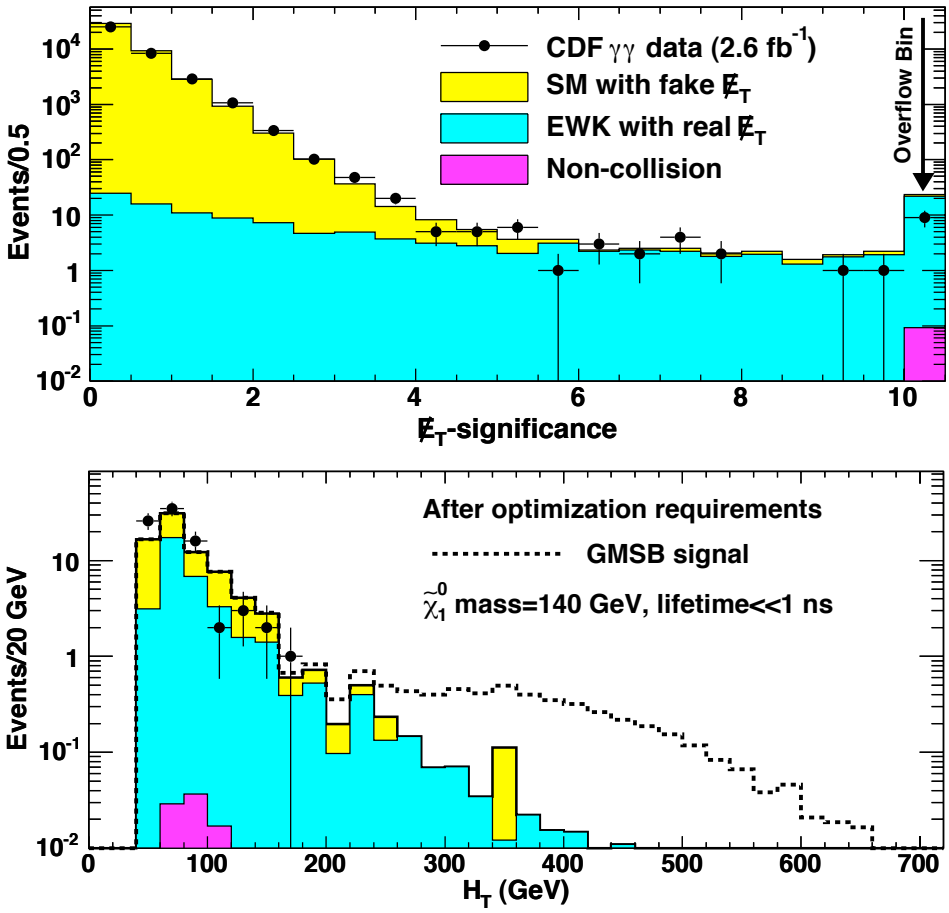

FIG. 51: The top plot shows the $\not\!\!E_T$-significance distribution for the inclusive $\gamma\gamma$ candidate sample, along with the background predictions. The bottom plot shows the predicted H_T distribution after all but the final H_T requirement.

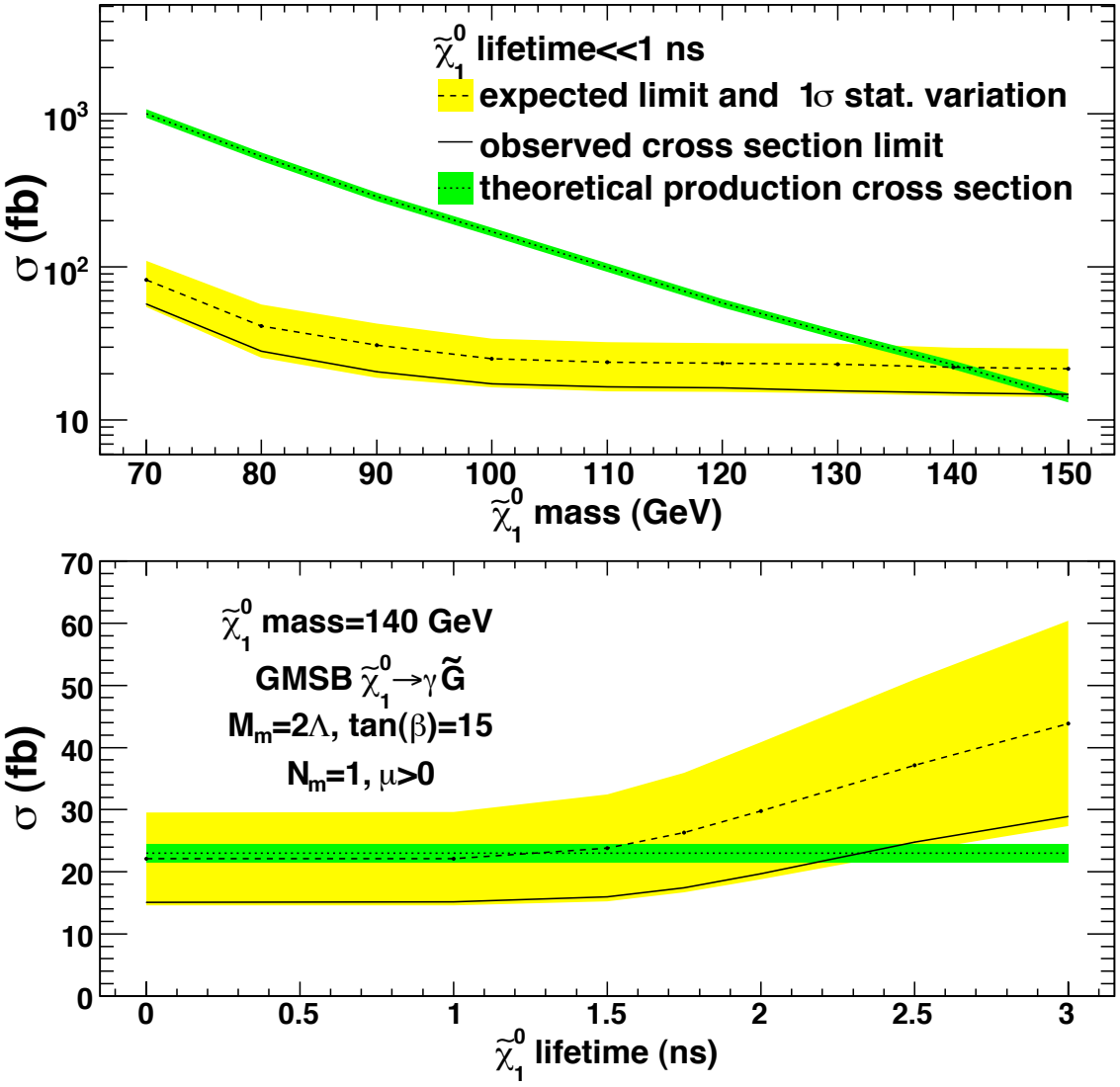

FIG. 52: The predicted and observed 95% C.L. cross section upper limits as a function of the $\tilde{\chi}_1^0$ mass at $\tau_{\tilde{\chi}_1^0} \ll 1$ ns (top) and as a function of the $\tilde{\chi}_1^0$ lifetime at $m_{\tilde{\chi}_1^0}$=140 GeV/c^2 (bottom). Indicated in green (darker shading) is the production cross section, along with its 8.0% uncertainty-band. In yellow (lighter shading) is the RMS variation on the expected cross section limit.

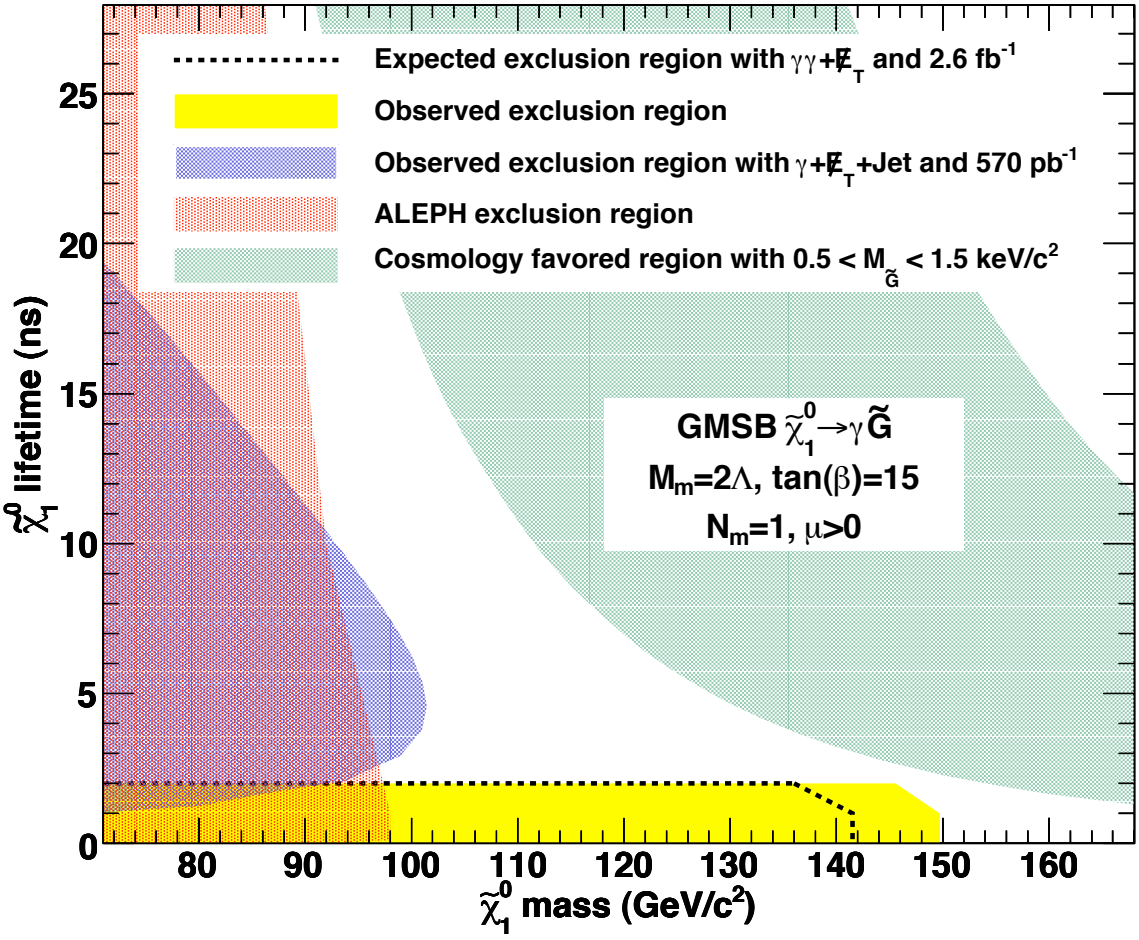

FIG. 53: The predicted and observed exclusion region along with the limits found in [18, 19]. The shaded band shows the parameter space where $0.5 < m < 1.5$ keV/c^2, favored by cosmological models [35].

VITA

Eun Sin Lee was born in Seoul, Korea. He graduated from Korea University with a B.S. in Physics in February 2000. He joined Texas A&M University in Fall 2002 as a graduate student in Physics. He received his M.S. in December 2005, specializing in experimental particle physics. In the Spring of 2005 he began working as a part of the CDF collaboration in experimental particle physics. He received a Ph.D. in Physics in May 2010. His permanent mailing address is Department of Physics, TAMU MS4242, College Station, TX 77843.

The typist for this dissertation was Eun Sin Lee.